Velocity Synchronous Approaches for Planetary Gearbox Fault Diagnosis under Non-Stationary Conditions

Yunpeng Guan

A thesis submitted to the Faculty of Graduate and Postdoctoral Studies in partial fulfillment of the requirements for the degree of

Doctor of Philosophy

in Mechanical Engineering

Ottawa-Carleton Institute for Mechanical and Aerospace Engineering
University of Ottawa
Ottawa, Canada

Abstract

Time-frequency methods are widely used tools to diagnose planetary gearbox fault under non-stationary conditions. However, the existing time-frequency methods still have some problems, such as smearing effect and cross-term interference, and these problems limit the effectiveness of the existing time-frequency methods in planetary gearbox fault diagnosis under non-stationary conditions.

To address the aforementioned problems, four time-frequency methods are proposed in this thesis. As nowadays a large portion of the industrial equipment is equipped with tachometers, the first three methods are for the cases that the shaft rotational speed is easily accessible and the last method is for the cases of shaft rotational speed is not easily accessible. The proposed methods are itemized as follows:

(1) The velocity synchronous short-time Fourier transform (VSSTFT), which is a type of linear transform based on the domain mappings and short-time Fourier transform to address the smear effect of the existing linear transforms under known time-varying speed conditions;

(2) The velocity synchrosqueezing transform (VST), which is a type of remapping method based on the domain mapping and synchrosqueezing transform to address the smear effect of existing remapping methods under known time-varying speed conditions;

(3) The velocity synchronous bilinear distribution (VSBD), which is a type of bilinear distribution based on the generalized demodulation and Cohen's class bilinear distribution to address the smear effect and cross-term interference of existing bilinear distributions under known time-varying speed conditions and

(4) The velocity synchronous linear chirplet transform (VSLCT), which is a non-parametric combined approach of linear transform and concentration-index-guided parameter determination to provide a smear-free and cross-term-free TFR under unknown time-varying speed conditions.

In this work, simple algorithms are developed to avoid the signal resampling process required by the domain mappings or demodulations of the first three methods (i.e., the VSSTFT, VST and VSBD). They are designed to have different resolutions, readabilities,

noise tolerances and computational efficiencies. Therefore, they are capable to adapt different application conditions. The VSLCT, as a kind of linear transform, is designed for unknown rotational speed conditions. It utilizes a set of shaft-rotational-speed-synchronous bases to address the smear problem and it is capable to dynamically determine the signal processing parameters (i.e., window length and normalized angle) to provide a clear TFR with desirable time-frequency resolution in response to condition variations.

All of the proposed methods in this work are smear-free and cross-term-free, the TFRs generated by the methods are clearer and more precise compared with the existing time-frequency methods. The faults of planetary gearboxes, if any, can be diagnosed by identifying the fault-induced components from the obtained TFRs. The four methods are all newly applied to fault diagnosis. The effectiveness of them has been validated using both simulated and experimental vibration signals of planetary gearboxes collected under non-stationary conditions.

Acknowledgement

First of all, I would like to thank my supervisor Professor Ming Liang and co-supervisor Professor Dan-Sorin Necsulescu for their help, time, guidance, detailed discussions and revisions of my work.

I would like to thank Professor Ming Liang and University of Ottawa for their financial supports during my Ph.D. study.

I am grateful to the students and visiting scholars in the group of Professor Liang. I learnt from them and had some good time with them during my study.

I would like to thank the committee members for reviewing this thesis.

Last but not least, I cannot find the words to express my gratitude to my family members who love me and always support me.

Table of Contents

List of figures

Lists of tables

Nomenclature

AOR	Angle-order representation
CWT	Continuous wavelet transform
DFS	Doppler frequency shift
FNR	Frequency-normalized-angle representation
FWR	Frequency-window-length representation
GD	Generalized demodulation
GLCT	Generalized linear chirplet transform
IF	Instantaneous frequency
ISAF	Instantaneous shaft angular frequency
ISRF	Instantaneous shaft rotational frequency
ISRP	Instantaneous shaft rotational phase
PCT	Polynomial chirplet transform
RMS	Root mean square
SNR	Signal-to-noise ratio
SET	Synchroextracting transform
SST	Synchrosqueezing transform
STFT	Short-time Fourier transform
TFNR	Time-frequency-normalized-angle representation
TFR	Time-frequency representation
TFWNR	Time-frequency window-length-normalized-angle representation
TFWR	Time-frequency-window-length representation
VSDFT	Velocity synchronous discrete Fourier transform
VSBD	Velocity synchronous bilinear distribution

VSLCT	Velocity synchronous linear chirplet transform
VSSTFT	Velocity synchronous short-time Fourier transform
VST	Velocity synchrosqueezing transform
WVD	Wigner-Ville distribution
ZAM	Zhao-Atlas-Marks distribution

Symbol

A	Ambiguity function
a	Scale
b	Translational value
C	Concentration index
c	Chirp rate
E	Average operation
F	Fourier transform
f	Frequency
f_{basis}	Frequency of basis
f_{carrier}	Carrier rotational frequency
f_{mesh}	Meshing frequency
f_{planet}	Planet gear fault characteristic frequency
f_{ring}	Ring gear fault characteristic frequency
f_{sht}	Sampling frequency
f_{shaft}	Instantaneous shaft rotational frequency
f_{sun}	Sun gear fault characteristic frequency
f_{sunrot}	Sun gear rotational frequency
f_{w}	Frequency covered by the window
$\overline{f}_{\text{w}}$	Averaged shaft rotational frequency within the window
g	Frequency-order relationship function
H	Hilbert transform
h	Transfer path effect
K	Concentration index

k	proportional ratio
N	Noise
N_p	Number of planet gears
M	Mask function
o	Order
$\overline{P}$	Linear transform kernel
P	Inverse linear transform kernel
p	Demodulator
$\overline{Q}$	Linear transform kernel
R	Representation of signal or Auto-correlation function
T	Synchrosqueezed representation
Z_{planet}	Planet gear tooth number
Z_{ring}	Ring gear tooth number
Z_{sun}	Sun gear tooth number
t	Time
W	Continuous wavelet transform or Wigner-Ville distribution
w	Window length
X_{AOR}	Angle-order representation
X_{TFR}	Time-frequency representation
x_{ana}	Analytic signal
x_{angle}	Angle-domain signal
x_{time}	Time-domain signal
x_{win}	Windowed signal
α	Normalized angle

ΔA_{TF}	Time-frequency area covered by the window
ΔA_{AO}	Angle-order area covered by the window
Δf	Window length in frequency
$\overline{\Delta f}$	Averaged frequency window length
$\Delta\tau$	Window length in time
$\Delta\phi$	Window length
δ	Dirac delta function
η	Doppler frequency shift
θ	Shaft phase (shaft angle)
λ	Window function
ξ	Angular frequency
τ	Time of the time-frequency representation or time delay
τ_w	Time covered by the window
φ	Shaft angle
Ψ	Complex mother wavelet,
ϕ_w	Angle covered by window
Ω	Order
Ω_w	Order covered by window
ω	Instantaneous angular frequency
ω_0	Centre angular frequency of the wavelet
σ	Parameter of window function

1 Introduction

1.1 Overview

Planetary gearboxes are extensively used in industrial applications, such as wind turbines (Zimroz et al., 2011), helicopters (Samuel and Pines, 2005) and cranes (Assaad et al., 2014), because of their compact size and high torque-to-weight ratio. The planetary gearboxes are often operated in severe working conditions and undergo variable heavy loads, therefore they are vulnerable to fault development. The faults of a planetary gearbox could lead to run time breakdowns, production losses and even catastrophic accidents. Therefore condition monitoring and fault diagnosis are important for applications of planetary gearbox (Lei et al., 2014).

The techniques of condition monitoring and fault diagnosis for rotational machinery have been widely developed. Various types of data have been analysed for fault diagnosis, including the vibration amplitude (Randall, 2011), acoustic emissions (Elforjani and Mba, 2011), thermal image (Younus and Yang, 2012) and oil debris particles amount (Bozchalooi and Liang, 2010). Among them, vibration analysis is the most widely used method in real applications, as vibration is easy to be measured and it contains rich information related to machine health conditions.

For a rotating machinery, bearings and gears are the most fault-prone parts due to the frequent metal-to-metal contact. Under a constant shaft speed condition, such faulty part will periodically contact other parts at fault characteristic frequency of that faulty part and generate some frequency components associated with that fault (McFadden, 1986; Wang et al., 2014). The frequency-domain methods diagnose faults by identifying such frequency components from the signal. To diagnose the planetary gearbox fault using frequency-domain methods, understanding the spectral pattern of planetary gearbox vibration is a prerequisite. Feng and Zuo (2012) investigated the sideband structures of the faulty planetary gearbox vibrations and provided models of the faulty planetary gearbox vibrations with sun, planet and ring gear faults. They found faulty gear would cause amplitude modulation and frequency modulation of meshing frequency and its harmonics, which in return generate some specific sidebands. Based on this vibration model, planetary

gear fault can be diagnosed by identifying the sidebands associated with fault from the spectrum (Feng and Liang, 2014a) or by identifying the frequency components associated with fault from the spectrum of the demodulated signal (Feng et al., 2012; Feng et al., 2013b).

Planetary gearbox often works under non-stationary conditions (non-stationary condition refers to a state that the external load and/or gearbox running speed varies over time), e.g., the planetary gearboxes of helicopters (Zhou et al., 2018) and wind turbines (He et al., 2018). The vibration signals collected under non-stationary conditions commonly contain more abundant fault symptoms, which cannot be found under stationary conditions (Li et al., 2005). Hence, fault diagnosis of planetary gearbox under non-stationary conditions draws increasing attentions nowadays. Under non-stationary conditions, the vibration signal components are non-stationary (a non-stationary signal in this thesis denotes a signal containing components with time-varying frequencies and/or amplitudes).

The time-frequency method is a good technique for processing non-stationary signals. It analyses signals in both time and frequency domains simultaneously (Feng et al., 2013a), thus it provides more information than the order-domain method, which only analyses signals in one domain. In the field of fault diagnosis of gearboxes, the time-frequency method commonly works by generating a time-frequency representation (TFR) of the collected vibration signal and the fault, if any, can be diagnosed by identifying the time-varying sidebands and impulses caused by gear fault. To date, various time-frequency methods have been proposed. Linear transform, remapping method and bilinear distribution are three main families of widely used time-frequency methods.

Linear transform is realized by calculating the inner product of the sliding-window-covered signal and the transform basis (Feng et al., 2013a). The advantage of linear transform is that it is easy to be implemented and has good computational efficiency. However, Linear transforms are subject to the Heisenberg uncertainty principle, thus their time-frequency resolutions are limited (Hlawatsch and Boudreaux-Bartels, 1992), and the energy concentration of the linear transform is relatively low. The short-time Fourier transform (STFT), continuous wavelet transform (CWT) (Zheng et al., 2002) and chirplet

transforms (Mann and Haykin, 1995) are significant representations of linear transform family. One of their drawbacks is that they have TFR smear effects for analysing the vibration signals collected from rotational machinery under non-stationary conditions. To illustrate the smear effect, two example signals are introduced here. The first signal is stationary, with length 4 s and frequency 6 Hz, expressed by

$$s_1(t) = \sin\left(12\pi t\right) \tag{1-1}$$

The second signal is a non-stationary signal with time-varying frequency. The signal length is also 4 s and expressed by

$$s_2(t) = \sin\left[2\pi \int_0^t f_2(\tau)\,\mathrm{d}\tau\right] \tag{1-2}$$

where

$$f_2(t) = 10\text{-}2t\,. \tag{1-3}$$

The frequency trajectory of the first signal is shown in Fig. 1-1(A) and the TFR obtained by the STFT is shown in Fig. 1-1 (B). It can be seen that the TFR clearly reveals the signal frequency. The frequency trajectory of the second signal is shown in Fig. 1-2(A) and the STFT result is shown in Fig. 1-2 (B). The smear effect can be easily seen in the result (i.e., the revealed signal energy is scattering compared with Fig. 1-1 (B)).

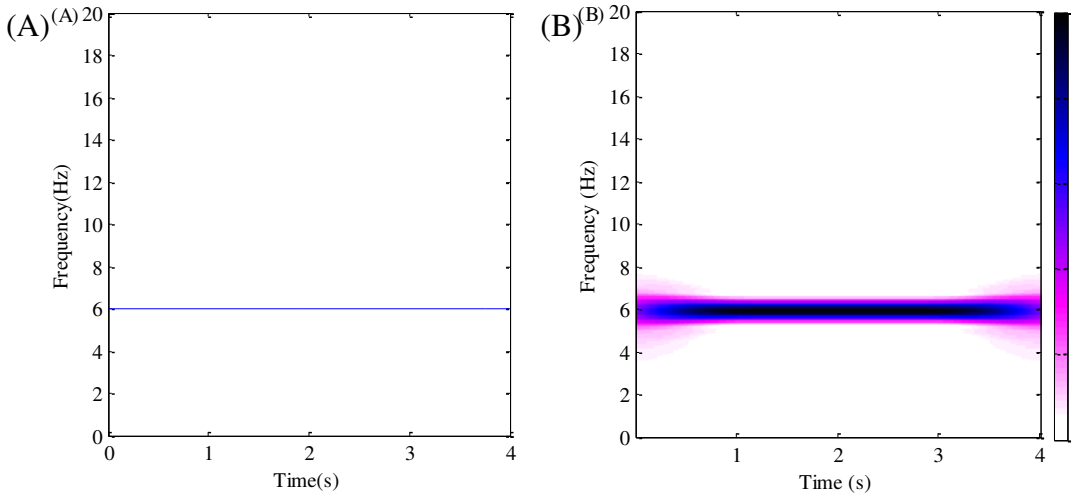

Fig. 1-1. TFR of the signal s_1: (A) True instantaneous frequency and (B) TFR obtained by the STFT

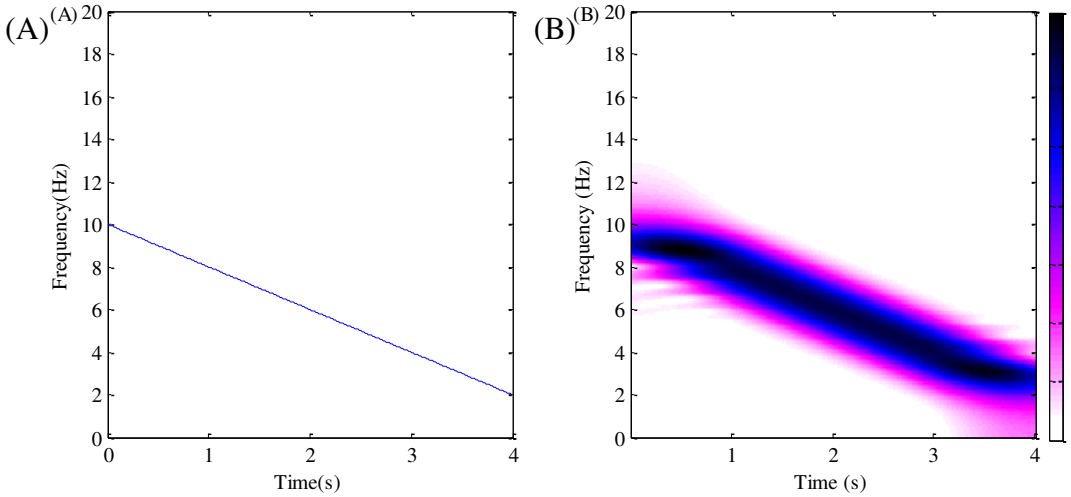

Fig. 1-2. TFR of the signal s_2: (A) True instantaneous frequency and (B) TFR obtained by the STFT

The remapping method is a kind of post-processing technique based on the linear transform. Two well-known examples of remapping method are the reassignment method (Auger and Flandrin, 1995) and synchrosqueezing transform (SST) (Daubechies et al., 2011). The remapping methods firstly employ a linear transform (commonly the wavelet transform) to obtain an initial TFR and then remap the initial TFR data to new locations to obtain a TFR with better energy concentration and readability. However, such methods cannot completely solve the smear problem (Li and Liang, 2012b, a; Feng et al., 2015a) and the recent research showed the remapping methods cannot improve the time-frequency resolution (Iatsenko et al., 2015).

Bilinear distribution is another kind of time-frequency method (Hlawatsch and Boudreaux-Bartels, 1992), it has better time-frequency resolution and energy concentration than linear transform. However, bilinear distributions have smear effect for the frequency components that cannot be characterized by linear law (Boashash and Shea, 1994) and it has cross-term interference for multi-component signals. To illustrate the cross-term interference, a two-component signal is introduced here. This signal contains two linearly increasing frequency. The signal length is 3 s and expressed by

$$s_3(t) = \sin\left[2\pi\int_0^t f_3(\tau)\,\mathrm{d}\tau\right] + \sin\left[2\pi\int_0^t 2f_3(\tau)\,\mathrm{d}\tau\right] \tag{1-4}$$

where

$$f_3(t)=15t+60. \tag{1-5}$$

The frequency trajectory of the first signal is shown in Fig. 1-3(A) and the TFR obtained by the WVD is shown in Fig. 1-3(B). It can be seen that two signal components are clearly revealed. However, an additional component is also introduced and it does not have any physical meaning. This is the cross term and it interferes the interpretation of the TFR. To resolve the smear problem and cross-term interference, many methods have been proposed, for example, polynomial Wigner-Ville distribution (Boashash and Shea, 1994) and Cohen class bilinear distributions (CCBD) (Cohen, 1989). However, none of them is able to resolve these two problems simultaneously.

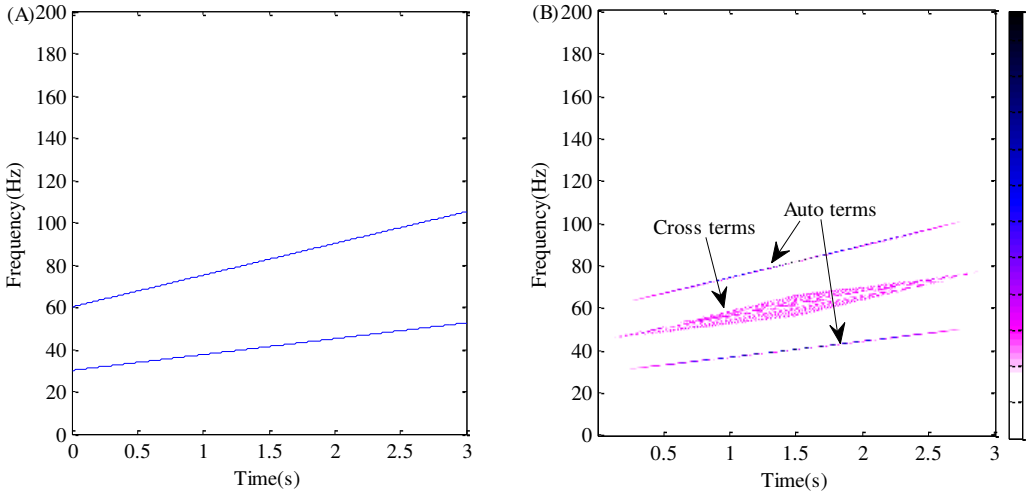

Fig. 1-3. TFR of the signal s_3: (A) True instantaneous frequencies and (B) TFR obtained by the WVD

The computational efficiency is important for condition monitoring and fault diagnosis, especially for online applications. Linear transform is realized by applying an integral transform on a matrix formed by segmented signals. The remapping method is realized by calculating the linear transform and remapping the result, thus the computational efficiency of remapping method is commonly worse than the linear transform (Guo et al., 2014; Li et al., 2016; Yu et al., 2017; Hu et al., 2018). Bilinear distributions generally have worse computational efficiency than both the linear transforms and remapping method (Zhenyu et al., 1994; Boultadakis et al., 2009; Li et al., 2016). This is because the bilinear

distribution is realized by applying an integral transform on a matrix that is much larger than the counterpart matrix of linear transform. Besides, the bilinear distribution spends additional time on supressing the cross terms, compared with linear transform and remapping method.

Based on the above analysis, the features of these three types of time-frequency methods are summarized in Table 1-1. It can be seen that for the application of vibration analysis under non-stationary conditions, these three types of methods share the problem of smear effects. The bilinear distribution is the only type of methods having cross-term interference. The performances of these three types of methods are assessed from two aspects, time-frequency resolution and energy concentration. The linear transform performs badly in both aspects. The remapping method improves the readability of linear transform. The bilinear distribution has both good time-frequency resolution and good energy concentration inherently. Therefore, their performances can be ranked: bilinear distribution > remapping method > linear transform. Their rank in order of computational efficiency, on the contrary, is ordered as linear transform > remapping method > bilinear distribution. This shows that better performance requires longer computational time. Based on the above analysis, each type of time-frequency methods has its own advantages and disadvantages and different methods are suited to serving under different application environments (for example, online or offline).

Table 1-1 Features of the time-frequency methods for analyzing non-stationary vibration signals

Method name		Linear transform	Remapping method	Bilinear distribution
Drawback	Smear effect	Yes	Yes	Yes
	Cross-term interference	No	No	Yes
Performance	Energy concentration	Low	High	High
	Time-frequency resolution	Low	Low	High
Computational efficiency		Fast	Medium	Slow

1.2 Motivation and proposed study

Based on the above analysis, the objectives of this thesis are to develop time-frequency methods to address the drawbacks of existing time-frequency methods mentioned above for fault diagnosis of planetary gearbox under non-stationary conditions. Nowadays, tachometers have been installed in a large portion of industrial planetary gearboxes to record the running speeds. In some situations, the running speed can also be easily estimated from the signal TFR obtained from the STFT. Such speed information has not been utilized yet by the existing time-frequency methods to address their drawbacks. Therefore, the first three objectives of this thesis are to address the drawbacks of existing linear transforms, remapping methods and bilinear distributions with the help of shaft rotational speed information. That is to develop

1) a smear-free linear transform;

2) a smear-free remapping method and

3) a cross-term-free and smear-free bilinear distribution.

Hence, three time-frequency methods, the velocity synchronous short-time Fourier transform (VSSTFT), velocity synchrosqueezing transform (VST) and velocity synchronous bilinear distribution (VSBD), are proposed. They employ domain mapping technique or demodulation technique according to the shaft rotational speed to address the drawbacks of existing linear transforms, remapping methods and bilinear distributions respectively. These methods have different resolution, readability, noise tolerance and computational efficiency, thus they can be selected by user according to the application environment and user needs.

In industrial applications, there also some planetary gearboxes that do not have tachometer to record its running speed and the shaft speed may not be easily estimated from the STFT of the vibration signal due to the noise or smear effect of the STFT.. Therefore, the last objective of this thesis is to develop a cross-term-free and smear-free time-frequency method for fault diagnosis of planetary gearbox under non-stationary conditions without using shaft rotational speed and the corresponding developed method is named velocity synchronous linear chirplet transform (VSLCT).

The rest of the thesis is structured as follows. Chapter 2 gives a literature review of the planetary gearbox vibration models and existing signal processing techniques for planetary gearbox fault diagnosis. The VSSTFT, VST, VSBD and VSLCT for planetary gearbox fault diagnosis under non-stationary conditions are presented in Chapter 3, 4, 5 and 6 respectively. A comparison study about the four proposed methods are presented in Chapter 7. Conclusions and suggested future work are given in Chapter 8.

2 Literature review

In this chapter, the vibration models of planetary gearbox are reviewed first. Then the signal processing methods for fault diagnosis of planetary gearbox are summarized with reviews according to their categories, i.e., time-domain method, frequency-domain method, order-domain method and time-frequency method.

2.1 Planetary gearbox vibration models

In order to detect and diagnose gear fault of planetary gearboxes from their vibration signals, it is important to know their vibration behaviours. For this purpose, researchers have constructed several vibration models of planetary gearboxes.

To measure the planetary gearbox vibration signals, the sensor is often mounted on a fixed location of the gearbox housing. McFadden and Smith (1985) found that the spectrums of the vibration signals collected under such sensor setup have asymmetrical sidebands. To explain this phenomenon, they investigated the vibration of planetary gearbox and constructed a simple model. The sensor-perceived vibration was modelled as a summation of the sensor-perceived vibrations from all the planet gears. As the transfer paths between the vibration origins and the sensor are time-varying and the planet gears and carrier revolve with respect to the fixed sensor, the sensor-perceived vibration from individual gear was modelled as an amplitude modulation process. In this model, the meshing frequency and its harmonics act as the carrier frequencies, and carrier rotating frequency act as the modulating frequency. Based on this model, the asymmetry of sidebands was explained as the result of the phase difference of the individual vibrations from different planet gears. This work was later generalized by McNames (2001) using continuous-time Fourier series analysis.

Chaari et al. (2006c) investigated the vibration of planetary gearbox with eccentricity or profile errors. They found such faults change the dynamic behaviour seriously and cause modulation of the gear meshing vibration, which generates sidebands around gear meshing frequency and its harmonics. They also found tooth cracks and pitting will cause reduction of gear stiffness and this leads to amplitude modulations of gear meshing vibration. Such modulation can be reflected by the high activity of sidebands in the spectrum (Chaari et al., 2006a).

Inalpolat and Kahraman (2009) constructed an analytic model to explain the modulation sidebands of planetary gearbox. The model employed the geometry parameters of planetary gearbox, such as number of planets, the position angles (defined as the angles between the planet gears), and the reference planet gear and planet phasing relationships (defined by the position angles and the number of teeth of the gears). Based on that model, Inalpolat and Kahraman (2009) found the symmetric sidebands only occur when the planet gears are in-phase and equally spaced. They further extended this model by taking periodically time-varying gear mesh stiffness and the nonlinearities into consideration and applied the new model to predict modulation sidebands of planetary gearbox having manufacturing errors (Inalpolat and Kahraman, 2010).

Mark and Hines (2009) developed a vibration model of planetary gearbox considering angular errors of planet-support angular locations, non-uniform planet gear loading and ring-gear manufacturing errors. This model was later extended by including the effects of planet-carrier torque modulations (Mark, 2009).

Hong et al. (2014) presented vibration model of both healthy and faulty equally spaced planetary gearbox, considering both the gear meshes between the planets and the annulus as well as the meshes between the planets and the sun gear. Based on this model, the gear fault will cause specific sidebands around meshing frequency and its harmonics. Feng and Zuo (2012) modeled the faulty planetary gearbox vibrations and summarised the symptoms of both local and distributed faults of sun, planet and ring gears and derived the equations for calculating the fault characteristic frequencies of planetary gearboxes. The sensor-perceived vibration is modeled as a modulated signal with meshing frequency and its harmonics as carrier frequencies. This model is provided in Appendix A and employed in the simulation evaluation sections of this thesis.

2.2 Time-domain methods

Time-domain methods directly process the signal in time domain for fault diagnosis. The main time-domain methods for condition monitoring and fault diagnosis of planetary gearbox include condition indicators based on statistical parameter, time synchronous averaging (TSA) and vibration separation.

The TSA method is a classic time-domain method of separating periodic signals from non-periodic noise. In practice it is implemented by averaging a series of signal segments that are synchronised with the rotation of the gear of interest (McFadden, 1987b, a, 1989). Based on the TSA, McFadden presented a vibration separation technique to isolate the tooth meshing vibration of individual planet gears and the sun gear (McFadden, 1991). The technique was further improved by using a Hanning window to suppress the sidelobe (McFadden, 1994). Yip (2011) applied health indicators and statistical control charts based on the TSA model to diagnose planetary gearboxes used in oil sands operations. Yu (2011) employed the wavelet transform to the residual signal of TSA signal to evaluate the planetary gear fault advancement quantitatively.

Researchers proposed various time-domain fault indicators, for example, root mean square (RMS) (Rzeszucinski et al., 2012), kurtosis (Heng and Nor, 1998) and crest factor (Pachaud et al., 1997). In the presence of damage, the values of such indicators may change, thus the fault can be detected by comparing the current indicator value with the value in healthy condition. Zhao et al. (2013b) summarized 18 time-domain statistical indicators for fault detection of planetary gearbox. Keller and Grabill (2003) modified several standard time domain fault indicators, such as FM0 and FM4, for planetary gearbox carrier fault detection. Samuel and Pines (2003) calculated the prediction error of wavelet transform using the time domain lifting scheme and used the prediction error as a fault indicator of planetary gearbox. They later improved this method by introducing a time-domain diagnostic metric based on the lifting prediction error vector (Samuel and Pines, 2009). Lei et al. (2012) applied the RMS to the filtered signal instead of the original signal to exclude the interference components, such as meshing components and sideband components. Liu et al. (2014) developed a time-domain feature selection algorithm to determine fault-sensitive features and select them for fault level diagnosis of planetary gearboxes. Abouel-seoud (2017) tested various condition monitoring indicators for evaluating the fault severity of planetary gearbox via stationary vibration signal. These indicators include RMS, skewness, kurtosis, crest factor and higher order statistics indices. Among them, the RMS performs best for early fault detection. Liang et al. (2016) decomposed the signal into the vibration waveforms of each planet gears using windowing-and-mapping method and found that the vibration waveform of faulty planet gear tooth has

relatively higher RMS value. Chen and Shao (2013) proposed a vibration mode of planetary gearbox and the simulation result showed that the crack growth caused significant change of crest factor. Lei et al. (2012) developed two novel statistical indicators for fault diagnosis of planetary gearbox, i.e., normalized summation of the positive amplitudes of the difference spectrum between the signal under analysis and the healthy signal, and RMS of the filtered signal.

Though the above time domain methods can possibly diagnose planetary gearbox fault under a stationary condition, they are not suitable for analysing the planetary gearbox vibration signal collected under non-stationary conditions. The TSA and vibration separation assume the vibration signals are stationary. For these method, even small speed fluctuation would cause great loss of information in the averaged result. The time domain fault indicators are sensitive to shaft speed and load, and thus are only suitable for analysing stationary signals. Furthermore, to apply such methods to the signal collected under a non-stationary condition, the reference indicator levels when the machine operate at the same non-stationary condition must be known in advance for comparison. However, such information is not always easily accessible.

2.3 Frequency-domain methods

Frequency-domain analysis is a widely used approach in the field of fault diagnosis and condition monitoring of rotational machinery and it is commonly done by analysing the spectrum obtained using the Fourier transform. The frequency-domain methods for gearbox fault diagnosis are based on the fact that under a constant shaft speed, the gears with tooth fault will periodically contact other parts, thus generating some specific frequency components. As such, a fault may be detected by tracking the number and amplitude of such components, and fault location can be detected by identifying the features of the revealed frequency components (Randall, 1982; McFadden, 1986; Dalpiaz et al., 2000).

In real applications of planetary gearbox fault diagnosis, the signals are usually pre-processed before applying Fourier transform to extract frequency domain information. This is because a practical vibration signal commonly contains noise and interference of other mechanical components. Pre-processing techniques can strengthen such fault features and

supress the noise and interference to increase the accuracy of fault diagnosis. For example, Mark et al. (2010) proposed a method to eliminate the effects of transducers and structural-path-caused amplitude changes for early fault detection of a planetary ring gear. Liu et al. (2012) employed local mean decomposition to extract the gear fault frequency feature from vibration signals and diagnose a seeded crack fault in a wind turbine planetary gearbox. Feng and Liang (2014a) applied an iterative atomic decomposition approach to suppress background noise interferences before spectral analysis. Though the above methods successfully diagnose fault from planetary gearbox, they require the analyst to have a thorough knowledge about the spectral property of a planetary gearbox, because the vibration signal from a planetary gearbox has complex sidebands regardless whether it is in healthy or faulty conditions.

Recently, Bartelmus et al. developed several frequency-based methods for planetary gearbox fault diagnosis under time-varying load working conditions (Bartelmus and Zimroz, 2009a, b; Bartelmus et al., 2010; Zimroz and Bartkowiak, 2013). They introduced an indicator that reflects the linear dependence between the meshing frequency amplitude and the operating condition (Bartelmus and Zimroz, 2009a) and found that planetary gearbox in a bad condition is more load-susceptible than a gearbox in a good condition (Bartelmus and Zimroz, 2009b). Bartelmus et al. (2010) introduced planetary gearbox vibration models under time-varying non-stationary load and adopted energy-based parameters for fault diagnosis. More recently, Zimroz and Bartkowiak (2013) suggested two multivariate methods, principal component analysis and canonical discriminant analysis for planetary gearbox condition monitoring under time-varying load conditions.

As the gear faults may cause amplitude and frequency modulations and the modulating frequencies are related to the fault characteristic frequencies, it was proposed to analyse the demodulated signals instead of the raw vibration signal for planetary gearbox fault diagnosis (Feng et al., 2012; Feng et al., 2013b). As most demodulation techniques require the target signal to be a mono-component signal, it is suggested to decompose the signal into mono-components before demodulation. For example, Feng et al. (2012) employed the empirical mode decomposition to decompose the signal into intrinsic mode functions, and then applied energy separation algorithm to estimate the amplitude envelope and

instantaneous frequency of the selected intrinsic mode function. The fault diagnosis of a wind turbine planetary gearbox can be accomplished by analysing the envelope spectrum and instantaneous frequency spectrum. Later, Feng et al. (2013b) proposed to use local mean decomposition to decompose the signal and applied it to diagnose pitting and wear fault of a planetary gearbox. Recently, Feng et al. (2016b) proposed to use intrinsic time-scale transform to decompose the signal and diagnose gear fault by analysing one of the obtained mono-component whose frequency is around meshing frequency or its harmonics. Wen et al. (2016) proposed to demodulate the signal by wavelet enveloping, then reduce the noise by manifold learning and finally diagnose gear fault by analysing the envelope spectrum for planetary gearbox. One difficulty of demodulation of planetary gearbox vibration is that the carrier frequency (i.e., meshing frequency or its harmonics) may be weak because the sensor-perceived vibration is the combination of the vibrations from each planet gear and they may cancel out each other (McFadden and Smith, 1985).

Most frequency-based methods assume that the rotating speed is constant or has limited speed fluctuation. Large speed variation will cause spectral smearing problem. As a result, those frequency-based tools are valid only under the condition that the rotational speed is constant or near constant.

2.4 **Order-domain methods**

Most vibration signals collected from rotational machinery contain strong components that are synchronous with the shaft rotational speed. It is usually more effective to analyse the signal using orders (multiples of shaft rotational speed) than using absolute frequencies. The order domain methods can be classified into three main groups, i.e., Vold-Kalman filter based methods (Vold et al., 1997), computed order tracking (COT) methods (Fyfe and Munck, 1997) and transform based methods (Blough et al., 1997).

The Vold-Kalman filter based methods separate the signal components using time-varying Kalman filter and estimate the amplitudes of these components using demodulation techniques. The potential difficulties in the implementation of this method include its complexity in solving the complex structure and data equations of the Kalman filter. The family of the COT methods converts the time-domain signal into the stationary angular-domain signal by resampling the vibration signal at a constant shaft angular increment and

then calculates the signal order spectrum by applying Fourier transform to the resampled signal. One disadvantage of COT is that it introduces interpolation errors into the result, as stated in the introduction chapter. The family of the transform based methods directly converts the signal from time domain into order domain, and thus it is simpler than the Vold-Kalman filter based methods and COT methods. The transform based methods do not resample the signal, so they avoid the interpolation errors of the COT methods. The first transform based method is probably the time variant discrete Fourier transform (Blough et al., 1997; Blough, 2003). Borghesani et al. (2014) improved this method by correcting the non-orthogonality problem of the kernels and the new method was named the velocity synchronous discrete Fourier transform (VSDFT). One difficulty of the above three types of methods is that they require an accurate tachometer to provide the information of shaft speed. The additional tachometer will increase the cost, cause possible problem of machine adjustment and may not be always technically feasible to mount on a less accessible location. To resolve these difficulties, it was proposed to extract shaft speed from the vibration signal firstly and then perform order-domain methods accordingly (Bonnardot et al., 2005; Combet and Gelman, 2007; Urbanek et al., 2013; Zhao et al., 2013a; Coats and Randall, 2014). The author of this thesis et al. proposed an order-domain method, named generalized velocity synchronous Fourier transform (GVSFT), for fault diagnosis of fixed-shaft gearbox under non-stationary conditions (Guan et al., 2018) and the scheme of this method is briefly given in Appendix C.

There are limited researches on the order-domain methods for planetary gearbox condition monitoring and fault diagnosis. Villa et al. (2011) suggested performing the COT on the planetary gearbox vibration signal of wind turbine by employing some holes on rotor to measure shaft speed. However, this method is only applicable to the situation where such hardware is available. Combet and Zimroz (2009) estimated the speed fluctuation of planetary gearbox using the short-time scale transform and performed COT according to the estimated speed fluctuation to diagnose planetary gearbox with tooth wear. However, this method is not applicable when the speed fluctuations are strong. Popiołek and Pawlik (2016) generated the order spectrum by signal resampling and used Multilayer Perceptron Network to classify the fault type for fault diagnosis of planetary gearbox under time-varying speed and load conditions. Feng et al. (2016a) suggested to generate order

spectrums of raw signal, amplitude-demodulated signal and frequency-demodulated signal for fault diagnosis using iterative generalized demodulation. This method first identifies the signal component from the TFR obtained by the STFT, then extracts them by iteratively applying generalized demodulation and generating the order spectrums by combining the Fourier spectrums of the extracted components. This method has component missing problem, because some components may be not detected in the TFR due to the limited resolution and smear effects of the STFT. He et al. (2016) proposed a method for order analysis of planetary gearbox vibration without tachometer. With this method, the meshing frequency is firstly estimated based on energy centrobaric correction and the first moment of TFR, then the signal is resampled according to obtained meshing frequency for order analysis.

Though the methods mentioned above diagnosed gear faults of planetary gearboxes to some extent, the order-domain methods cannot provide any time-domain information. The peaks in the order spectrum can be roughly seen as the average amplitude of the corresponding harmonic. Under non-stationary conditions, some of the harmonics may only occur in a short time duration in comparison to the whole time span of the signal under analysis. The average amplitudes of such components are relatively low, thus they may be buried in the noise of order spectrum. In addition, these methods are realized by resampling the vibration signals of planetary gearboxes, thus they suffer from interpolation errors. The above mentioned drawbacks limit the effectiveness of the order-domain methods.

2.5 Time–frequency methods

Time-frequency methods analyse the signal in both time and frequency domain simultaneously and they are widely used in the field of non-stationary signal analysis. In the applications of fault diagnosis, these methods commonly firstly generate a time-frequency representation (TFR) for the collected vibration signal and the fault, if any, can be diagnosed by identifying the time-frequency components related with fault or the spacing between the impulses induced by fault (Feng et al., 2013a). Three main types of time-frequency methods are linear transform, remapping method and bilinear distribution. They are reviewed in the forthcoming sections and other important time-frequency methods that do not belong to these three families are reviewed after these sections.

2.5.1 Linear transforms

Linear transform is one big family of the time-frequency methods and it can be seen as a process to represent the signal using the weighted and phase-shifted bases of the transform employed. One of the linear transform advantages is good computational efficiency, because the linear transforms can be realized using simple and fast algorithms.

One drawback of linear transform is that smearing effects occur on the signal components whose frequencies do not match the frequencies of the corresponding transform bases. The short-term Fourier transform (STFT) (Allen, 1977; Allen and Rabiner, 1977) and continuous wavelet transform (CWT) (Daubechies, 1992) are two traditional linear transforms. The frequencies of their bases are fixed, thus their capabilities in analysing the signals with varying frequencies are limited. The TFRs of the non-stationary signals obtained by the STFT and CWT are commonly smeared due to this reason. The chirplet transform and its variants employ bases with time-varying frequencies, thus they are able to address the smear issues to some extent. Some examples are the chirplet transform (Mann and Haykin, 1995), polynomial chirplet transform (PCT), (Peng et al., 2011; Yang et al., 2013), Spline-Kernelled Chirplet Transform (Yang et al., 2012b)and warblet transforms (Yang et al., 2012a). The drawbacks of these methods are that the chirp rates of their bases are identical, thus they can only address the smear issue of the component(s) whose chirp rate match the pre-set chirp rate of the transform. The non-stationary vibration signals usually contain multiple components and their chirp rates are different. Thus the TFR obtained by the chirplet transforms can only eliminate the smear of one component but all the other components are still subjected to smearing effect.

Another pitfall of linear transform is that its time-frequency resolution is limited due to the Heisenberg uncertainty principle (Hlawatsch and Boudreaux-Bartels, 1992). The increase of the resolution over one dimension (time or frequency) will cause the decrease of the resolution over another dimension (Gabor, 1947). The resolution is controlled by one parameter, the window length, which commonly must be provided by the user. Most of the existing linear transforms employ windows with time-invariant window lengths, thus the time resolution and frequency resolution of the resulted TFR are time-invariant. However, the features of the non-stationary signals are time-varying thus the existing linear transforms may lack the ability to provide a suitable time-frequency resolution. Some linear

transforms also involve other parameters, such as the bases-chirp-rates-related parameters of the linear chirplet transform and its variants. For the fault diagnosis applications, wrongly selected parameters may lead to inaccurate TFRs and incorrect diagnostic decisions. Therefore, the existing linear transforms require the user to have a good knowledge of the signal and the linear transform mechanism. The problems of smearing effect and parameter requirement limit the effectiveness of linear transform family.

Some applications of linear transforms on the planetary gearbox condition monitoring and fault diagnosis are reviewed as follows. Samuel and Pines (1997) computed the mean square wavelet map using the harmonic wavelet transform algorithm to classify planet gear faults. Samuel and Pines (2000) separated the vibration signal into the vibrations of individual planet gears and diagnosed planet seeded fault by analysing the separated signal using the CWT. Saxena et al. (2005) applied the CWT to analyse vibration signal of a helicopter planetary gearbox and diagnosed a crack fault of carrier using a feature extraction technique based on wavelet domain. Zimroz et al. (2010) estimated the instantaneous shaft frequency of planetary gearbox from an average of the less-noisy meshing harmonics identified from signal TFR obtained by the STFT. Jiang et al. (2011) proposed a de-noising method based on adaptive Morlet wavelet transform and singular value decomposition, and then applied it to diagnose wind turbine planetary gearbox faults.

2.5.2 Remapping methods

The remapping method is a family of post-processing techniques based on the linear transforms, including the reassignment method (RM), (Auger and Flandrin, 1995; Chen and Feng, 2016b), synchrosqueezing method (SST) (Daubechies et al., 2011; Thakur and Wu, 2011) , synchroextracting method (SET) (Yu et al., 2017) and many variants of them. These methods firstly employ a classic linear transform (commonly the CWT) to obtain an initial TFR and then generate the final TFR by remapping the initial TFR data to new coordinates based on the phase of the initial TFR. In this way, the remapping method sharpens the ridges of the employed linear transform and provides a TFR with better energy concentration and readability. The SST may be the most widely used remapping method. However, research shows the SST still has smearing effects along time dimension for the components with time-varying frequencies, whereas it does not have smearing effect for the components with fixed frequencies (Li and Liang, 2012a, b). To resolve the smear

problem of the SST, Li and Liang (2012b) proposed a remapping method, named generalized synchrosqueezing transform (GST), based on the generalized demodulation (GD) and the SST. The GD is a technique to map one component of a signal into a component with the pre-set frequency with its original amplitude (Olhede and Walden, 2005; Shi et al., 2016a; Shi et al., 2016b). The GST firstly employs the GD to map the component of interest into a component with fixed frequency, then apply the SST and finally restore the signal TFR based on the SST result. However, this method can only eliminate the smearing effect on the selected component and the smearing effects on other components still remain. A research conducted by Iatsenko et al. (2015) showed if the adjacent signal components cannot be separated by the linear transform employed by the remapping method, they cannot be separated after the post processing of the remapping method either. In other words, the remapping methods cannot improve the time-frequency resolution of the linear transform.

The applications of remapping methods on the planetary gearbox fault diagnosis are limited, so the review is extended to the ones on the fault diagnosis of general gearboxes. Li and Liang (2012b) applied the GST to detect the fault of fixed-shaft gearbox by identifying the fault-induced sidebands of meshing frequency. Imaouchen et al. (2015) introduced a gear fault diagnosis method based on the SST and Lempel-Ziv complexity method. Chen and Feng (2016a) applied the reassigned method to reveal the fault-induced abnormal sidebands and impulses from planetary gearbox vibration signals collected from in situ wind turbine. Hu et al. (2018) employed higher-order SST to generate the signal TFR and identified the fault features from a planetary gearbox vibration signal via the multi-taper empirical wavelet transform algorithm.

2.5.3 Bilinear distributions

Bilinear distribution is another widely used family of time-frequency methods. The name of the bilinear distribution origins from that it employs the quadratic form of the signal in the formula. The Wigner-Ville distribution (WVD) may be the most basic version of all the bilinear transforms and it is formulated by the Fourier transform of the autocorrelation function of the signal with respect to the time delay (Hlawatsch, 1991; Pereira de Souza Neto et al., 2001). One of the advantages of the WVD is that it has better

time-frequency resolution inherently and can perfectly reveal the impulse, constant frequency and linear chirp.

However, the WVD still has several drawbacks which limit its effectiveness. The first drawback is that it has smear effect on the components with non-linear frequencies. To address this issue, Boashash and Shea (1994) proposed the polynomial WVD, which uses a higher order kernel to supress the smear. However, this method requires that the signal must be finely sampled for interpolation and the signal frequency must be able to be well represented by a polynomial.

The second drawback of the WVD is cross-term interference. To resolve this drawback, many methods were proposed, for example, the Affine class bilinear distributions and Cohen class bilinear distributions (CCBDs). The CCBDs may be the most widely used bilinear distributions with suppressed cross terms and they work by using a kernel in ambiguity domain to filter out the cross terms (Cohen, 1989), e.g., Choi-Williams distribution (Choi and Williams, 1989b) and Zhao-Atlas-Marks distribution (ZAM) (Zhao et al., 1990; Rajagopalan et al., 2008; Climente-Alarcon et al., 2013). For most signals in general, in ambiguity domain, the unwanted cross terms are tend to be away from the origin, whereas the auto terms are tend to be close to the origin. More specifically, the auto terms of impulses, fixed frequencies and linear frequencies are located at Doppler frequency shift axis, delay axis and a straight line passing the origin respectively in ambiguity domain. Hence, a properly designed kernel function with passband around the origin may filter out the cross-terms. However, the reduced interference is at the cost of resolution and to select a suited kernel, one needs prior knowledge of the locations of the cross terms and auto terms in ambiguity plane. Such kernels commonly contain one or several parameters that need to be provided by the user, and unsuitable parameters may lead to an inaccurate TFR.

The computational complexity of bilinear distribution is generally higher than their counterparts, thus most bilinear distributions are not suited for online applications. The drawbacks mentioned above limit the applications of bilinear distributions in the field of condition monitoring and fault diagnosis of planetary gearboxes.

Some applications of bilinear distributions on fault diagnosis of planetary gearboxes are reviewed as follows. Meltzer and Ivanov (2003) applied the Choi–Williams distribution

with rotational-speed-adapted integral kernels to diagnose planetary gearbox fault of a passenger car. Chaari et al. (2006b) applied the WVD to analyze the simulated signals of planetary gearbox with tooth pitting and crack faults. Feng and Liang (2014b) employed the CCBD with the adaptive optimal kernel to diagnose gear faults of planetary gearboxes of a lab wind turbine and an in situ wind turbine.

2.5.4 Other time-frequency methods

The last three sections reviewed three big families of time-frequency families, however, there also exists some important time-frequency methods that do not belong to these three families. Such methods are review in this section.

The decomposition-based methods may be the first ones worth mentioning. These methods are developed based on the feature that some time-frequency methods, such as the WVD, chirplet transforms and GST, generate more accurate TFRs for mono-component signals than for multi-component signals. In other words, they have mono-component requirement. The decomposition-based methods commonly consist of the following steps: 1) signal decomposition, i.e., decomposing the signal into mono-component signals to fulfill the mono-component requirement of the desired time-frequency method, 2) individual TFRs calculation, i.e., constructing the TFR for each mono-component signal using the desired time-frequency method, and 3) TFR fusion, i.e., superposing the individual TFRs to obtain the final TFR. The Hilbert-Huang transform (Huang et al., 1998) may be one of the best known decomposition-based time-frequency methods. It uses empirical mode decomposition method to decompose the signal and employs the Hilbert transform to generate the individual TFRs. Some similar methods have also been proposed, such as the methods given in (Liu et al., 2017) and (Wang et al., 2009). However, such methods are not always reliable due to the possible mode mixing problem. This problem is commonly caused by the intermittences or the crossings of the frequency components in signals (Feng et al., 2013a). This problem is shown as the phenomenon that the signal is decomposed into the components that are far different from the real signal components and this will lead to misinterpretation of the signal components. Another type of decomposition-based methods decompose the signal according to the signal TFR obtained by the STFT and the drawback of such methods are the possible component missing (Feng et al., 2015a; Feng et al., 2015b; Chen and Feng, 2016b; Feng et al., 2016c). This is because

some components may not be identified due to the poor resolution and smearing effect of the STFT.

Another method worth mentioning is the general linear chirplet transform (GLCT) (Yu and Zhou, 2016). This method was designed to alleviate the smearing problem of the linear chirplet transform. It firstly generates several sub-TFRs using the linear chirplet transform with a series of chirp rates and then fuses the sub-TFRs into one TFR by selecting the maximum at each time-frequency point. However, this method still requires the user to provide window length.

Some applications on the fault diagnosis of planetary gearbox using the time-frequency methods that do not belong to the three big families are reviewed as follows. Feng and his colleagues proposed several decomposition-based method to diagnose gear fault of planetary gearbox under non-stationary conditions in recent years (Feng et al., 2015a; Chen and Feng, 2016b; Feng and Chen, 2018). The differences of these methods are the tools employed in the decomposition and TFR calculation. The decomposition tool they employed includes iterative generalized demodulation (Feng et al., 2015a; Chen and Feng, 2016b), Vold-Kalman filter (Feng et al., 2015a) and adaptive iterative generalized demodulation (Feng and Chen, 2018). The methods used for TFR generation include the GST (Feng et al., 2015a), reassignment method (Chen and Feng, 2016b), Higher order energy operator (Feng et al., 2015a) and Hilbert transform (Feng and Chen, 2018). These methods were used to diagnose gear faults by identifying the fault-induced components from the obtained TFR. Guo et al. (2017) proposed a decomposition-based method using the local mean decomposition to decompose the signal and employing the SST to generate the TFR. This method was used to diagnose both gear faults and bearing faults of wind turbine planetary gearbox. However, these methods suffer either the possible component missing problem or the mode mixing problem, as mentioned above.

2.6 Summary and motivation

The above review of the vibration models of planetary gearbox shows that gear faults cause frequency modulation and amplitude modulation with gear meshign frequency and its harmonics as carrier frequencies, hence fault can be diagnosed by identifying the corresponding sidebands phenomenon (e.g the frequency distance, amplitudes,

distributions, etc.). The review of the time-domain methods and frequency-domain methods presents that these methods are based on the assumption of stationary signal and sensitive to speed change, thus they are not suitable for vibration signal analysis collected under non-stationary conditions. Order-domain methods and time-frequency methods are good tools to analyse such non-stationary signals. Time-frequency method provides the information of two domains (time and frequency), whereas the order-domain method is only able to provide the information of one domain (frequency), therefore the time-frequency method has the potential to provide more precise and reliable diagnostic decisions. The literature review of time-frequency methods indicates that the three widely used kinds of time-frequency methods are linear transform, remapping method and bilinear distribution. Each kind of methods has its own advantages and disadvantages.

It has been introduced in chapter 1 that the proposed VSSTFT, VST and VSBD belong to the families of linear transform, remapping method and bilinear distribution, respectively. These methods employ the shaft rotational speed to address some problems of the existing time-frequency methods in these three families. The shaft rotational speed can be obtained from the tachometer installed in the drive train or from the STFT of the collected vibration signal. The three big families of time-frequency methods share a similar problem, the smear effect. The STFT and SST may be the two most widely used methods in the linear transform family and remapping method family respectively. They do not have smear effects on the components with fixed frequencies, whereas they have smear effects on the components with time-varying frequencies. The researches on the order-domain methods showed that a non-stationary signal can be transferred to a stationary one via a mapping from time domain into angle domain and correspondingly, the shaft-speed-synchronous components will change from time-varying frequencies to fixed frequencies. Hence, this thesis employs the domain mapping technique to address the smear issues in the existing linear transforms and remapping methods and the corresponding proposed methods are the VSSTFT and VST respectively.

The review of the bilinear distributions shows that they have smear effect on the components with non-linear frequencies. Hence, for bilinear distributions, one possible solution of addressing smear effect is changing the non-linear frequencies of the signal into linear frequencies before applying the bilinear distribution. The review also presents that

the unwanted cross terms are away from the origin in ambiguity domain and the auto terms of fixed frequencies and linear frequencies are located at delay axis and a straight line passing the origin in ambiguity domain. Hence one possible solution of addressing the cross-term interference is changing the components with time-varying frequencies into components with fixed frequencies and using a kernel function with passband around the delay axis in ambiguity domain. The above review shows the GD can demodulate one signal component from a time-varying frequency into the pre-set frequency. Hence, the GD has the potential to solve the problems of the existing bilinear distributions. Based on the above analysis, this thesis employs the GD to address the smear effect and cross-term interference problems of the existing bilinear distributions and the corresponding proposed method is named the VSBD.

A non-parametric smear-free cross-term-free time-frequency method (i.e., VSLCT) is also developed for the cases that tachometer is not easily accessible and the signal STFT is not clear enough for speed estimation. The VSLCT uses the linear transform frame and hence it is inherently free from cross-term interference. The review of the linear transforms shows that the smear is caused by that the bases frequencies of the transform do not match the frequencies of the signal components. Hence, the VSLCT employs a set of linear chirplets that are synchronous with shaft rotational velocity to solve the smear problem of linear transform. The VSLCT contains two parameters, the window length and normalized angle. A concentration-index-guided approach is developed to automatically determine the two parameters, therefore the TFR can be obtained adaptively without human intervention.

3 Velocity synchronous short-time Fourier transform (VSSTFT)

3.1 Motivation

The signal collected from a planetary gearbox under non-stationary conditions is usually non-stationary. The STFT (Hlawatsch and Boudreaux-Bartels, 1992) is widely used for non-stationary vibration signal analysis and fault diagnosis of rotating machinery, as it is simple to implement and its computational load is relatively low. It generates clear TFRs for stationary signals. Taking a synthetic stationary signal containing two frequency components as an example, the signal trajectory is shown in Fig. 3-1(A) and the TFR obtained by the STFT is shown in Fig. 3-1(B). It can be seen that the TFR clearly reveals the two frequency components. However, the STFT has the problem of smear effects when processing non-stationary signals. In other words, the STFT has a stationarity requirement. The vibration signals from rotational machinery under non-stationary conditions commonly contain time-varying frequencies that are proportional with each other. The STFT commonly generates a smeared TFR for such signals. Taking a synthetic non-stationary vibration as an example, its frequency trajectories are shown in Fig. 3-2(A) and the STFT is shown in Fig. 3-2 (B). It can be seen that the STFT cannot reveal the signal frequencies clearly due to the smear problem. Smear effects may mask the signal components related to fault and lead to incorrect diagnosis. If the smear effects can be avoided, the TFR and diagnosis result will be more accurate. To avoid the smear effect, it is crucial to convert the signal into a stationary one. Fortunately, the non-stationary vibration signal collected from rotational machinery can be transformed into a stationary angle-domain one by a mapping from time domain into angle (shaft rotational angle) domain (Fyfe and Munck, 1997). It should be noted that the angle-domain signal can also be seen as a 'time-domain signal' using the relative time instead of absolute time (second) as time base. For example, the angle-domain signal $x_{\text{angle}}(\varphi)$ can be interpreted as the vibration amplitude at the time when the shaft rotates φ radians.

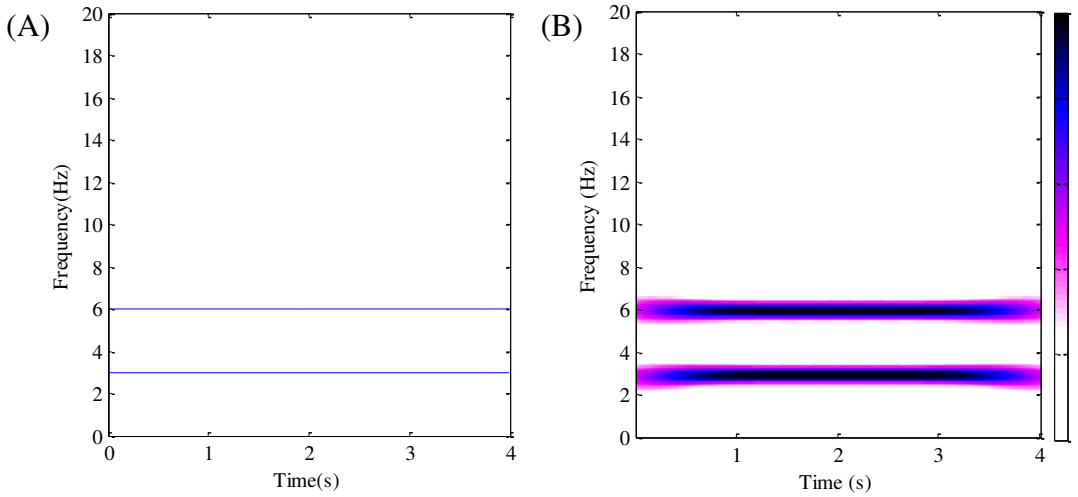

Fig. 3-1. TFR of the synthetic stationary signal: (A) True instantaneous frequencies and (B) TFR obtained by the STFT

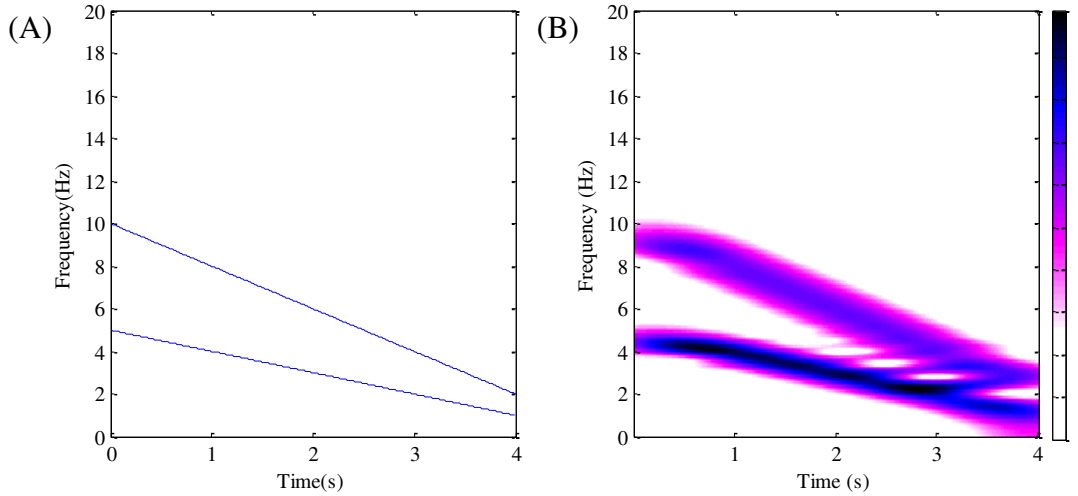

Fig. 3-2. TFR of the synthetic non-stationary signal: (A) True instantaneous frequency and (B) TFR obtained by the STFT

Based on the above analysis, a new time-frequency method, named velocity synchronous short-time Fourier transform (VSSTFT), is proposed to provide a smearing-free TFR. With the proposed method, the signal is firstly mapped into stationary angular domain to obtain its stationary domain representation to satisfy the stationarity requirement of the STFT. Then the STFT is applied to the stationary angle-domain signal to obtain the signal TFR. It should be noted here as the STFT process the angle-domain signal (which

can also be seen as a time-domain signal using relative time as time base), this resulted TFR uses the relative time and relative frequency (multiples of shaft rotational frequency or simply orders) as the time and frequency bases respectively. This resulted 'time-frequency representation' is termed angle-order representation (AOR) to distinguish from traditional TFR that uses absolute time (second) and frequency (Hz) as bases. Next, a time-frequency-domain restoration is presented to obtain the signal TFR by another mapping from angle-order domain back to time-frequency domain. Finally, the fault can be diagnosed by identifying the signal components associated with the fault in the TFR. The proposed method is also able to provide desirable time-frequency resolution for the entire TFR of a non-stationary vibration signal. Furthermore, a new linear transform is also developed to realise the above procedures. In this way, the TFR can be obtained via the VSSTFT in one step for planetary gearbox fault diagnosis under non-stationary conditions.

The rest of this chapter is structured as follows: Section 3.2 presents the proposed VSSTFT method. Sections 3.3 and 3.4 examine the effectiveness of the proposed method using simulation and experimental vibration signals respectively. The conclusions are drawn in Section 3.5.

3.2 Presentation of the VSSTFT

3.2.1 Derivation of the VSSTFT

The proposed VSSTFT can be derived in the following three steps.

Step 1. Map the signal from time domain to angle domain

The time-domain signal is firstly pre-processed by time-angle-domain mapping to get a stationary angle-domain signal. The accelerometer signal $x_{\text{time}}(t)$ measures vibration amplitude over time t and is a time-domain signal. The instantaneous shaft rotational angle $\theta(t)$ presents the relationship between shaft angle φ and time t (Borghesani et al., 2014) and is expressed by

$$\varphi = \theta(t). \tag{3-1}$$

The function θ gives relationship between time and shaft angle and is named time-angle relationship function. It can be calculated by integrating the shaft speed. The shaft speed can be obtained from tachometer signal or estimated from the TFR obtained by the

STFT (Urbanek et al., 2013). The time t can then be expressed as a function of shaft angle using the inverse function of θ, represented by

$$t = \theta^{-1}(\varphi). \tag{3-2}$$

The time-domain signal $x_{\text{time}}(t)$ can be mapped into angle domain by substituting Eq. (3-2) into time-domain signal $x_{\text{time}}(t)$, expressed by

$$x_{\text{angle}}(\varphi) = x_{\text{time}}\left(\theta^{-1}(\varphi)\right), \tag{3-3}$$

where $x_{\text{angle}}(\varphi)$ is an angle-domain signal.

Step 2. Transform the signal from angle domain to angle-order domain using the STFT.

The STFT is a simple method to determine the energy and phase information of a time-domain signal over time and frequency. However, the STFT requires that the signal be stationary, otherwise the TFR obtained by the STFT will have smearing effects. To satisfy this requirement, we apply the STFT to the stationary signal in angle domain directly. It should be emphasized that, since the STFT is applied on the signal in angle domain rather than in time domain, the resulted energy-and-phase representation is over shaft angle and order (multiples of shaft rotational frequency), instead of absolute time and frequency. Therefore, the resulted energy-and-phase information obtained by the STFT of the mapped signal is named angle-order representation (AOR). The AOR is given by

$$X_{\text{AOR}}(\eta, \Omega) = \int_{-\infty}^{\infty} x_{\text{angle}}(\varphi)\lambda(\varphi - \eta)\exp(-\mathrm{j}\Omega\varphi)\,\mathrm{d}\varphi, \tag{3-4}$$

where $\lambda(\cdot)$ is the window function, normally a Gaussian function or a Hanning function, η is shaft angle and Ω is order. Since the angle-domain signal is stationary, the AOR can eliminate the smear problem present in the frequency-domain.

Step 3. Map the energy-and-phase representation from angle-order domain to time-frequency domain.

In the last step, we map the STFT result from the angle-order domain (η, Ω) to time-frequency domain (τ,f) according to their relationship. For AOR angle η, it can be linked to TFR time τ by the function θ given by Eq. (3-1), represented by

$$\eta = \theta(\tau). \tag{3-5}$$

For order Ω, it denotes multiples of the shaft rotating frequency. The shaft rotating angle frequency can be represented as the derivative of shaft rotational phase $\theta(t)$. Therefore, the order Ω can be linked to frequency f by the following equation

$$\Omega = \frac{f}{f_{\text{shaft}}(\tau)}, \tag{3-6}$$

where $f_{\text{shaft}}(\tau)$ is the instantaneous shaft rotational frequency at time τ and can be obtained by taking derivative of instantaneous shaft rotational phase $\theta(\tau)$ over time and dividing the result by 2π, i.e.,

$$f_{\text{shaft}}(\tau) = \frac{\theta'(\tau)}{2\pi}, \tag{3-7}$$

where $\theta'(\tau)=d\theta(\tau)/d\tau$ and is the instantaneous shaft rotational angular frequency. Substituting Eq. (3-7) into Eq. (3-6) leads to a function that maps frequency to order. This function is denoted as g, expressed by

$$\Omega = g(f) = \frac{2\pi f}{\theta'(\tau)}. \tag{3-8}$$

The function g gives relationship between frequency and order and is named frequency-order relationship function.

The AOR $X_{\text{AOR}}(\eta, \Omega)$ can be mapped into time-frequency domain using the time-angle relationship function θ and angle-order relationship function g, i.e. substituting Eq. (3-5) and Eq. (3-8) into the AOR $X_{\text{AOR}}(\eta, \Omega)$. Then

$$X_{\text{TFR}}(\tau, f) = X_{\text{AOR}}(\theta(\tau), g(f)) = X_{\text{AOR}}\left(\theta(\tau), \frac{2\pi f}{\theta'(\tau)}\right), \tag{3-9}$$

where $X_{\text{TFR}}(\tau,f)$ is the time-frequency representation.

With the three steps described above, the flowchart of the proposed VSSTFT method can now be presented in Fig. 3-3(A). As shown in the flowchart, the VSSTFT can be implemented in three steps, i.e., 1) mapping the non-stationary time-domain signal into

stationary angle domain, 2) applying the STFT to the angle-domain signal to obtain the AOR and 3) mapping the signal AOR into time-frequency domain to obtain the signal TFR.

The proposed VSSTFT method can eliminate the smear effect. This is because Steps 1 and 3 only change the domains, thus the smear effects are not involved in these two steps. Step 2 applies the STFT to the stationary angle-domain signal, thus the resulted energy-and-phase representation does not have the smear effect. As none of the three steps of the proposed method has the smear problem, the resulting TFR should not be affected by smearing.

To better understand the proposed VSSTFT, it is demonstrated step by step using the synthetic non-stationary signal presented in the last subsection. Fig. 3-4(A) shows the signal waveform and the unit is volt. After mapping from time domain into angle domain, the obtained angle-domain signal is shown in Fig. 3-4(B). It can be seen that the non-periodic signal becomes periodic, i.e., a non-stationary signal becomes stationary. The AOR is then obtained by computing the STFT of the mapped signal as displayed in Fig. 3-4(C). It can be found that the AOR reveals the two signal components clearly without smear problem. The TFR of the raw signal is finally restored by a mapping from angle-order domain into time-frequency domain as shown in Fig. 3-4(D). It can be seen that the two signal constituents are clearly revealed without smearing artifact. Comparing with the TFR by the STFT (Fig. 3-2(B)) shows that the proposed VSSTFT outperforms the STFT in generating a smear-free TFR.

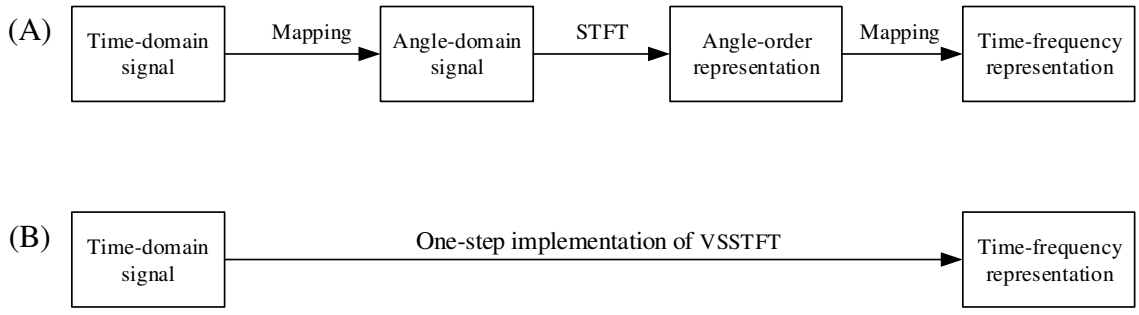

Fig. 3-3. Flowchart of the proposed VSSTFT method: (A) three-step implementation, and (B) one-step implementation

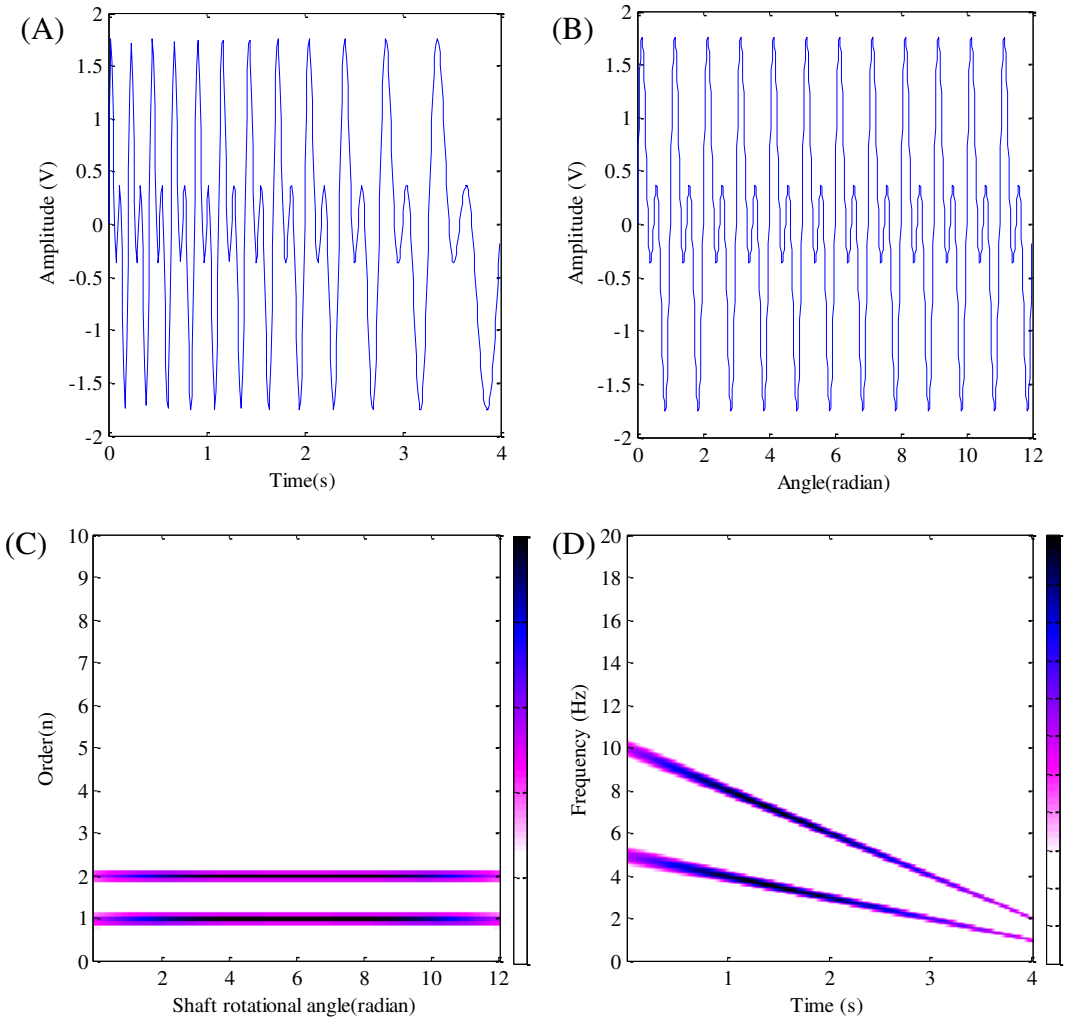

Fig. 3-4. Demonstration of the effectiveness of the proposed VSSTFT: (A) raw signal, (B) mapped stationary signal, (C) STFT of the mapped stationary signal, and (D) TFR obtained by TFR restoration

3.2.2 Fast implementation of the VSSTFT

The proposed VSSTFT method involves twice domain mappings. In practice, the signal is discrete and domain mappings may require additional signal processing techniques such as signal resampling, which may increase the complexity of the proposed method. To simplify the proposed method, the one-step implementation of the proposed method is developed. With equations (3-4) and (3-9), the TFR is expressed by

$$X_{\mathrm{TFR}}(\tau, f) = \int_{-\infty}^{\infty} x_{\mathrm{angle}}(\varphi)\,\lambda\big(\varphi - \theta(\tau)\big)\exp\left(-\frac{j2\pi\varphi f}{\theta'(\tau)}\right)\mathrm{d}\varphi\,. \tag{3-10}$$

Substituting Eq. (3-1) and operating a change of variables in the integration leads to

$$X_{\mathrm{TFR}}(\tau, f)=\int_{-\infty}^{\infty} x_{\mathrm{angle}}(\theta(t))\lambda(\theta(t)-\theta(\tau))\exp\left(-\frac{j2\pi f\theta(t)}{\theta'(\tau)}\right)\frac{\mathrm{d}\theta(t)}{\mathrm{d}t}\mathrm{d}t\,. \qquad (3\text{-}11)$$

As $x_{\mathrm{angle}}(\theta(t))$ maps time t to vibration amplitude, it can be substituted for time-domain signal $x_{\mathrm{time}}(t)$. The TFR is then simplified as

$$X_{\mathrm{TFR}}(\tau, f)=\int_{-\infty}^{\infty} x_{\mathrm{time}}(t)\theta'(t)\lambda(\theta(t)-\theta(\tau))\exp\left(-\frac{j2\pi f\theta(t)}{\theta'(\tau)}\right)\mathrm{d}t\,, \qquad (3\text{-}12)$$

where $\theta'(t)=\mathrm{d}\theta/\mathrm{d}t$. It can be seen that the smearing-free TFR can be obtained using the above linear transform in a single step. The flowchart of the one-step implementation of the proposed three-step method is shown in Fig. 3-3(B). It shows that the one-step implementation of the proposed method using Eq. (3-12) significantly simplify the previous three-step implementation.

In real applications the VSSTFT must be implemented using digital signal processing techniques, the algorithm of the VSSTFT can be obtained by discretizing the above function, expressed by

$$\begin{aligned} &X_{\mathrm{TFR}}[m\Delta\tau, n\Delta f] \\ &=\sum_{n=1}^{N} x_{\mathrm{time}}[k\Delta t]\theta'[k\Delta t]\lambda(\theta[k\Delta t]-\theta[m\Delta\tau])\exp\left(-\frac{j2\pi n\Delta f\theta[k\Delta t]}{\theta'[m\Delta\tau]}\right)\cdot \end{aligned} \qquad (3\text{-}13)$$

It can be seen that the smearing-free TFR can be obtained in a single step.

3.2.3 Time-frequency resolution of the VSSTFT

Fine frequency resolution is important in fault identification and good time resolution is desirable to capture transient behavior. This subsection explains that the proposed VSSTFT method is capable of multiresolution analysis in response to the need in fault diagnosis or transience detection.

The STFT is commonly used for processing time-domain signal and its time-frequency resolution is limited (Hlawatsch and Boudreaux-Bartels, 1992). Before applying the STFT to time-domain signal, the window function $\lambda(\,)$ must be specified by the user and its length is termed time window length. The STFT $X(\tau,f)$ of a time-domain signal $x(t)$ localizes the signal with a constant-length time window centered at τ and a constant-length frequency window centered at f, and the product of the time window length and the frequency window

length are equal or greater than 1/2(Gabor, 1947). In the proposed method, the STFT is used to process the angle-domain signal, thus similarly the STFT $X(\phi,\Omega)$ of the angle-domain signal localizes the signal information using an angle window $[\phi-\Delta\phi/2, \phi+\Delta\phi/2]$ and an order window $[\Omega-\Delta\Omega/2, \Omega+\Delta\Omega/2]$, and the product of the angle window length and the order window length are equal or greater than 1/2, expressed by

$$\Delta\phi\Delta\Omega \geq \frac{1}{2}, \tag{3-14}$$

where $\Delta\Omega$ is constant order window length and $\Delta\phi$ is constant angle window length and specified by the user.

In this study, the order window length should be not greater than any one of fault characteristic orders of the faulty gears, expressed by

$$\Delta\Omega \geq \min\left[\text{fault characteristic orders}\right], \tag{3-15}$$

where fault characteristic orders of the faulty gears are the proportionality constant of the corresponding fault characteristic frequencies and the rotational frequency of the reference shaft. The reason is that at most one modulation order sideband should be covered in an order domain window after any shifting in the order domain and in this way the sidebands generated by faults will be separable and identifiable in order domain. Therefore, the constant angle window length $\Delta\phi$ should be specified by the user such that

$$\Delta\phi \geq \frac{1}{2\min\left[\text{fault characteristic orders}\right]}. \tag{3-16}$$

We use symbols ϕ_w and Ω_w to represent the angle and order covered by the window respectively and their ranges are respectively

$$\phi_w \in \left[\phi-\frac{1}{2}\Delta\phi, \phi+\frac{1}{2}\Delta\phi\right], \tag{3-17}$$

$$\Omega_w \in \left[\Omega-\frac{1}{2}\Delta\Omega, \Omega+\frac{1}{2}\Delta\Omega\right]. \tag{3-18}$$

Now we have a rectangular region covered by the angle-order window as shown in Fig. 3-5. This rectangle is called elementary tile of the angle-order plane. The whole angle-

order plane can be divided into the elementary tiles by the STFT in a non-overlapping manner as shown in Fig. 3-6.

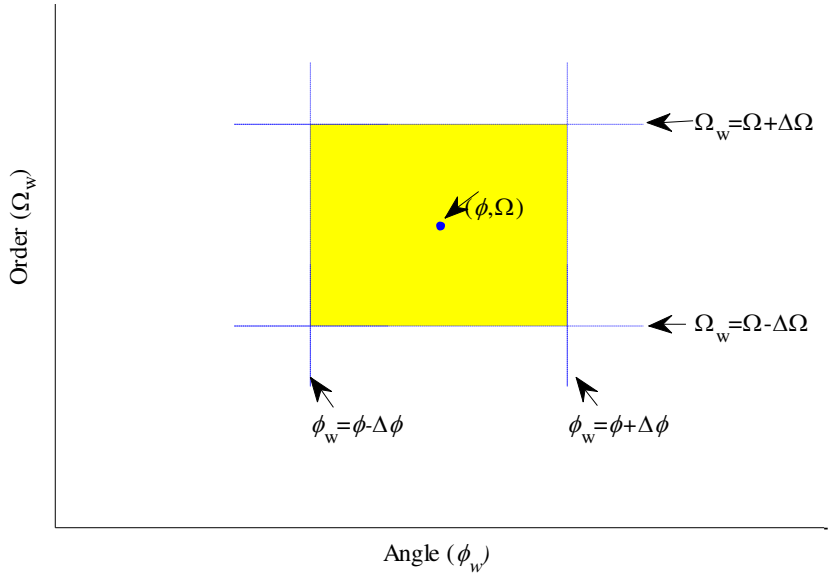

Fig. 3-5. Arbitrary angle-order window at angle ϕ and order Ω

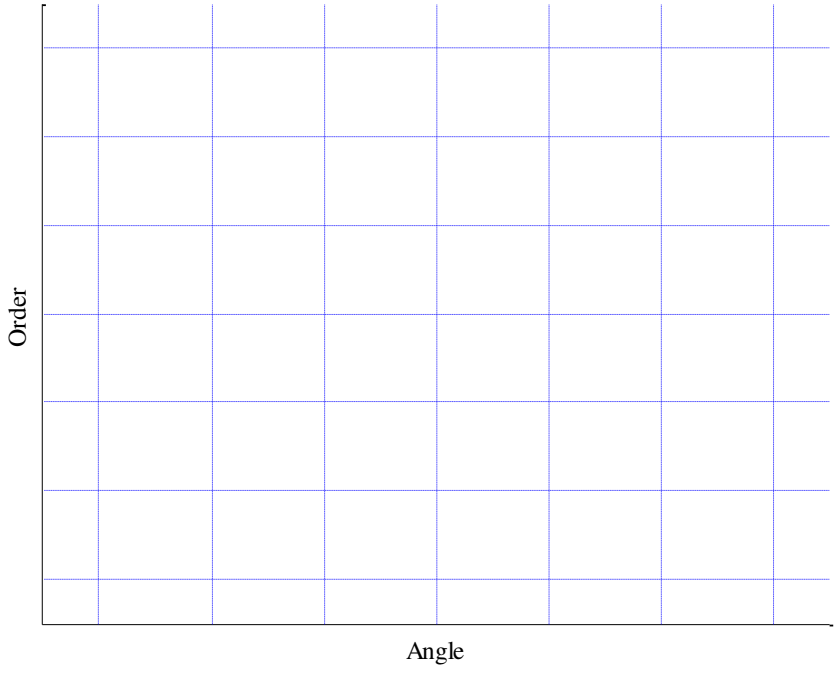

Fig. 3-6. Angle-order tiling of the STFT

Then the AOR is mapped from the angle-order plane to time-frequency plane. With the time-angle relationship function θ and frequency-order relationship function g, the

angle and order covered by the window can be related to time and frequency covered by the window, expressed by

$$\tau_{\mathrm{w}} = \theta^{-1}\left(\phi_{\mathrm{w}}\right), \tag{3-19}$$

$$f_{\mathrm{w}} = g^{-1}\left(\Omega_{\mathrm{w}}\right) = \frac{\Omega_{\mathrm{w}}\theta'\left(\tau_{\mathrm{w}}\right)}{2\pi}, \tag{3-20}$$

where τ_{w} and f_{w} are the time and frequency covered by the window.

The angle interval of the window can be mapped into time-frequency plane to obtain the time interval of the window. This is done by substituting equations (3-5) and (3-19) into Eq. (3-17) and replacing ϕ_{w} by τ_{w} on the left hand side of the equation, i.e.

$$\tau_{\mathrm{w}} \in \left[\theta^{-1}\left(\theta\left(\tau\right) - \frac{1}{2}\Delta\phi\right), \theta^{-1}\left(\theta\left(\tau\right) + \frac{1}{2}\Delta\phi\right)\right]. \tag{3-21}$$

Similarly, the order interval of the window can be mapped into time-frequency plane to obtain the frequency interval of the window by substituting the equations (3-5), (3-6), (3-19) and (3-20) into Eq. (3-18) and replacing Ω_{w} with f_{w} on the left hand side of the equation. Hence

$$f_{\mathrm{w}} \in \left[\frac{f\theta'\left(\tau_w\right)}{\theta'\left(\tau\right)} - \frac{\Delta\Omega\theta'\left(\tau_w\right)}{4\pi}, \frac{f\theta'\left(\tau_w\right)}{\theta'\left(\tau\right)} + \frac{\Delta\Omega\theta'\left(\tau_w\right)}{4\pi}\right]. \tag{3-22}$$

Based on the above analysis, the VSSTFT $X_{\mathrm{TFR}}(\tau,\mathrm{f})$ localizes a time-domain signal $x_{\mathrm{time}}(t)$ with a time window $\left[\theta^{-1}\left(\theta\left(\tau\right) - \frac{1}{2}\Delta\phi\right), \theta^{-1}\left(\theta\left(\tau\right) + \frac{1}{2}\Delta\phi\right)\right]$ and a frequency window $\left[\left(\frac{2\pi f}{\theta'\left(\tau\right)} - \frac{1}{2}\Delta\Omega\right)\frac{\theta'\left(\tau_w\right)}{2\pi}, \left(\frac{2\pi f}{\theta'\left(\tau\right)} + \frac{1}{2}\Delta\Omega\right)\frac{\theta'\left(\tau_w\right)}{2\pi}\right]$.

The time window length and frequency window length of the window can be expressed as the endpoints difference of the time interval of the window and endpoints difference of the frequency interval of the window, expressed respectively by

$$\Delta\tau\left(\tau\right) = \theta^{-1}\left(\theta\left(\tau\right) + \frac{1}{2}\Delta\phi\right) - \theta^{-1}\left(\theta\left(\tau\right) - \frac{1}{2}\Delta\phi\right), \tag{3-23}$$

and

$$\Delta f\left(\tau_w\right)=\left(\frac{2\pi f}{\theta'(\tau)}+\frac{1}{2}\Delta\Omega\right)\frac{\theta'\left(\tau_w\right)}{2\pi}-\left(\frac{2\pi f}{\theta'(\tau)}-\frac{1}{2}\Delta\Omega\right)\frac{\theta'\left(\tau_w\right)}{2\pi}=\frac{\Delta\Omega\theta'\left(\tau_w\right)}{2\pi}. \tag{3-24}$$

The time-frequency area covered by the window can be calculated by integrating the frequency window length over time:

$$\begin{aligned}\Delta \mathrm{A}_{\mathrm{TF}}&=\int_{\theta^{-1}\left(\theta(\tau)-\frac{1}{2}\Delta\phi\right)}^{\theta^{-1}\left(\theta(\tau)+\frac{1}{2}\Delta\phi\right)}\frac{\Delta\Omega\theta'\left(\tau_w\right)}{2\pi}\mathrm{d}\tau_{\mathrm{w}}=\frac{\Delta\Omega}{2\pi}\int_{\theta^{-1}\left(\theta(\tau)-\frac{1}{2}\Delta\phi\right)}^{\theta^{-1}\left(\theta(\tau)+\frac{1}{2}\Delta\phi\right)}\theta'\left(\tau_w\right)\mathrm{d}\tau_{\mathrm{w}}\\&=\frac{\Delta\Omega}{2\pi}\left(\theta\left(\theta^{-1}\left(\theta(\tau)+\frac{1}{2}\Delta\phi\right)\right)-\theta\left(\theta^{-1}\left(\theta(\tau)-\frac{1}{2}\Delta\phi\right)\right)\right)\\&=\frac{\Delta\Omega}{2\pi}\left(\theta_{\mathrm{s}}(\tau)+\frac{1}{2}\Delta\phi-\left(\theta_{\mathrm{s}}(\tau)-\frac{1}{2}\Delta\phi\right)\right)=\frac{\Delta\Omega\Delta\phi}{2\pi}=\frac{\Delta \mathrm{A}_{\mathrm{AO}}}{2\pi}\end{aligned}, \tag{3-25}$$

where $\Delta \mathrm{A}_{\mathrm{TF}}$ and $\Delta \mathrm{A}_{\mathrm{AO}}$ is the time-frequency area covered by the window and the angle-order area covered by the window respectively. It can be seen that the time-frequency area covered by the window is constant and equal to the angle-order area covered by the window divided by 2π.

The frequency window length $\Delta f(\tau_{\mathrm{w}})$ varies with time covered by the window τ_{w}. To better estimate the frequency resolution, we define the averaged frequency window length $\overline{\Delta f}(\tau)$ as the constant time-frequency window area $\Delta \mathrm{A}_{\mathrm{TF}}$ divided by the time window length $\Delta\tau(\tau)$, expressed as

$$\overline{\Delta f}(\tau)=\frac{\Delta \mathrm{A}_{\mathrm{TF}}}{\Delta\tau(\tau)}=\frac{\Delta\Omega\Delta\phi}{2\pi\Delta\tau(\tau)}. \tag{3-26}$$

In the above equation, $\Delta\phi$ is the angle window length, and thus $\Delta\phi/(2\pi)$ is the shaft revolution window length. $\Delta\tau(\tau)$ is the angle window length, and hence $\Delta\phi/(2\pi\Delta\tau(\tau))$ can be seen as the averaged shaft rotational frequency within the window, given by

$$\bar{f}_{\mathrm{w}}(\tau)=\frac{\Delta\phi}{2\pi\Delta\tau(\tau)}. \tag{3-27}$$

The averaged frequency window length can then be simplified as

$$\overline{\Delta f}(\tau)=\frac{\Delta \mathrm{A}_{\mathrm{TF}}}{\Delta\tau(\tau)}=\Delta\Omega\bar{f}_{\mathrm{w}}(\tau). \tag{3-28}$$

According to Eq. (3-27), the time window length can be expressed as

$$\Delta\tau(\tau)=\frac{\Delta\phi}{2\pi\bar{f}_{\mathrm{w}}(\tau)}. \tag{3-29}$$

By observing equations (3-28) and (3-29), it can be seen that the averaged shaft speed within the window $\bar{f}_{\mathrm{w}}(\tau)$ is inversely proportional to time window length $\Delta\tau(\tau)$ and proportional to averaged frequency window length $\overline{\Delta f}(\tau)$. Therefore when the shaft speed is higher, the VSSTFT has worse frequency resolution and better time resolution; when the shaft speed is lower, the VSSTFT has better frequency resolution and worse time resolution.

Now consider a vibration signal containing only shaft frequency and its harmonics. Assuming shaft speed increases linearly an arbitrary time-frequency window of the VSSTFT at time τ and frequency f is shown in Fig. 3-7. This window can be seen as the elementary tile of the time-frequency plane. The whole time-frequency plane can be divided into the elementary tiles by the VSSTFT in a non-overlapping manner as shown in Fig. 3-8 (blue dotted line). The ideal trajectories of the signal components along time (red solid line) are also shown in Fig. 3-8. It can be seen that within any time window interval, each of the trajectories of shaft frequency and its harmonics falls exactly into one non-overlapping tile. This means that the smearing caused by frequency variation no longer manifests itself here. It can also be seen when the shaft speed is slower, the frequency components are squeezed and thus difficult to be discerned. In this case, the VSSTFT provides a better frequency resolution with reduced time resolution in order to better separate the components. On the other hand, when the shaft speed is faster, the components become more distant and it is easier to separate the components. In response to this, the VSSTFT provides a better time resolution than the STFT with reduced frequency resolution in order to better reveal the transit characteristics. This will be further illustrated using simulated signal in section 3.3.

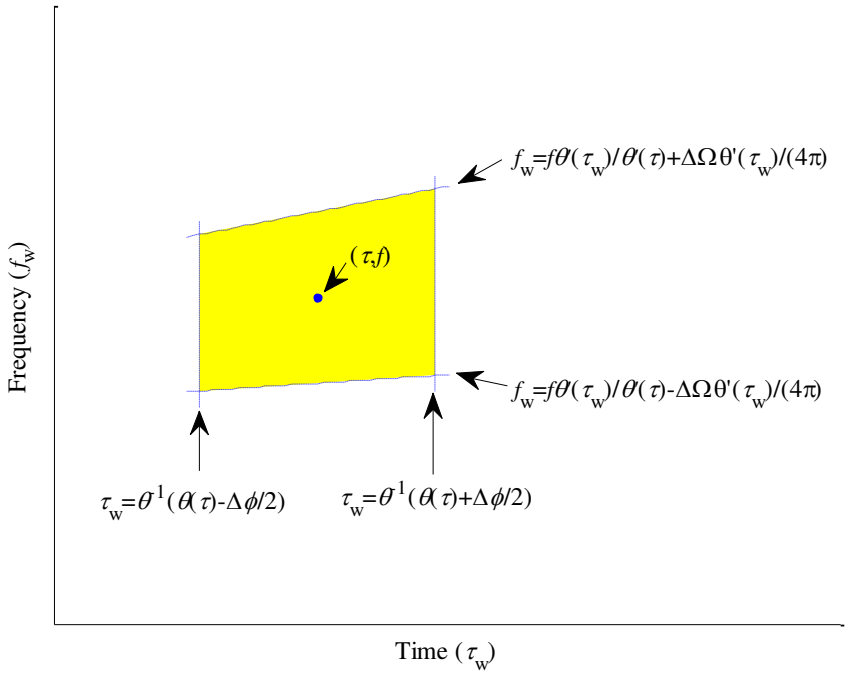

Fig. 3-7. Arbitrary time-frequency window at time τ and frequency *f*

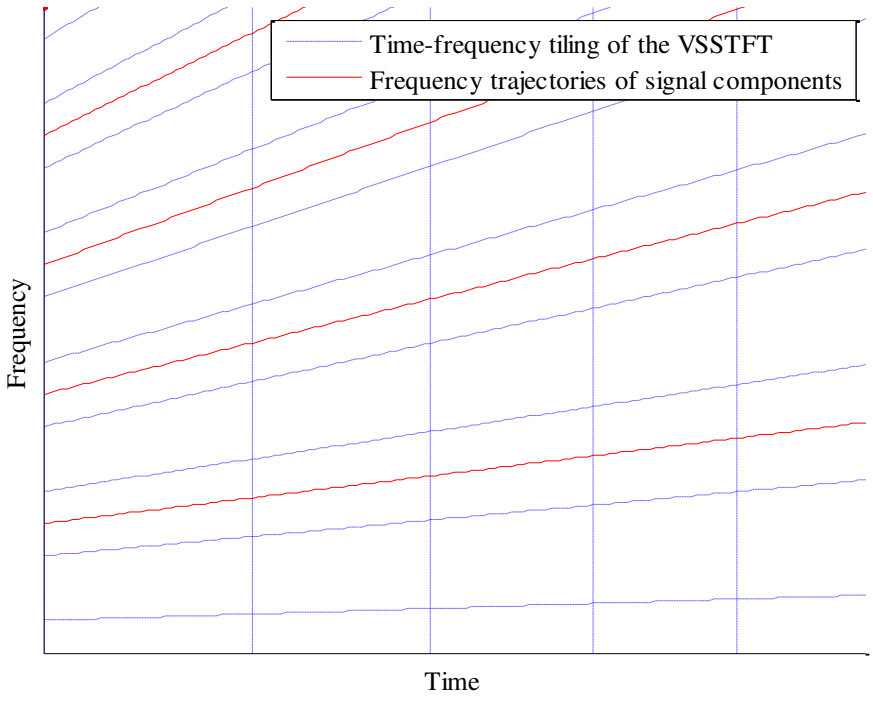

Fig. 3-8. Time-frequency tiling of the VSSTFT

3.2.4 Comparison with other linear time-frequency transforms

The STFT, CWT and chirplet transform are three linear transforms which are widely used in the time-frequency analysis of rotational machinery vibration signals under time-varying speed conditions. The kernel frequencies of the STFT and CWT are time-variant, thus the frequency tailings are parallel to time axis. Within a certain time window interval, the trajectories of the shaft-speed-locked components may fall into multiple non-overlapping tiles, thus causing smearing. Taking the signal used in the last subsection for an example again, the ideal trajectories of the signal components along time (red solid line) and the time-frequency tilling of the STFT (blue dotted line) are plotted together in Fig. 3-9. As shown in the figure, any trajectory may cross the frequency tiles and within a certain time interval it may fall into multiple tiles, which leads to smearing.

The chirplet transform involves the inner product between the signal and chirp basis functions, characterised by the time-invariant frequency changing rate (chirp rate). The chirplet transform thus represents a frequency-sheared tiling of the time–frequency plane. When the chirp rate of the chirplet transform matches the chirp rate of analyzed signal, a concentrated TFR could be obtained. Nevertheless, the vibration signal of rotational machinery under time-varying speed conditions may contain multiple harmonics whose frequency changing rates are different, thus it is impossible to choose one chirp rate that matches the multiple different changing rates of the components. However, in real applications, the chirp rate of the chirplet transform is commonly set at the chirp rate of a single component of interest. Thus only the smearing of a single component of interest will be eliminated, the smearing of all other components is left intact. For instance, consider the signal used in the last subsection. The chirp rate parameter is set as the chirp rate of shaft frequency, the ideal trajectories of the signal components along time (red solid line) and the non-overlapping tiles of the chirplet transform (blue dotted line) are shown together in Fig. 3-10. It can be seen that within a frequency band (e.g., the band bounded by the 3rd and 4th blue lines from the bottom of Fig. 3-10), the trajectory of shaft frequency (i.e., the first red solid line from bottom of the figure) falls exactly into one non-overlapping tile and this means that smearing does not occur on the shaft frequency component. However, the trajectories of shaft frequency harmonics (i.e., the other red solid lines above the first one) as well as meshing frequency can still cross the frequency tiles and fall into multiple non-

overlapping tiles. This means that smearing still occurs on all other components whose chirp rates are different from the pre-set chirp rate of the chirplet transform. As such, the proposed method should outperform the chirplet transform because in the diagnosis of a planetary gearbox multiple frequency components such as meshing frequency and shaft frequency harmonics as well as gear fault characteristic frequency co-exist and they can all be made smear-free by the proposed method but not the chirplet transform.

In addition, both the STFT and chirplet transform have fixed time and frequency resolution, which can be reflected by the identical shapes and "dimensions" of the time-frequency tiles. The wavelet transform has different time-frequency resolution at different frequency regions of the TFR, however, the time-frequency resolution does not change with time. Under time-varying shaft speed conditions, the frequency "distances" of the shaft-speed-locked components are time-varying. When the distance is greater, the components are easier to be separated in the TFR and opposite is true when the distance is lower. Therefore, under time-varying shaft speed conditions, these three transforms, i.e., STFT, CWT and chirplet transform, with time-invariant resolution cannot provide desirable resolution for the entire signal.

Compared with the above linear transforms, the proposed VSSTFT can provide a better time-resolution to separate all the time-frequency components without smearing effects caused by frequency variation. This will be shown with sample signals and then experimental signals.

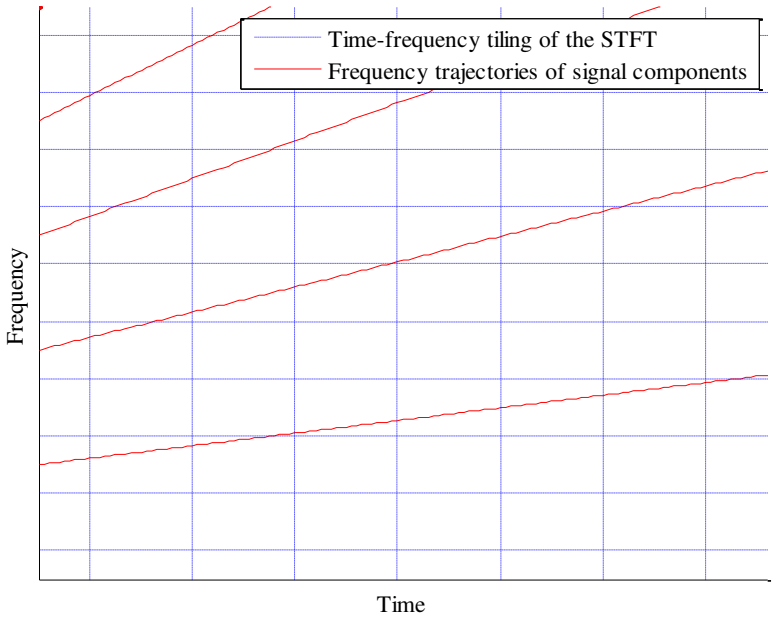

Fig. 3-9. Time-frequency tiling of the STFT

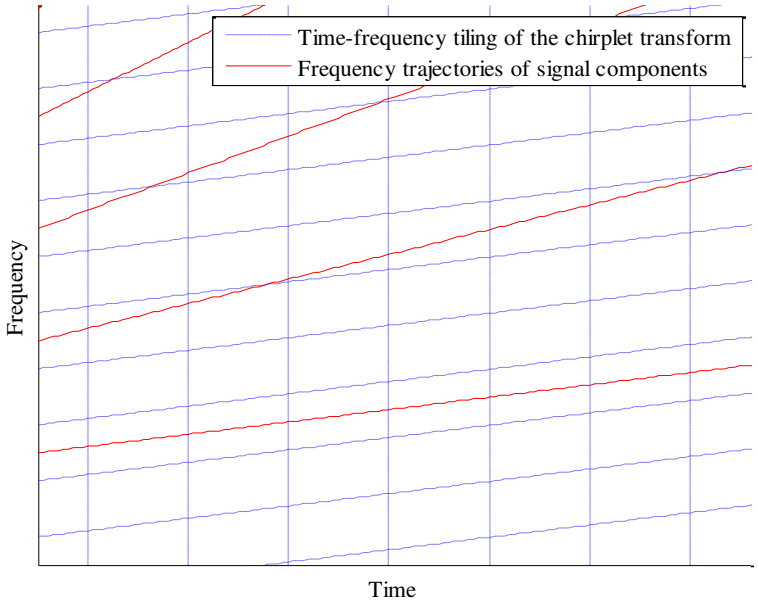

Fig. 3-10. Time-frequency tiling of the chirplet transform

3.3 Simulation evaluations

In this section, a simulated signal is constructed according to the vibration model provide in Appendix A (Feng and Zuo, 2012). Assuming the gearbox has a sun gear fault and the shaft rotational speed is time varying, this signal is expressed by

$$x(t)=\left\{1-\cos\left[2\pi\int_0^t f_{\text{sunrot}}(\tau)\,\mathrm{d}\tau\right]\right\}\left\{1+\cos\left[2\pi\int_0^t f_{\text{sun}}(\tau)\,\mathrm{d}\tau+\phi\right]\right\} \times\cos\left[2\pi\int_0^t f_{\text{mesh}}(\tau)\,\mathrm{d}\tau+\theta\right]+\mathrm{N}(t) \tag{3-30}$$

In the above model, the term $\left\{1-\cos\left[2\pi\int f_{\text{sunrot}}(t)\,\mathrm{d}t\right]\right\}$ corresponds to amplitude modulation caused by vibration transfer path and $f_{\text{sunrot}}(t)$ denotes sun gear rotational frequency. The term $\left\{1+\cos\left[2\pi\int f_{\text{sun}}(t)\,\mathrm{d}t+\phi\right]\right\}$ corresponds to amplitude modulation caused by sun gear fault and $f_{\text{sun}}(t)$ is sun gear fault characteristic frequency. The term $\cos\left[2\pi\int f_{\text{mesh}}(t)\,\mathrm{d}t+\theta\right]$ corresponds to the vibration caused by gear meshing and $f_{\text{mesh}}(t)$ is the frequency of the gear meshing frequency. N(t) is an added Gaussian white noise. The initial phrases $\phi=\theta=0$. The relationship of gear meshing frequency, sun gear rotational frequency and sun gear fault characteristic frequency are set as $f_{\text{sunrot}}(t)=0.3f_{\text{sun}}(t)=0.06f_{\text{mesh}}(t)$. The signal length is five seconds and the sampling rate is 240 Hz. To simulate the speed-varying state, we set the sun gear rotating frequency $f_{\text{sunrot}}(t)=3-1.2\cos(2\pi\cdot 0.3t)$. Based on this setup, the sun gear rotating frequency first decreases from 1.8 Hz to 4.2 Hz, and then increases to almost 6 Hz in five seconds. We tested the proposed VSSTFT method and several compared methods using this synthetic signal under different noise levels and the result shows that for this specific signal, under SNR 6 dB, the VSSTFT result is obviously clearer than other methods. Therefore, we set the signal SNR as 6 dB to show the advantage of the VSSTFT. The SNRs used in other chapters are also selected using such strategy.

The waveform of the simulated signal and its frequency spectrum are presented in Fig. 3-11(A) and (B). It can be seen that the frequency spectrum is smeared due to speed variation and it does not provide sufficient information regarding to the fault. The sun gear rotating frequency curve is shown in Fig. 3-11 (C).

The simulated signal contains nine components with time-varying frequencies as shown in Fig. 3-12 (A). The TFR produced by the VSSTFT approach is shown in Fig. 3-12 (B). It can be seen that the frequencies trajectory revealed by the VSSTFT are close to the

true frequency trajectories shown in Fig. 3-12 (A). The VSSTFT result reveals the nine time-frequency components. Among them, eight components are sidebands, which can be represented by $f_{\text{mesh}} \pm nf_{\text{sunrot}} \pm mf_{\text{sun}}$. As they are related to sun gear fault, it is diagnosed that the gearbox has a sun gear fault.

To further assess the performance of the proposed method, we then compare it with STFT and some advanced methods, with the results shown in Fig. 3-12 (C-F), respectively. The STFT can roughly show the frequency trends of the constituent components, as shown in Fig. 3-12(C). However, the sidebands cannot be recognized due to the smearing effect. The TFR in Fig. 3-12(D) obtained by the SET (Yu et al., 2017) shows a clearer structure of the constituent components than STFT. However, the TFR ridges does not match the true frequency trajectories of the signal. The GLCT (Yu and Zhou, 2016) result is presented in Fig. 3-12(E) and the meshing frequency is clearly revealed, however, none of the sidebands are revealed. The PCT (Peng et al., 2011) is method that uses signal frequency information to enhance the TFR. The TFR obtained by the PCT still suffers from smearing effect, as plotted in Fig. 3-12(F). Though the meshing frequency and a few sidebands are revealed, . Comparing Fig. 3-12(B) with Fig. 3-12(C-F) shows that the proposed VSSTFT performs better than the other tested methods. The above comparison shows that the proposed VSSTFT performs better than the other tested methods. The above comparison demonstrates that the VSSTFT is superior to the other compared methods in addressing the time–frequency smear issue and providing an accurate and clear TFR for fault diagnosis.

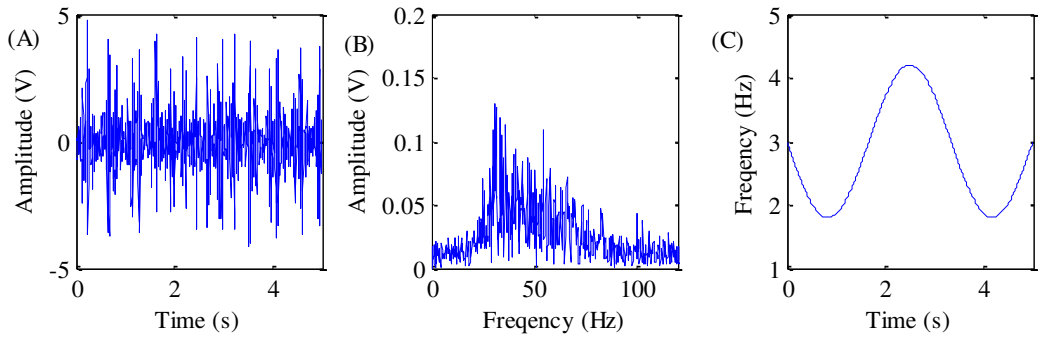

Fig. 3-11. Simulated case: (A) vibration signal, (B) frequency spectrum of vibration signal and (C) sun gear rotational speed

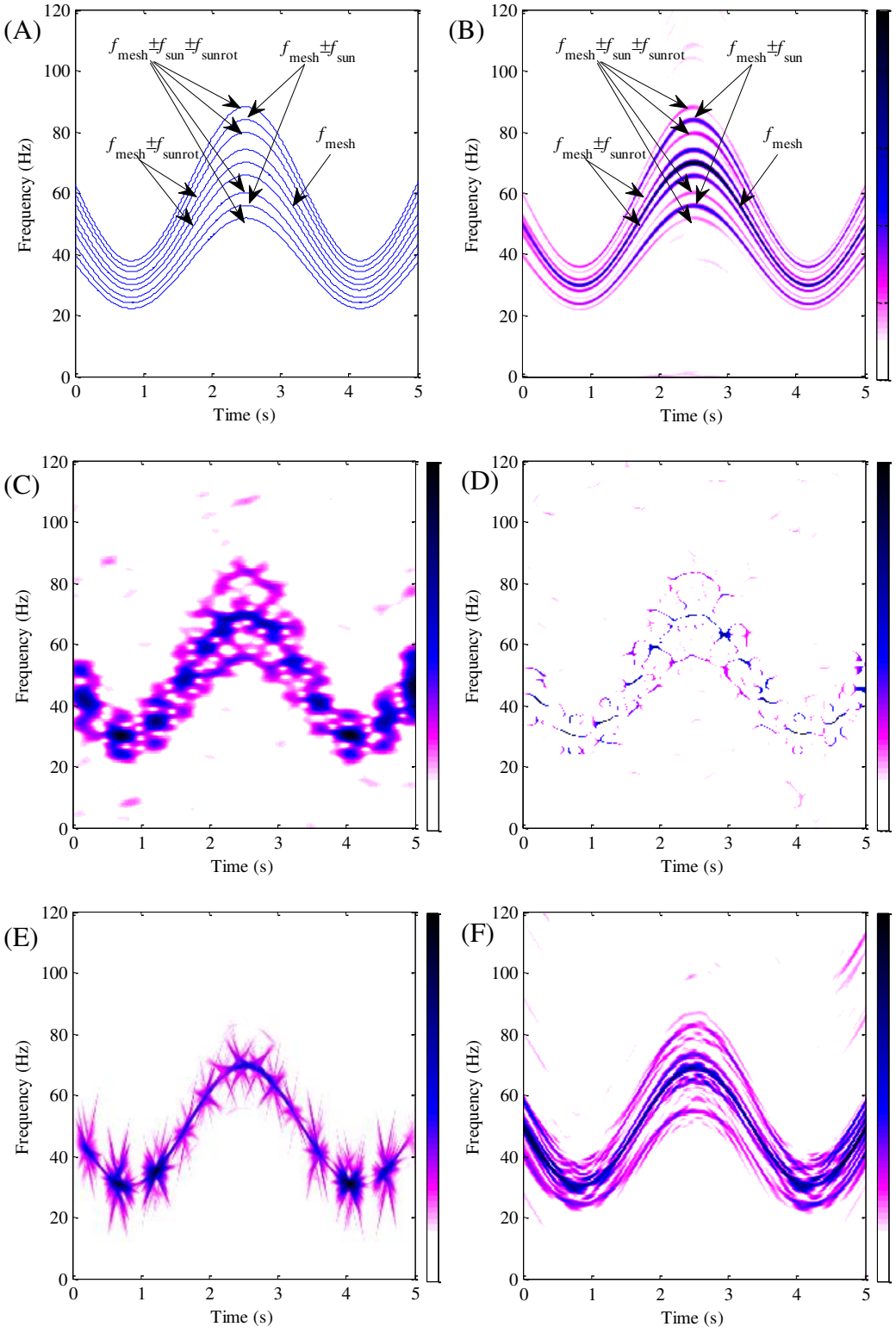

Fig. 3-12. TFR of the synthetic signal obtained by (A) real instantaneous frequency, (B) VSSTFT, (C) STFT, (D) SET, (E) GLCT and (F) PCT

3.4 Experimental tests

3.4.1 Experimental setup

In this section, we test the VSSTFT method on the experimental signals. The experimental signals are collected from a lab wind turbine drivetrain test rig. As shown in Fig. 3-13, the input shaft of the two-stage planetary gearbox is connected to a motor and the output shaft is connected a magnetic brake. In both stages, four planet gears are installed. In the test, the motor drives the planetary gearbox and the brake provides load. Two accelerometers are installed on the housing of the gearbox to collect the vibrations of the first stage and the second stage respectively. The tachometer measures the output speed of the planetary gearbox.

To generate fault signals, two faulty sun gears are used: one with wear damage to be installed in first stage of the gearbox, and the other with a chipped tooth to be mounted in second stage of the gearbox as shown in Fig. 3-14 (A) and (B) respectively. Three tests are carried out: healthy sun gears (normal sun gears are used for the both stages of the planetary gearbox), sun gear wear (sun gear in stage one is worn and sun gear in stage two is healthy), sun gear chipping (sun gear in stage two has a chipped tooth but sun gear in stage one is normal).

The sampling rate is set as 40 kHz. The load is set as 3.0 Nm. The motor rotational frequency f_d rises approximately from 20 Hz to 35 Hz and then decreases to 20 Hz. The parameters of the planetary gearbox are listed in Table 3-1. According to these parameters, the planetary gearbox characteristic frequencies, including the rotational frequencies of the gears, the fault characteristic frequencies of the gears and the gear meshing frequency, are computed and shown in Table 3-2 (Feng and Zuo, 2012). For the purpose of convenience, we select motor rotational speed as reference shaft speed and it is obtained according to its relationship with the gearbox output speed (i.e., $f_{carrier2}=(1/28)\,f_d$ as listed in Table 3-2).

Table 3-1 Configuration parameters of the gearbox

Gear name		Ring gear	Planet gear	Sun gear
Number of gear teeth	Stage 1	100	40 (4)	20
	Stage 2	100	36 (4)	28

Note: the number of planet gears is given in the parenthesis

Table 3-2 Characteristic frequency of the planetary gearbox

Characteristic frequency	First stage	Second stage
Ring gear fault frequency	$f_{ring1}=(1/6)\,f_d$	$f_{ring2}=(7/192)\,f_d$
Planet gear fault frequency	$f_{planet1}=(5/12)\,f_d$	$f_{planet2}=(175/1728)\,f_d$
Sun gear fault frequency	$f_{sun1}=(5/6)\,f_d$	$f_{sun2}=(175/1344)\,f_d$
Meshing frequency	$f_{mesh1}=(50/3)\,f_d$	$f_{mesh2}=(175/48)\,f_d$
Sun gear rotational frequency	$f_{sunrot1}=f_d$	$f_{sunrot2}=(1/6)\,f_d$
Carrier rotational frequency	$f_{carrier1}=(1/6)\,f_d$	$f_{carrier2}=(1/28)\,f_d$

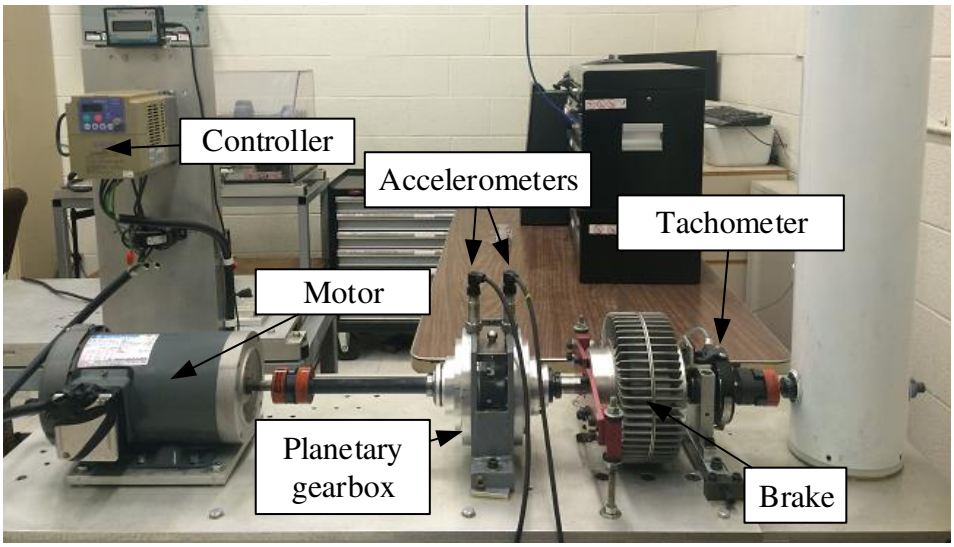

Fig. 3-13. Test rig and test setup

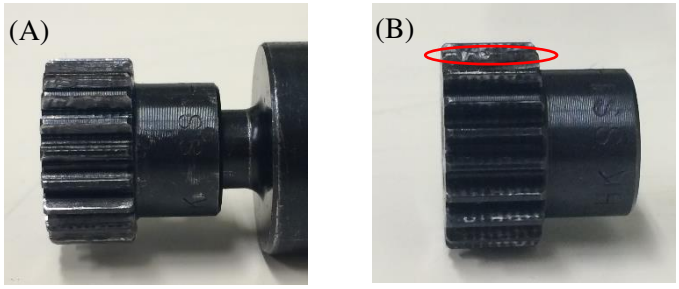

Fig. 3-14. Sun gear: (A) with wear damage and (B) with chipping damage

3.4.2 Healthy planetary gearbox

Fig. 3-15(A-C) show the normal planetary gearbox vibration signal waveform, its frequency spectrum and the shaft speed profile. As the speed of the drive motor ranges between 23 Hz and 32 Hz, the meshing frequency of the planetary gearbox stage 1 is

between 383.33 Hz and 533.33 Hz. As the key task of planetary gearbox fault diagnosis is identifying the frequencies of the sidebands around the meshing frequency, the frequency band of TFR is set as 0-800 Hz which covers enough sideband frequencies of the meshing frequencies of the two stages. The Fourier spectrum of the signal, shown in Fig. 3-15(B), suffers from spectral smearing problem. Although some peaks appear in the spectrum, it is challenging to identify them under a time-varying running speed condition. Fig. 3-16 shows the time-frequency distribution of the vibration signal of the healthy planetary gearbox obtained by the VSSTFT. As the VSSTFT is smearing-free, the components with time-varying frequency can be clearly revealed. As displayed in Fig. 3-16, the dominant frequencies are the first stage sun gear rotating frequency f_{sunrot1}, its harmonics and the planetary gearbox first stage gear meshing frequency f_{mesh1}, the difference between meshing frequency and first stage carrier rotational frequency f_{mesh1}-f_{carrier1}, the difference between meshing frequency and first stage sun gear rotational frequency f_{mesh1}+f_{sunrot1}. As the revealed sidebands do not correlate with the fault characteristic frequencies, the planetary gearbox is diagnosed as healthy.

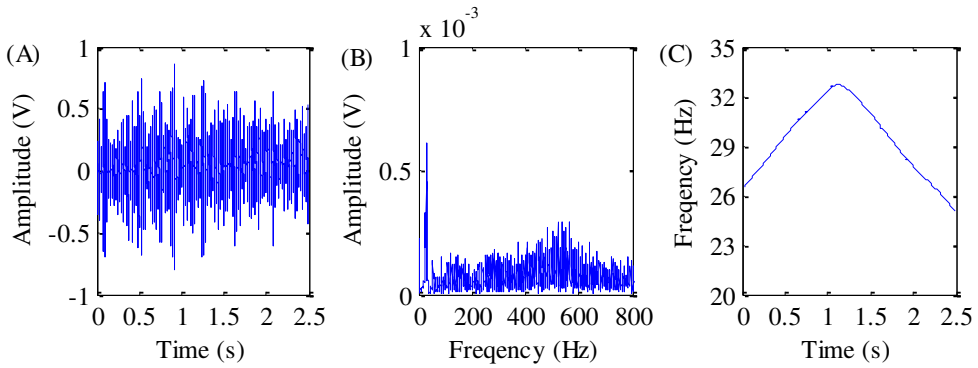

Fig. 3-15. Healthy planetary gearbox: (A) vibration signal, (B) Fourier spectrum of vibration signal, and (C) motor rotational speed

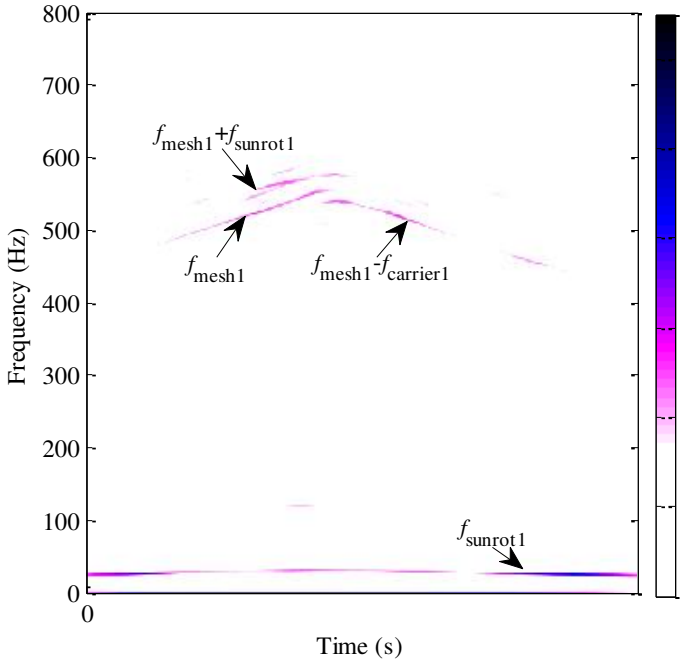

Fig. 3-16. TFR of the healthy planetary gearbox

3.4.3 Detection of sun gear wear

Now the proposed method is evaluated in diagnosing the sun gear wear fault. Fig. 3-17(A-C) shows the vibration signal waveform and its Fourier spectrum, as well as the associated drive motor speed. Similar to the healthy planetary gearbox case, the motor also rotates between 23 Hz and 32 Hz, therefore we focus on the frequency band 0-800 Hz again. The proposed VSSTFT method is applied to attain the TFR shown in Fig. 3-18. Similar to the healthy planetary gearbox case, the meshing frequency of the planetary gearbox stage 1 f_{mesh1}, the motor rotating frequency $f_{sunrot1}$, and its sidebands dominate the TFR. The sidebands $f_{mesh1}\pm 8f_{carrier1}$ are related with carrier rotation, thus do not provide information of fault. However, apart from them, several other strong sidebands also appear in the TFR. They are $f_{mesh1}-2f_{sun1}$, $f_{mesh1}\pm 4f_{sun1}$, $f_{mesh1}+6f_{sun1}$ and $f_{mesh1}+2f_{sun1}+2f_{sunrot1}$ and they are associated with the sun gear fault of the first stage of the planetary gearbox. These components have pronounced amplitudes, indicating that the planetary gearbox stage one has a sun gear fault. This result is consistent with the experimental setting of faulty sun gear.

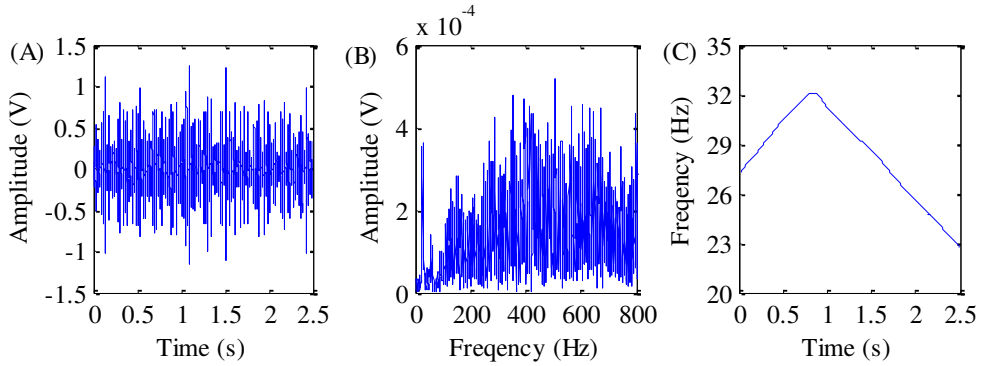

Fig. 3-17. Planetary gearbox with sun gear wear fault in the first stage: (A) vibration signal, (B) Fourier spectrum of vibration signal and (C) motor rotational speed,

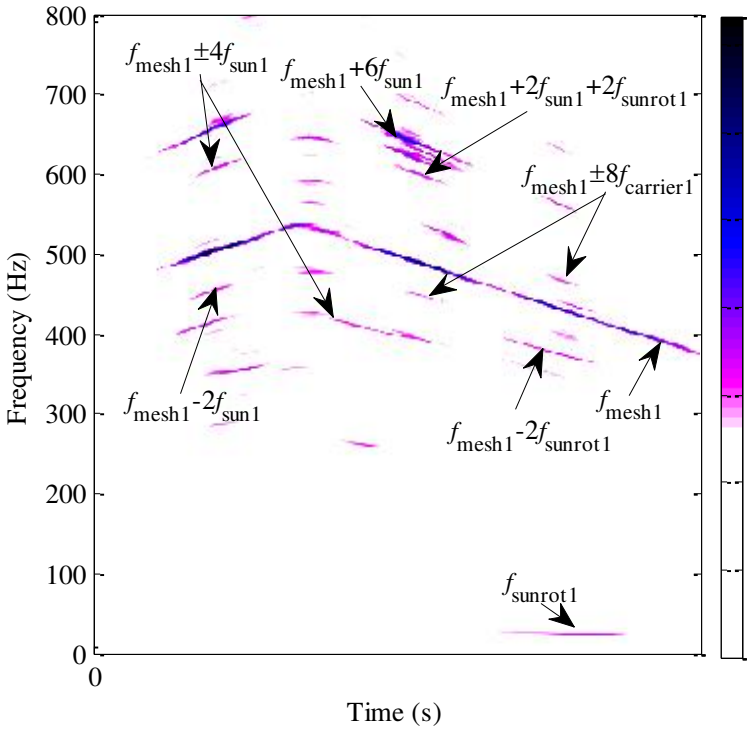

Fig. 3-18. TFR of the planetary gearbox with sun gear wear fault in the first stage

3.4.4 Detection of sun gear chipping

This subsection demonstrates the effectiveness of the VSSTFT method in detecting sun gear chipping at the planetary gearbox stage 2. The associated vibration signal and its Fourier spectrum, as well as the drive motor speed are presented in Fig. 3-19(A-C), respectively. The motor rotates between 23 Hz and 32 Hz and accordingly, the meshing frequency of the planetary gearbox stage 2 is between 83.9 Hz and 116.7 Hz. The frequency band of interest is set as 0-200 Hz, which covers enough possible sidebands of meshing

frequency of planetary gearbox stage 2. To reveal the chipping fault, the VSSTFT method is once again applied to analyze the experimental data. The obtained TFR is shown in Fig. 3-20. The dominant components are the motor rotating frequency $f_{sunrot1}$, the meshing frequency of the second stage f_{mesh2} and its sidebands. The revealed sidebands can be expressed as $f_{mesh2}+f_{sun2}+f_{sunrot2}$, $f_{mesh2}+4f_{sun2}+f_{sunrot2}$, $f_{mesh2}+8f_{sun2}+f_{sunrot2}$ and $f_{mesh2}-4f_{sun2}-f_{sunrot2}$. These sidebands are associated with the sun gear fault of stage two. This is sign of a fault on the sun gear of stage two which is again consistent with the condition of the sun gear used in the experiment.

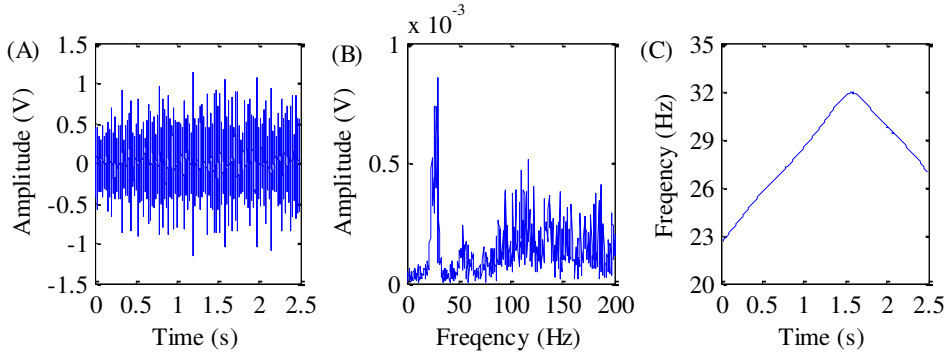

Fig. 3-19. Planetary gearbox with sun gear chipping fault in the second stage: (A) vibration signal, (B) Fourier spectrum of vibration signal and (C) motor rotational speed

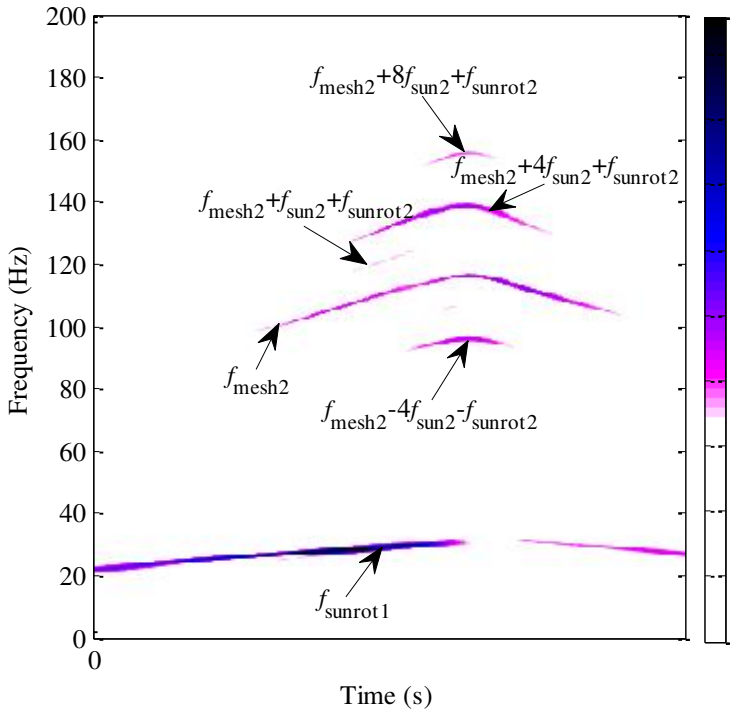

Fig. 3-20. TFR of the planetary gearbox with sun gear chipping fault in the second stage

3.5 Conclusions

In this chapter, the VSSTFT method for the fault diagnosis of planetary gearbox under non-stationary conditions is proposed. The VSSTFT has two advantages, 1) it is free of TFR smearing caused by time-varying running speed, thus the time-frequency components have concentrated ridges in the TFR and can be easily identified; 2) the window length is determined according to the gearbox configuration and the corresponding resolution of the VSSTFT varies with more suitable time-frequency resolution to better separate the TFR components. These advantages make the VSSTFT particularly suitable for analysing complex nonstationary vibration signals of planetary gearbox. We have validated the proposed VSSTFT method using both simulated and experimental signals. By applying the proposed VSSTFT, the time-frequency structures of planetary gearboxes vibration signals are clearly revealed in time-frequency plane and fault patterns are identified according to the revealed sidebands related to gear faults. The analyses demonstrate that the presented VSSTFT gives promising performances for the fault diagnosis of planetary gearbox under non-stationary conditions.

4 Velocity synchrosqueezing transform (VST)

4.1 Motivation

The VSSTFT method proposed in the last chapter is able to generate a smear-free TFR for fault diagnosis of planetary gearbox under non-stationary conditions, however, its readability is relatively low. Readability here denotes the ease with which a reader can distinguish individual components in the obtained TFR. The reason of low readability is because the linear transform has relatively low energy concentration. Readability is important for fault diagnosis, because the users may find more useful components from a sharpen TFR and they may miss important frequency components from a TFR with low energy concentration.

The recently proposed SST (Daubechies et al., 2011) is able to sharpen the TFR obtained by the CWT (Daubechies, 1992), thus generating a more condensed TFR with better readability (Feng et al., 2015a). The CWT (Daubechies, 1992) reveals the signal time-frequency structure by decomposing the signal into a weighted sum of scaled mother wavelets. The frequency of the mother wavelet selected is usually time-invariant, thus the CWT lacks the adaptability to analyse nonstationary signals. This is reflected by the smearing effects in the scalogram of the nonstationary signal. The SST sharpens the scalogram along the frequency direction, thus achieving a better resolution and eliminating the smear in the frequency direction. However, the smear occurs in both the time and frequency directions, and therefore the synchrosqueezed TFR is still smeared in the time dimension for nonstationary signals (Li and Liang, 2012b, a; Feng et al., 2015a).

In a running gearbox, the movements of gearbox parts, e.g., gear meshing, are synchronous with shaft rotational angle. Such movements usually generate strong vibration components, for example, gear meshing frequency, its harmonics and sidebands. These components are therefore synchronous with shaft rotational speed. Under a nonstationary condition, the shaft rotational speed is time-varying, therefore the frequencies of the signal components are also time-varying and the signal collected is nonstationary. For this reason, the SST result of the signal collected under nonstationary conditions remains smeared. The smearing effects can be illustrated by a simple example using a synthetic nonstationary vibration signal. This signal contains only the shaft rotational frequency and its second

harmonic. It is assumed that the signal is collected under a nonstationary condition and the shaft rotational frequency oscillates between 8 Hz and 18 Hz. This signal is defined by

$$s_1(t) = \sin\left[2\pi\int_0^t f_{\text{shaft1}}(\tau)\,\mathrm{d}\tau\right] + \sin\left[2\pi\int_0^t 2f_{\text{shaft1}}(\tau)\,\mathrm{d}\tau\right] \qquad 0 \le \mathrm{t} \le 1 \qquad (4\text{-}1)$$

where

$$f_{\text{shaft1}}(t) = 13 + 5\cos(2\pi t) \qquad (4\text{-}2)$$

The signal waveform, the true instantaneous frequencies of the two constituents of the nonstationary signal and the signal scalogram obtained by the CWT are shown in Fig. 4-1(A-C) respectively. As shown in Fig. 4-1(C), the scalogram has serious smearing effects, the signal time-frequency structure is vague and the constituents cannot be uncovered. The smearing effect remains even after synchosqueezing as plotted in Fig. 4-1(D). It can be seen that the signal components are still difficult to discern due to the smearing effects.

For comparison, we generate a synthetic stationary signal which also contains only the shaft rotational frequency and its second harmonic. Suppose this stationary signal is collected under a stationary condition and the shaft rotational frequency is 10 Hz for the whole time duration. This signal is also described by Eq.(4-1) with a fixed frequency

$$f_{\text{shaft1}} = 10\,. \qquad (4\text{-}3)$$

Fig. 4-2 (A-C) show the waveform of the synthetic stationary signal, its true instantaneous frequencies and its scalogram obtained by the CWT. From Fig. 4-2(C), it can be seen that the two components related to 10 Hz and 20 Hz can be roughly identified in the scalogram. It can be found that the components related to 20 Hz occupies a wider frequency region than the components associated to 10 Hz. This is because the CWT has lower frequency resolution in higher frequency region and higher frequency resolution in lower frequency region. To obtain a TFR with better readability, the SST is employed to sharpen Fig. 4-2 (C) and the sharpened result is shown in Fig. 4-2 (D). By comparing the true frequency trajectories (Fig. 4-2 (B)) and the signal TFR obtained by the SST (Fig. 4-2 (D)), it can be seen that the SST clearly and accurately reveals the time-frequency structure of the stationary signal. Comparing the TFR of the synthetic nonstationary signal (Fig. 4-1(D)) with the TFR of the synthetic stationary signal (Fig. 4-2 (D)) indicates that the SST

is able to generate smear-free TFR for a stationary signal but not for a nonstationary signal. This observation motivates us to map a nonstationary signal into a corresponding stationary signal to facilitate the SST.

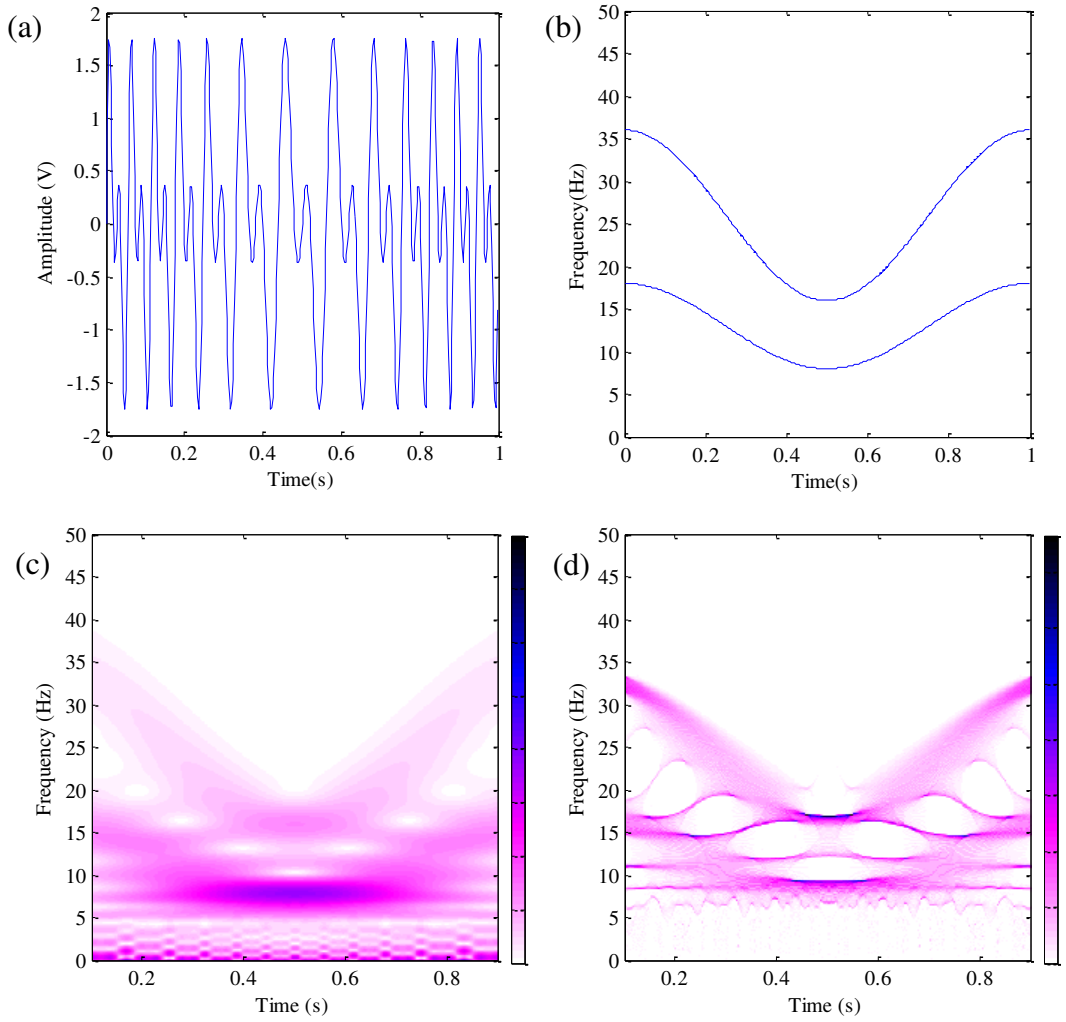

Fig. 4-1. The synthetic nonstationary signal: (A) waveform, (B) True instantaneous frequencies, (C) scalogram obtained by the CWT and (D) TFR obtained by the SST

As most of the signal components are synchronous with shaft rotational speed, the nonstationary signal can be mapped into a stationary one by mapping from time domain to angular domain (i.e., the domain of shaft rotational angle) (Fyfe and Munck, 1997; Borghesani et al., 2014), thereby enabling the signal to fulfill the stationarity requirement by the SST for a smear-free TFR. Combining the SST with the mapping of the signal from time domain into angular domain will thus effectively address the smear issue of the SST

and yield a smear-free TFR with better readability for fault diagnosis of planetary gearbox under nonstationary conditions.

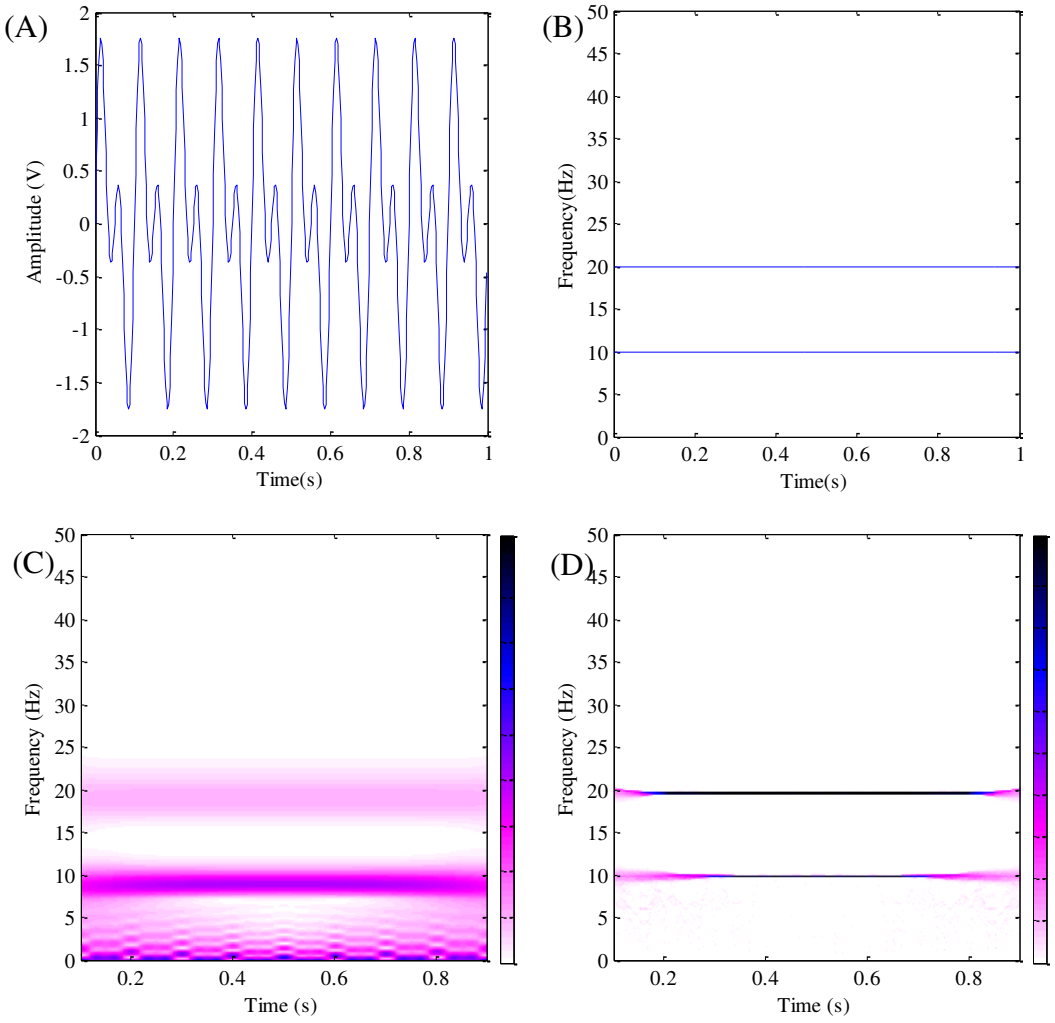

Fig. 4-2. The synthetic stationary signal: (A) waveform, (B) true instantaneous frequencies, (C) scalogram obtained by the CWT, and (D) TFR obtained by the synchrosqueezing transform

Based on the above analysis, the procedure of the proposed method is summarised as follows: 1) Map the raw vibration signal into angle domain to obtain a corresponding stationary signal; 2) Synchrosqueezing transform the resulting stationary signal and 3) Restore the signal TFR from the synchrosqueezed signal. The proposed method is named velocity synchrosqueezing transform (VST) because the SST is directly performed on the signal mapped according to the shaft velocity. It yields a much more concentrated TFR without unwanted smearing.

4.2 Presentation of the VST

4.2.1 Overview of the SST

The SST (Daubechies et al., 2011) improves the TFR readability by relocating the scalogram obtained by the CWT of a signal of interest. The CWT (Daubechies, 1992) of a signal $x(t)$ is given by

$$W_s(a,b) = a^{-1/2}\int_{-\infty}^{\infty} x(t)\overline{\psi\left(\frac{t-b}{a}\right)}\mathrm{d}t, \tag{4-4}$$

where the overhead bar denotes complex conjugate operation, $\psi(t)$ is a complex mother wavelet, a is scale and b is translational value. The wavelet $\psi(t)$ can be expressed by

$$\psi(t) = \lambda(t)\exp(i\omega_0 t), \tag{4-5}$$

where $\lambda(t)$ is a window function centred at t=0 and ω_0 is the centre frequency of the wavelet. The Fourier transform of $\psi(t)$ is given by

$$\hat{\psi}(\xi) = \hat{\lambda}(\xi) * \delta(\xi - \omega_0), \tag{4-6}$$

where the hat operator represents Fourier transform operation, * means convolution and ξ is angular frequency. As $\delta(\xi-\omega_0)$ is concentrated at ω_0 and $\hat{\lambda}(\xi)$ is spread around 0, the Fourier transform of the wavelet $\hat{\psi}(\xi)$ will be spread around ω_0.

For a purely harmonic signal $x(t) = A\cos(\omega t)$, Eq. (4-4) can be rewritten as (based on the Plancherel's theorem (Plancherel and Leffler, 1910))

$$\begin{aligned} W_s(a,b) &= \frac{1}{2\pi}\int_{-\infty}^{\infty}\hat{x}(\xi)a^{1/2}\overline{\hat{\psi}(a\xi)}\exp(ib\xi)\mathrm{d}\xi \\ &= \frac{A}{4\pi}\int_{-\infty}^{\infty}\left[\delta(\xi-\omega)+\delta(\xi+\omega)\right]a^{1/2}\overline{\hat{\psi}(a\xi)}\exp(ib\xi)\mathrm{d}\xi \\ &= \frac{A}{4\pi}a^{1/2}\overline{\hat{\psi}(a\omega)}\exp(ib\omega) \end{aligned}. \tag{4-7}$$

As the Fourier transform of the wavelet $\hat{\psi}(\xi)$ is spread around ω_0, the wavelet transform $W_s(a, b)$ will be spread around the horizontal line $a=\omega_0/\omega$ rather than being concentrated at that line. This means the resolution of the wavelet transform is limited.

However, the part $\exp(ib\omega)$ in Eq. (4-7) directly indicates the signal angular frequency ω, regardless of the value of scale a. Based on this characteristic, a candidate instantaneous angular frequency of the signal s for any (a, b) for which $W_s(a,b)\neq 0$ is introduced (Daubechies et al., 2011), expressed by

$$\omega(a,b) = -i\left(W(a,b)\right)^{-1}\frac{\partial}{\partial b}W(a,b). \tag{4-8}$$

In order to improve the TFR readability, i.e., to make the TFR ridge more condensed, the TFR can be constructed by reallocating the contributions of the CWT result $W_s(a,b)$ with candidate angular frequency ω into the location (ω,b) in the time-frequency plane. This reallocation operation generates the TFR by squeezing the CWT in time-scale plane to achieve a better resolution, and thus this method is termed SST. As the data is discrete in real applications, the wavelet transform $W_s(a, b)$ is calculated only at discrete values a_k with $\Delta a=a_k-a_{k-1}$ and its SST $T_s(\omega,b)$ is computed by summing different contributions satisfying $|\omega_l-\omega_s(a_k,b)|\leq\Delta\omega/2$ at discrete values ω_l with $\Delta\omega=\omega_l-\omega_{l-1}$ (Daubechies et al., 2011):

$$T(\omega_l,b) = (\Delta\omega)^{-1}\sum_{a_k:\left|\omega_l-\omega_s(a_k,b)\right|\leq\Delta\omega/2} W(a_k,b)a_k^{-3/2}(\Delta a)_k. \tag{4-9}$$

4.2.2 The velocity synchrosqueezing transform (VST)

Based on the analysis in subsection 4.1, the procedure of the proposed VST is detailed below.

Step 1. Map the signal from time domain to angle domain to obtain a corresponding stationary signal.

As discussed in chapter 2, a time-domain signal $x_{\text{time}}(t)$ (i.e, a function relating time to vibration amplitude) can be mapped into angle domain based on Eq.(3-1). The obtained stationary angle-domain signal can then be expressed by

$$x_{\text{angle}}(\varphi) = x_{\text{time}}\left(\theta^{-1}(\varphi)\right), \tag{4-10}$$

where $x_{\text{angle}}(\varphi)$ is an angle-domain signal and θ^{-1} is the inverse function of θ.

In this step, the function of angle-domain signal is obtained based on raw time-domain vibration signal $x_{\text{time}}(t)$ and shaft rotational angle $\theta(t)$ using Eq. (4-10). In real world, the signal is discrete, thus signal mapping cannot be realised directly and has to be realised by using interpolation techniques (Fyfe and Munck, 1997). However, in the implementation of the proposed method, interpolation can be avoided by using the fast implementation algorithm detailed in subsection 4.2.3.

Step 2. Synchrosqueezing transform the resulting signal.

Though the SST is able to generate a high-resolution TFR, it requires the signal to be stationary. To satisfy this requirement, the SST is applied to the corresponding stationary angle-domain signal directly, i.e., to squeeze the CWT of the angle-domain signal. As the CWT processes angle-domain signal, the mother wavelet employed should be an angle-domain wavelet. Also the scale and translational value of the CWT employed here should control the scaling and translation of the mother wavelet over shaft angle, rather than over time. Hence the scale and translational value here are represented using new symbols c and η respectively. The CWT of the angle-domain signal is expressed by

$$W_{\text{Scale-Angle}}\left(c,\eta\right)=a^{-1/2}\int_{-\infty}^{\infty}x_{\text{angle}}\left(\varphi\right)\overline{\psi\left(\frac{\varphi-\eta}{c}\right)}\mathrm{d}\varphi\,. \tag{4-11}$$

Traditionally, the SST squeezes the CWT according to the candidate instantaneous frequency at any (a, b) on the time–scale plane (Eq. (4-8)). Similarly, in the proposed method, a candidate order at any (c, η) on the angle-scale plane is employed, expressed by

$$\Omega_{\text{Scale-Angle}}\left(c,\eta\right)=-i\left(W_{\text{Scale-angle}}\left(c,\eta\right)\right)^{-1}\frac{\partial}{\partial\eta}W_{\text{Scale-Angle}}\left(c,\eta\right). \tag{4-12}$$

In the traditional SST, the squeezing is performed in time-frequency domain according to the candidate frequency to obtain signal TFR (Eq. (4-9)). Similarly in the proposed method, by squeezing the CWT of angle-domain signal according to the calculated candidate order, the energy distribution in the angle-scale plane is thus squeezed and converted to the angle-order plane, expressed by

$$T_{\text{Angle-Order}}\left(\eta,\Omega\right)=\left(\Delta\Omega\right)^{-1}\sum_{c_k:\left|\Omega_{\text{Scale-Angle}}\left(c_k,\eta\right)-\Omega\right|\le\Delta\Omega/2}W_{\text{Scale-Angle}}\left(c_k,\eta\right)c_k^{-3/2}\left(\Delta c\right)_k, \tag{4-13}$$

where Ω is order. As $T_{\text{Angle-Order}}(\eta,\Omega)$ is obtained by processing the stationary angle-domain signal using the SST, it should be smear-free and of high resolution.

Step 3. Restore the TFR from the synchrosqueezed signal.

The SST of the corresponding signal obtained in the last step expresses the signal energy over angle and order. The TFR should present the signal energy over time and frequency. Therefore the TFR can be obtained by mapping the SST result of the corresponding signal computed in step 2 from angle-order domain into time-frequency domain, i.e., by converting $T_{\text{Angle-Order}}(\eta,\Omega)$ to $T_{\text{Time-Freq}}(\tau,f)$ (where $T_{\text{Time-Freq}}(\tau,f)$ is the signal TFR, τ and f represents time and frequency of the TFR respectively). As discussed in the chapter 2, the angle-order representation can be mapped into time-frequency domain using the relationship function Eqs. (3-5) and (3-8). The TFR can then be computed by mapping the $X_{\text{AOR}}(\eta, \Omega)$ into time-frequency domain, i.e., substituting the relationship functions (Eq. (3-5) and Eq. (3-8)) into the SST of the corresponding signal $T_{\text{Angle-Order}}(\eta, \Omega)$, expressed by

$$T_{\text{Time-Freq}}\left(\tau, f\right) = T_{\text{Angle-Order}}\left(\theta\left(\tau\right), \mathrm{g}\left(\tau, f\right)\right). \tag{4-14}$$

In this step, the TFR is obtained via mapping. Similar to step 1, the realization of mapping requires interpolations. The interpolation can be avoided in the implementation of the proposed method which is detailed in subsection 4.2.3.

The proposed method can generate a smear-free fine-resolution TFR. This is because a) Steps 1 and 3 only change the domains, which do not introduce smearing effects and do not alter resolution, and b) Step 2 applies the SST to the stationary angle-domain signal to improve the resolution without introducing smearing effects. Based on the analysis of the above three steps, the resulting TFR of the proposed VST method ought to be smear-free with improved resolution.

To better understand the VST process, the three steps of the proposed VST method are summarised in a flowchart (Fig. 4-3). As shown in the flowchart, the corresponding stationary angle-domain is first obtained by mapping the vibration signal from time domain into angle domain, then the SST is applied to the corresponding signal, and finally TFR is restored from the SST result of the corresponding signal via another mapping from angle-

order domain to time-frequency domain. To further facilitate the understanding of the proposed VST, it is demonstrated step by step using the synthetic nonstationary signal used in the subsection 4.1. This synthetic nonstationary signal is first mapped from time domain into angle domain and the obtained corresponding stationary angle-domain signal is shown in Fig. 4-4(A). It can be seen that the signal becomes stationary (this is reflected by the periodicity of the signal). The SST of the corresponding signal is then carried out and the result is displayed in Fig. 4-4 (B). It can be found that the synchrosqueezed signal is no longer smeared and the two horizontal components at first order and second order correspond to shaft rotational frequency and its second harmonic can be identified with high resolution. The TFR of the original synthetic signal is finally restored by a mapping from angle-order domain into time-frequency domain as shown in Fig. 4-4 (C). It can be seen that the signal constituents are clearly and accurately revealed without smearing effect. Comparing the TFR of the synthetic nonstationary signal obtained by the VST (Fig. 4-4 (C)) and the TFR obtained by the SST (Fig. 4-1(D)) indicates that the proposed VST outperforms the SST in generating a smear-free TFR.

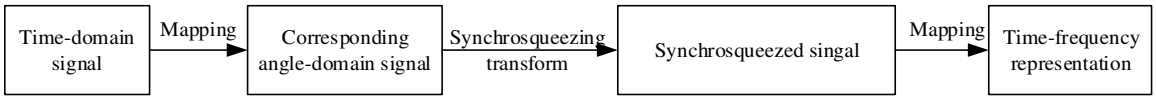

Fig. 4-3. Flowchart of the VST method

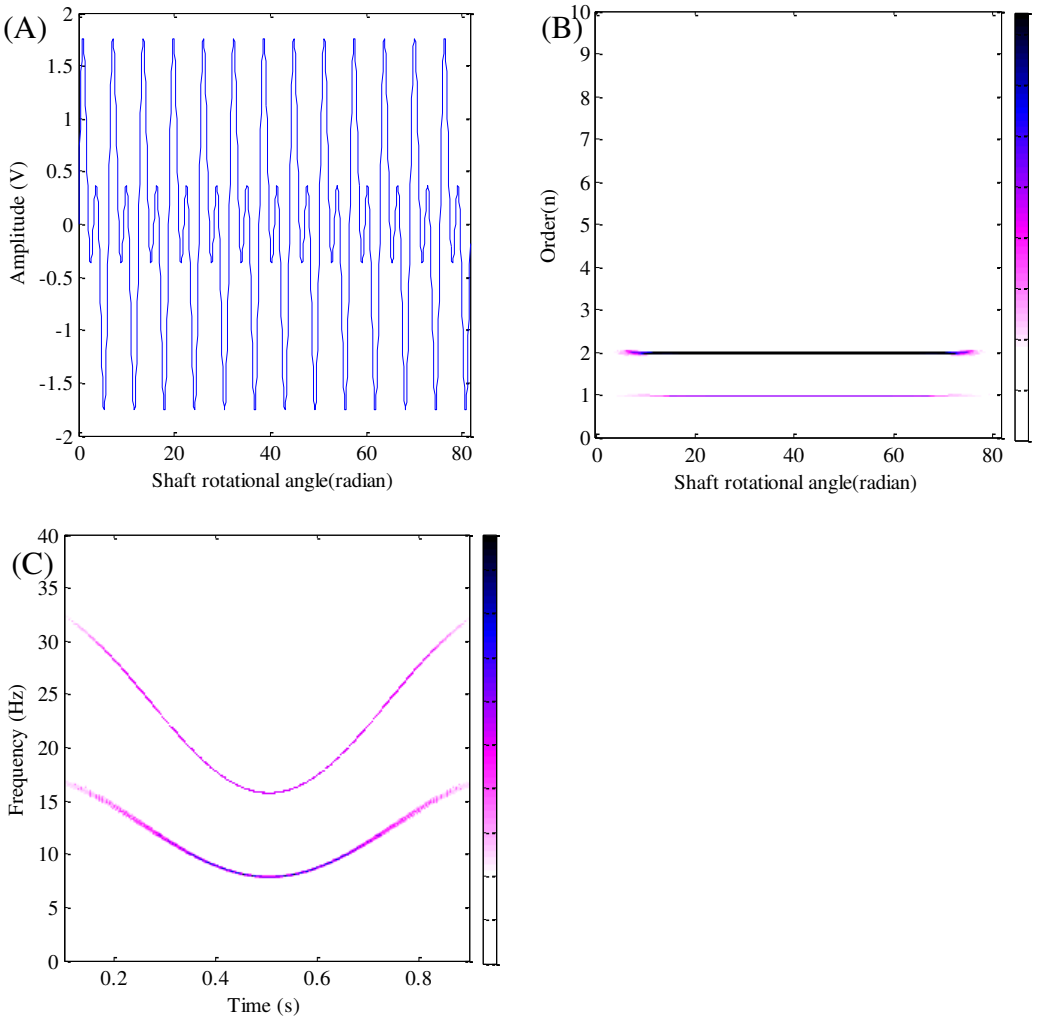

Fig. 4-4. Demonstration of the proposed VST: (A) mapped stationary signal, (B) SST of the mapped stationary signal, and (C) TFR of the synthetic nonstationary signal obtained by the VST.

4.2.3 Fast implementation of the VST

One difficulty in the implementation of the VST is that the domain mappings involved in step 1 and step 3 may require signal resampling, as the signal is discrete in real applications (Fyfe and Munck, 1997). Signal resampling is commonly realised using interpolation techniques, which not only increase the complexity but also introduce interpolation errors, thus compromising the accuracy of the result. To mitigate this difficulty, the proposed method is simplified so that the smear-free high-resolution TFR can be obtained in a single step without resampling the signal. The simplification process is inspired by the derivation of the velocity synchronous discrete Fourier transform, which

paves a direct path from angle domain to order domain without resampling the signal (Borghesani et al., 2014).

With equations (4-13) and (3-8), the TFR is expressed as

$$\begin{aligned} T_{\text{Time-Freq}}\left(\tau, f\right) &= X_{\text{Angle-Order}}\left(\theta(\tau), \frac{2\pi f}{\theta'(\tau)}\right) \\ &= \left(\Delta\Omega\right)^{-1} \sum_{c_k : \left|\Omega_{\text{Scale-Angle}}\left(c_k, \theta(\tau)\right) - \frac{2\pi f}{\theta'(\tau)}\right| \le \Delta\Omega/2} W_{\text{Scale-Angle}}\left(c_k, \theta(\tau)\right) c_k^{-3/2} \left(\Delta c\right)_k \end{aligned} . \tag{4-15}$$

In the following derivations, the new symbols $W_{\text{Scale-Time}}(c_k,\tau)$ and $\Omega_{\text{Scale-Time}}(c_k,\tau)$ are used to represent $\Omega_{\text{Scale-Angle}}(c_k,\theta(\tau))$ and $W_{\text{Scale-Angle}}(c_k,\theta(\tau))$. The energy representation $W_{\text{Scale-Time}}(c_k,\tau)$ can be obtained by substituting equations (4-10) and (3-5) into Eq. (4-11), i.e.,

$$\begin{aligned} W_{\text{Scale-Time}}\left(c_k, \tau\right) &= W_{\text{Scale-Angle}}\left(c_k, \theta(\tau)\right) \\ &= c_k^{-1/2} \int_{-\infty}^{\infty} x_{\text{angle}}\left(\theta(t)\right) \overline{\psi\left(\frac{\theta(t) - \theta(\tau)}{c_k}\right)} \mathrm{d}\theta(t) \end{aligned} . \tag{4-16}$$

As $x_{\text{angle}}(\theta(t))$ maps time t to vibration amplitude, it can be substituted for time-domain signal $x_{\text{time}}(t)$. $W_{\text{Scale-Time}}(c_k,\tau)$ is then given by

$$W_{\text{Scale-Time}}\left(c_k, \tau\right) = c_k^{-1/2} \int_{-\infty}^{\infty} x_{\text{time}}\left(t\right) \overline{\psi\left(\frac{\theta(t) - \theta(\tau)}{c_k}\right)} \mathrm{d}\theta(t) . \tag{4-17}$$

Changing the domain of integration leads to

$$\begin{aligned} W_{\text{Scale-Time}}\left(c_k, \tau\right) &= c_k^{-1/2} \int_{-\infty}^{\infty} x_{\text{time}}\left(t\right) \overline{\psi\left(\frac{\theta(t) - \theta(\tau)}{c_k}\right)} \frac{\mathrm{d}\theta(t)}{\mathrm{d}t} \mathrm{d}t \\ &= c_k^{-1/2} \int_{-\infty}^{\infty} x_{\text{time}}\left(t\right) \theta'(t) \overline{\psi\left(\frac{\theta(t) - \theta(\tau)}{c_k}\right)} \mathrm{d}t \end{aligned} . \tag{4-18}$$

The candidate order $\Omega_{\text{Scale-Time}}(c_k, \tau)$ can be calculated using Eq. (4-12):

$$
\begin{aligned}
&\Omega_{\text{Scale-Time}}\left(c_k,\tau\right)=\Omega_{\text{Scale-Angle}}\left(c_k,\theta\left(\tau\right)\right)\\
&=-i\left(W_{\text{Scale-Angle}}\left(c_k,\theta\left(\tau\right)\right)\right)^{-1}\frac{\partial}{\partial\theta\left(\tau\right)}W_{\text{Scale-Angle}}\left(c_k,\theta\left(\tau\right)\right)\\
&=-i\left(W_{\text{Scale-Angle}}\left(c_k,\theta\left(\tau\right)\right)\right)^{-1}\left(\frac{\partial\theta\left(\tau\right)}{\partial\tau}\right)^{-1}\frac{\partial}{\partial\tau}W_{\text{Scale-Time}}\left(c_k,\tau\right)\\
&=-i\left(W_{\text{Scale-Angle}}\left(c_k,\theta\left(\tau\right)\right)\theta'\left(\tau\right)\right)^{-1}\frac{\partial}{\partial\tau}W_{\text{Scale-Time}}\left(c_k,\tau\right)
\end{aligned}
\tag{4-19}
$$

Based on the above analysis, the algorithm for fast implementation of the proposed VST can be summarised below

$$
T_{\text{Time-Freq}}\left(\tau,f\right)=\left(\Delta\Omega\right)^{-1}\sum_{a_k:\left|\Omega_{\text{Scale-Time}}\left(c_k,\tau\right)-\frac{2\pi f}{\theta'\left(\tau\right)}\right|\le\Delta\Omega/2}W_{\text{Scale-Time}}\left(c_k,\tau\right)a_k^{-3/2}\left(\Delta c\right)_k,
\tag{4-20}
$$

where

$$
\Omega_{\text{Scale-Time}}\left(c_k,\tau\right)=-i\left(W_{\text{Scale-Time}}\left(c_k,\tau\right)\theta'\left(\tau\right)\right)^{-1}\frac{\partial}{\partial\tau}W_{\text{Scale-Time}}\left(c_k,\tau\right),
\tag{4-21}
$$

and

$$
W_{\text{Scale-Time}}\left(c_k,\tau\right)=c_k^{-1/2}\int_{-\infty}^{\infty}x_{\text{time}}\left(t\right)\theta'\left(t\right)\overline{\psi\left(\frac{\theta\left(t\right)-\theta\left(\tau\right)}{c_k}\right)}\mathrm{d}t\,.
\tag{4-22}
$$

The fast implementation simplifies the procedure from original three steps to only one step, which is important for on-line fault detection.

4.3 Simulation evaluations

In this section, the VST method is evaluated using a numerically synthetic signal. The simulated vibration signal of a planetary gearbox with a faulty sun gear under a speed-oscillating state is generated using the model given in Appendix A (Feng and Zuo, 2012). Without loss of generality, only the fundamental frequencies of the gear meshing frequency $f_{\text{mesh}}\left(t\right)$, sun gear rotating frequency $f_{\text{sunrot}}\left(t\right)$ and sun gear characteristic frequency $f_{\text{sun}}\left(t\right)$ are considered in the simulation. To mimic the background noise, a Gaussian white noise is added to generate a noisy signal with a signal-to-noise ratio (SNR) of 0 dB. The simulated signal is expressed below,

$$x(t)=\left\{1-\cos\left[2\pi\int_0^t f_{\text{sunrot}}(\tau)\,\mathrm{d}\tau\right]\right\}\left\{1+\cos\left[2\pi\int_0^t f_{\text{sun}}(\tau)\,\mathrm{d}\tau+\phi\right]\right\}\times\cos\left[2\pi\int_0^t f_{\text{mesh}}(\tau)\,\mathrm{d}\tau+\theta\right]+\mathrm{N}(t) \tag{4-23}$$

where the initial phrases $\phi=\theta=0$ and N(t) is noise. The signal lasts five seconds and is sampled at a rate of 2 kHz. The sun gear rotating frequency is set at $f_{\text{sunrot}}(t)$=3+0.9cos(0.6πt) to simulate a scenario where the sun gear rotates at an oscillating frequency between 2.1 Hz and 3.9 Hz, The gear meshing frequency and the sun gear characteristic frequency are set at $f_{\text{mesh}}(t)$=50/3$f_{\text{sunrot}}(t)$ and $f_{\text{sun}}(t)$=10/3$f_{\text{sunrot}}(t)$, respectively. Accordingly they oscillate between 35 Hz and 65 Hz and between 7 Hz and 13 Hz respectively. Fig. 4-5 (A-C) show the waveform, the Fourier spectrum of the simulated signal and the rotational speed profile of the sun gear. Due to the time-varying rotational frequency, the Fourier spectrum suffers from smearing effect. It can be seen that the signal energy is distributed mostly between 0 to 100 Hz. However, the signal components are not clearly revealed and fault cannot be diagnosed from the Fourier spectrum. The simulated signal described by Equation (4-23) can be rewritten as the sum of harmonics of sun gear rotating frequency, given by

$$x(t)=\sum_{n=1}^{9}B_n\cos\left[2\pi k\int f_n(t)\,\mathrm{d}t\right]+\mathrm{N}(t) \tag{4-24}$$

where B_n=[0.25,0.5,0.25,0.5,1,0.5,0.25,0.5,0.25] and $f_n(t)$=[f_{mesh}-f_{sun}-f_{sunrot}, f_{mesh}-f_{sun}, f_{mesh}-f_{mesh}+f_{sunrot}, f_{mesh}, f_{mesh}+f_{sunrot}, f_{mesh}+f_{sun}-f_{sunrot}, f_{mesh}+f_{sun}, f_{mesh}+f_{sun}+f_{sunrot}]. This means that the signal consists of nine time-varying frequency components, i.e, $f_n(t)$ (n=1,2, …, 9). Based on the sun gear rotational speed, the frequency trajectories of these nine frequency components are presented in Fig. 4-6(A). The VST is applied to analyse the simulated signal and the produced TFR is shown in Fig. 4-6 (B).Thanks to the fine time-frequency resolution and smearing-free properties of the VST, the signal components of interest are clearly uncovered. The revealed sideband components are associated with sun gear fault, indicating the gearbox has sun gear fault. This finding is consistent with the setups.

A comparative study is also conducted here to evaluate the proposed VST method. The TFRs obtained by the short-time Fourier transform, Morlet CWT, SST and GST are shown

in Fig. 4-6 (C-F) respectively. As shown in Fig. 4-6 (C) and (D), the STFT and the CWT methods suffer from serious smearing, one can only roughly recognise the signal frequency trend but the signal components cannot be identified due to the smearing effects. The SST (Daubechies et al., 2011), shown in Fig. 4-6 (E), sharpens the CWT result, however, it still has time-frequency smear effects and does not uncover all the signal components. The GST (Li and Liang, 2012b) is performed according to the meshing frequency, which removes the smearing effect of meshing frequency component as displayed in Fig. 4-6 (F). However, it does not completely remove the smear effects of the sidebands of meshing frequency. As a result, the sidebands are not clearly discerned as the smear effects of the sidebands remain intact. Compared with them, the VST as shown in Fig. 4-6 (B) clearly reveals the signal components with high time-frequency resolution and the TFR components concentrate along their real frequencies without smear. The above analysis and comparison demonstrate the effectiveness of the VST method in addressing the smear and time-frequency resolution issues caused by shaft speed variation.

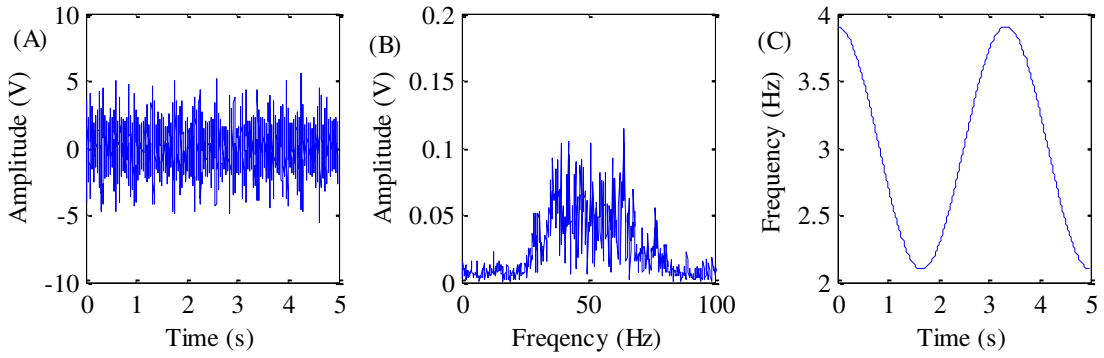

Fig. 4-5. Simulated case: (A) vibration signal, (B) frequency spectrum of vibration signal, and (C) motor speed

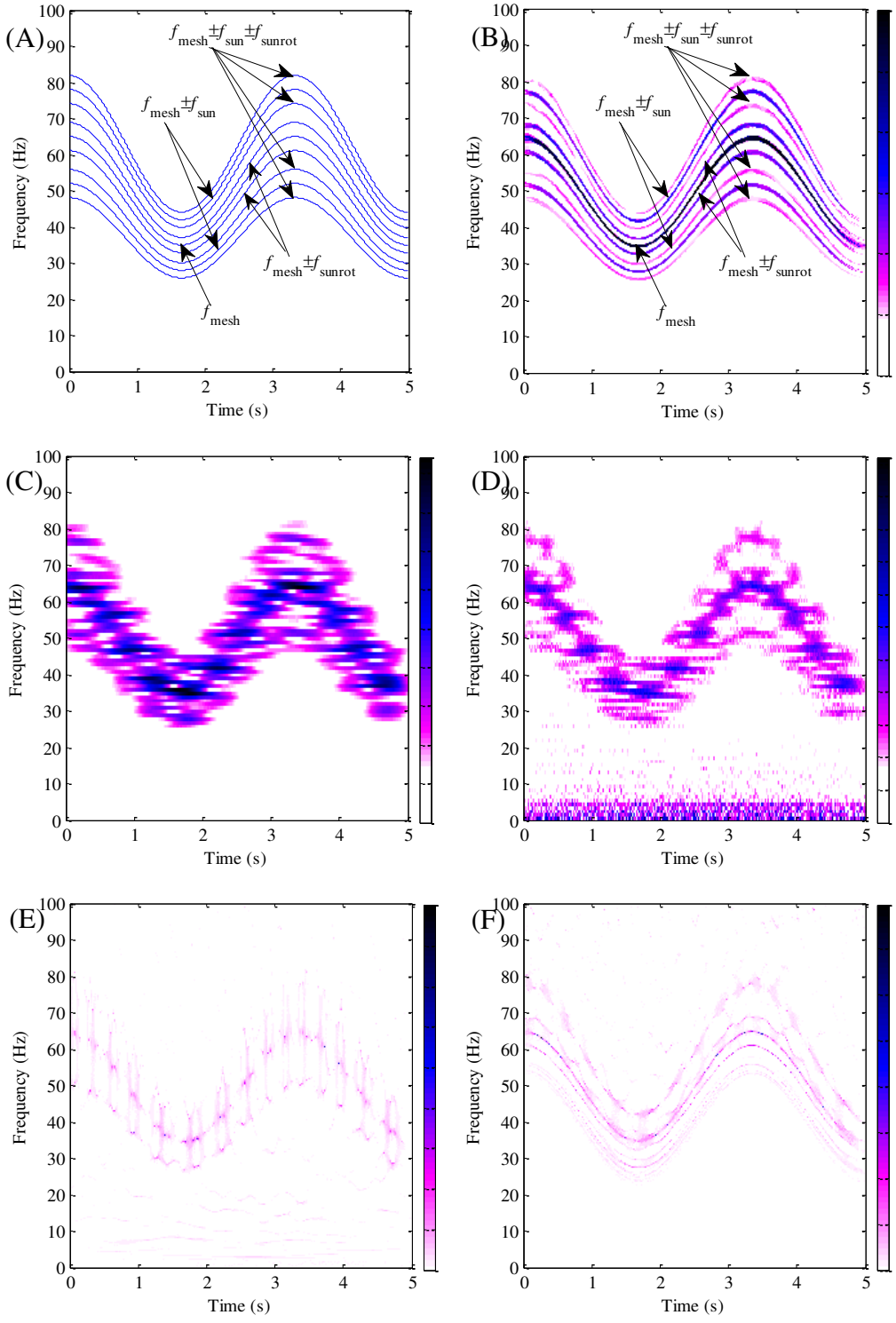

Fig. 4-6. TFR of synthetic signal: (A) real instantaneous frequencies, (B) VST, (C) SST, (D) CWT, (E) SST and (F) GST

4.4 Experimental tests

To examine the performance of the proposed VST method, tests were carried out on a wind turbine drivetrain test rig. The test rig includes an AC drive motor for powering the gearboxes, a two-stage fixed-shaft gearbox, a two-stage planetary gearbox and a magnetic brake for loading as shown in Fig. 4-7. The power transmission direction is AC motor → fixed-shaft gearbox → planetary gearbox → brake. The configurations of the two gearboxes are listed in Table 4-1.

The tests are carried out for three conditions: worn sun gear, sun gear with a chipped tooth and healthy planetary gearbox. The pictures of the two damaged gears are displayed in Fig. 3-14. In the case of worn sun gear, a sun gear with wear on every tooth is installed in stage 1 of the planetary gearbox while all the other gears are healthy. In the test of sun gear chipping fault, a sun gear with chipped fault on one tooth is mounted in stage 2 of the planetary gearbox while all the other gears are healthy. In the healthy planetary gearbox test, all the gears employed are healthy.

The experimental data are collected from accelerometers mounted on top of the casings of the planetary gearbox's stage 1 and stage 2 at a sampling frequency of 20 kHz during a speed-varying process. The motor rotational frequency, measured using a tachometer, increases approximately from 40 Hz to 60 Hz then drops to 40 Hz. A load of 13.2 Nm is generated by the brake and is applied to stage 2 output shaft of the planetary gearbox. The characteristic frequencies of the planetary gearbox are calculated using the formulas given in (Feng and Zuo, 2012) according to the configuration of the two gearboxes. As the shaft speed is time-varying, the characteristic frequencies are represented as the multiples of the motor rotational frequency f_d as listed in Table 4-2.

Table 4-1 Configuration parameters of the gearboxes

Gearbox	Gear	Number of gear teeth	
		Stage 1	Stage 2
Fixed shaft	Drive	32	40
	Driven	80	72
Planetary	Sun	20	28
	Planet (planet gears number)	40(4)	36(4)
	Ring	100	100

Table 4-2 Characteristic frequency of the planetary gearbox

Characteristic frequency	First stage	Second stage
Ring gear fault frequency	$f_{ring1}=(4/27)\,f_d$	$f_{ring2}=(7/216)\,f_d$
Planet gear fault frequency	$f_{planet1}=(5/54)\,f_d$	$f_{planet2}=(175/7776)\,f_d$
Sun gear fault frequency	$f_{sun1}=(20/27)\,f_d$	$f_{sun2}=(175/1512)\,f_d$
Meshing frequency	$f_{mesh1}=(100/27)\,f_d$	$f_{mesh2}=(175/216)\,f_d$
Sun gear rotational frequency	$f_{sunrot1}=(2/9)\,f_d$	$f_{sunrot2}=(1/27)\,f_d$
Carrier rotational frequency	$f_{carrier1}=(1/27)\,f_d$	$f_{carrier2}=(7/864)\,f_d$

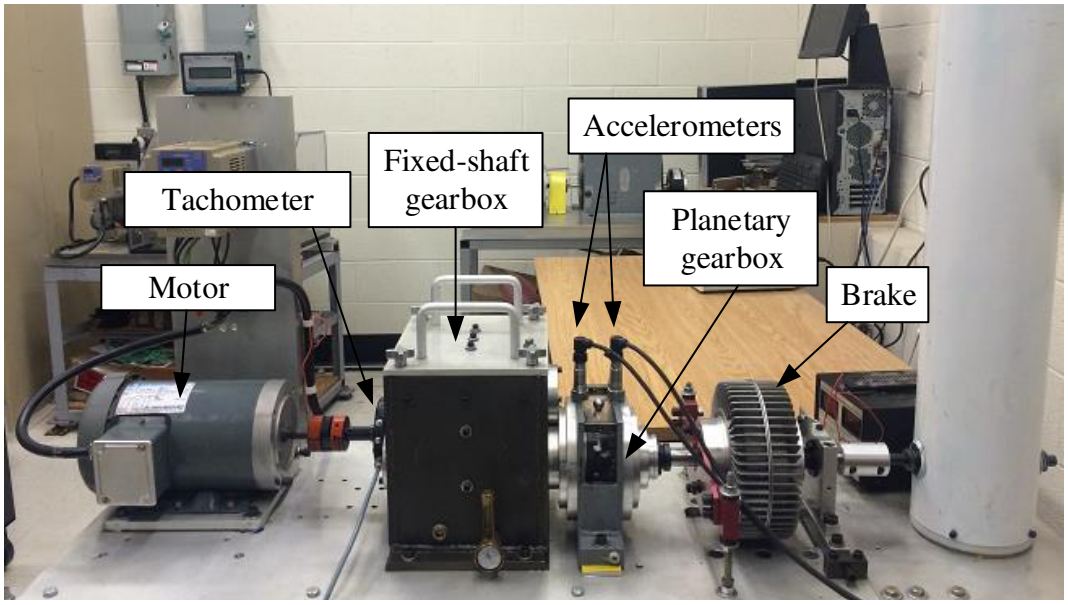

Fig. 4-7. Test rig and test setup

4.4.1 Detection of sun gear wear

This section demonstrates the effectiveness of the VST method in detecting planetary gearbox sun gear wear fault. The waveform, the signal Fourier spectrum and motor speed are plotted in Fig. 4-8(A-C). The speed of the drive motor increases from 40 Hz to 60 Hz and then drops back to 40 Hz as displayed in Fig. 4-8(C). According to the formula of calculating the meshing frequency of the planetary gearbox stage 1 (i.e., $f_{mesh1}=100/27\,f_d$ as shown in Table 4-2), the meshing frequency of the planetary gearbox stage 1 changes approximately between 148 Hz and 222 Hz. Therefore, the frequency band of interest is selected as 0-400 Hz, as this band convers enough possible sidebands of meshing frequency for fault diagnosis. Because of the time-varying speed, one cannot detect the fault feature from either the waveform or the Fourier spectrum. The VST is then applied to process the

vibration signal and the resulting TFR is shown in Fig. 4-9. The main dominant components are the motor rotating frequency f_d and its harmonics. These components are produced by the motor revolution and do not provide any information of the condition of the planetary gearbox. Apart from motor frequency and its harmonics, meshing frequency of planetary gearbox stage 1 and its sidebands are also present in the TFR. The sideband components are the combinations of meshing frequency and sun gear fault characteristic frequency (f_{mesh1}-$2f_{sun1}$ and f_{mesh1}+$2f_{sun1}$), the combination of meshing frequency, sun gear fault characteristic frequency and sun gear rotating frequency (f_{mesh1}-$2f_{sun1}$-$2f_{sunrot1}$). These sidebands have significant amplitudes and are related to sun gear fault characteristic frequency, indicating that stage 1 of the planetary gearbox has sun gear fault. This finding is in agreement with the sun gear condition.

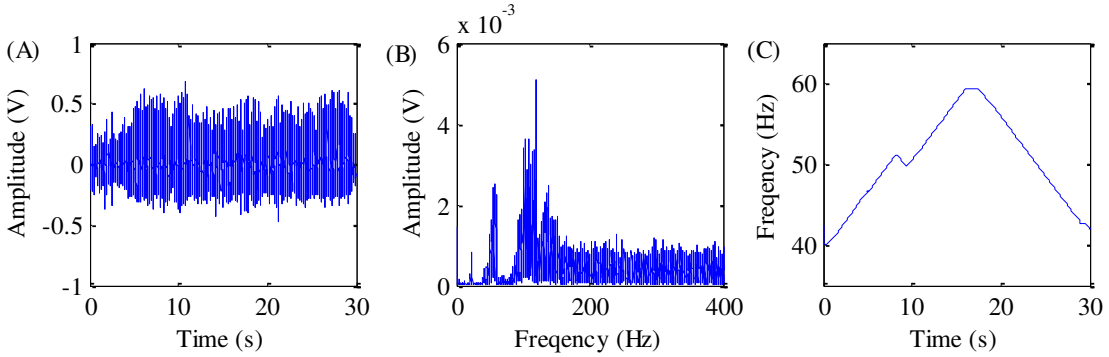

Fig. 4-8. Planetary gearbox with stage 1 sun gear wear fault: (A) vibration signal, (B) frequency spectrum of vibration signal and (C) motor speed.

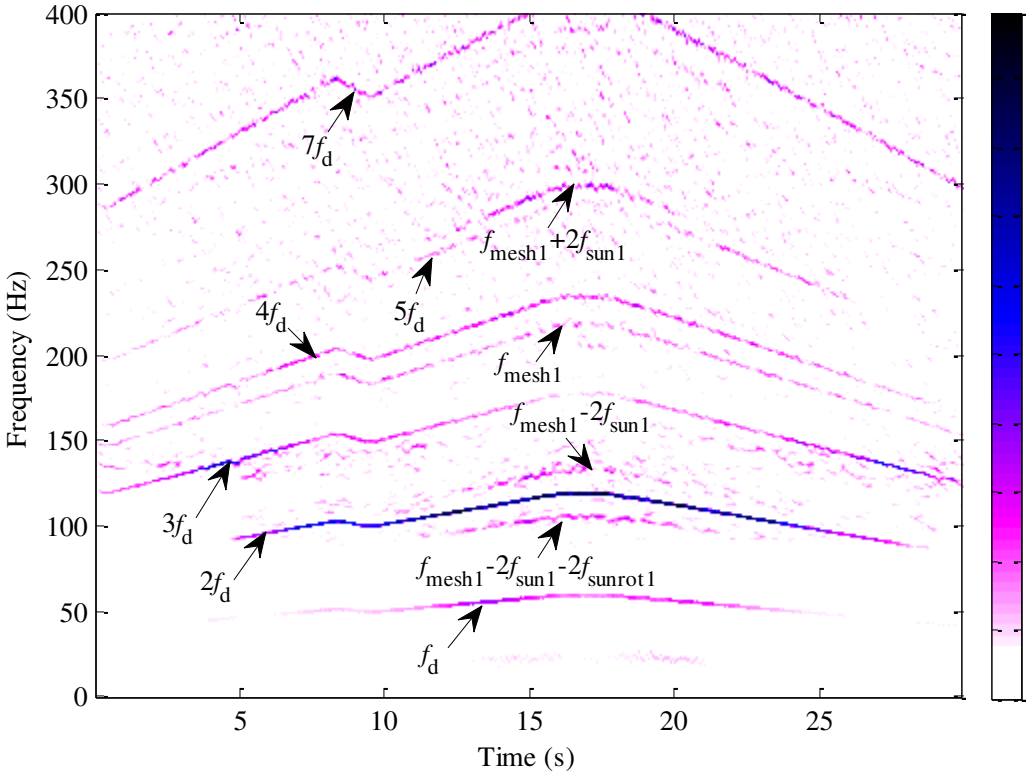

Fig. 4-9. TFR of the vibration signal of stage 1 sun gear wear fault

4.4.2 Detection of sun gear chipping

In this section, the effectiveness of the VST is assessed in detecting sun gear chipping at stage 2 of the planetary gearbox. Fig. 4-10(A-C) present the vibration signal, its frequency spectrum and the drive motor speed. Similar to the sun gear wear case, the motor speed falls in the range between 40 Hz and 60 Hz as shown in Fig. 4-10(C). According to the relationship between the stage 2 meshing frequency of the planetary gearbox and the motor rotational frequency (i.e., f_{mesh2}=(175/216) f_d as shown in Table 4-2), the stage 2 meshing frequency of the planetary gearbox changes between 32 Hz and 48 Hz. The frequency band of interest is then focused on the range between 0 Hz and 80 Hz to investigate the stage 2 sideband structures of the planetary gearbox for fault diagnosis. Though several peaks appear in the frequency spectrum (Fig. 4-10 (B)) of the raw vibration signal, it is difficult to identify them under a time-varying shaft speed condition. The signal TFR is then generated by applying the VST to uncover the signal structures as shown in Fig. 4-11. The dominant frequency is the motor rotating frequency f_d, which is generated by the rotations of the drive motor. Besides motor rotating frequency, several other

components can also be clearly identified from the TFR, they are the sum of the meshing frequency, the third harmonic of sun gear fault characteristic frequency and the sun gear rotating frequency $f_{mesh2}+3f_{sun2}+f_{sunrot2}$, the difference between the meshing frequency and the sun gear rotating frequency of stage $f_{mesh2}-f_{sunrot2}$, the sum of the meshing frequency and the sun gear rotating frequency of stage $f_{mesh2}+f_{sunrot2}$, and the difference between meshing frequency and the sum of the third harmonic of sun gear fault characteristic frequency and the second harmonic of sun gear rotating frequency $f_{mesh2}-(3f_{sun2}+2f_{sunrot2})$. Based on these revealed sidebands associated with sun gear fault characteristic frequency, it can be concluded that the fault is located at the stage 2 sun gear of the planetary gearbox. This is in agreement again with the stage 2 sun gear condition.

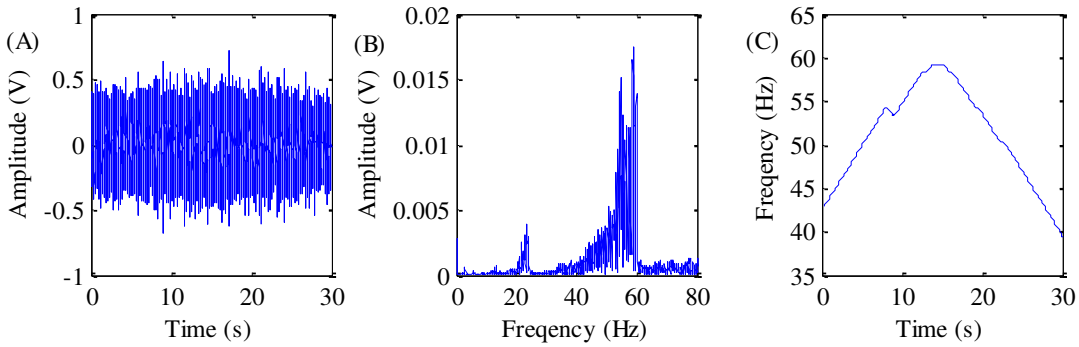

Fig. 4-10 Planetary gearbox with stage 2 sun gear chipping fault: (A) vibration signal, (B) frequency spectrum of vibration signal and (C) motor speed

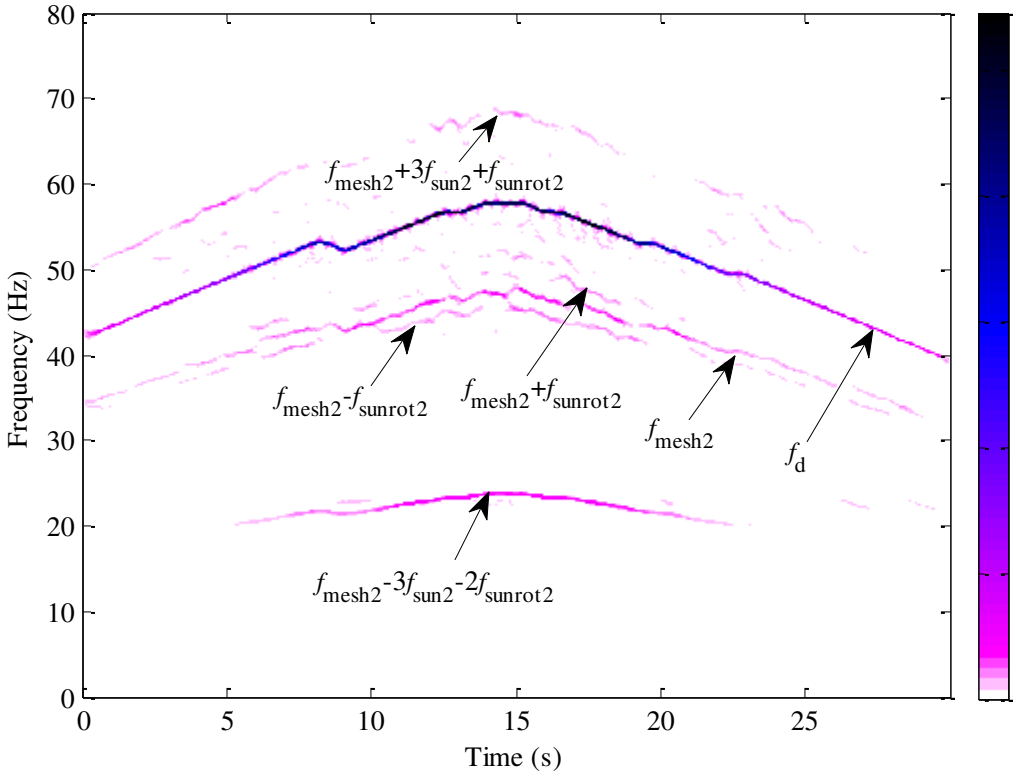

Fig. 4-11 TFR of the vibration signal of stage 2 sun gear chipping fault

4.4.3 Healthy planetary gearbox

In this section, the experimental vibration data of the healthy planetary gearbox is used to show the results when the proposed VST method is used. The vibration waveform, the corresponding frequency spectrum and motor speed profile are, respectively, shown in Fig. 4-12(A-C). Similar to the faulty planetary gearbox cases, the speed of the drive motor increases from 40 Hz to 60 Hz and then drops back to 40 Hz as shown in Fig. 4-12(C). Though the Fourier spectrum of the signal, shown in Fig. 4-12(B), contains some peaks, it is difficult to identify them under a time-varying speed condition. The VST is once again employed to process the signal, and the signal features are hence uncovered as shown in Fig. 4-13. The dominant frequencies are the planetary gearbox stage 1 gear meshing frequency f_{mesh1}, the drive motor rotating frequency f_d and its harmonics. No sidebands associated with planetary gearbox fault can be observed in the TFR. This suggests that the planetary gearbox is in a healthy condition.

The findings of the above three cases are expected and show that the VST is well suited to planetary gearbox diagnosis under nonstationary conditions.

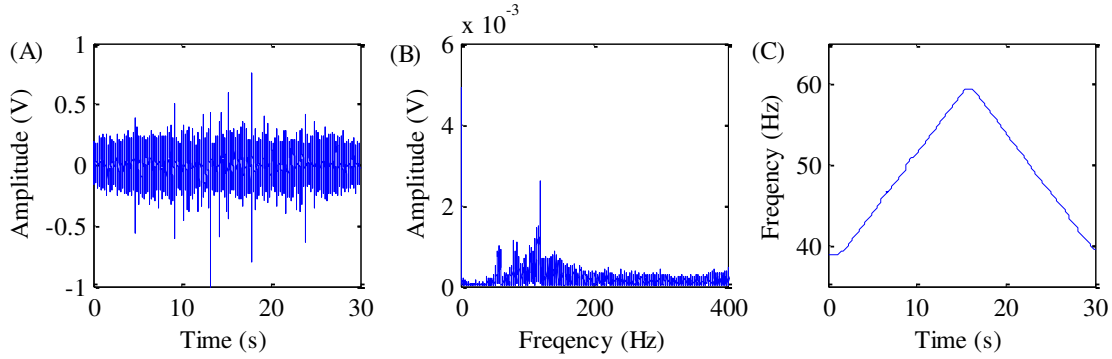

Fig. 4-12. Healthy planetary gearbox: (A) vibration signal, (B) frequency spectrum of vibration signal, and (C) motor speed

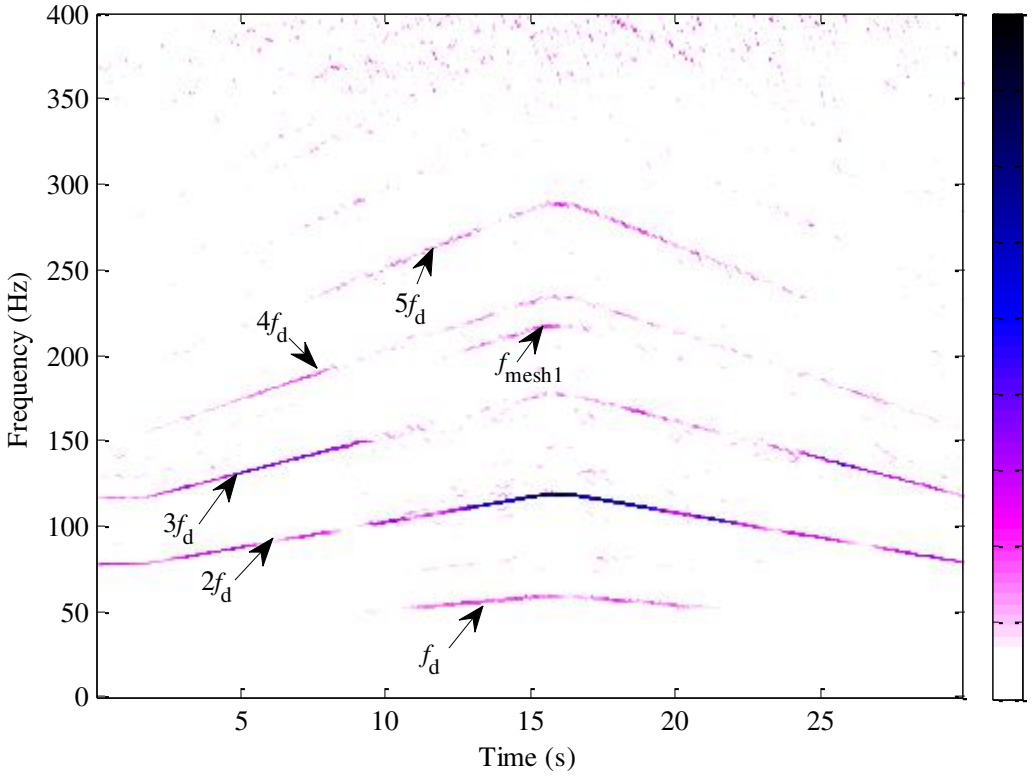

Fig. 4-13. TFR of the healthy planetary gearbox vibration signal

4.5 Conclusions

In this chapter, a time-frequency analysis method, named VST, is proposed for the fault diagnosis of planetary gearbox under non-stationary conditions. The VST improves

the traditional SST by eliminating the smear effects of SST when processing the non-stationary vibration signal of rotational machinery. It should be noted that though theoretically the VST works by two domain mappings and an application of SST to the angle-domain signal, the process can be substantially simplified as single step operation using the proposed fast implementation algorithm. Similar to the VSSTFT proposed in chapter 2, the VST is also smear-free and thus the signal components can be easily detected and identified. Compared with the VSSTFT, the VST leads to better time-frequency resolution to capture more details of signal structure. The performance of the VST has been compared with the traditional time-frequency analysis method using simulated data. The effectiveness of the VST method is further validated in diagnosing sun gear wear and chipped faults from the experimental data.

5 Velocity synchronous bilinear distribution (VSBD)

5.1 Motivation

The VSSTFT method and VST method proposed in the last two chapters are able to generate a smear-free TFR for fault diagnosis of planetary gearbox under non-stationary conditions. However, they have limited time-frequency resolution. This is because the linear transform is subject to the Heisenberg uncertainty principle (Hlawatsch and Boudreaux-Bartels, 1992) and the remapping method is based on linear transform result without improving its resolution (Iatsenko et al., 2015). Time-frequency resolution is important for fault diagnosis, as a good frequency resolution can facilitate the identification of the close-packed frequency components and fine time resolution can help uncover the transient impulses. These tightly packed components and transient impulses may contain rich information related to the faults of machinery.

The bilinear distribution is a big family of time-frequency methods (Hlawatsch, 1991; Hlawatsch and Boudreaux-Bartels, 1992) and it features relatively better time-frequency resolution. The WVD may be the base of all the bilinear distributions. One of its advantages is that it can perfectly reveal the following types of components, impulse, constant frequency and linear chirp. However, it has smear effects for the components other than those three types of components. The polynomial Wigner-Ville distribution uses a higher order kernel to supress the smear effects (Boashash and Shea, 1994). However, this method requires that the signal must be finely sampled for interpolation and the signal frequency must be well represented by polynomials. Another main drawback of the WVD is that it has cross term interferences for multi-component signals. The Cohen's class bilinear distribution (CCBD) may be the most widely used type of bilinear distributions. It uses a kernel function in ambiguity domain to filter out the cross terms and commonly the auto terms of the impulses and constant frequencies can survive. However, other auto terms may be partly filtered out and this may cause the information loss and resolution reduction (Choi and Williams, 1989a; Cohen, 1989; Zhao et al., 1990; Baraniuk and Jones, 1993a; Jones and Baraniuk, 1995). This shows that the CCBD requires the signal harmonics to have constant frequencies. The above mentioned drawbacks limit the performance and effectiveness of bilinear distributions.

To resolve these drawbacks and provide a clear TFR for reliable planetary gearbox diagnosis, the Velocity synchronous bilinear distribution (VSBD) method is proposed in this chapter. The VSBD is based on the GD and CCBD. The GD is a technique that is able to map one harmonic component of a signal into a pre-set frequency (Olhede and Walden, 2005). By applying the GDs with parameters specially designed according to the shaft speed, the possible signal components of the vibration signal can be mapped into constant frequencies in the demodulated signals. As the constant-frequency requirement of the CCBD is met, the mapped components can be conserved by the CCBD without time-frequency reduction and information loss. Finally the obtained CCBDs of the demodulated signals are fused into a clear TFR with good time-frequency resolution for planetary gearbox fault diagnosis.

5.2 Presentation of the VSBD

As the proposed VSBD is based on the CCBD and GD, they are briefly reviewed in section 5.2.1 and 5.2.2 respectively.

5.2.1 Review of the Cohen class bilinear distributions

The CCBDs are effective tools to obtain the time-frequency representation of a signal. The WVD may be the base of all the Cohen's class distributions (Feng et al., 2013a). The WVD of an analytic signal $x(t)$ is defined as applying Fourier transform to the auto-correlation function of signal $x(t)$ with respect to delay τ (Cohen, 1989), expressed by

$$W(t,f)=\int_{-\infty}^{\infty} R(t,\tau)\exp(-j2\pi f\tau)\,\mathrm{d}\tau \tag{5-1}$$

where t is time, f is frequency and the auto-correlation function R is represented by

$$R(t,\tau)=x\left(t+\frac{\tau}{2}\right)\overline{x\left(t-\frac{\tau}{2}\right)} \tag{5-2}$$

where the overhead bar denotes complex conjugate operation and τ is time delay. The signal under analysis must be an analytic signal. For a real-valued signal, it can be transformed to an analytic one using the Hilbert transform. The WVD can be seen as a process that transforms the signal from time-domain into the time-frequency domain.

We introduce three simple signals, i.e., the impulse signal, the analytic signal with constant frequency, and the analytic signal with linear frequency f_0+ct (linear chirp signal).

Their representations are presented in Table 5-1. The autocorrelation function of these signals are represented by the following functions respectively

$$R_{\text{imp}}(t,\tau)=\delta\left(t+\frac{\tau}{2}-t_0\right)\delta\left(t-\frac{\tau}{2}-t_0\right), \tag{5-3}$$

$$R_{\text{con}}(t,\tau)=\exp\left(j2\pi f_0\left(t+\frac{\tau}{2}\right)\right)\exp\left(-j2\pi f_0\left(t-\frac{\tau}{2}\right)\right)=\exp\left(j2\pi f_0\tau\right), \tag{5-4}$$

and

$$\begin{aligned}R_{\text{linear}}(t,\tau)&=\exp\left(j2\pi\left(\frac{1}{2}c\left(t+\frac{\tau}{2}\right)^2+f_0\left(t+\frac{\tau}{2}\right)-\frac{1}{2}c\left(t-\frac{\tau}{2}\right)^2-f_0\left(t-\frac{\tau}{2}\right)\right)\right)\\&=\exp\left(j2\pi\left(f_0\tau+ct\tau\right)\right)\end{aligned}. \tag{5-5}$$

The WVDs of these signals are then calculated, represented by

$$\begin{aligned}W_{\text{imp}}(t,f)&=\int_{-\infty}^{\infty}R_{\text{imp}}(t,\tau)\exp\left(-j2\pi f\tau\right)\mathrm{d}\tau\\&=\int_{-\infty}^{\infty}\delta\left(t+\frac{\tau}{2}-t_0\right)\delta\left(t-\frac{\tau}{2}-t_0\right)\exp\left(-j2\pi f\tau\right)\mathrm{d}\tau=\delta\left(t-t_0\right)\end{aligned}, \tag{5-6}$$

$$\begin{aligned}W_{\text{con}}(t,\tau)(t,f)&=\int_{-\infty}^{\infty}R_{\text{con}}(t,\tau)\exp\left(-j2\pi f\tau\right)\mathrm{d}\tau\\&=\int_{-\infty}^{\infty}\exp\left(j2\pi f_0\tau\right)\exp\left(-j2\pi f\tau\right)\mathrm{d}\tau=\delta\left(f-f_0\right)\end{aligned}, \tag{5-7}$$

and

$$\begin{aligned}W_{\text{linear}}(t,f)&=\int_{-\infty}^{\infty}R_{\text{linear}}(t,\tau)\exp\left(-j2\pi f\tau\right)\mathrm{d}\tau\\&=\int_{-\infty}^{\infty}\exp\left(j2\pi\left(f_0+ct\right)\tau\right)\exp\left(-j2\pi f\tau\right)\mathrm{d}\tau=\delta\left(t-\left(f_0+ct\right)\right)\end{aligned}. \tag{5-8}$$

Their auto-correlation functions and WVDs are also presented in Fig. 5-1. Based on the above result, we illustrate the WVDs of these three types of signal using three example signals as shown in Fig. 5-1(A-C). It can be seen that the WVD can effectively reveal the signal structure of these three types of signals. However, the WVD cannot reveal the signal with non-linear frequencies well. The WVD of a quadratic chirp (as an example of non-linear chirp) is shown in Fig. 5-1(D), it can be seen that the WVD has smear problems and the signal frequency is not clearly revealed.

Table 5-1 Functions of the example signals

	Impulse signal	Constant frequency	Linear frequency
Signal	$\delta(t-t_0)$	$\exp(j2\pi f_0 t)$	$\exp\left(j2\pi\left(0.5ct^2+f_0 t\right)\right)$
Auto-correlation function	$\delta\left(t+\frac{\tau}{2}-t_0\right)\delta\left(t-\frac{\tau}{2}-t_0\right)$	$\exp(j2\pi f_0\tau)$	$\exp\left(j2\pi\left(f_0\tau+ct\tau\right)\right)$
WVD	$\delta(t-t_0)$	$\delta(f-f_0)$	$\delta\left(f-\left(f_0+ct\right)\right)$
Ambiguity function	$\delta(\tau)\exp(-j2\pi t_0\eta)$	$\delta(\eta)\exp(j2\pi f_0\tau)$	$\delta(\eta-c\tau)\exp(j2\pi f_0\tau)$

Another drawback of the WVD is that it introduces cross-term interference for mono-component signals. Considering a signal $x(t)$ with two components $x_1(t)$ and $x_2(t)$, its WVD is given by

$$W_x(t,f)=\int_{-\infty}^{\infty}\left(x_1\left(t+\frac{\tau}{2}\right)+x_2\left(t+\frac{\tau}{2}\right)\right)\left(\overline{x_1\left(t-\frac{\tau}{2}\right)}+\overline{x_2\left(t-\frac{\tau}{2}\right)}\right)\exp(-j2\pi f\tau)\,\mathrm{d}\tau$$
$$=W_{x1}(t,f)+W_{x2}(t,f)+W_{x1x2}(t,f)+W_{x2x1}(t,f) \tag{5-9}$$

It can be seen that the WVD of the signal $x(t) = x_1(t) + x_2(t)$ contains four terms. The terms $W_{x1}(t,f)$ and $W_{x2}(t,f)$ are called auto terms and they are the WVD of $x_1(t)$ and $x_2(t)$ respectively, and therefore the auto terms can reveal the signal frequency trajectories. However, the terms $W_{x1x2}(t,f)$ and $W_{x2x1}(t,f)$ are cross terms and interfere the interpretation of the WVD.

To illustrate the auto terms and cross terms, we shows the WVD of four two-component example signals. They are the signal containing two impulses, the signal containing two constant frequencies, the signal containing two linear chirps and the signal containing two quadratic chirps (as an representation of the signal containing two non-linear chirps). Their WVDs are shown in Fig. 5-2(A-D) respectively. It can be seen the cross terms seriously interfere the WVD and they may be mistakenly identified as the signal component.

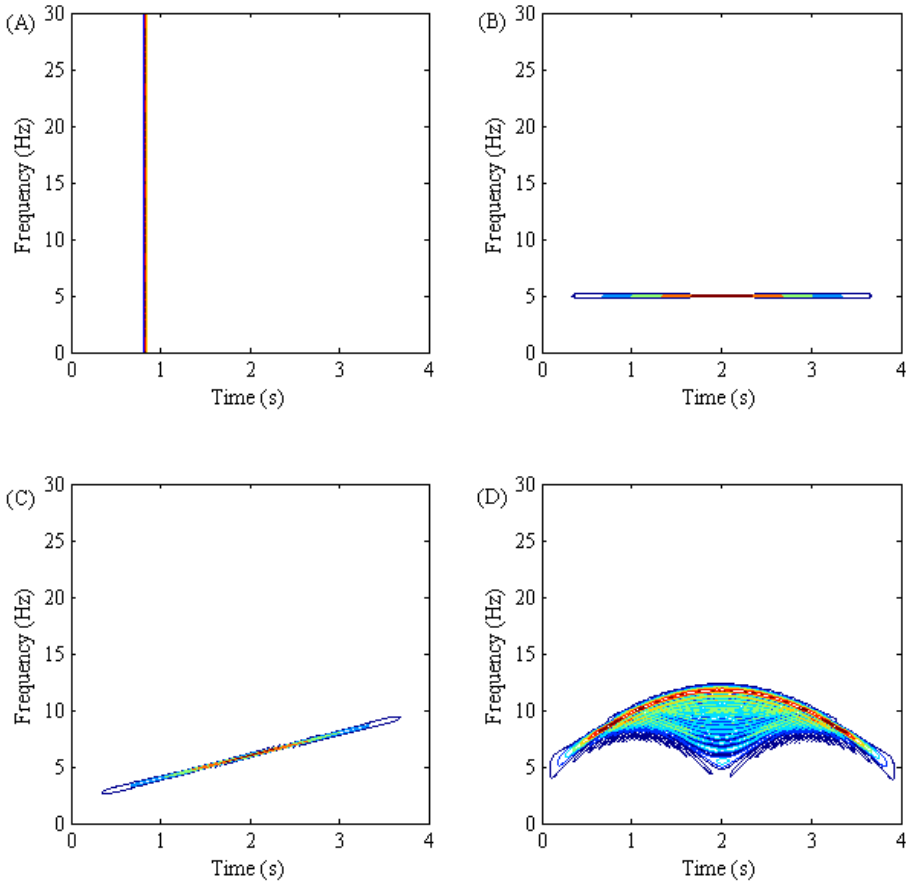

Fig. 5-1. WVDs of mono-component signals: (A) impulse, (B) constant frequency, (C) linear chirp and (D) quadratic chirp

To address the cross-term interference issue, many methods have been proposed and the CCBD may be the mostly widely used one. The CCBD is expressed by

$$W_{\text{Cohen}}(t,f)=\int_{-\infty}^{\infty}\int_{-\infty}^{\infty}A(\tau,\eta)M(\tau,\eta)\exp\left(j2\pi\left(t\eta-f\tau\right)\right)\mathrm{d}\eta\,\mathrm{d}\tau \tag{5-10}$$

where η is the Doppler frequency shift (DFS), $M(\tau,\eta)$ is a mask function in the delay-DFS domain and $A(\tau,\eta)$ is the signal ambiguity function, expressed by

$$A(\tau,\eta)=\int_{-\infty}^{\infty}R(t,\tau)\exp\left(-j2\pi\eta t\right)\mathrm{d}t \tag{5-11}$$

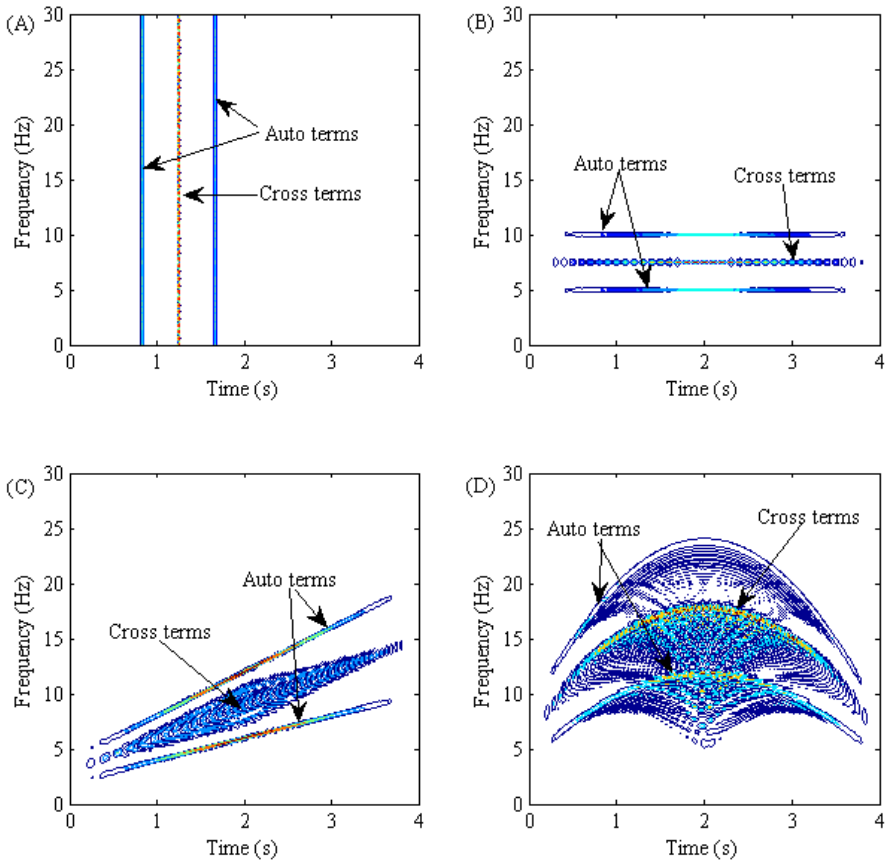

Fig. 5-2. WVDs of multi-component signals containing two: (A) impulses, (B) constant frequencies, (C) linear chirps and (D) quadratic chirps

It can be observed that the ambiguity function is obtained as the Fourier transform of the auto-correlation function. The delay-DFS plane representations of the auto terms of the impulse component, constant-frequency component and linear–chirp component can be obtained as

$$\begin{aligned} A_{\text{imp}}(\tau,\eta) &= \int_{-\infty}^{\infty} R_{\text{imp}}(t,\tau)\exp(-j2\pi t\eta)\,\mathrm{d}t \\ &= \int_{-\infty}^{\infty} \delta\left(t+\frac{\tau}{2}-t_0\right)\delta\left(t-\frac{\tau}{2}-t_0\right)\exp(-j2\pi t\eta)\,\mathrm{d}t = \delta(\tau)\exp(-j2\pi t_0\eta) \end{aligned}, \tag{5-12}$$

$$\begin{aligned} A_{\text{con}}(\tau,\eta) &= \int_{-\infty}^{\infty} R_{\text{con}}(t,\tau)\exp(-j2\pi t\eta)\,\mathrm{d}t \\ &= \int_{-\infty}^{\infty} \exp(j2\pi f_0\tau)\exp(-j2\pi t\eta)\,\mathrm{d}t = \exp(j2\pi f_0\tau)\delta(\eta) \end{aligned}, \tag{5-13}$$

and

$$A_{\text{linear}}(\tau,\eta)=\int_{-\infty}^{\infty}R_{\text{linear}}(t,\tau)\exp(-j2\pi t\eta)\,\mathrm{d}t$$
$$=\int_{-\infty}^{\infty}\exp\left(j2\pi\left(f_0\tau+ct\tau\right)\right)\exp(-j2\pi t\eta)\,\mathrm{d}t=\exp(j2\pi f_0\tau)\,\delta(\eta-c\tau) \quad (5\text{-}14)$$

The above functions show that in the delay-DFS plane, the impulse component is at the DFS axis (τ=0), constant frequency is at the delay axis (η=0), and linear chirp is at a line passing the origin with incline slope c. These features can be reflected by the two-component example signals represented in delay-DFS plane illustrated in Fig. 5-3(A-D) respectively. The locations of the auto terms of impulses, constant frequencies and linear chirps are expected as shown in Fig. 5-3(A-C). However, the locations of the auto terms and cross terms of non-linear chirps (using quadratic chirps as an example here) are difficult to expect as shown in Fig. 5-3(D).

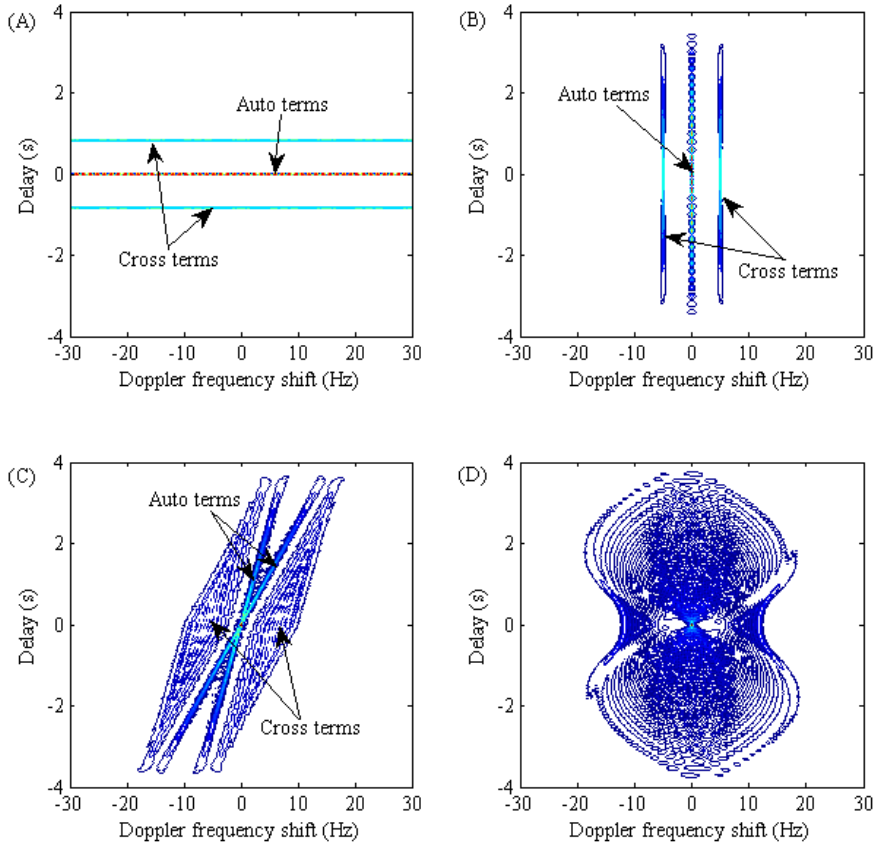

Fig. 5-3. Ambiguity function of multi-component signals: (A) impulse, (B) constant frequency, (C) linear chirp and (D) non-linear chirp

The ambiguity function of these three types of signals are also presented in Table 5-1. It can be seen that the ambiguity functions of these three types of signals all pass the origin.

This means that the auto terms of impulse component, constant-frequency component and linear-frequency component all pass the origin. Therefore a low-pass two-dimensional mask function $M(\tau,\eta)$ can be designed and by multiplying the ambiguity function $A(\tau,\eta)$ with it, most information of the auto terms can be filtered. Finally this result is processed by the inverse Fourier transform with respect to the DFS η and the Fourier transform with respect to delay τ to obtain the representation in the time-frequency domain. The CCBD of the four example signals are shown in Fig. 5-4.

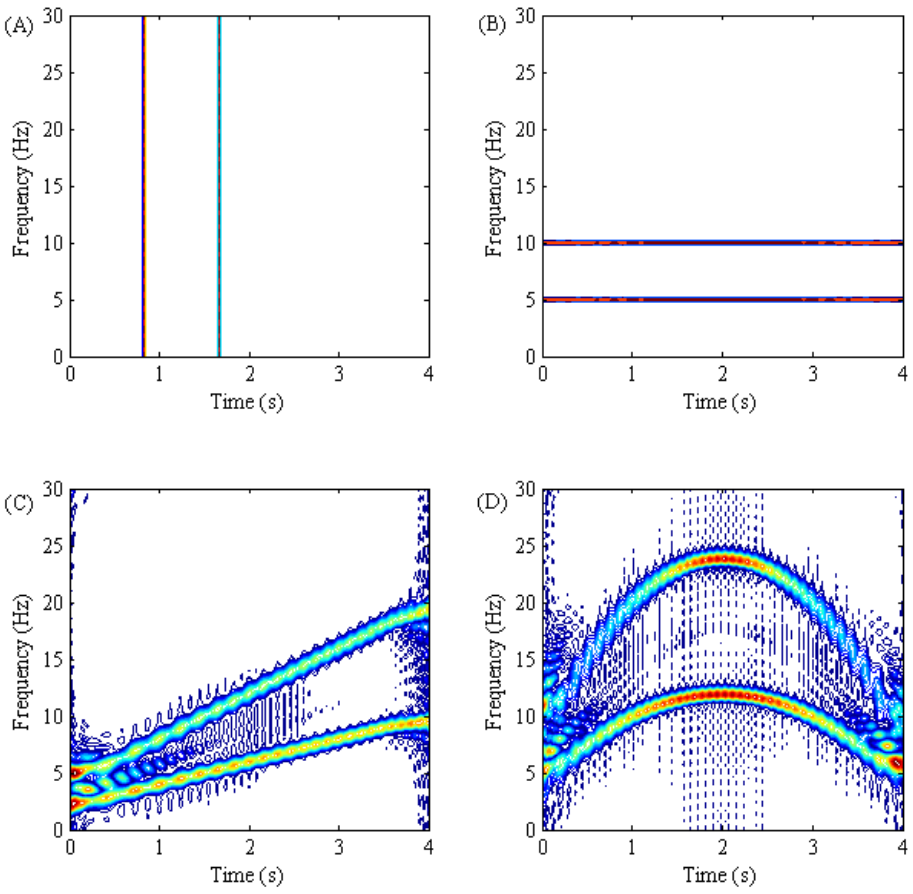

Fig. 5-4. CCBD of multi-component signals: (A) impulse, (B) constant frequency, (C) linear frequency and (D) non-linear frequency

The CCBDs cannot conserve all the information of the auto terms. The passbands of mask functions of most CCBDs concentrate around the two axes, e.g., the Choi-Williams distribution mask function as shown in Fig. 5-5. From Fig. 5-5, it can be found that the ambiguity functions of impulse and constant frequency are located on the axes and hence the auto terms of them can be perfectly conserved. However, as the auto terms of other

types of components are not located on the axes, these components will suffer from information loss and poor time-frequency resolution. Most components of the vibration signals collected from a planetary gearbox under non-stationary conditions have time-varying frequencies, not constant frequencies. Therefore, the CCBD is not suited to analysing such vibration signals.

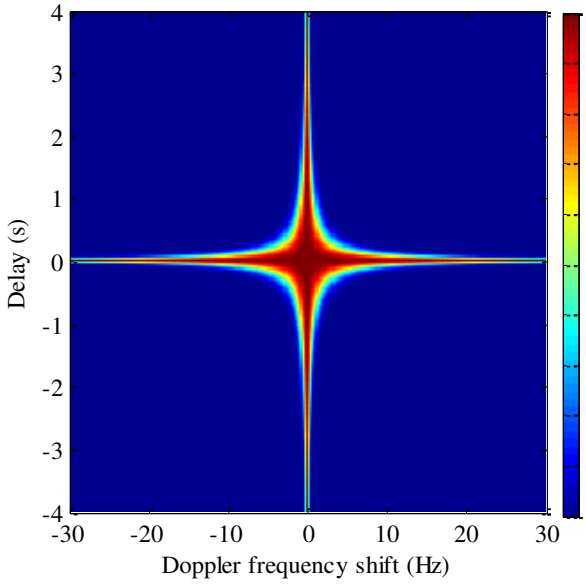

Fig. 5-5. Mask function of the Choi-Williams distribution

5.2.2 Review of the generalized demodulation (GD)

The GD defines a demodulation function according to a specified instantaneous phase. By multiplying the signal with it, the time-variant frequency of the interested component can be mapped into a constant one (Olhede and Walden, 2005). For an arbitrary mono-component analytic signal with time varying frequency $f(t)$ expressed by

$$x_{\text{mono}}(t) = \text{Aexp}\left(j\int_{-\infty}^{\infty} 2\pi f\left(t\right)dt \right). \tag{5-15}$$

It can be mapped into a constant target frequency f_{target} with amplitude conserved using the following demodulator

$$p(t) = \exp\left(-j\int_{-\infty}^{\infty} 2\pi f\left(t\right)dt + j2\pi f_{\text{target}}t \right). \tag{5-16}$$

This is because the demodulated signal is represented by

$$x_D(t) = x(t)\,p(t) = \mathrm{A}\exp\left(j\int_{-\infty}^{\infty} 2\pi f\left(t\right)dt\right)\exp\left(-j\int_{-\infty}^{\infty} 2\pi f\left(t\right)dt + j2\pi f_{\text{target}}t\right) \\ = \mathrm{A}\exp\left(j2\pi f_{\text{target}}t + \text{constant}\right) \quad (5\text{-}17)$$

5.2.3 Derivation of the VSBD

The vibration signal collected from a rotational machinery with time-varying rotational speed can be roughly modeled as a combination of waveforms with frequencies synchronizing with shaft rotational speed, given by

$$x_{\text{vib}}\left(t\right) = \sum_{k=1}^{\mathrm{K}} A_k \exp\left(-j\Omega_k\theta\left(t\right)\right), \quad (5\text{-}18)$$

where K is the number of components, Ω_k is the order of the kth component, A_k is the amplitude of the kth component and $\theta(t)$ is the phase of shaft rotational frequency, represented by

$$\theta\left(t\right) = \int_{-\infty}^{\infty} 2\pi f_{\text{shaft}}\left(t\right)\mathrm{d}t\,. \quad (5\text{-}19)$$

where f_{shaft} is the shaft rotational frequency. As the frequencies of the signal components are not constant, the current CCBDs cannot provide a good TFR. It has been shown that the constant frequency can be perfectly conserved by the CCBD in the subsection 5.2.1 and the GD can map any signal component with time-varying frequency into a constant frequency. It is therefore proposed to process the signal using the GD before applying the CCBD. However, one difficulty is that the vibration signal is a multi-component signal, the demodulator can only be designed according to the frequency of one of the signal components. Such demodulator is able to map the selected component into constant frequency but cannot map other components into fixed frequencies. We select the lth component of vibration signal as the component to be mapped and the mapped signal can be shown as

$$x_D(t) = x_{\text{vib}}(t)\,p(t) = \sum_{k=1}^{K} A_k \exp\left(j2\pi\left(f_{\text{target}}t + \int_{-\infty}^{\infty}\left(\Omega_k f_{\text{shaft}}\left(t\right) - \Omega_l f_{\text{shaft}}\left(t\right)\right)\mathrm{d}t\right)\right) \\ = A_l \exp\left(j2\pi f_{\text{target}}t + \mathrm{c}\right) + \sum_{k=2}^{K} A_k \exp\left(j2\pi\left(\int_{-\infty}^{\infty}\left(\left(\Omega_k - \Omega_l\right) f_{\text{shaft}}\left(t\right) + f_{\text{target}}\right)\mathrm{d}t\right)\right) \quad (5\text{-}20)$$

It be seen that the *l*th component is mapped into a component with frequency f_{target}, but the *k*th ($k \neq l$) component is mapped to the frequency $\left(\Omega_k - \Omega_l\right) f_{\text{shaft}}\left(t\right) + f_{\text{target}}$, which is a time-varying frequency.

To solve this problem, an additional argument, order Ω, is introduced into the demodulator. In other words, countless demodulators can be constructed and each one is designed for one possible component. The demodulator is represented by

$$p_{(\Omega)}\left(t\right) = \exp\left(-j\Omega\theta\left(t\right) + j2\pi f_{\text{target}} t\right). \tag{5-21}$$

The demodulated signals are represented by

$$x_{D(\Omega)}\left(t\right) = x_{\text{vib}}\left(t\right) p_{(\Omega)}\left(t\right). \tag{5-22}$$

For any component with order Ω, we have a demodulated signal in which the component with order Ω is at target frequency. The ambiguity functions of the demodulated signals are then obtained by applying Fourier transform with respective to time *t*, i.e.,

$$A_{D(\Omega)}\left(\eta,\tau\right) = \int_{-\infty}^{\infty} x_D\left(t + \frac{\tau}{2}\right)\overline{x_D\left(t - \frac{\tau}{2}\right)}\exp\left(-j2\pi\eta t\right)\mathrm{d}\,t\,. \tag{5-23}$$

As the frequency of the demodulated component is constant, this component is located at the delay axis in ambiguity plane based on the analysis in the subsection 5.2.1, and then a new kernel function with passband around delay axis is designed to filter the demodulated component, expressed by

$$M\left(\tau,\eta\right) = \exp\left(-\sigma\eta^2\right) \tag{5-24}$$

After the filtering, the signals are transformed into time-frequency domain by applying inverse Fourier transform with respective to DFS η and Fourier transform with respective to delay τ, represented by

$$W_{D(\Omega)}\left(t, f_1\right) = \int_{-\infty}^{\infty}\left(\int_{-\infty}^{\infty} A\left(\eta,\tau,\Omega\right) M\left(\tau,\eta\right)\exp\left(j2\pi t\eta\right)\mathrm{d}\,\eta\right)\exp\left(-j2\pi f_1\tau\right)\mathrm{d}\,\tau \tag{5-25}$$

As this time-frequency plane shows the demodulated signals, not the original signal, to avoid ambiguity, these TFRs are denoted as the demodulated TFRs and the frequency here is named demodulated frequency and denoted as f_1 instead of *f*. Here we have obtained

the TFRs of the demodulated signals and every demodulated signal only contains the mapped target frequency with the original amplitude, and so for the demodulated TFR $W_{D(\Omega)}(t, f_1)$, only the data at

$$f_1 = f_{\text{target}} \tag{5-26}$$

contains useful information. Then we merge these demodulated TFRs into one TFR containing all the information by combining data at $f_1 = f_{\text{target}}$ for each demodulated TFR $W_{D(\Omega)}(t, f_1)$ and the combined TFR is represented by $W_{D(\Omega)}(t, f_{\text{target}})$. The TFR of the original signal can be restored from the combined TFR according to the relationship between order and frequency, i.e., order represents multiple of shaft rotational frequency, expressed by

$$\Omega = \frac{f}{f_{\text{shaft}}(t)}, \tag{5-27}$$

therefore the restored TFR is

$$W(t, f) = W_{D\left(\frac{f}{f_{\text{shaft}}(t)}\right)}\left(t, f_{\text{target}}\right). \tag{5-28}$$

Here, we have restored the TFR of the original signal. This method is named velocity synchronous bilinear distribution (VSBD). To facilitate the understanding of the proposed method, the steps of the proposed VSBD method are presented in a flowchart as shown in Fig. 5-6, where F and F^{-1} denote Fourier transform and inverse Fourier transform respectively.

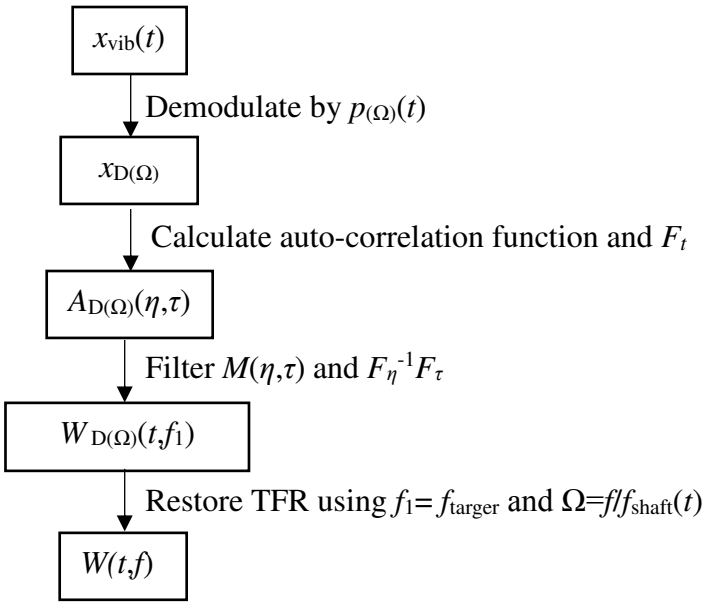

Fig. 5-6. Flowchart of the proposed VSBD method

To facilitate the realization of the proposed VSBD method, the proposed method can be simplified as the following algorithms from the Eqs. (5-22 to 5-28)

$$W(t,f)=\int_{-\infty}^{\infty}\int_{-\infty}^{\infty}A_{D(f,t)}(\eta,\tau)M(\tau,\eta)\exp(j2\pi\eta t)\,\mathrm{d}\eta\,\mathrm{d}\tau\,, \tag{5-29}$$

where

$$A_{D(f,t)}(\eta,\tau)=\int_{-\infty}^{\infty}x_{D(f,t)}\left(t_1+\frac{\tau}{2}\right)\overline{x_{D(f,t)}\left(t_1-\frac{\tau}{2}\right)}\exp(-j2\pi\eta t)\,\mathrm{d}t\,, \tag{5-30}$$

$$M(\tau,\eta)=\exp(-\sigma\eta^2), \tag{5-31}$$

$$x_{D(f,t)}(t_1)=x(t_1)\exp\left(-\frac{j2\pi f\theta(t_1)}{\theta'(t)}\right). \tag{5-32}$$

In the above simplified algorithms, the target frequency is set as 0 to reduce computational burden. In real applications, the shaft speed can be obtained by the tachometer/encoder installed on the gearbox shaft. If such tachometer is not accessible, the shaft speed can be estimated from the signal TFR obtained by the STFT (Combet and Zimroz, 2009; Peng et al., 2011; Urbanek et al., 2013).

The proposed VSBD method is tested on the signals containing two linear chirps and two quadratic chirps and the results are shown in Fig. 5-7(A) and (B). It can be seen that the VSBD reveals the signal time-frequency structure clearly with fine time-frequency resolution and without cross-term interference.

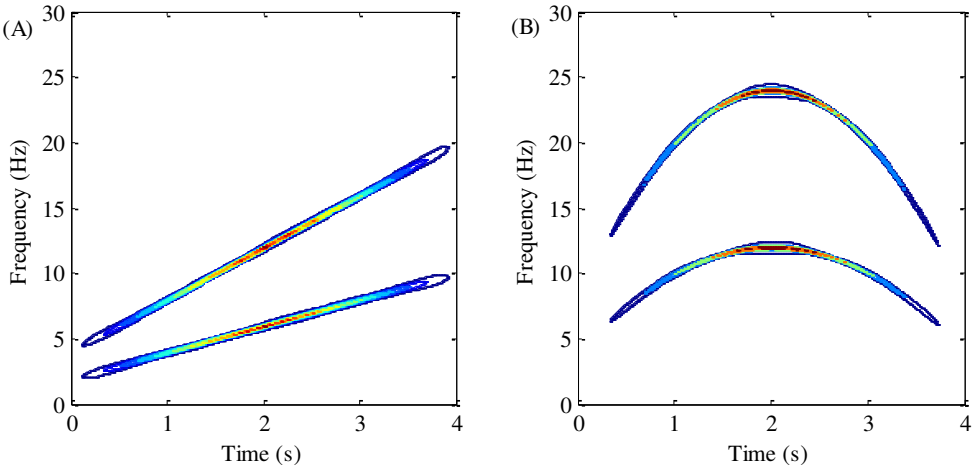

Fig. 5-7. VSBD of the signal containing: (A) two linear chirps and (B) two quadratic chirps

5.3 Simulation evaluations

5.3.1 Signal containing fault-induced harmonics

In this section, the proposed method is tested on a synthetic vibration signal of planetary gearbox with a sun gear fault using the vibration model provided in Appendix A (Feng and Zuo, 2012). This model is based on the amplitude and frequency modulation features of the vibration caused by gear fault and it assumes that the signal is collected under a fixed rotational speed. Under the non-stationary condition, the model must be adjusted. As in a non-stationary condition, the characteristic frequencies of the gearbox are time-varying, the fixed characteristic frequencies in the model should be replaced with the corresponding time-varying characteristic frequencies. Compared with the frequency modulation effect caused by shaft speed variation, the frequency modulation caused by gear fault is relatively weak, thus it is neglected here and only the amplitude modulation of the gear fault is considered. A Gaussian white noise is added to achieve a signal-to-noise ratio (SNR) of 5 dB to mimic the background noise. Based on the above analysis, the simulated signal is expressed below,

$$x(t)=\left\{1-\cos\left[2\pi\int_0^t f_{\text{srot}}(\tau)\,\mathrm{d}\tau\right]\right\}\left\{1+\cos\left[2\pi\int_0^t f_{\text{sun}}(\tau)\,\mathrm{d}\tau\right]\right\}\times\cos\left[2\pi\int_0^t f_{\text{mesh}}(\tau)\,\mathrm{d}\tau\right]+\mathrm{N}(t), \tag{5-33}$$

where N(t) is Gaussian white noise, f_{srot} is the sun gear rotational frequency, f_{mesh} is the gear meshing frequency and f_{sun} is the sun gear fault characteristic frequency. The signal-to-noise ratio (SNR) of this signal is set as 3 dB (SNR is defined as the ratio of the root mean square of the pure desired signal and the noise signal N(t)).The relationship between these characteristic frequencies are set as $f_{\text{srot}}=f_{\text{mesh}}/10=f_{\text{sun}}/3$. The signal length is one second and the sampling rate is 512 Hz. The sun gear rotating frequency is set as $f_{\text{srot}}(t)=10+2\sin(2\pi t)$. The signal waveform is shown in Fig. 5-8(A).

Based on the convolution theory, the signal contains nine components, which can be represented by f_{mesh}, $f_{\text{mesh}}\pm f_{\text{sun}}$, $f_{\text{mesh}}\pm f_{\text{srot}}$, $f_{\text{mesh}}\pm f_{\text{sun}}\pm f_{\text{srot}}$, as shown in Fig. 5-8 (B). The VSBD is tested on the synthetic signal and the result is shown in Fig. 5-8 (C). Compared with the ideal time-frequency features of the synthetic signal shown in Fig. 5-8 (B), the VSBD clearly reveals all the nine signal components with good time-frequency resolution. Except the meshing frequency, all the other eight revealed frequency components are associated with sun gear fault, thus the gearbox is diagnosed as having a sun gear fault. This is consistent with the simulation setup, which validates the effectiveness of the VSBD. The same signal defined by Eq. (5-33) is then processed by the order-tracking method (Guan et al., 2018) for comparison and the obtained order spectrum is shown in Fig. 5-8 (D). It can be seen that the order-tracking method also reveals the nine components of the signal.

The VSBD is compared with some traditional time-frequency methods and advanced time-frequency methods, and the obtained TFRs are presented in Fig. 5-9. The STFT is shown in Fig. 5-9(A) and it can be seen that the sidebands are buried in strong smear background. The Choi-Williams distribution (CWD) (Choi and Williams, 1989b), as a representation of the CCBD, is shown in Fig. 5-9(B). It can be seen that the meshing frequency is recognized. However, the sidebands are not revealed and it introduces some unexpected impulses. The signal is then processed by two methods that utilize both vibration signal and speed information, the polynomial chirplet transform (PCT) (Peng et

al., 2011) and the generalized synchrosqueezing transform (GST) (Li and Liang, 2012b). The results are shown in Fig. 5-9(C) and (D), respectively. Though these two methods can discern the signal meshing frequency and part of sidebands, some sidebands are not revealed. Finally, two advanced methods, the GLCT (Yu and Zhou, 2016) and SET (Yu et al., 2017), are tested and the results are presented in Fig. 5-9(E) and (F), respectively.

The GLCT reveals the meshing frequency, but the sidebands are smeared. Similar to the GLCT, the SET is also only able to reveal the meshing frequency and introduces additional interferences to the TFR. By comparing these TFRs shown in Fig. 5-9 with the TFR obtained by the VSBD, it can be found that the VSBD is superior to them in generating a clear TFR with good time-frequency resolution.

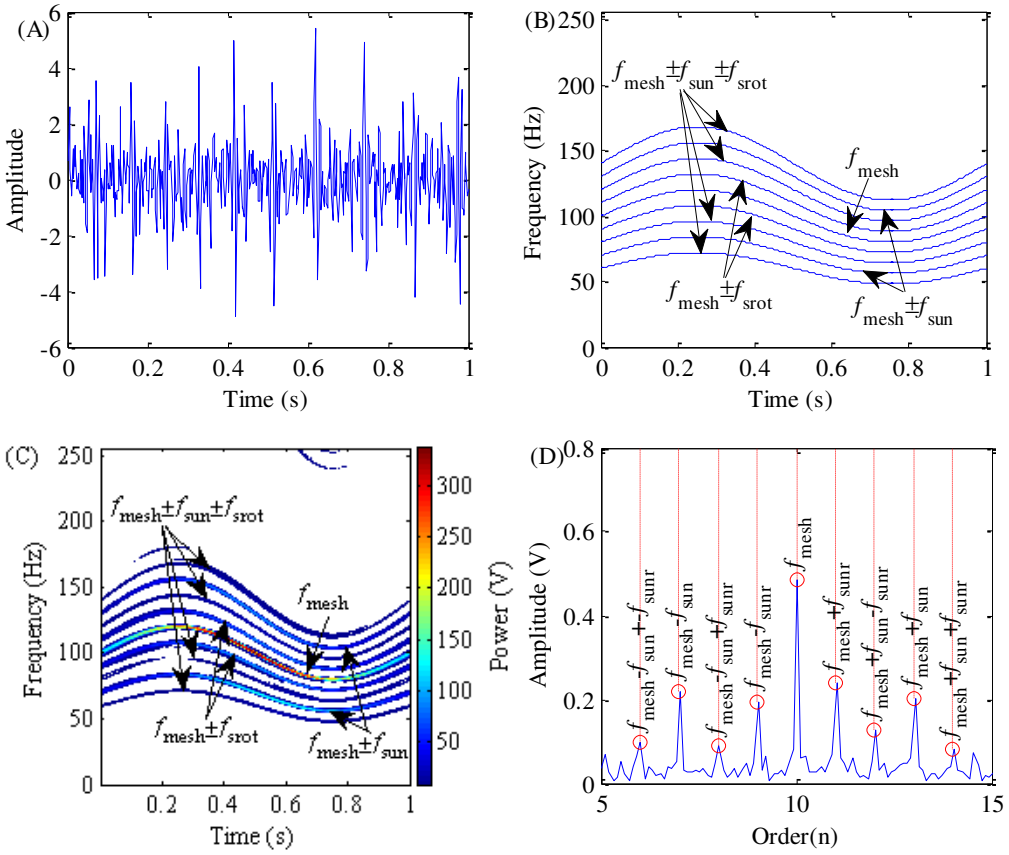

Fig. 5-8. Synthetic signal 1: (A) waveform and (B) ideal TFR, (C) VSBD result and (D) order spectrum

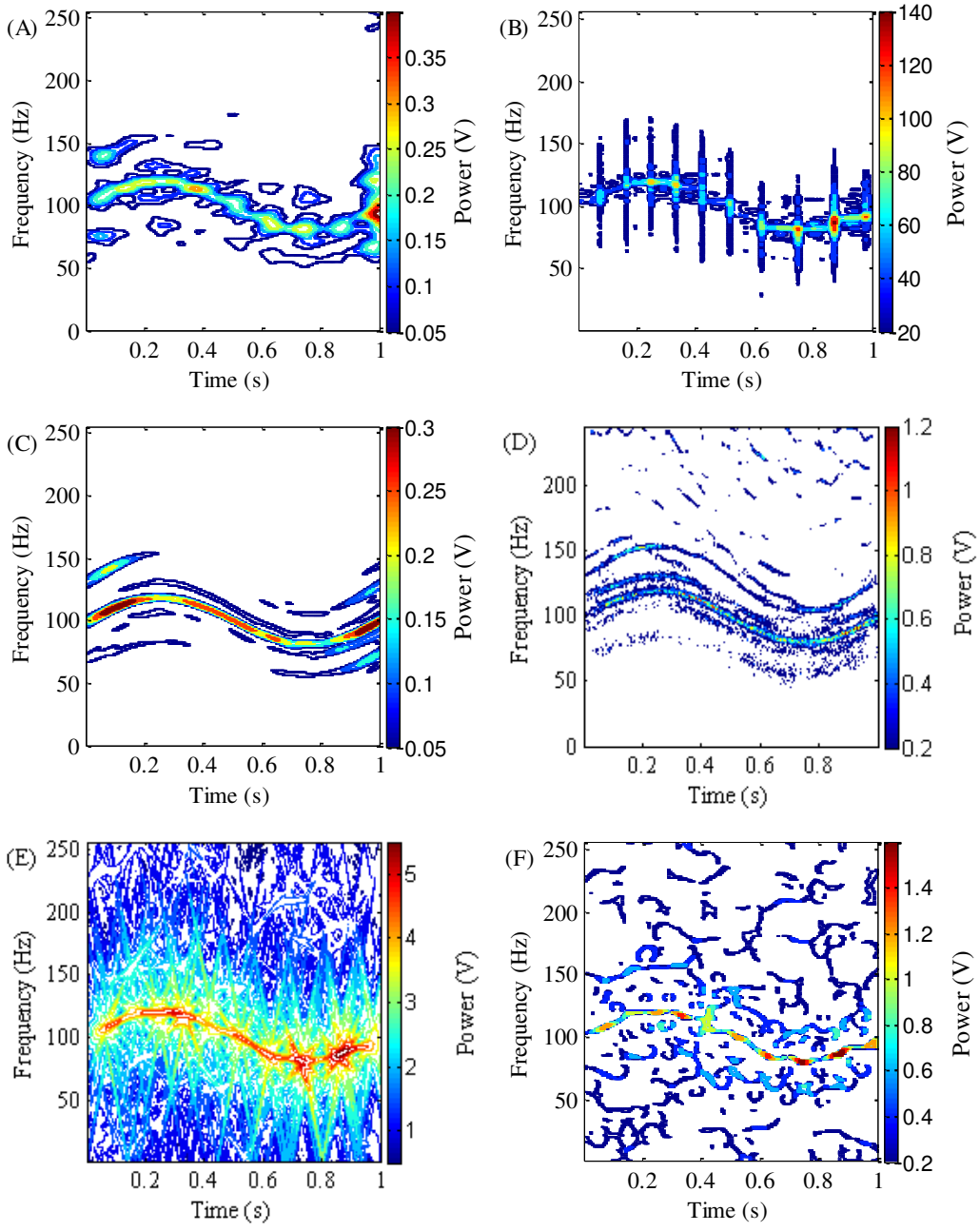

Fig. 5-9. TFRs of the synthetic signal 1 obtained by: (A) STFT, (B) CWD, (C) PCT, (D) GST, (E) GLCT and (F) SET

5.3.2 Signal containing fault-induced impulses

The planetary gearbox may also experience instantaneous impact due to the occurrence of fault (Feng and Liang, 2014b). In this section, we evaluate the proposed method in revealing the fault-induced impacts using a synthetic signal. The effects of impacts can be

modeled as a set of impulses. The fault characteristic frequency of the faulty gear f_{fault} is therefore the repetition frequency of fault-induced impulses. The synthetic signal containing fault-induced impulses is represented by

$$x(t) = \mathrm{A}\cos\left[2\pi\int_0^t f_{\text{mesh}}(\tau)\,\mathrm{d}\tau\right] + \sum_{k=1}^{\mathrm{K}} \delta(t-t_k) + N(t) \tag{5-34}$$

where A=0.1 is the amplitude of meshing frequency, δ is Dirac delta function. t_k corresponds the time point when the impact occurs and $N(t)$ represents Gaussian white noise. Under a time-varying speed condition, the time points when impulses occur t_k can be determined by solving (assuming t_0=0)

$$\int_{t=t_k}^{t=t_{k+1}} f_{\text{fault}}(t)\,\mathrm{d}t = 1. \tag{5-35}$$

It is assumed that the gearbox has a sun gear fault. The relationships between the characteristic frequencies are set as $f_{\text{srot}} = 6f_{\text{mesh}}/100 = 6f_{\text{sun}}/5$. The SNR, signal length and sampling rate are set as 0 dB, 1 s and 512 Hz, respectively. Sun gear rotational frequency is set as $f_{\text{srot}}(t)=3+6t^2$. Solving Eq (5-35) yields t_k = [0.369, 0.633, 0.8262, 0.979]. The signal waveform and the time-frequency trajectories of the signal components are shown in Fig. 5-10 (A) and (B), respectively.

The TFR obtained by the VSBD is presented in Fig. 5-10(C), which clearly and precisely reveals the meshing frequency and four fault-induced impulses. Each time interval between adjacent impulses corresponds to a complete cycle (2π radians of continuous phase) of fault characteristic frequency. Integrating the shaft rotational frequency in this interval leads to its continuous phase (in cycle) in this interval. The ratio of fault characteristic frequency and shaft rotational frequency can then be determined as the ratio of continuous phases of these two frequencies in the chosen interval, expressed by

$$n = \frac{f_{\text{fault}}(t)}{f_{\text{srot}}(t)} = \frac{p_{\text{fault}}}{p_{\text{srot}}} = \frac{1}{\int_{T_{\text{adj}}} f_{\text{srot}}(t)\,\mathrm{d}t}. \tag{5-36}$$

where T_{adj} denotes length of the time interval between the two chosen adjacent impulses, p_{fault} and p_{srot} represent the phases of fault characteristic frequency and sun gear rotational

frequency, respectively. The fault can then be diagnosed by comparing this ratio with the ratios of ideal fault characteristic frequencies and shaft rotational frequency. Using the time interval between the first impulse and second impulse as an example, the frequency ratio n is determined as

$$n = \frac{1}{\int_{t=0.369}^{t=0.633} f_{\text{srot}}(t)\,\mathrm{d}t} = \frac{1}{1.2021} = 0.8312, \tag{5-37}$$

which is close to the ideal ratio of sun gear fault characteristic frequency and sun gear rotational frequency (i.e., $f_{\text{sun}}/f_{\text{srot}}=5/6$.). This indicates that the sun gear has a fault, which is consistent with the simulation setup.

In order to show the advantage of the VSBD, we consider a comparison study. Firstly, this signal is processed by the order-tracking method. The resulted order spectrum, as shown in Fig. 5-10 (D), does reveal the meshing frequency. However, it cannot reveal the fault-induced impulses. The same time-frequency methods that were used in the subsection 5.3.1 are employed again to demonstrate the advantage of the VSBD and the results are shown in Fig. 5-11(A-F). The STFT (Fig. 5-11(A)) displays smear effects on the meshing frequency and cannot reveal the impulses. The CWD (Fig. 5-11(B)) is able to reveal the meshing frequency and impulses. However, the meshing frequency is clouded by serious smear effects. Though the PCT, GST, GLCT and SET, as shown in Fig. 5-11(C-F), are able to reveal the meshing frequency, they cannot reveal the impulses.

The analyses in this section clearly show that in terms of revealing harmonics, the VSBD performance is similar to the order tracking, but better than other tested time-frequency methods. In terms of revealing impulses, the VSBD outperforms the order tracking method and the tested time-frequency methods.

It has been shown that the VSBD-based fault diagnosis relies on the detection of fault-induced harmonics or impulses. Noise may influence the fault diagnosis in two ways, 1) noise may lead to unwanted and unexpected "ridges" in the TFR and such ridges may be misidentified as fault-induced signal components; and 2) noise may bury the true signal components in the TFR and make them undiscoverable.

The efficiency of the proposed VSBD is evaluated using the signal defined by Eq. (5-34). The characteristics of the used computer and software are provided as follows: 8 GB DDR3 RAM, Intel® i7-3615QM 2.3GHz CPU, 256 GB flash storage and MATLAB® R2014a. The computational time of processing the signal used in this subsection is listed in Table 5-2. It can be found that the VSBD method is faster than the GLCT, but slower than other methods. However, the absolute computational time of the VSBD is reasonably short (only 2.11 s) and this may be acceptable for most applications.

Table 5-2 Computational time

Method	VSBD	STFT	CWD	PCT	GST	GLCT	SET
Time (s)	2.11	0.29	1.57	1.16	1.82	2.20	0.43

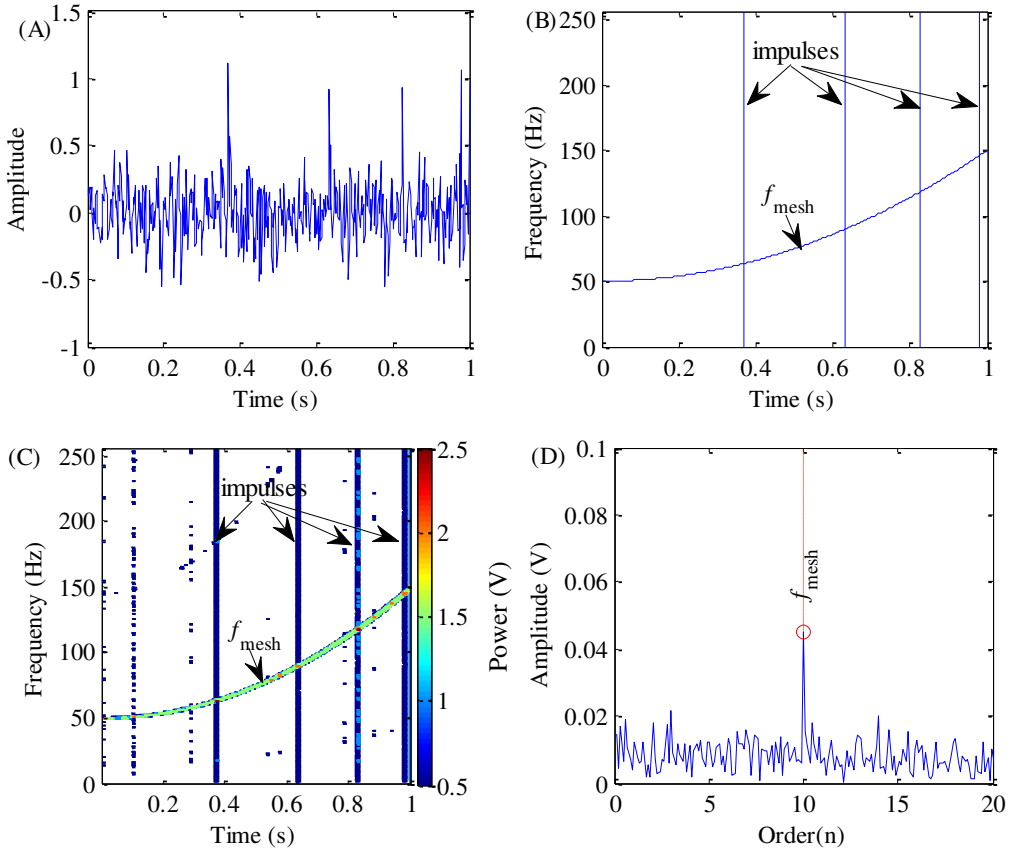

Fig. 5-10. Synthetic signal 2: (A) waveform and (B) ideal TFR, (C) VSBD result and (D) order spectrum

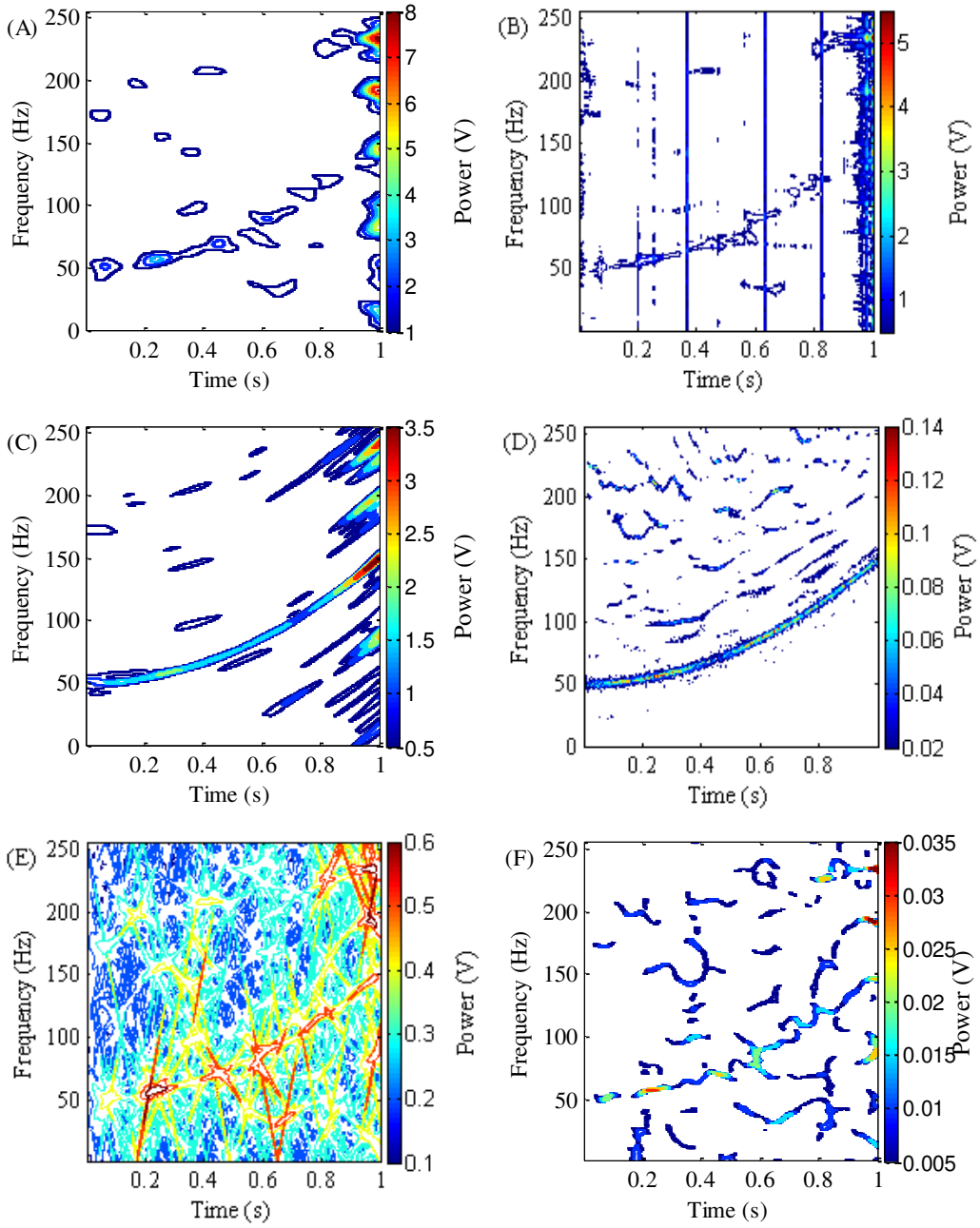

Fig. 5-11. TFRs of the synthetic signal 2 obtained by: (A) STFT, (B) CWD, (C) PCT, (D) GST, (E) GLCT and (F) SET

5.4 **Experimental evaluations**

In this section, the VSBD is evaluated on diagnosing sun gear fault of a planetary gearbox in our lab. We carry out three tests on the planetary gearbox test rig shown in Fig. 3-13. The test rig contains an AC drive motor, a two-stage planetary gearbox and a magnetic brake. The motor drives the planetary gearbox and the load is applied on the

output end of the planetary gearbox by the magnetic bake. Two accelerometers are mounted on the casings of the two stages of the gearbox to collect the vibration signals and a tachometer is installed at the output end of the system to measure the output speed of the planetary gearbox (i.e., the carrier rotational speed of the second stage). The configuration parameters of the planetary gearbox are listed in Table 5-3. The characteristic frequencies are calculated based on the planetary gearbox configuration using the formulas given in Appendix B (Feng and Zuo, 2012) and presented in Table 5-4. The characteristic frequencies are expressed as the multiples of the system output shaft rotational frequency, because they are time-varying. The meshing frequency corresponds to the gear-meshing vibration. The fault characteristic frequencies of the sun gear, planet gear and ring gear indicate the occurrence of the corresponding fault. The rotational frequencies of the carrier and sun gear correspond to the rotation of carrier and sun gear. In a common vibration signal of planetary gearbox, the meshing frequency acts as carrier frequency, and the rotational frequencies and the fault characteristic frequencies act as modulation frequencies.

In the three tests, the motor speed approximately varies between 23 Hz and 32 Hz and the corresponding system output shaft rotational speed is between 0.8 Hz to 1.2 Hz. The load is set as 3.0 Nm. The sampling frequency is 40 kHz. In the first test, all the gears are healthy. In the second test, the sun gear in the first stage is a gear with wear fault and all the other gears are healthy. In the third test, the sun gear in the second stage is a gear with chipping fault and all the other gears are healthy. The photos of the two fault sun gears are presented in Fig. 3-14(A) and (B) respectively.

Table 5-3 Configuration parameters of the gearboxes

Gear	Number of gear teeth	
	Stage 1	Stage 2
Sun	20	28
Planet	40(4)	36(4)
Ring	100	100

Note: the number of planet gears is presented in the parenthesis

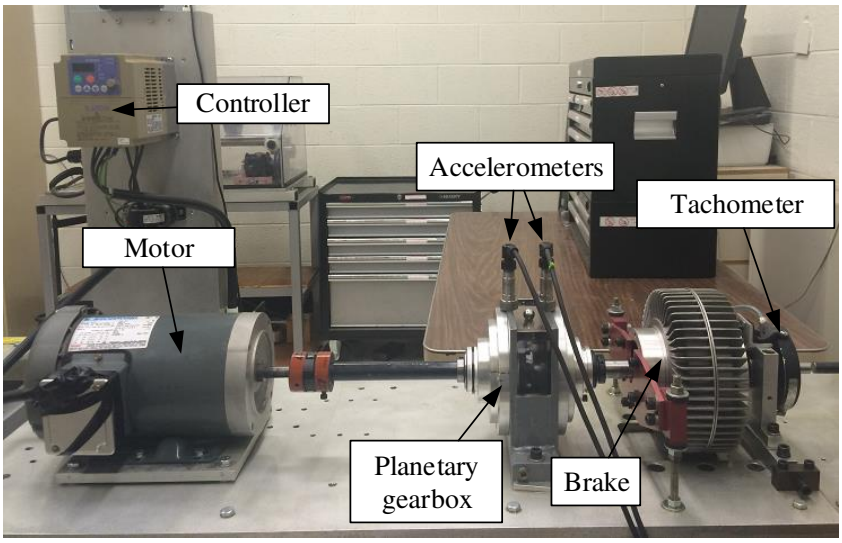

Fig. 5-12. Test rig

Table 5-4 Characteristic frequency of the planetary gearbox

Frequency	Stage 1	Stage 2
Sun gear fault	$f_{sun1}=(70/3)f_{out}$	$f_{sun2}=(175/48)f_{out}$
Planet gear fault	$f_{planet1}=(35/3)f_{out}$	$f_{planet2}=(1225/432)f_{out}$
Ring gear fault	$f_{ring1}=(14/3)f_{out}$	$f_{ring2}=(49/48)f_{out}$
Carrier rotating	$f_{crot1}=(14/3)f_{out}$	$f_{crot2}=f_{out}$
Sun gear rotating	$f_{sunrot1}=28f_{out}$	$f_{sunrot2}=(14/3)f_{out}$
Meshing	$f_{mesh1}=(1400/3)f_{out}$	$f_{mesh2}=(1225/12)f_{out}$

5.4.1 Healthy planetary gearbox

The vibration signal of the healthy planetary gearbox, its frequency spectrum and the gearbox output speed are shown in Fig. 5-13(A), (B) and (C) respectively. It can be found the output speed fluctuates approximately between 0.8 Hz and 1.2 Hz. The corresponding meshing frequencies of the first stage and the second stage are thus between 373.33 and 560 Hz, and between 81.67 Hz and 122.5 Hz respectively according to their relationships with the output speed (i.e., ($f_{mesh1}=(1400/3)f_{out}$ and $f_{mesh2}=(1225/12)\ f_{out}$) as listed in Table 6-4). As the fault features are mostly contained in the sidebands of meshing frequencies, the frequency band of interest is selected as from 0 Hz to 800 Hz, which is sufficient to cover the possible sidebands of the meshing frequencies of both stages. The proposed VSBD is then applied on the data and the obtained TFR is presented in Fig. 5-14. According

to the relationship between the motor speed and the characteristic frequencies of the gearbox listed in Table 6-4, the signal components in the TFR can be revealed. They are rotational frequency of the first stage sun gear f_{srot1}, the meshing frequency of the first stage f_{mesh1}, two sidebands of first stage meshing frequency $f_{mesh1}+f_{srot1}$ and $f_{mesh1}-f_{crot1}$. It can be seen that some of the frequency components only occur in a short duration, this is because in a nonstationary condition, the amplitudes of the signal components are also time-varying. These components either relates to the rotation of the planetary gearbox components or the meshing of the gears and no frequency component relating to the gear faults is uncovered, therefore the gearbox is diagnosed as healthy.

This signal is then processed by the PCT, GST, GLCT and SET for comparison. The obtained TFRs are shown in Fig. 5-15(A), (B), (C) and (D), respectively. It can be seen that these methods can barely uncover the meshing frequency of the first stage but the sidebands are not clearly revealed.

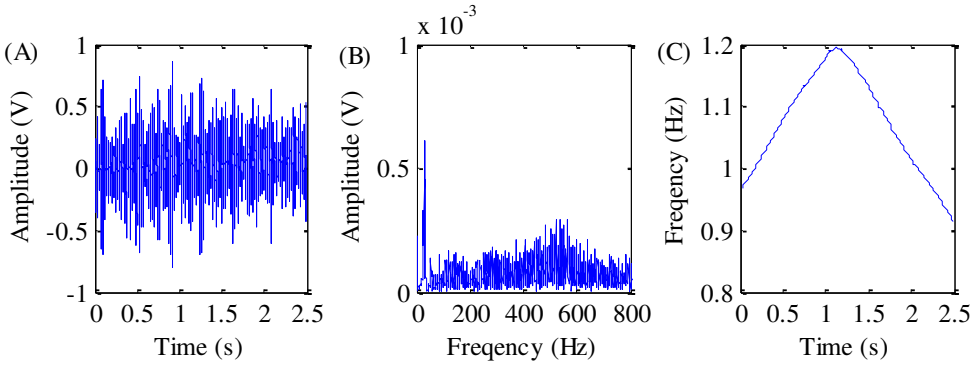

Fig. 5-13. Healthy gearbox test: (A) vibration signal waveform, (B) Fourier spectrum and (C) output shaft rotational speed

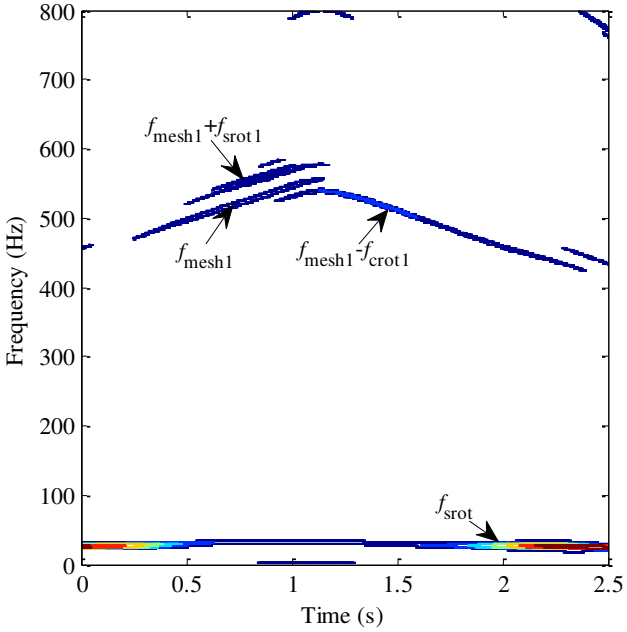

Fig. 5-14. VSBD of the signal of the healthy gearbox test

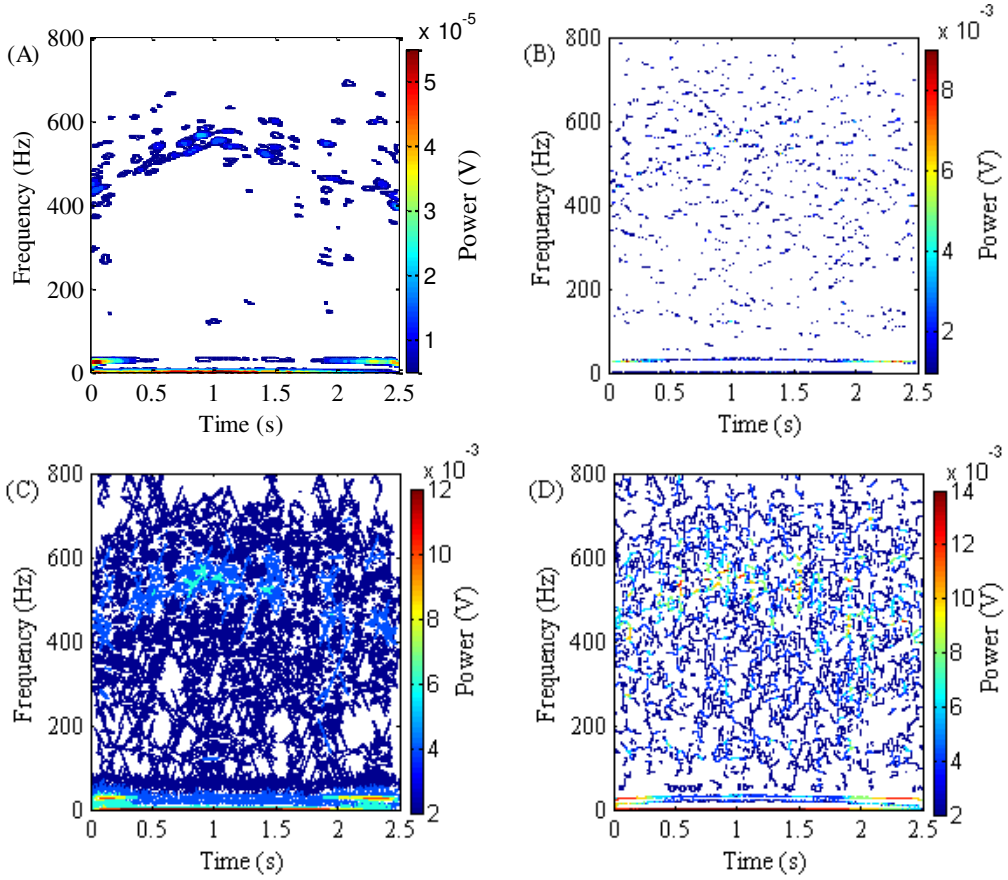

Fig. 5-15. TFRs of the signal from the healthy gearbox obtained by: (A) PCT, (B) GST, (C) GLCT and (D) SET

5.4.2 Sun gear wear fault detection

In this subsection, the VSBD is tested on the signal collected from the planetary gearbox with sun gear wear fault on stage 1. The vibration signal and the corresponding Fourier spectrum are shown is Fig. 5-16(A) and (B) respectively. As plotted in Fig. 5-16(C), the gearbox output velocity is again between 0.8 Hz to 1.2 Hz, thus the frequency band of interest is also chosen as from 0 Hz to 800 Hz. The signal is then processed by the VSBD and the resulting TFR is present in Fig. 5-17. Many signal components are revealed. Some of them are caused by the rotation of the gearbox components and the meshing of the gears, and thus they do not indicate a faulty condition, including the gear rotational frequency of the first stage sun gear f_{srot1}, the meshing frequency of the first stage f_{mesh1} and the sidebands related to sun gear rotational frequency $f_{mesh1}\pm nf_{srot1}$. Apart from them, the sidebands related to the fault characteristic frequency of the first stage are also dominant and they are $f_{mesh1}\pm nf_{sun1}$ and $f_{mesh1}+2f_{sun1}+2f_{srot1}$, indicating a faulty condition of the first stage sun gear.

This signal is then processed by the PCT, GST, GLCT and SET again for comparison purpose. The generated TFRs are displayed in Fig. 5-18(A), (B), (C) and (D), respectively. It can be seen that these methods can barely reveal the meshing frequency of the first stage but the sidebands are not clearly identified.

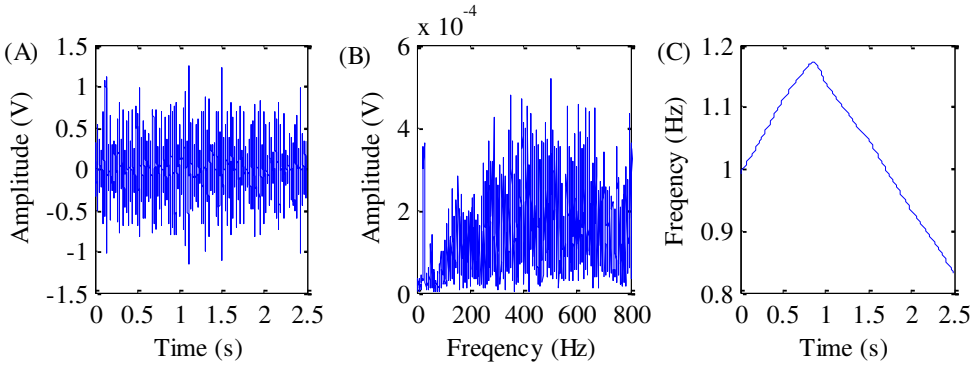

Fig. 5-16. Sun gear wear fault test: (A) vibration signal waveform, (B) Fourier spectrum and (C) output shaft rotational speed

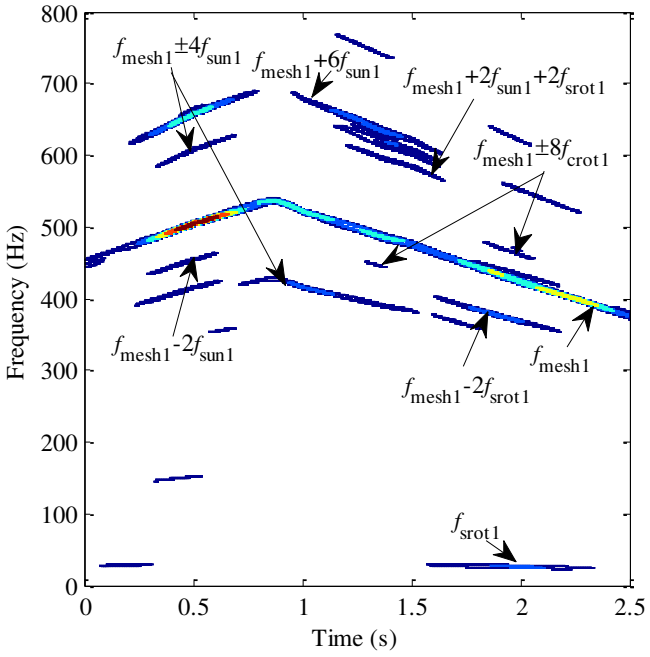

Fig. 5-17. VSBD of the signal of the sun gear wear fault test

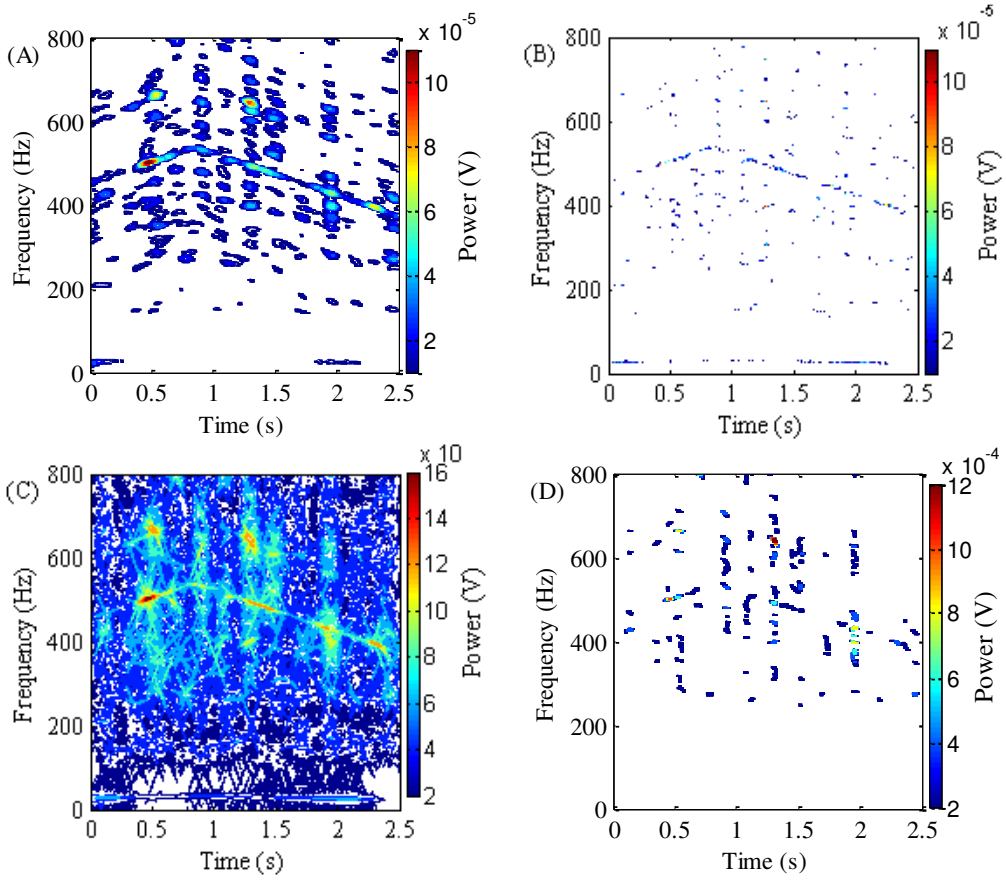

Fig. 5-18.TFRs of the signal of sun gear wear fault obtained by: (A) PCT, (B) GST, (C) GLCT and (D) SET

5.4.3 Sun gear chipping fault detection

In this section, we evaluate the VSBD in diagnosing the chipping fault of the second stage sun gear. The vibration signal, its Fourier spectrum and the gearbox output speed are presented in Fig. 5-19 (A), (B) and (C) respectively. The motor speed is also approximately between 23 and 32 Hz. Accordingly the meshing frequency of the second stage is between 83.9 Hz and 116.7 Hz. The frequency band of interest is thus selected as [0, 200 Hz] to investigate the sidebands of the second stage meshing frequency. The VSBD result is shown in Fig. 5-20 and it can be found that several dominant components related to sun gear fault are revealed and represented by $f_{mesh2}\pm nf_{sun2}\pm f_{srot2}$. These components are related to the second stage sun gear fault, indicating that the second stage has a sun gear fault.

Again, we process the signal of chipping fault using the PCT, GST, GLCT and SET and the obtained TFRs are presented in Fig. 5-21(A), (B), (C) and (D), respectively. It can be seen that these methods can only reveal the sun gear rotational frequency. However, they cannot recognize the meshing frequency of the second stage and its sidebands.

The three tests have demonstrated that the proposed VSBD is effective in providing a clear TFR with good time-frequency resolution and diagnosing local and distributed fault gear faults of planetary gearbox. The comparisons with the other methods show that the VSBD is superior to them in revealing the time-frequency components from planetary gearbox vibration signals.

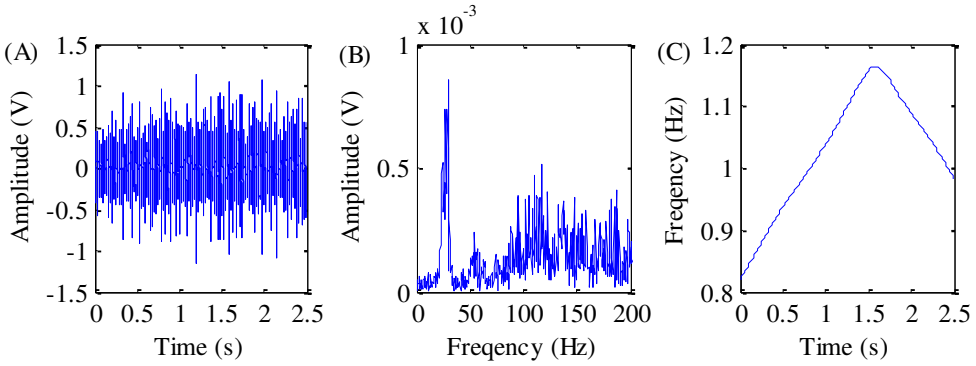

Fig. 5-19. Sun gear chipping fault test: (A) vibration signal waveform, (B) Fourier spectrum and (C) output shaft rotational speed

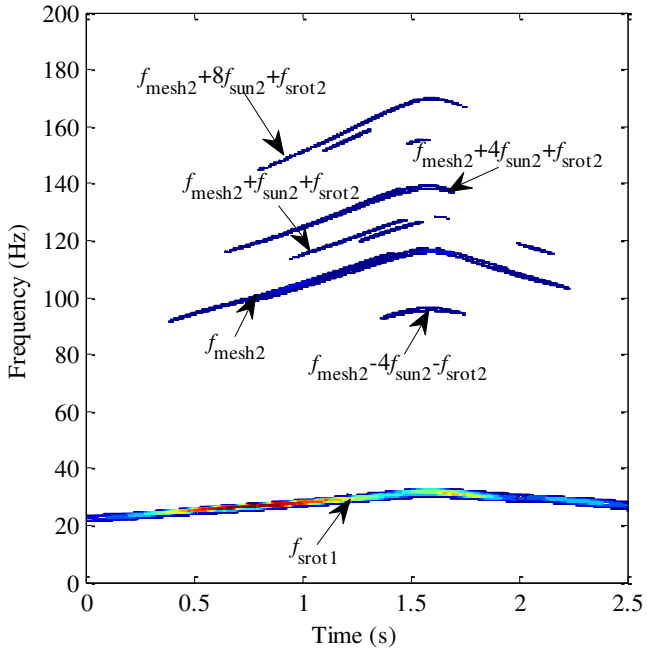

Fig. 5-20. VSBD of the signal of the sun gear chipping fault test

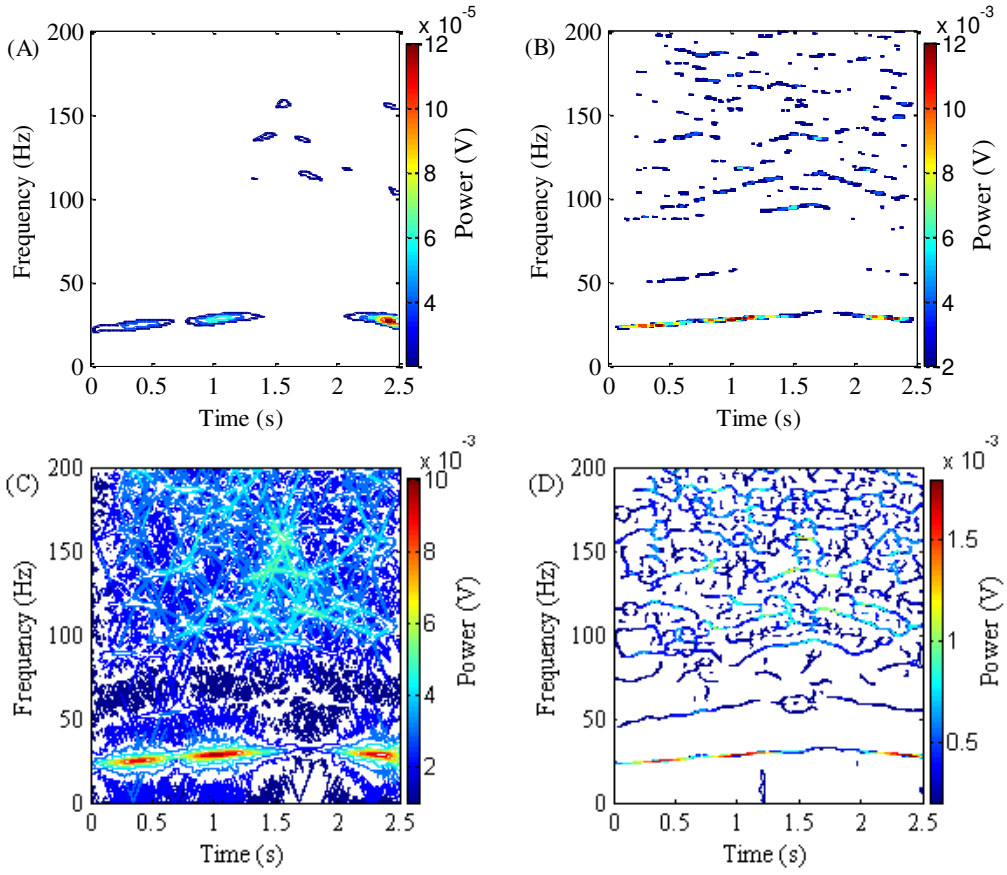

Fig. 5-21: TFRs of the signal of sun gear chipping fault obtained by: (A) PCT, (B) GST, (C) GLCT and (D) SET

5.5 Conclusions

In this chapter, a bilinear distribution named the VSBD for planetary gearbox fault diagnosis has been presented. This method is based on the GD and CCBD and a simple algorithm is also developed to realize the proposed method. Compared with the existing time-frequency methods, the main advantages of the proposed VSBD include: a) it is free from the interference caused by cross terms and the smear effect caused by the time-varying frequency components, and b) it has better time-frequency resolution. The effectiveness of the VSBD has been demonstrated in analyzing both simulation and experimental vibration signals under non-stationary conditions.

6 Velocity synchronous linear chirplet transform (VSLCT)

6.1 Introduction

Though the VSSTFT, VST and VSBD proposed in the last three chapters are able to generate a smear-free TFR for fault diagnosis of planetary gearbox under non-stationary conditions, they still require the shaft speed information. The shaft speed can be calculated from the tachometer or estimated from the TFR obtained by the STFT of the vibration signal. However, under some certain conditions, the tachometer is not easily accessible and the STFT is not clear enough for shaft speed estimation due to noise and smearing effect. To resolve this problem, the VSLCT method is proposed in this chapter. It employs a set of linear chirplets that are synchronous with shaft rotational velocity to solve the smear problem. It also employs a window with time-varying window length to provide more desirable time-frequency resolution. The parameters of the VSLCT can be adaptively determined from the signal without user intervention. On the other hand, as the proposed VSLCT employs a non-orthogonal kernel and a window with time-varying window length, it is beyond the definition of traditional linear transform and thus the definition of linear transform is extended before proposing the VSLCT.

6.2 Presentation of the VSLCT

6.2.1 Review of the traditional linear transform

The traditional linear transform for time-frequency analysis is reviewed in this subsection. The wavelet transform is excluded in this review, as it commonly analyses the signal in time-scale plane, not the traditional time-frequency plane and it is rarely used in the time-frequency analysis of non-stationary vibration signal of rotational machinery.

The linear transform of a signal $x(t)$ is defined as the following integral transform

$$X(\tau,\nu)=\int_{t=-\infty}^{t=+\infty} x_{\mathrm{win}(\tau)}(t)\overline{P_{(\tau,\nu)}(t)}\mathrm{d}t\,, \tag{6-1}$$

where τ and ν denote time and frequency respectively, $x_{\mathrm{win}(\tau)}(t)$ represents the windowed signal, $\overline{P_{(\tau,\nu)}(t)}$ represents the linear transform kernel and the overhead bar denotes complex conjugation. The windowed signal $x_{\mathrm{win}(\tau)}(t)$ is expressed by

$$x_{\mathrm{win}(\tau)}(t)=x_{\mathrm{ana}}(t)\lambda_{(\mathrm{w})}(t-\tau)\,, \tag{6-2}$$

where $\lambda_{(w)}(t)$ denotes the window function centered at time t=0 with window length w>0 and its role is to truncate the analytic signal $x_{ana}(t)$. The analytic signal is obtained from the real-valued signal using the Hilbert transform (Peng et al., 2011), expressed by

$$x_{ana}(t) = x(t) + jH(x(t)), \tag{6-3}$$

where H denotes the Hilbert transform. The reason of using analytic signal rather the real-valued signal is to avoid the interference of negative frequency. The expression of Gaussian window is given below as an example of the window function:

$$\lambda_{(w)}(t) = \begin{cases} \frac{1}{\sqrt{2\pi}\sigma}\exp\left(-\frac{1}{2}\left(\frac{t}{\sigma}\right)^2\right), t \in \left[-\frac{w}{2}, \frac{w}{2}\right] \\ 0, t \in \left(-\infty, -\frac{w}{2}\right) \cup \left(\frac{w}{2}, +\infty\right) \end{cases}, \tag{6-4}$$

where σ is the coefficient of the Gaussian window.

The linear transform kernel $\overline{P_{(\tau,\nu)}(t)}$ must form complete orthonormal sets for square-integrable functions L^2 over both time t and frequency ν (Baraniuk and Jones, 1993b), expressed by

$$\int_{t=-\infty}^{t=+\infty} P_{(\tau,\nu_n)}(t)\overline{P_{(\tau,\nu_m)}(t)}\mathrm{d}t = \delta(\nu_m - \nu_n) \tag{6-5}$$

and

$$\int_{\nu=-\infty}^{\nu=+\infty} P_{(\tau,\nu)}(t_n)\overline{P_{(\tau,\nu)}(t_m)}\mathrm{d}\nu = \delta(t_m - t_n), \tag{6-6}$$

where δ is the Dirac delta function.

$P_{(\tau,\nu)}(t)$ must form a set of complex waves with unit amplitude as bases (i.e., elements of a basis), expressed by

$$P_{(\tau,\nu)}(t) = \exp\left(j\int_{-\infty}^{\infty} 2\pi f_{basis(\tau,\nu)}(t)\mathrm{d}t\right), \tag{6-7}$$

where $f_{basis(\tau,\nu)}(t)$ represents the frequencies of the bases. The bases must have localised energy around time τ and frequency ν, therefore $f_{basis(\tau,\nu)}(t)$ is equal to ν at time t=τ, expressed by

$$f_{\text{basis}(\tau,\nu)}(\tau)=\nu\,. \tag{6-8}$$

The windowed signal $x_{\text{win}(\tau)}(t)$ can be recovered by an inverse linear transform (Baraniuk and Jones, 1993b), expressed by

$$x_{\text{win}(\tau)}(t)=\int_{\nu=-\infty}^{\nu=+\infty} X(\tau,\nu)\,P_{(\tau,\nu)}(t)\,\mathrm{d}\nu\,. \tag{6-9}$$

The linear transform and the inverse linear transform form a linear transform pair. The definitions of the linear transform pair (Eq. (6-1) and Eq. (6-9)) show that the windowed signal $x_{\text{win}(\tau)}(t)$ and the linear transform result $X(\tau,\upsilon)$ are reversible and this is proved below.

$$\begin{aligned}
&\int_{\nu=-\infty}^{\nu=+\infty} X(\tau,\nu)P_{(\tau,\nu)}(t_n)\,\mathrm{d}\nu \\
&=\int_{\nu=-\infty}^{\nu=+\infty}\left(\int_{t=-\infty}^{t=+\infty} x_{\text{win}(\tau)}(t_m)\overline{P_{(\tau,\nu)}(t_m)}\mathrm{d}t_m\right)P_{(\tau,\nu)}(t_n)\,\mathrm{d}\nu \\
&=\int_{t=-\infty}^{t=+\infty} x_{\text{win}(\tau)}(t_m)\left(\int_{\nu=-\infty}^{\nu=+\infty}\overline{P_{(\tau,\nu)}(t_m)}P_{(\tau,\nu)}(t_n)\,\mathrm{d}\nu\right)\mathrm{d}t_m \\
&=\int_{t=-\infty}^{t=+\infty} x_{\text{win}(\tau)}(t_m)\,\delta(t_m-t_n)\,\mathrm{d}t_m = x_{\text{win}(\tau)}(t_n)
\end{aligned} \tag{6-10}$$

$$\begin{aligned}
&\int_{t=-\infty}^{t=+\infty} x_{\text{win}(\tau)}(t)\overline{P_{(\tau,\nu_n)}(t)}\mathrm{d}t \\
&=\int_{t=-\infty}^{t=+\infty}\left(\int_{\nu_n=-\infty}^{\nu_n=+\infty} X(\tau,\nu_m)\,P_{(\tau,\nu_m)}(t)\,\mathrm{d}\nu_m\right)\overline{P_{(\tau,\nu_n)}(t)}\mathrm{d}t \\
&=\int_{\nu_n=-\infty}^{\nu_n=+\infty} X(\tau,\nu_n)\left(\int_{t=-\infty}^{t=+\infty} P_{(\tau,\nu_m)}(t)\overline{P_{(\tau,\nu_n)}(t)}\mathrm{d}t\right)\mathrm{d}\nu_m \\
&=\int_{\nu_n=-\infty}^{\nu_n=+\infty} X(\tau,\nu_m)\,\delta(\nu_m-\nu_n)\,\mathrm{d}\nu_m = X(\tau,\nu_n)
\end{aligned} \tag{6-11}$$

The proof utilizes the orthogonality of the linear transform kernel $\overline{P_{(\tau,\nu)}(t)}$. The reversibility means that the windowed signal $x_{\text{win}(\tau)}(t)$ can be formed by the combination of the weighted bases, where the weights are represented by the linear transform result $X(\tau,\nu)$ and the bases are formed by $P_{(\tau,\nu)}(t)$. As the bases represented by $P_{(\tau,\nu)}(t)$ also have localised energy around time τ and frequency ν, the linear transform result $X(\tau,\nu)$ represents the weights of the bases having localized energy at time τ and frequency ν. For this reason, the TFR can be obtained by presenting the absolute value of the linear transform result $X(\tau,\nu)$ in time-frequency plane.

To facilitate the understanding of the mechanism of the linear transform, we give two illustrations using two traditional linear transforms, the STFT and the chirplet transform. A synthetic vibration signal is introduced. This signal is named example signal and is used for illustrations in this section and next section. This signal is assumed to be collected from rotational machinery under non-stationary condition and it contains two frequency components, the shaft rotational frequency and the 1.8 multiples of shaft rotational frequency. The phases of the two components are neglected and the signal length is 6 s. This example signal is expressed by

$$x_1(t) = \sin\left(\int_0^t 2\pi f_{\text{shaft}}(\tau)\,\mathrm{d}\tau\right) + \sin\left(1.8\int_0^t 2\pi f_{\text{shaft}}(\tau)\,\mathrm{d}\tau\right), \tag{6-12}$$

where $f_{\text{shaft}}()$ is the synthetic shaft rotational frequency, expressed by

$$f_{\text{shaft}}(t) = 14\exp\left(-0.7(t-1.15)^2\right) + 3. \tag{6-13}$$

The signal waveform is plotted in Fig. 6-1(A). The frequency trajectories of the signal components are plotted in Fig. 6-1(B), it can be seen that the signal contains two components. The lower component is shaft rotational frequency which rises from 8 Hz to 17 Hz then drops to 3 Hz and the upper component is the 1.8 multiples of the shaft rotational frequency.

The STFT is expressed by

$$X_{\text{STFT}}(\tau,\nu) = \int_{t=-\infty}^{t=+\infty} x_{\text{win}(\tau)}(t)\exp(-j2\pi\nu t)\,\mathrm{d}t. \tag{6-14}$$

By observing the STFT expression, the basis frequency is expressed by

$$f_{\text{STFT-basis}(\tau,\nu)}(t) = \frac{\mathrm{d}(2\pi\nu t)}{2\pi\mathrm{d}t} = \nu. \tag{6-15}$$

From the above equation, it can be seen that the STFT bases have time-invariant frequencies. The frequencies of the STFT bases of the example signal defined by Eq. (6-15) are plotted in Fig. 6-2(A), it can be seen that the time-invariant frequencies of the bases do not match the time-varying frequencies of the signal components in 0-3 s, however, they approximately match each other in 3-6s. The TFR obtained by the STFT with 1.5 s

Gaussian window is shown in Fig. 6-2(B). It can be seen that this TFR has smear problem in 0-3 s and has better energy concentration in 3-6 s. The above analysis shows that the degree of TFR energy concentration depends on the frequency matching degree of the bases and the signal components.

The function of the chirplet transform is represented by

$$X_{\mathrm{CT}}(\tau,\nu)=\int_{t=-\infty}^{t=+\infty} x_{\mathrm{win}(\tau)}(t)\exp\left(-j2\pi\left(\frac{c}{2}(t-\tau)^2+\nu t\right)\right)\mathrm{d}t\,. \tag{6-16}$$

Using a similar procedure of the STFT case, the frequencies of the chirplet transform bases are obtained as

$$f_{\text{CT-basis}(\tau,\nu)}(t)=\frac{\mathrm{d}\left(2\pi\left(\frac{\mathrm{c}}{2}(t-\tau)^2+\nu t\right)\right)}{\mathrm{d}t}=\nu+\mathrm{c}(t-\tau)=\mathrm{c}t+(\nu-\mathrm{c}\tau)\,. \tag{6-17}$$

It can be seen the basis representation is a linear function of time *t* with a fixed positive slope c. We set the incline slope as 10. The frequencies of the chirplet transform bases are plotted in Fig. 6-3(A). It can be seen the positive slopes of the frequencies of the bases are fixed and thus the bases cannot completely match the frequencies of the signal components with time-varying inclined angles. The bases approximately match the lower component in 0-1 s and match the upper component in 0-1.5 s, but they do not match each other elsewhere. This means only the lower component in 0-1 s and the upper component in 0-1.5 s have relatively better energy concentration. The TFR obtained by the chirplet transform shown in Fig. 6-3 (B) confirms this expectation. This validates that the degree of TFR energy concentration depends on the frequency matching degree of the bases and the signal components.

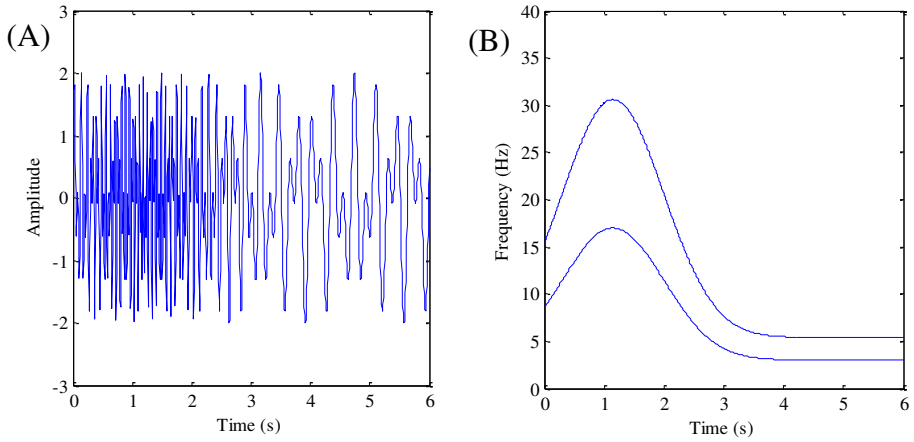

Fig. 6-1. The example signal: (A) waveform, and (B) frequency trajectories

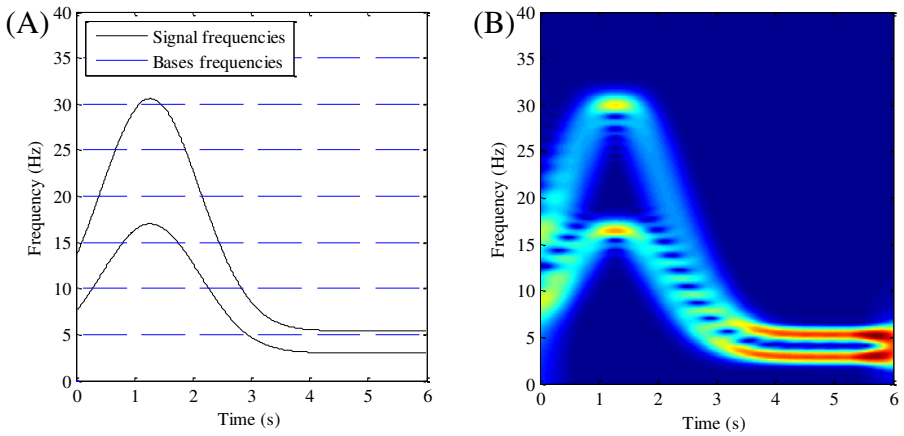

Fig. 6-2. Illustration of the STFT: (A) frequencies of the bases, and (B) the TFR obtained with window length 1.5 s

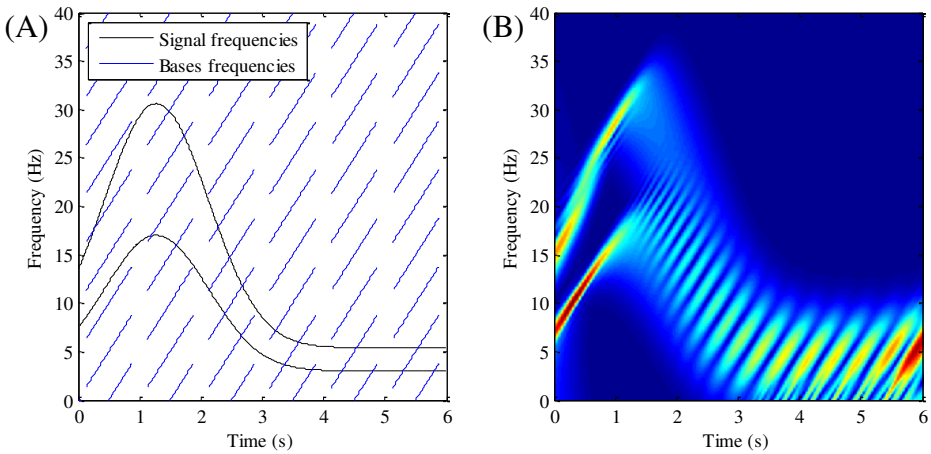

Fig. 6-3. Illustration of the chirplet transform: (A) frequencies of the bases, and (B) the TFR obtained with window length 1.5 s

6.2.2 Extension of the linear transform

It has been shown in the last subsection that the linear transforms have smear problems in analysing the non-stationary vibration signals because the frequencies of the bases do not match the frequencies of the non-stationary vibration signal components. To address the issue of the smear problem, the bases of the linear transform must match the frequencies of the non-stationary vibration signal components. As most of the vibration signal components are proportional to shaft rotational velocity, the linear transform bases must be synchronous with shaft rotational velocity. However, this cannot be achieved, because such bases are not pairwise orthogonal (this will be proved in the next subsection), and thus do not meet the linear transform requirement. The requirement of orthogonality is because the linear transform kernel $\overline{P_{(\tau,\nu)}(t)}$ is the complex conjugate of the inverse linear transform $P_{(\tau,\nu)}(t)$. However, we find that it is not necessary because if we change the linear transform kernel $\overline{P_{(\tau,\nu)}(t)}$ to an arbitrary kernel in all the equations of linear transform, these equations still hold.

The time-frequency resolution is controlled by the window length. Traditional linear transforms use a window with time-variant length thus their time-frequency resolutions are time-variant. They lack the adaptability in analysing the non-stationary signal whose features change over time. For non-stationary signals, the most suitable time-frequency resolution may vary over time. A time-varying resolution requires a window function with time-varying window length. We find such window is also tenable because if we replace the fixed window length w with a time-varying window length function $w(\tau)$, all the equations of linear transform still hold.

Based on the above analysis, to solve the smear problem and make the time-frequency resolution more suitable, the definition of the linear transform should be extended. The extension of the linear transform definition is detailed and proved below.

Considering an arbitrary linear transform kernel represented by symbol $\overline{Q_{(\tau,\nu)}(t)}$, which may or may not equal $\overline{P_{(\tau,\nu)}(t)}$, the linear transform can be redefined as

$$X(\tau,\nu)=\int_{t=-\infty}^{t=+\infty} x_{\mathrm{win}(\tau)}(t)\overline{Q_{(\tau,\nu)}(t)}\mathrm{d}t\ . \tag{6-18}$$

A window with time-varying length $w(\tau)$, represented by $\lambda_{(w(\tau))}(t)$, is introduced here and such a window can be obtained by replacing the fixed window length w with the time-varying length $w(\tau)$ in the traditional window function. The time-varying Gaussian window is given below as an example:

$$\lambda_{(w(\tau))}(t)=\begin{cases}\dfrac{1}{\sqrt{2\pi}\sigma}\exp\left(-\dfrac{1}{2}\left(\dfrac{t}{\sigma}\right)^2\right), t\in\left[-\dfrac{w(\tau)}{2},\dfrac{w(\tau)}{2}\right] \\ 0, t\in\left(-\infty,-\dfrac{w(\tau)}{2}\right)\cup\left(\dfrac{w(\tau)}{2},+\infty\right)\end{cases}. \tag{6-19}$$

Under the new definition, the analytic signal is truncated by a window with time-varying length, expressed by

$$x_{\mathrm{win}(\tau)}(t)=x_{\mathrm{ana}}(t)\lambda_{(w(\tau))}(t-\tau). \tag{6-20}$$

There is no change in the inverse linear transform (Eq. (6-9)) and the energy localisation requirements (Eq. (6-7) and Eq. (6-8)). With the extended definition of the linear transform, $\overline{P_{(\tau,\nu)}(t)}$ should be replaced with $\overline{Q_{(\tau,\nu)}(t)}$ in the functions of requirements of orthogonality (Eq. (6-5) and Eq. (6-6)), expressed by

$$\int_{t=-\infty}^{t=+\infty}\overline{Q_{(\tau,\nu_n)}(t)}P_{(\tau,\nu_m)}(t)\,\mathrm{d}t=\delta(\nu_m-\nu_n) \tag{6-21}$$

and

$$\int_{\nu=-\infty}^{\nu=+\infty}\overline{Q_{(\tau,\nu)}(t_n)}P_{(\tau,\nu)}(t_m)\,\mathrm{d}\nu=\delta(t_m-t_n). \tag{6-22}$$

The key of the mechanism of the linear transform is that the windowed signal $x_{\mathrm{win}(\tau)}(t)$ and the linear transform result $X(\tau,\nu)$ are reversible via the linear transform pair. Under the new definition, the reversibility still holds and the proof is given as follows:

$$
\begin{aligned}
&\int_{\nu=-\infty}^{\nu=+\infty} X(\tau,\nu) P_{(\tau,\nu)}(t_m)\,\mathrm{d}\nu \\
&= \int_{\nu=-\infty}^{\nu=+\infty} \left(\int_{t=-\infty}^{t=+\infty} x_{\mathrm{win}(\tau)}(t_n) \overline{Q_{(\tau,\nu)}(t_n)}\,\mathrm{d}t_n \right) P_{(\tau,\nu)}(t_m)\,\mathrm{d}\nu \\
&= \int_{t=-\infty}^{t=+\infty} x_{\mathrm{win}(\tau)}(t_m) \left(\int_{\nu=-\infty}^{\nu=+\infty} \overline{Q_{(\tau,\nu)}(t_n)} P_{(\tau,\nu)}(t_m)\,\mathrm{d}\nu \right) \mathrm{d}t_n \\
&= \int_{t=-\infty}^{t=+\infty} x_{\mathrm{win}(\tau)}(t_m) \delta(t_m - t_n)\,\mathrm{d}t_m = x_{\mathrm{win}(\tau)}(t_n)
\end{aligned}
\tag{6-23}
$$

and

$$
\begin{aligned}
&\int_{t=-\infty}^{t=+\infty} x_{\mathrm{win}(\tau)}(t) \overline{Q_{(\tau,\nu_n)}(t)}\,\mathrm{d}t \\
&= \int_{t=-\infty}^{t=+\infty} \left(\int_{\nu_n=-\infty}^{\nu_n=+\infty} X(\tau,\nu_m) P_{(\tau,\nu_m)}(t)\,\mathrm{d}\nu_m \right) \overline{Q_{(\tau,\nu_n)}(t)}\,\mathrm{d}t \\
&= \int_{\nu_n=-\infty}^{\nu_n=+\infty} X(\tau,\nu_m) \left(\int_{t=-\infty}^{t=+\infty} \overline{Q_{(\tau,\nu_n)}(t)} P_{(\tau,\nu_m)}(t)\,\mathrm{d}t \right) \mathrm{d}\nu_m \\
&= \int_{\nu_n=-\infty}^{\nu_n=+\infty} X(\tau,\nu_m) \delta(\nu_m - \nu_n)\,\mathrm{d}\nu_m = X(\tau,\nu_n)
\end{aligned}
\tag{6-24}
$$

According to the proofs given above, the extended definition of linear transform, which allows non-orthogonal bases and time-varying window length, is tenable. The traditional linear transform definition can be seen as the extended linear transform with additional restrictions $Q_{(\tau,\nu)}(t)=P_{(\tau,\nu)}(t)$ and $w(\tau)=\mathrm{w}$. It should be emphasized that in both the traditional definition and the extended definition, the bases are formed by $P_{(\tau,\nu)}(t)$ and the difference is that in the traditional definition, the linear transform kernel is represented by $\overline{P_{(\tau,\nu)}(t)}$, whereas in the extended definition, the linear transform kernel is represented by $\overline{Q_{(\tau,\nu)}(t)}$.

The requirement of the traditional linear transform (Eq. (6-5) and Eq. (6-6)) is that the bases generated by $P_{(\tau,\nu)}(t)$ must be strictly pairwise orthogonal over both time t and frequency ν. By contrast, the extended linear transform does not require the bases to be orthogonal, instead, the requirement (Eq. (6-21) and Eq. (6-22)) becomes that the vector generated by $P_{(\tau,\nu_m)}(t)$ must be orthogonal with the vector generated by $Q_{(\tau,\nu_n)}(t)$ and the vector generated by $P_{(\tau,\nu)}(t_m)$ must be orthogonal with the vector generated by $Q_{(\tau,\nu)}(t_n)$, where $m\neq n$. The requirement of the traditional linear transform can be seen as the

combination of the requirement of the extended linear transform with the additional requirement $Q_{(\tau,\nu)}(t)=P_{(\tau,\nu)}(t)$. This shows that the requirement of the extended linear transform is less strict than that of the traditional one. The extended linear transform no longer requires orthogonal bases and this may make the bases that are synchronous with shaft rotational frequency possible. The extended linear transform also has the potential to provide more suitable time-frequency resolution as the window length can be time-varying.

6.2.3 Derivation of the VSLCT

Based on the analysis in the subsection 6.2.2, in order to have a clear TFR without smear effect, the frequencies of the linear transform bases must match the frequencies of the vibration signal components. The linear transform with such bases is proposed in this subsection. The employed bases are linear chirplets which are synchronous with shaft rotational velocity. For this reason, the proposed transform is named velocity synchronous linear chirplet transform (VSLCT). The design of the VSLCT is detailed below.

For the vibration signal collected from rotational machinery under non-stationary conditions, most of the signal frequency components are proportional to shaft rotational frequency. In order to resolve the smear problem, the frequencies of the VSLCT bases must match the frequencies of the vibration signal components, therefore they must be proportional to shaft rotational frequency, expressed by

$$f_{\text{VSLCT-basis}(\tau,\nu)}(t)=k_{(\tau,\nu)}f_{\text{shaft}}(t), \tag{6-25}$$

where $f_{\text{VSLCT-basis}}(t)>0$ represents the frequencies of the VSLCT bases, $f_{\text{shaft}}(t)>0$ is the shaft rotational frequency and $k_{(\tau,\nu)}>0$ is the proportional ratio. One requirement of the linear transform is that the frequencies of the bases must be equal to ν at time $t=\tau$ (Eq. (6-8)), therefore

$$f_{\text{VSLCT-basis}(\tau,\nu)}(\tau)=k_{(\tau,\nu)}f_{\text{shaft}}(\tau)=\nu\,. \tag{6-26}$$

The frequencies of the bases are the multiples of the shaft rotational frequency. In a short time window, the shaft rotational frequency can be assumed linear, and thus the bases can be simplified as a set of linear chirplets. The linear approximation of shaft rotational frequency within the short time window around time τ can be obtained using the Taylor series method, represented by

$$f_{\text{shaft}}(t) \approx f_{\text{shaft}}(\tau) + f_{\text{shaft}}^{'}(\tau)(t-\tau), \tag{6-27}$$

where $f_{\text{shaft}}^{'}$ is the derivative of the shaft rotational frequency and expressed as

$$f_{\text{shaft}}^{'}(t) = \frac{\mathrm{d}f_{\text{shaft}}(t)}{\mathrm{d}t}. \tag{6-28}$$

However, the farther away from $t=\tau$, the worse the approximation will be. Thus the window length cannot be very long. A loose limit of the window length is that the approximated frequency inside the window must be greater than zero, as negative frequency does not exist in the real signal collected. Since the approximated shaft rotational frequency is linear, if it is positive at both ends of the window, it is positive in the whole window interval, expressed by

$$\begin{aligned} f_{\text{shaft}}\left(\tau \pm \frac{w(\tau)}{2}\right) &= f_{\text{shaft}}(\tau) + f_{\text{shaft}}^{'}(\tau)\left(\tau \pm \frac{w(\tau)}{2} - \tau\right) \\ &= f_{\text{shaft}}(\tau) \pm \frac{w(\tau)}{2} f_{\text{shaft}}^{'}(\tau) > 0 \end{aligned}. \tag{6-29}$$

By analysing the above inequality under two conditions that $f_{\text{shaft}}^{'}(\tau) \geq 0$ and $f_{\text{shaft}}^{'}(\tau) < 0$ respectively, the above inequality can be further simplified as

$$w(\tau) < \left| \frac{2 f_{\text{shaft}}(\tau)}{f_{\text{shaft}}^{'}(\tau)} \right|. \tag{6-30}$$

The above inequality is named the parameter limit of the VSLCT.

Solving the Eqs. (6-25 - 6-27), the frequencies of the bases are given by

$$f_{\text{VSLCT-basis}(\tau,\nu)}(t) = \nu\left(1 + (t-\tau)\frac{f_{\text{shaft}}^{'}(\tau)}{f_{\text{shaft}}(\tau)}\right) = \frac{f_{\text{shaft}}^{'}(\tau)}{f_{\text{shaft}}(\tau)}\nu t - \frac{f_{\text{shaft}}^{'}(\tau)}{f_{\text{shaft}}(\tau)}\nu\tau + \nu. \tag{6-31}$$

Using the same example signal for illustration, the frequencies of the bases generated by Eq. (6-31) are plotted in Fig. 6-4(A) with the frequencies of the signal components. It can be seen that the frequencies of the bases around the signal components approximately match the frequency trajectories of the signal components in the whole time span. From Eq. (6-31), it can be found that $f_{\text{shaft}}^{'}(\tau) / f_{\text{shaft}}(\tau)$ is a function of the shaft rotational

frequency $f_{\text{shaft}}(t)$ and this function controls the inclined slopes of the frequencies of the bases. In real applications, the shaft rotational frequency $f_{\text{shaft}}(t)$ may not be easily accessible and in such conditions, the shaft rotational frequency $f_{\text{shaft}}(t)$ has to be approximated from the vibration signal. A method determining the parameters of the VSLCT from the vibration signal is proposed in the next section and this method requires the to-be-determined parameter bounded. However, the shaft rotational frequency $f_{\text{shaft}}(t)$ is not bounded, and hence it cannot be determined using this method. It is therefore recommended to transfer the function $f'_{\text{shaft}}(\tau)/f_{\text{shaft}}(\tau)$ to a function of a bounded parameter. Assuming the TFR is displayed as a square image and the range of time and frequency are [0, T] and [0, V] respectively, the incline angle of the basis at frequency v= V/2 is selected as the bounded parameter. It is named normalized angle, represented by $\alpha(\tau)$ and its range is $(-\pi/2, \pi/2)$. The normalized angles at some fixed time points are shown in Fig. 6-4(B) and marked by the arrows. The relationship between $f'_{\text{shaft}}(\tau)/f_{\text{shaft}}(\tau)$ and the normalized angle $\alpha(\tau)$ is represented by

$$\frac{f'_{\text{shaft}}(\tau)}{f_{\text{shaft}}(\tau)} = \frac{2\tan\alpha(\tau)}{\mathrm{T}}. \tag{6-32}$$

The normalized angle calculated from the shaft rotational frequency of the example signal using the above function is plotted in Fig. 6-4(C). It should be noted that the normalized angle can be positive or negative. As the incline angles of the frequencies of the bases are proportional to each other, they can be expressed as the multiples of the normalized angle.

The VSLCT basis frequency function (Eq. (6-31)) and the parameter limit (Eq. (6-30)) are then transferred to normalized-angle forms, expressed by

$$f_{\text{VSLCT-basis}(\tau,v)}(t) = v\left(1+\frac{2\tan\alpha(\tau)}{\mathrm{T}}(t-\tau)\right) \tag{6-33}$$

and

$$w(\tau) < \left|\frac{\mathrm{T}}{\tan\alpha(\tau)}\right|. \tag{6-34}$$

The representation of the bases $P_{\mathrm{VSLCT}}(t)$ is then calculated using Eq. (6-7), expressed by

$$\begin{aligned} P_{\mathrm{VSLCT}(\tau,\nu)}(t) &= \exp\left(j2\pi \int_{-\infty}^{\infty} f_{\mathrm{VSLCT\text{-}basis}(\tau,\nu)}(t)\,\mathrm{d}t \right) \\ &= \exp\left(j2\pi\nu \left(t + \frac{\tan\alpha(\tau)}{\mathrm{T}}(t-\tau)^2 \right) \right) = \exp\left(j\nu r_{(\tau,\alpha(\tau))}(t) \right) \end{aligned}, \tag{6-35}$$

where

$$r_{(\tau,\alpha(\tau))}(t) = 2\pi\left(t + \frac{\tan\alpha(\tau)}{\mathrm{T}}(t-\tau)^2 \right). \tag{6-36}$$

The set of bases formed by $P_{\mathrm{VSLCT}(\tau,\nu)}(t)$ are not always orthogonal and this can be proved by a special counter example. Assuming τ=1,ν_1=1, ν_2=2 and $f_{\mathrm{shaft}}(t)$=t, the function of the orthogonality requirement over time (Eq. (6-6)) is given as

$$\begin{aligned} &\int_{t=-\infty}^{t=+\infty} \exp\left(j2\pi 2\left(t + \frac{1}{1}(t-0)^2 \right) \right) \exp\left(-j2\pi 1\left(t + \frac{1}{1}(t-0)^2 \right) \right) \mathrm{d}t \\ &= \int_{t=-\infty}^{t=+\infty} \exp\left(j2\pi\left(t + t^2 \right) \right) \mathrm{d}t \end{aligned} \tag{6-37}$$

It can be seen the above function becomes an integral of a complex linear chirp signal over time and such integral gives a non-null result (Borghesani et al., 2014). This means the bases are not always orthogonal. Thanks to the extension of the linear transform, the set of bases formed by $P_{\mathrm{VSLCT}(\tau,\nu)}(t)$ are not required to be orthogonal. Instead, the bases representation $P_{\mathrm{VSLCT}(\tau,\nu)}(t)$ must meet the substitute requirements (Eq. (6-21) and Eq. (6-22)), represented by

$$\int_{t=-\infty}^{t=+\infty} P_{\mathrm{VSLCT}(\tau,\nu_n)}(t)\,\overline{Q_{\mathrm{VSLCT}(\tau,\nu_m)}(t)}\,\mathrm{d}t = \delta(\nu_n - \nu_m), \tag{6-38}$$

and

$$\int_{\nu=-\infty}^{\nu=+\infty} P_{\mathrm{VSLCT}(\tau,\nu)}(t_n)\,\overline{Q_{\mathrm{VSLCT}(\tau,\nu)}(t_m)}\,\mathrm{d}t = \delta(t_n - t_m). \tag{6-39}$$

The solution of the above two functions is

$$Q_{\mathrm{VSLCT}(\tau,\nu)}(t) = r'_{(\tau,\alpha(\tau))}(t)\exp\left(j\nu r_{(\tau,\alpha(\tau))}(t) \right), \tag{6-40}$$

where

$$f_{\text{shaft}}(\tau)\dot{r}_{(\tau,\alpha(\tau))}(t)=\frac{\mathrm{d}r(t)}{\mathrm{d}t}=2\pi\left(1+\frac{\tan\alpha(\tau)}{\mathrm{T}}(t-\tau)\right). \tag{6-41}$$

The proof that Eq. (6-40) is the solution of Eq. (6-38) is given by

$$\begin{aligned}
&\int_{t=-\infty}^{t=+\infty}\overline{Q_{\text{VSLCT}(\tau,\nu_n)}(t)}P_{\text{VSLCT}(\tau,\nu_n)}(t)\,\mathrm{d}t\\
&=\int_{t=-\infty}^{t=+\infty}\dot{r}_{(\tau,\alpha(\tau))}(t)\exp\left(-j\nu_n r_{(\tau,\alpha(\tau))}(t)\right)\exp\left(j\nu_m r_{(\tau,\alpha(\tau))}(t)\right)\mathrm{d}t\\
&=\int_{t=-\infty}^{t=+\infty}\frac{\mathrm{d}r_{(\tau,\alpha(\tau))}(t)}{\mathrm{d}t}\exp\left(j(\nu_m-\nu_n)r_{(\tau,\alpha(\tau))}(t)\right)\mathrm{d}t\\
&=\int_{t=-\infty}^{t=+\infty}\frac{\mathrm{d}u}{\mathrm{d}t}\exp\left(j(\nu_m-\nu_n)u\right)\mathrm{d}t\\
&=\int_{u=-\infty}^{u=+\infty}\exp\left(j(\nu_m-\nu_n)u\right)\mathrm{d}u=\delta(\nu_m-\nu_n)
\end{aligned}, \tag{6-42}$$

where $u=r_{(\tau,\alpha(\tau))}(t)$. The proof that Eq. (6-40) is the solution of Eq. (6-39) is given by

$$\begin{aligned}
&\int_{\nu=-\infty}^{\nu=+\infty}\overline{Q_{\text{VSLCT}(\tau,\nu)}(t_n)}P_{\text{VSLCT}(\tau,\nu)}(t_m)\,\mathrm{d}\nu\\
&=\int_{\nu=-\infty}^{\nu=+\infty}\dot{r}_{(\tau,\alpha(\tau))(t_n)}\exp\left(-j\nu r_{(\tau,\alpha(\tau))}(t_n)\right)\exp\left(j\nu r_{(\tau,\alpha(\tau))}(t_m)\right)\mathrm{d}\nu\\
&=\frac{\mathrm{d}r_{(\tau,\alpha(\tau))}(t_n)}{\mathrm{d}t_n}\delta\left(r_{(\tau,\alpha(\tau))}(t_n)-r_{(\tau,\alpha(\tau))}(t_m)\right)\\
&=\frac{\mathrm{d}r_{(\tau,\alpha(\tau))}(t_n)}{\mathrm{d}t_n}\delta(t_m-t_n)\left(\frac{\mathrm{d}t_n}{\mathrm{d}\left(r_{(\tau,\alpha(\tau))}(t_n)-r_{(\tau,\alpha(\tau))}(t_m)\right)}\right)=\delta(t_m-t_n)
\end{aligned}. \tag{6-43}$$

The above proofs use two properties of the Dirac delta function (Dirac, 1958). They are the scaling of the Dirac delta function expressed by

$$\delta(at)=\frac{\delta(t)}{|a|} \tag{6-44}$$

and the composition of the Dirac delta function with a function expressed by

$$\delta(g(t))=\frac{\delta(t-t_0)}{|g'(t_0)|}, \tag{6-45}$$

where g is a continuously differentiable function, g' is the derivative of g and t_0 is the root of $g(t)=0$.

As the VSLCT linear transform kernel $\overline{Q_{\mathrm{VSLCT}(\tau,\nu)}(t)}$ is solved, the VSLCT can be obtained and its expression is

$$\begin{aligned} X_{\mathrm{VSLCT}(w(\tau),\alpha(\tau))}(\tau,\nu) &= \int_{t=-\infty}^{t=+\infty} x_{\mathrm{ana}}(t)\lambda_{(w(\tau))}(t)\overline{Q_{\mathrm{VSLCT}(\tau,\nu)}(t)}\mathrm{d}t \\ &= \int_{t=-\infty}^{t=+\infty} x_{\mathrm{ana}}(t)\lambda_{(w(\tau))}(t)2\pi\left(1+\frac{2\tan\alpha(\tau)}{\mathrm{T}}(t-\tau)\right)\exp\left(-j2\pi\nu\left(t+\frac{\tan\alpha(\tau)}{\mathrm{T}}(t-\tau)^2\right)\right)\mathrm{d}t \end{aligned}, \tag{6-46}$$

where the window length $w(\tau)$ and normalized angle $\alpha(\tau)$ must meet the parameter limit, which is rewritten below

$$w(\tau) < \left|\frac{\mathrm{T}}{\tan\alpha(\tau)}\right|. \tag{6-47}$$

The TFR can then be obtained by plotting the absolute value of the VSLCT result in time-frequency plane, represented by

$$R_{\mathrm{TF}(w(\tau),\alpha(\tau))}(\tau,\nu) = \left|X_{\mathrm{VSLCT}(w(\tau),\alpha(\tau))}(\tau,\nu)\right|. \tag{6-48}$$

The VSLCT is also tested on the example signal and the resulted TFR is shown in Fig. 6-4(D). Compared with the TFR generated by the STFT (Fig. 6-2(B)) and the chirplet transform (Fig. 6-3 (B)), the proposed VSLCT performs much better in energy concentration and has avoided the smear effect. Some 'lobes' can be seen in the TFR beside the signal components around 1 s and the 'lobes' can be alleviated by using a suitable time-varying window length and its specification is detailed in the next section.

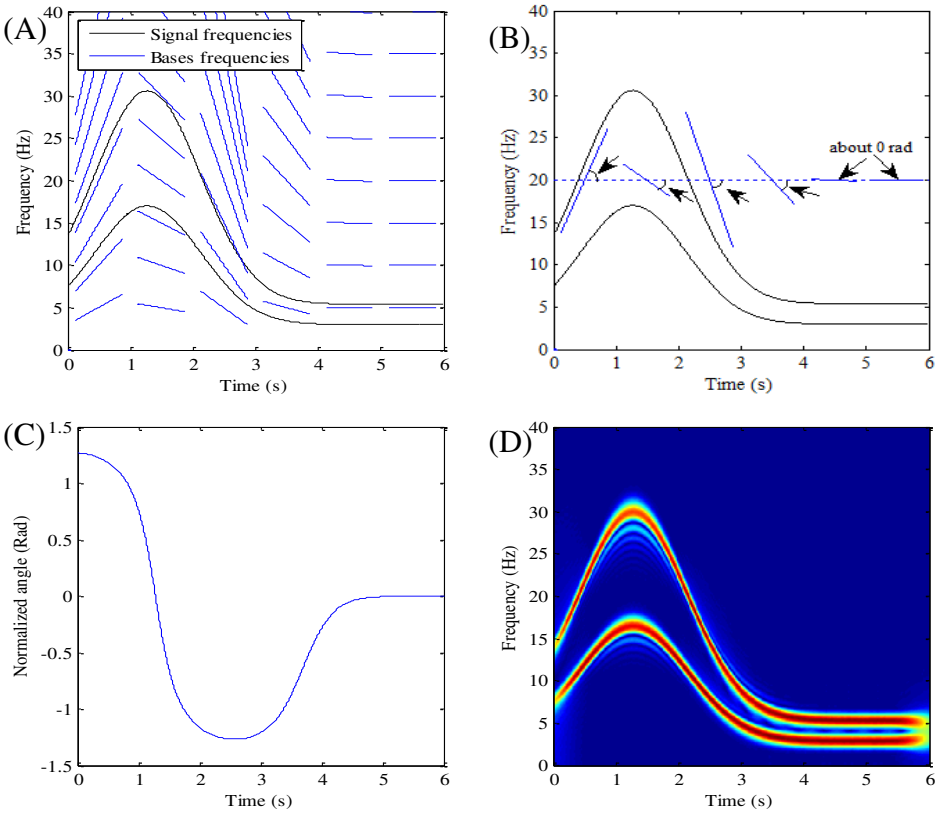

Fig. 6-4. Illustration of the VSLCT using the example signal: (A) VSLCT bases and (B) normalized angles of the bases, (C) normalized angle calculated and (D) TFR obtained by the VSLCT with window length 1.5 s

6.3 Dynamic determination of the two parameters

To effectively implement the VSLCT, two time-varying parameters, i.e., window length and normalized angle have to be determined properly. In this section, the method of determining these two parameters from vibration signal is proposed.

6.3.1 Dynamic determination of window length

According to the Heisenberg uncertainty principle, the time resolution and frequency resolution of the linear transform are limited and controlled by the window length (Gabor, 1947). A longer window length leads to better time resolution and worse frequency resolution, and a shorter window length leads to worse time resolution and better frequency resolution. In other words, the TFR value at a time-frequency point (τ, ν) represents the average energy magnitude of a time-frequency region around (τ, ν) instead of the true energy magnitude of the signal at (τ, ν). Such regions can be seen as tiles in the time-frequency plane and the TFR can be roughly represented as a tessellation formed by the

non-overlapping tiles (Baraniuk and Jones, 1992a, b, 1993b; Mann and Haykin, 1995). In the following, we firstly show the effect of window length using two TFRs with two different fixed window lengths and then illustrate how to determine the best time-varying window length in the condition that the shaft rotational frequency is known.

The example signal is used here for illustrations. A 3 s window and a 1 s window are used to show the effects of window length. The TFR tilling of the VSLCT with window length 3 s is shown in Fig. 6-5(A). The energies of the signal components fall to the tiles that the frequency trajectories of the signal components cover and such tiles are marked grey. The less grey area means the better energy concentration. In Fig. 6-5(A), there is obvious scattering energy in 0-3 s. This is because the VSLCT assumes the frequencies of the signal components are linear inside the window whereas in this case the window length is too long and the frequencies of the signal components in 0-3 s are strongly non-linear. In 3-6 s, two grey areas can be seen and each area represents one of the signal components. The two grey areas are separated by a blank area and thus the two signal components can be easily detected. This shows the energy concentration is relatively better in 3-6 s. The corresponding TFR generated with 3 s window is displayed in Fig. 6-5 (B) and it confirms our analysis. The scattering energy in 0-3 s is reflected by the 'lobes' beside the two signal frequency components and the signal components in 3-6 s are energy-concentrated.

A shorter 1 s window is then used for comparison and the corresponding TFR tiling is shown in Fig. 6-5 (C). Compared with the tiles of the 3 s window case, the tiles of the 1 s window case are longer over frequency direction and narrower over time direction, this is because a shorter window leads to worse frequency resolution and better time resolution. It can be seen that the energy concentration is better in 0-3 s, this is because the frequencies of the signal components limited by the shorter window in 0-3 s are approximately linear, which meets the linear assumption of the VSLCT. However, the energy concentration is worse in 3-6 s and this is due to the worse frequency resolution caused by the shorter window length. In 3-6 s, the areas of the two components mix with each other and it is difficult to detect the two individual components. The corresponding TFR obtained using 1 s window is shown in Fig. 6-5 (D) to verify the analysis. It can be seen that in 0-3 s, the unwanted lobes almost disappear and the two components are energy-concentrated,

however, in 3-6 s, the two components are energy-scattering and it is difficult to separate and detect them.

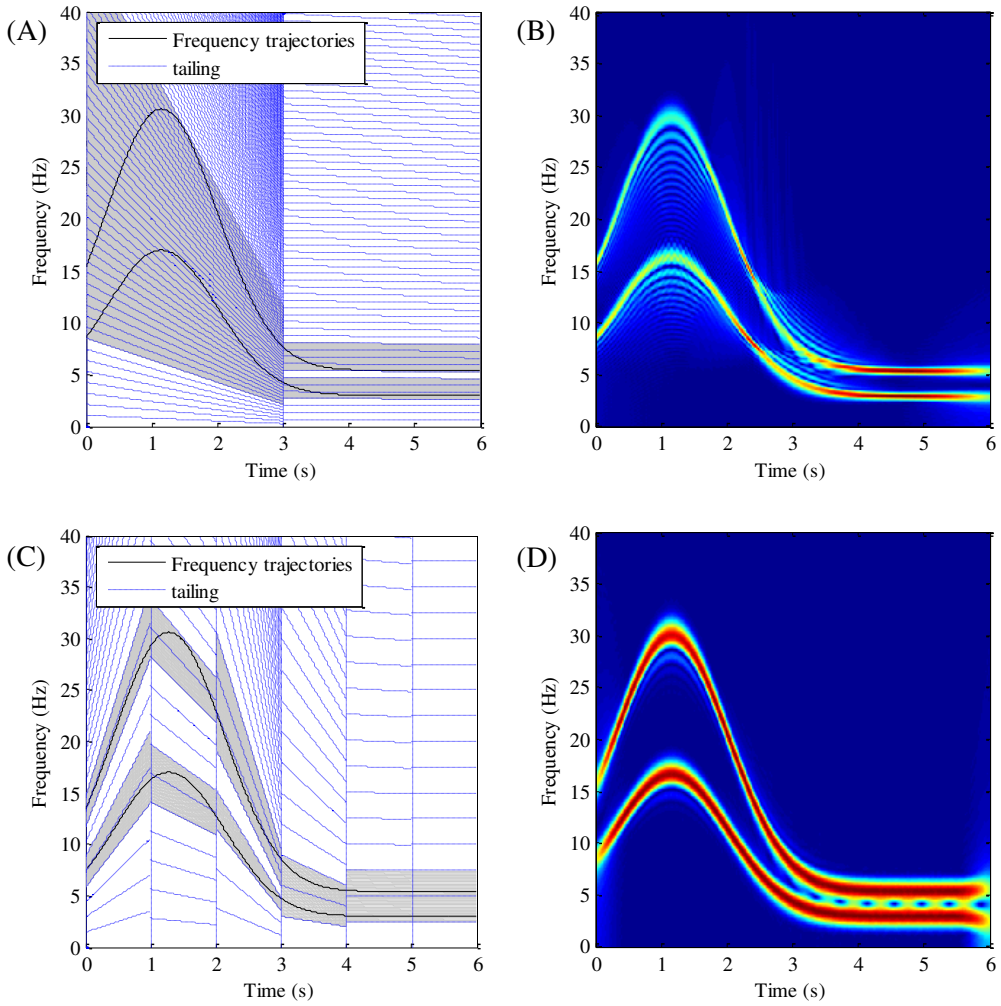

Fig. 6-5. The window length effect on the VSLCT: (A) tiling using 3 s window, (B)TFR using 3 s window, (C) tiling using 1 s window and (D)TFR uisng 1 s window

The above analysis shows a fixed window length may not provide good concentration for the whole TFR, and thus the VSLCT requires time-varying window length.

In order to determine the best window length, it is important to know how TFR varies continuously with window length. By continuously varying the window length, applying the VSLCT and calculating the absolute value, we obtain a window-length-varying TFR which can be named time-frequency-window-length representation (TFWR), represented by

$$R_{\mathrm{TFW}(\alpha(\tau))}(\tau,\nu,w)=\left|X_{\mathrm{VSLCT}(w,\alpha(\tau))}(\tau,\nu)\right|. \tag{6-49}$$

The TFWR can be illustrated as the TFRs with a series of window lengths in the time-frequency-window-length coordinate system as shown Fig. 6-6(A). From another perspective, it can also be illustrated as frequency-window-length representations (FWRs) at a series of time points as displayed in Fig. 6-6(B). As the FWR can be seen as a combination of spectrums with a series of window lengths, the best window length at a time point can be obtained by checking the energy-concentration degree of the corresponding FWR.

The FWR at time point 1.5 s is extracted from the FWRs and shown in Fig. 6-7(A). The null area in the figure is because the window length in this area do not satisfy the parameter limit (Eq.(6-47)). Null areas will also occur in other figures in this section. From Fig. 6-7(A), it can be seen that the energy concentration is best with window length 1.1 s. The spectrums have low frequency resolution with window lengths shorter than 1.1 s and we cannot even separate and detect the two signal components. As window length increases from 1.1 s, the 'lobe' interferences become stronger and energy concentration deteriorates. Based on the above analysis, an intermediate window length about 1.1 s is the best for the spectrum at time point 1.5 s.

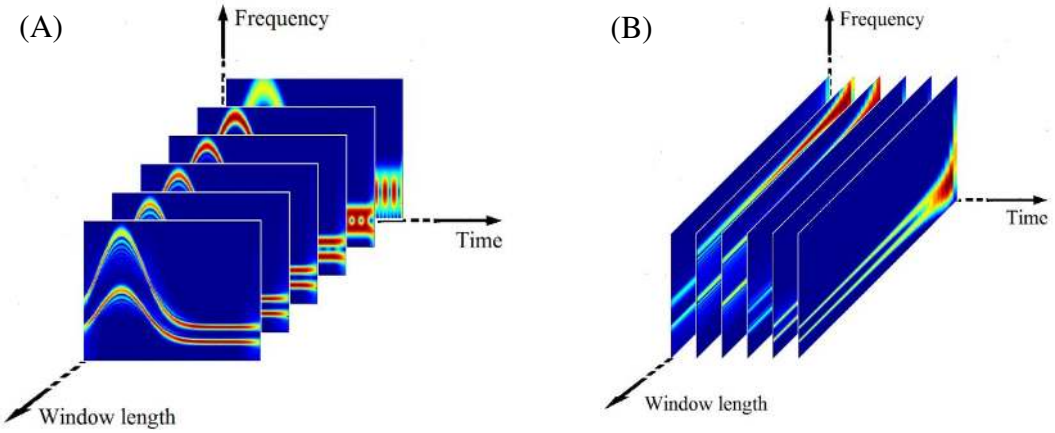

Fig. 6-6. TFWR shown as: (A)TFRs with a series of window lengths and (B) FWRs at a series of time points

However, manually examining the energy-concentration degree of every FWR is too cumbersome. In order to determine the window length automatically, an index reflecting the degree of energy concentration of spectrum is required and this index is named

concentration index. As the VSLCT is realized using digital signal processing techniques, the spectrum is composed of a set of elements with each element representing the amplitude of the corresponding frequency component. The spectrum elements are all above zero and the elements that are far greater than zero can be considered as extreme values. The spectrum having more elements with extreme values means the spectrum is energy-scattering, and thus it should lead to a concentration index with lower value. The spectrum having fewer elements with extreme values means that the spectrum is energy-concentrated, thus should lead to a higher concentration index value.

The energy concentration degree can be reflected by the sharpness of the spectrum. Many statistical index for measuring the sharpness of data have been proposed and kurtosis is one of the most widely used. The kurtosis is defined as the fourth central moment (central moment denotes the moment about mean) divided by the square of the second central moment. It outputs higher value for the set with fewer extreme values and lower value for the set with more extreme values. This is consistent with the objective of the concentration index. However, the definitions of extreme values in the concentration index and the kurtosis are different. The kurtosis considers the elements that are far greater or far smaller than the mean as the elements having extreme values and this is reflected by that the kurtosis is a function of the central moment. For this reason the kurtosis cannot be employed directly as concentration index and it should be changed. As their difference is that they measure the extreme degree of the elements with respective to mean and zero respectively, the concentration index can be defined as a raw-moment-versioned (raw moment denotes moment about zero) kurtosis with respective to frequency v. Based on the above analysis, the concentration index of an arbitrary spectrum $R(v)$ is defined as

$$C\left(R(v)\right)=\frac{E\left(R^4(v)\right)}{E^2\left(R^2(v)\right)}=\frac{\frac{1}{\mathrm{V}}\int_0^{\mathrm{V}} R^4(v)\,\mathrm{d}v}{\left(\frac{1}{\mathrm{V}}\int_0^{\mathrm{V}} R^2(v)\,\mathrm{d}v\right)^2}, \tag{6-50}$$

where $E()$ denotes the average operation and V is the right frequency bound of the TFR.

The concentration index based approach is tested on the FWR of the example signal at time instant of 1.5 s (Fig. 6-7(A)) and the result is plotted in Fig. 6-7(B). The concentration index reaches maximum of 10.32 when the window length is 1.1 s, which is

consistent with the analysis. Thus the argument of maximum, 1.1 s, is taken as the optimal window length of the spectrum at time instant 1.5 s. By successively determining the best fixed window lengths for each time point using the above concentration-index-based method, a series of optimal time-varying window lengths can be obtained for the entire time period over which the data are collected. This is done by obtaining the argument of maximum of the concentration index of the TFWR as the optimal time-varying window length for each time point τ, expressed by

$$\hat{w}(\tau) = \underset{w}{\operatorname{argmax}} \left(C\left(R_{\mathrm{TFW}(\alpha(\tau))}(\tau, \nu, w) \right) \right), \tag{6-51}$$

where $\hat{w}(\tau)$ denotes the optimal time-varying window length for time point τ.

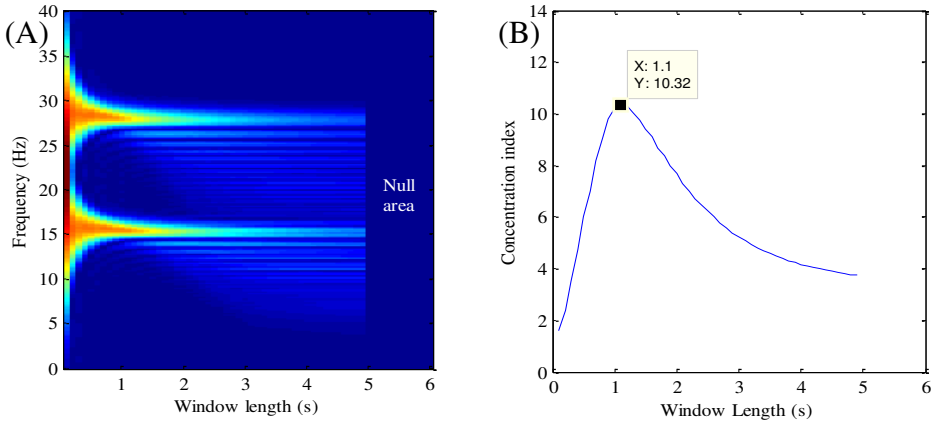

Fig. 6-7. Illustration of determining window length at a time point: (A) FWR at 1.5 s and (B) the corresponding concentration index

The dynamic determination of optimal window length is illustrated using the example signal. The concentration index of its TFWR is calculated and shown in Fig.6-8(A). The argument of maximum is extracted from the concentration index as the optimal window length as plotted in Fig.6-8(B) for each time point. It can be seen that in time period 0-3 s the calculated optimal window lengths are short, between 1 s and 2 s, and in time period of 3-6 s the obtained optimal window lengths become longer, ranging between 1.5 s and 5 s. This is consistent with the previous analysis in this subsection. The effect of the obtained time-varying optimal window lengths can be roughly illustrated using the TFR tiling shown in Fig.6-8(C). It can be seen in 0-3 s, a shorter window length fulfils the linear requirement of the VSLCT thus there is less leakage in 0-3 s. The signal components are roughly linear

and close to each other in 3-6 s, a longer window about 3 s provides good frequency resolution, therefore the two components can be separated and easily detected. The VSLCT is then applied with the obtained time-varying window lengths and the resulted TFR is shown in Fig.6-8(D). The time-varying time-frequency resolution is reflected by the fact that the components are thicker in 0-3 s and thinner in 3-6 s. Compared with the TFRs obtained by the VSLCT using fixed window length (Fig. 6-4(D), Fig. 6-5(B) and Fig. 6-5(D)), the TFR using time-varying window length has better energy concentration, the smear effect in 0-3 s is greatly avoided and the adjacent components are well separated in time period of 3-6 s.

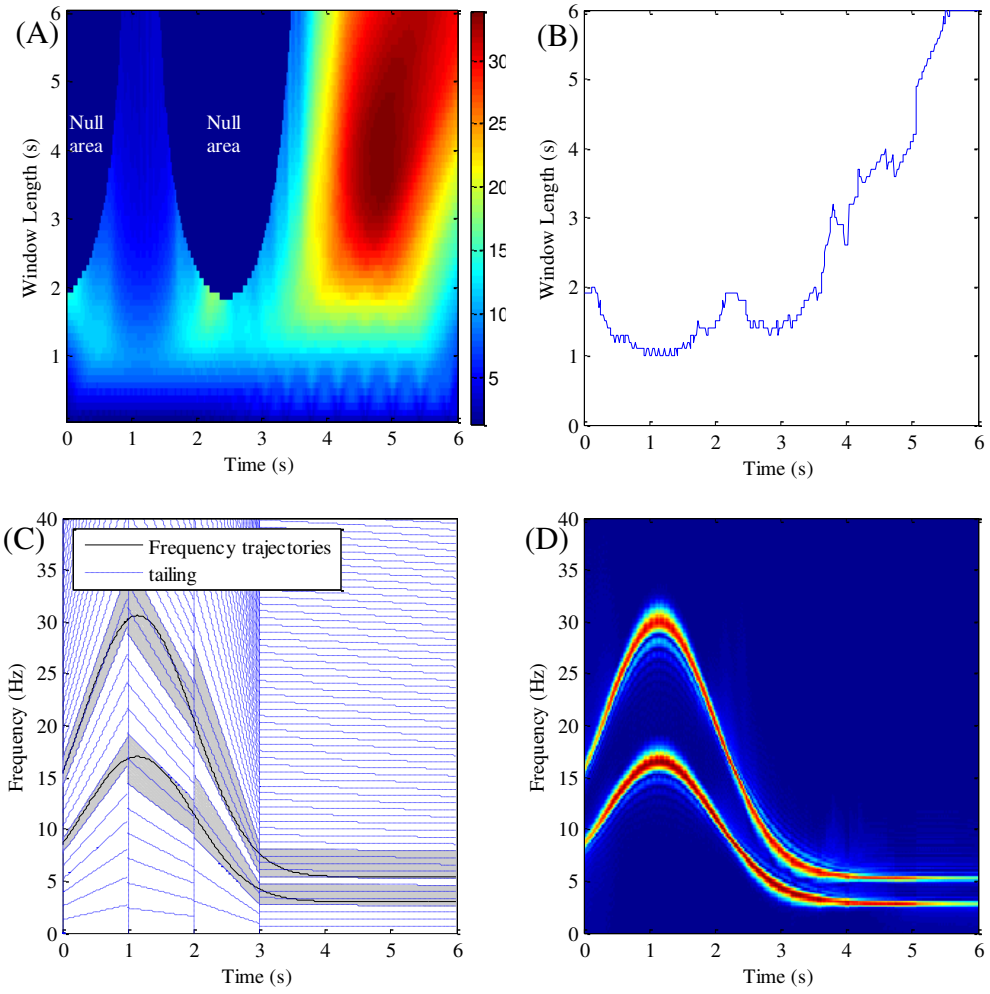

Fig.6-8. Illustration of dynamic determination of optimal time windows: (A)concentration index of time-frequency-window-length representation, (B) optimal window lengths determined based on the maximum concentration index, (C)Time-frequency tiling corresponding to the calculated optimal window lengths, and (D)TFR obtained using the optimized window lengths

6.3.2 Dynamic determination of normalized angle

The normalized angle can be calculated using the shaft rotational frequency collected from the tachometer. In the condition that the tachometer is not available, the normalized angle has to be approximated from the vibration signal and this is detailed in this subsection. Similar to the last subsection, we firstly show the effect of normalized angle using two TFRs with two different fixed normalized angles and then illustrate how to determine the time-varying normalized angle under the condition that the window length is known.

The example signal is employed again for illustration and the window length for each time point is set at the value determined in the last subsection. The normalized angle is firstly set as 0.6 rad and the corresponding tiling is shown in Fig. 6-9(A). The signal components can be separated by a blank zone in the time period of 0-1 s. However, in the time period of 1-6 s, the two frequency components are segmented by many tiles and each tile extracts part of the energy, which means the energies of the components leak to a wide frequency region. The corresponding TFR is shown Fig. 6-9(B) and it can be seen that the signal components are energy-concentrated in the first 1 s and there are obvious smear effects in 1-6 s, which supports the analysis of the tiling. The reason is that the tested normalized angle 0.6 rad is close to the true normalized angles only in the first 1 s but far from the true normalized angles from 1 s to 6 s (The true normalized angle can be found in Fig. 6-4(C)).

The normalized angle is then set as 0 rad for comparison and the corresponding tiling is shown in Fig. 6-9(C). It can be seen that the signal components are separated by a blank zone in 1-2 s and in 3-6 s and there are obvious energy leakages in the rest of the time periods. Leakage here means that the revealed signal energy is scattering in a wide region. The reason is that the pre-set inclined angle 0 rad is close to the true normalized angles in 1-2 s and in 3-6 s but it deviates from the true normalized angles in the rest of time periods. The corresponding TFR, shown in Fig. 6-9(D), confirms the above analysis and it can be seen that the two signal components have relatively good energy concentration in 1-2 s and 3-6 s.

Based on the above analysis, a normalized angle that is close to the true normalized angle leads to an energy-concentration spectrum, whereas a normalized angle that is far from the true normalized angle leads to an energy-scattering spectrum. This characteristic

is similar to window length, thus the normalized angle can also be determined using the concentration-index-based method proposed in the last subsection.

Similar to the case of the window length determination, here we introduce the time-frequency-normalized-angle representation (TFNR) and it is obtained by continuously varying the normalized angle, applying the VSLCT and calculating the absolute value. The TFNR is represented by

$$R_{\mathrm{TFN}(w(\tau))}(\tau,\nu,\alpha)=\left|X_{\mathrm{VSLCT}(w(\tau),\alpha)}(\tau,\nu)\right| \tag{6-52}$$

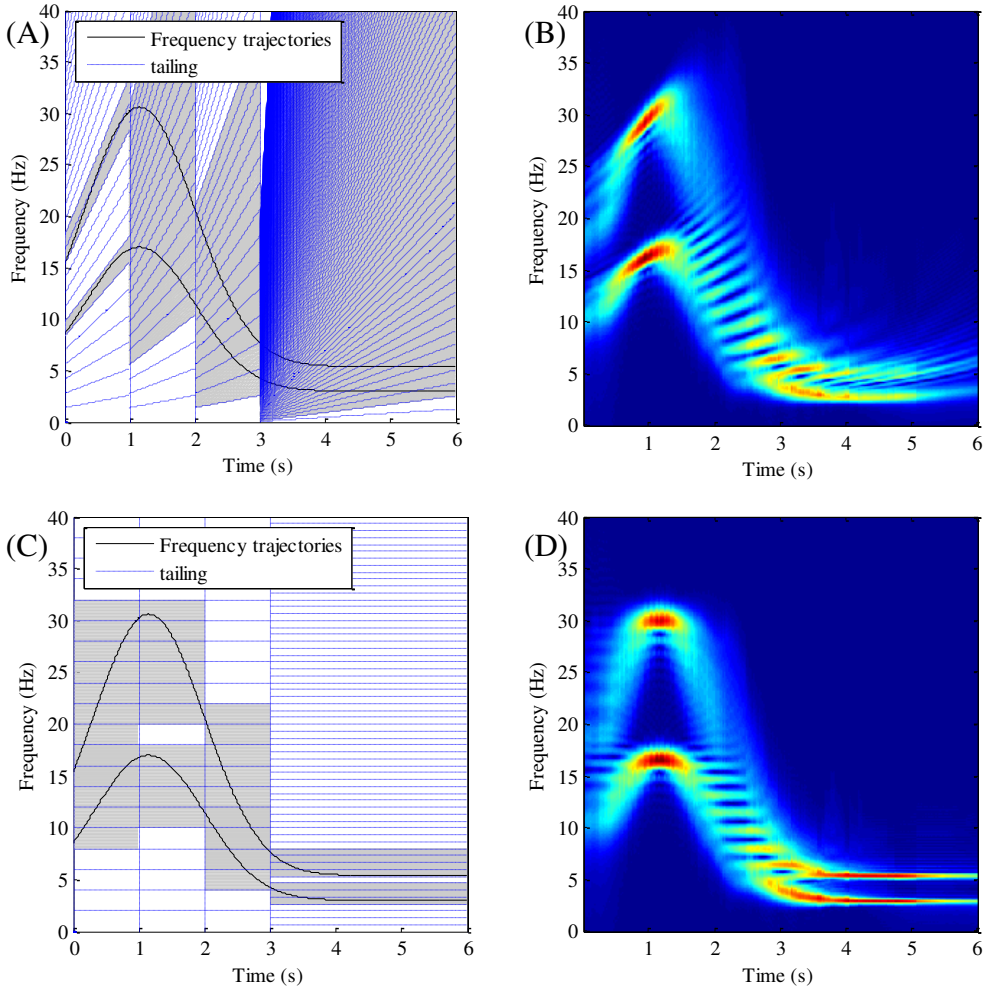

Fig. 6-9. Illustrations of normalized angle effect: (A) tiliing with normalized angle 0.6 rad, (B) TFR with normalized angle 0.6 rad, (C) tiliing with normalized angle 0 rad, (D) TFR with normalized angle 0 rad

The TFNR can be seen as a normalized-angle-varying TFR and illustrated as TFRs with a series of window lengths as shown in Fig.6-10(A), or from another perspective, illustrated as frequency-normalized-angle representations (FNRs) at a series of time points as shown in Fig.6-10(B). The FNR represents the spectrums at a time point with a series of normalized angles, thus the normalized angle at a time point can be approximated by checking the energy-concentration degree of the corresponding FNR.

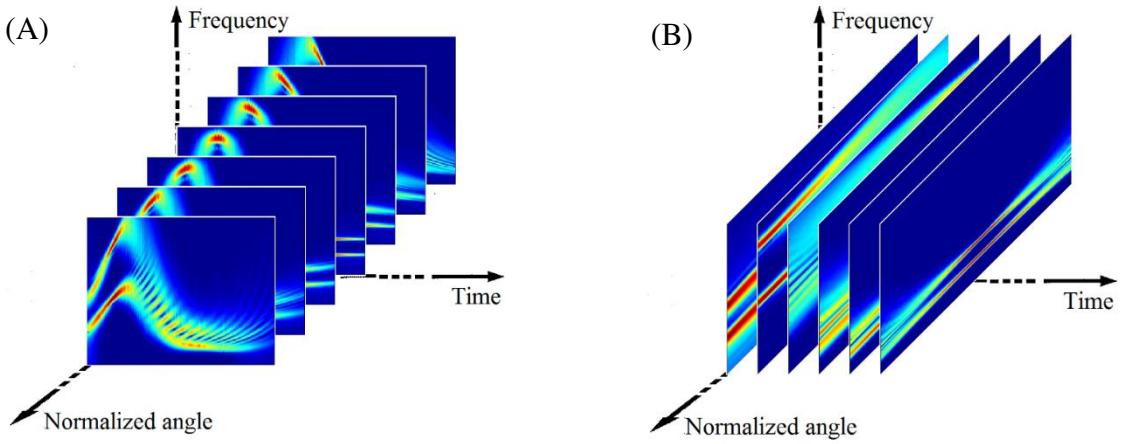

Fig.6-10. TFNR shown as: (A) TFRs with a series of normalized angles and (B) FNRs at a series of time points

The FNR at time point 0.5 s is extracted and shown in Fig. 6-11(A). It can be seen that the spectrum of the FNR with normalized angle around 1.1 rad leads to the highest energy concentration index, 12.69. As the normalized angle deviates, either increases or decreases from 1.1 rad, the energy concentration becomes worse. The concentration index of the FWR at 0.5 s, as shown in Fig. 6-11(B), reaches maximum at 1.1 rad and it declines as the normalized angle decreases or increases from 1.1 rad. The argument of maximum of the FRW at 0.5 s, 1.1 rad, is close to the true normalized angle at 0.5 s (shown in Fig. 6-4(C)). This shows that the concentration index can reveal the degree of energy concentration of a spectrum for the approximation of normalized angle. Extending this method to the whole time span, the best time-varying window length can be obtained. This is achieved by obtaining the argument of the maximum of the concentration index of the TFNR as the estimated normalized angle, expressed by

$$\hat{\alpha}(\tau) = \underset{\alpha}{\operatorname{argmax}}\left(C\left(R_{\mathrm{TFN}(w(\tau))}(\tau,\nu,\alpha)\right)\right) \tag{6-53}$$

where $\hat{\alpha}(\tau)$ denotes the approximated time-varying normalized angle.

We illustrate the procedure of dynamic determination of the time-varying normalized angle using the example signal again. The concentration index of the TFWR is determined and shown in Fig. 6-12(A). The argument of maximum is extracted and determined as the time-varying normalized angle for every time point as plotted in Fig. 6-12(B). The true normalized angle is also plotted for comparison and it can be seen the calculated normalized angles are close to the real ones. This validates the effectiveness of the energy concentration-index-guided method.

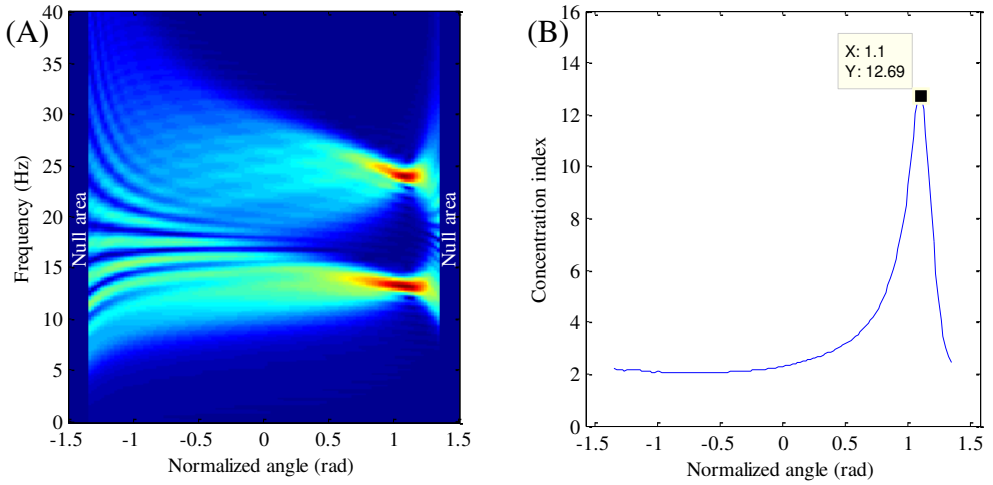

Fig. 6-11. Illustration of determining normalized angle at 1 s: (A) Frequency-normalized-angle representation, and (B) the concentration index

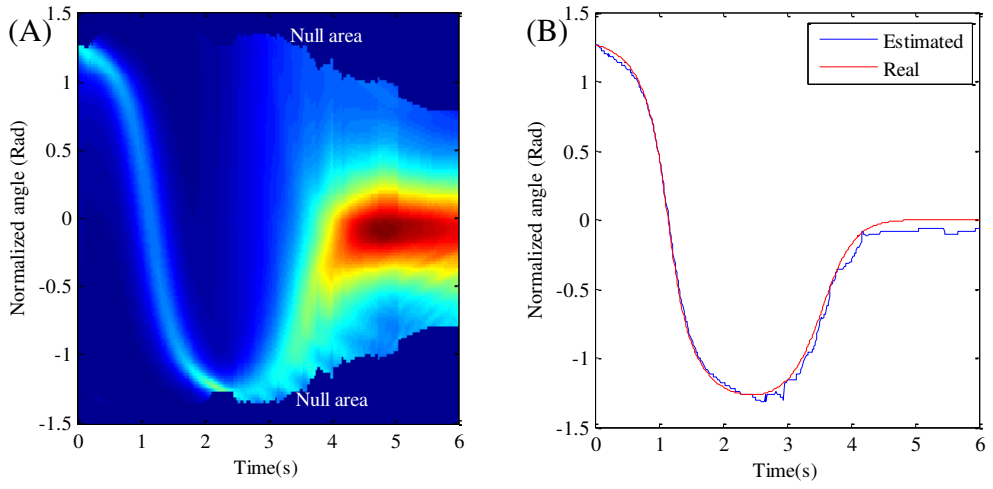

Fig. 6-12. Illustration of dynamic determination of normalized angles: (A) concentration index of the TFNR, and (B) normalized angle estimated from the concentration index

6.3.3 Simultaneous determination of window length and normalized angle

The VSLCT requires two time-varying parameters, the window length $w(\tau)$ and the normalized angle $\alpha(\tau)$. We have shown how to determine either of them assuming the other one is known already. Under certain circumstances, neither of the two may be available and both must be determined from the vibration signal simultaneously. As the TFR with best concentration is obtained by applying the VSLCT with the best window length and the right normalized angle, these two parameters can also be determined using the concentration-index-based method proposed. That is, firstly determine the time-frequency-window-length-normalized-angle representation (TFWNR) via the VSLCT, then evaluate its concentration index and finally simultaneously obtain the corresponding arguments of maximum of the concentration index as the optimal values of the two parameters.

This method is detailed step by step as follows:

The TFWNR is firstly generated via the VSLCT, represented by

$$R_{\mathrm{TFWN}}\left(\tau,\nu,w,\alpha\right)=\left|X_{\mathrm{VSLCT}(w,\alpha)}\left(\tau,\nu\right)\right| \tag{6-54}$$

The corresponding concentration index of the TFWNR is calculated, expressed by

$$K\left(R_{\mathrm{TFWN}}\left(\tau,\nu,w,\alpha\right)\right)=\frac{E\left(R_{\mathrm{TFWN}}^{4}\left(\tau,\nu,w,\alpha\right)\right)}{E^{2}\left(R_{\mathrm{TFWN}}^{2}\left(\tau,\nu,w,\alpha\right)\right)}=\frac{\frac{1}{\mathrm{V}}\int_{0}^{\mathrm{V}}R_{\mathrm{TFWN}}^{4}\left(\tau,\nu,w,\alpha\right)\mathrm{d}\nu}{\left(\frac{1}{\mathrm{V}}\int_{0}^{\mathrm{V}}R_{\mathrm{TFWN}}^{2}\left(\tau,\nu,w,\alpha\right)\mathrm{d}\nu\right)^{2}} \tag{6-55}$$

The best window length and normalized angle for each time point are simultaneously obtained by evaluating the corresponding arguments of maximum of the concentration index, expressed by

$$\hat{w}\left(\tau\right)=\underset{w}{\mathrm{argmax}}\left(C\left(R_{\mathrm{TFWN}}\left(\tau,\nu,w,\alpha\right)\right)\right) \tag{6-56}$$

and

$$\hat{\alpha}\left(\tau\right)=\underset{\alpha}{\mathrm{argmax}}\left(C\left(R_{\mathrm{TFWN}}\left(\tau,\nu,w,\alpha\right)\right)\right) \tag{6-57}$$

Finally the TFR with best concentration is obtained by applying the VSLCT with the determined window length and normalized angle, expressed by

$$R_{\mathrm{TF}(\hat{w}(\tau),\hat{\alpha}(\tau))}(\tau,\nu)=\left|X_{\mathrm{VSLCT}(\hat{w}(\tau),\hat{\alpha}(\tau))}(\tau,\nu)\right| \tag{6-58}$$

This concentration-index-guided approach is tested on the example signal and the determined parameters are plotted in Fig. 6-13. The determined window length is shorter in 0-3 s and longer in 3-6 s as shown in Fig. 6-13(a), which is consistent with the previous analysis of window length. The determined normalized angle is close to the real normalized angle as shown in Fig. 6-13(B). The robustness of this concentration-index-guided approach to noise is also tested here. The absolute errors of the determined parameters, expressed as percentages of the full length of the range of the corresponding parameter (i.e., 6 s for window length and π for normalized angle), under different SNRs are plotted in Fig. 6-14. It can be seen this approach has good accuracy (error < 3%) for SNR ≥ 0 dB and fair accuracy (error < 10%) for SNR between -3 dB and 0 dB, showing that the proposed approach is robust to noise.

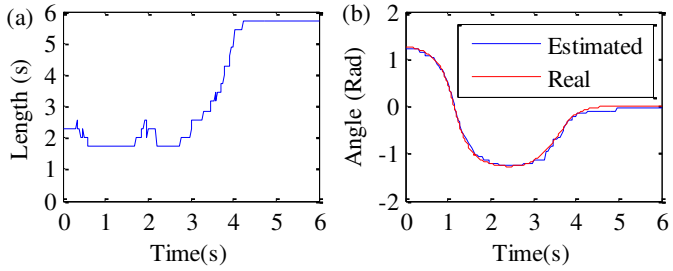

Fig. 6-13. Determined optimal parameters: (a) window length and (b) normalized angle

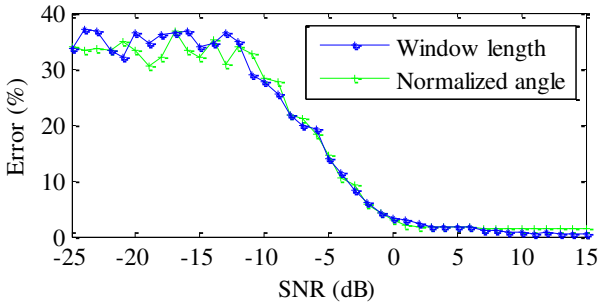

Fig. 6-14. Error of the determined parameters under different SNR levels

6.4 Simulation evaluations

The VSLCT is capable of processing mono-component frequency-modulated non-vibration signal because such signal can be seen as a mono-component vibration signal only containing the component of shaft rotational frequency. Therefore, the VSLCT is

evaluated using one mono-component frequency-modulated signal and one general multi-component non-stationary vibration signal.

6.4.1 Mono-component signal

A synthetic mono-component frequency-modulated signal is introduced in this subsection, represented as

$$x_{\text{mono}}(t) = \sin\left(2\pi\int_0^t f_1(\tau)\,\mathrm{d}\tau\right) + n(t) \tag{6-59}$$

where $n(t)$ is Gaussian white noise and the signal frequency $f_1()$ is expressed as

$$f(t) = -0.675t^3 + 0.975t^2 + 11.5t + 15\,. \tag{6-60}$$

The signal to noise ratio (SNR) is set as 0 dB. The signal length is 4 s and the sampling rate is 100 Hz. The signal waveform and its frequency trajectory are shown in Fig. 6-15(a) and (b), respectively. The proposed VSLCT method is then applied to reveal the signal time-frequency structure and the resulted TFR is shown in Fig. 6-16 (a). Compared with the true signal trajectory, the VSLCT clearly reveals the signal time-frequency structure.

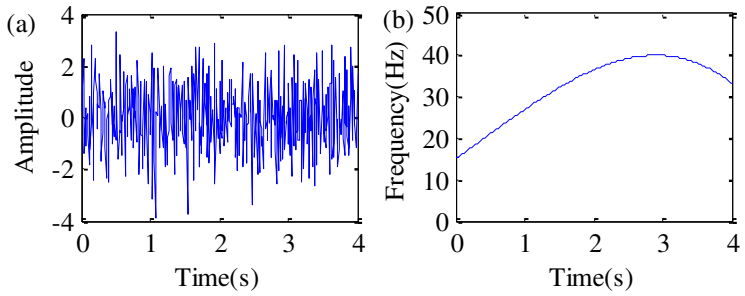

Fig. 6-15. Synthetic mono-component signal: (a) waveform and (b) frequency trajectory

To evaluate the performance of the proposed VSLCT method, a comparison study is carried out. Some traditional methods and advanced methods are employed. They are the the STFT (Allen, 1977), ZAM (Zhao et al., 1990), PCT (Peng et al., 2011), GLCT (Yu and Zhou, 2016), SET (Yu et al., 2017), RM (Auger and Flandrin, 1995), and SST (Daubechies et al., 2011) . Their results are shown in Fig. 6-16(b-h). Some of the compared methods require the user to provide window lengths and they are all set as 0.7 s. The STFT suffers from smear effect and only a coarse time frequency trend can be revealed as shown in Fig. 6-16(b). As a representation of the advanced bilinear distribution, the ZAM is employed and the result is presented in Fig. 6-16(C). It can be seen that the ZAM cannot reveal the

signal frequency in the first second. The PCT and GLCT are employed as representations of advanced linear transform. Their results are shown in Fig. 6-16(d) and (e) respectively. The PCT has less smear effect than the STFT, however, its energy concentration is still worse than the VSLCT. As shown in Fig. 6-16(e), the GLCT reveals the signal frequency trajectory but the TFR has high background noise and it has bad energy concentration in the first second. The SET, RM and SST are utilized as representations of advanced TFR-data-remapping method and their results are shown in Fig. 6-16(f-h) respectively. It can be seen these three methods successfully detect the signal component but the revealed frequency trajectories either break or are not clear in the first second.

To quantitatively evaluate the noise robustness of the VSLCT on the mono-component signal, the frequency estimation error is employed as an indicator. The frequency is firstly estimated as the arguments of maxima of the corresponding TFR. The estimation errors are then calculated as a percentage of the true signal frequency and it is plotted in Fig. 6-17. It can be seen as the SNR rises, the error generally shows a decreasing trend. For most applications, if the error of estimation is greater than 10%, the estimated frequency is too inaccurate and it can be considered that the frequency is not detected. Therefore, we consider 10% as the error threshold for frequency detection. From Fig. 6-17, it can be seen that for the signal with SNR $\leq$ -5 dB, the errors of all the methods are above 10%, thus it is considered that no method can detect the frequency of the signal with SNR $\leq$ -5 dB. For this reason, it is meaningless to discuss which method performs relatively better below the SNR -5 dB. For SNR $\geq$ -5 dB, the errors of the VSLCT are lower than 10%. For the signals with SNR between -5 dB and 3 dB, the VSLCT has the best performance among all the methods. For SNR $\geq$ 3 dB, the error of the VSLCT is below 1% and the VSLCT performance is either better than the other methods or comparable to them. The above analysis indicates that the VSLCT is generally robust to noise compared with the other methods in analyzing the mono-component signal.

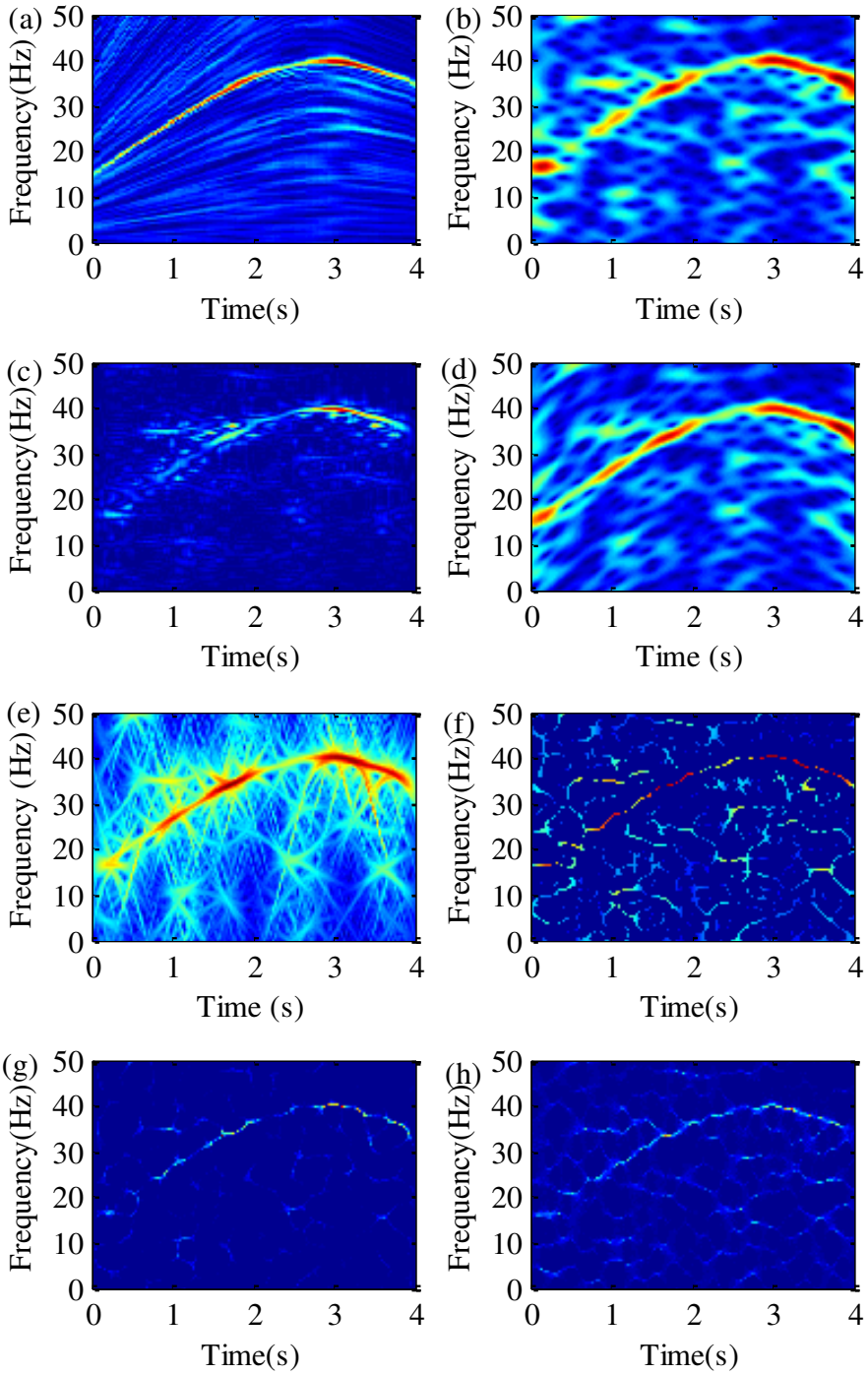

Fig. 6-16. TFRs of the mono-component signal using: (a) VSLCT, (b) STFT, (c) ZAM, (d) PCT, (e) GLCT, (f) SET, (g) RM and (h) SST

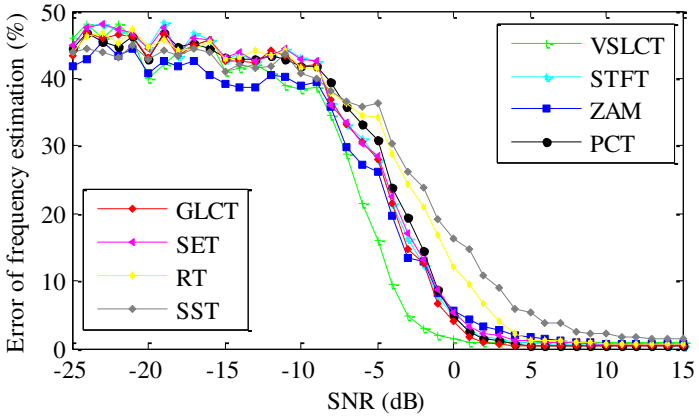

Fig. 6-17. Frequency estimation errors of the mono-component signals

The efficiency of a time-frequency method is important for online applications, thus the efficiency of the VSLCT is evaluated. The configuration of the computer used is given as follows: Intel® i7-3615QM 2.3 GHz CPU, 8 GB DDR3 RAM, 256 GB flash storage. The software used is MATLAB® R2014a. The computational time in processing this mono-component synthetic signal is listed in Table 6-1. It can be seen that the VSLCT is faster than the PCT, GLCT and RM, but slower than other methods. The STFT is the fastest method and the computational time of the VSLCT is about four times of that of the STFT method. Nevertheless, the absolute time is not long (only 0.651 s) and this should be acceptable for most applications.

Table 6-1 Computational time

Method	VSLCT	STFT	ZAM	PCT
Time (s)	0.651	0.153	0.577	0.764
Method	GLCT	SET	RM	SST
Time (s)	0.799	0.163	0.974	0.171

6.4.2 Multi-component vibration signal

In this subsection, we test the proposed VSLCT on the synthetic multi-component vibration signal. This signal employs the shaft rotational frequency of the example signal and contains three frequency components, which are the shaft rotational frequency, its 1.8 multiples and 2.6 multiples. This synthetic multi-component vibration signal is represented by

$$x_3(t)=\sum_{n=1}^{3}\sin\left(k_n\int_0^t 2\pi f_{\text{shaft}}(\tau)\,\mathrm{d}\tau\right)+n(t)\ , \tag{6-61}$$

where k_1=1, k_2=1.8 and k_3=2.6. The SNR is 1 dB and the sampling rate is 100 Hz.The signal waveform is potted in Fig. 6-18(a) and the ideal frequency trajectories of the signal components are shown in Fig. 6-18(b).

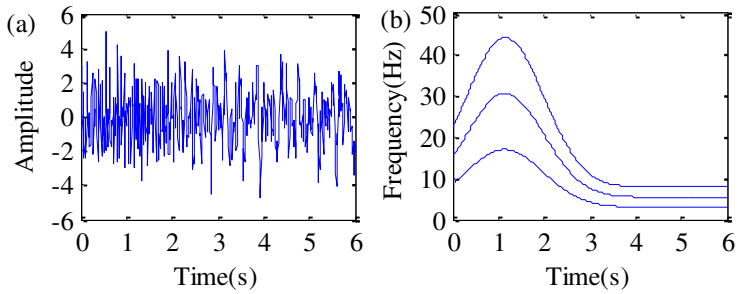

Fig. 6-18. Synthetic multi-component signal: (a) waveform and (b) frequency trajectories

The VSLCT result is shown in Fig. 6-19(a). By comparing with the ideal frequency trajectories of the signal components, it can be found the VSLCT precisely reveal the frequencies of the three signal components. The VSLCT is then compared with the same methods that are employed in the last subsection and the results are shown in Fig. 6-19(b-h). The window lengths are set as 1 s for the methods requiring windows. The STFT, shown in Fig. 6-19 (b), only reveals a smeared signal frequency trend. The ZAM, as presented in Fig. 6-19(c), reveals the signal components in the last three seconds. However, it cannot uncover the signal components in the first three seconds due to cross-term interference. The PCT result is shown in Fig. 6-19(d) and it can be seen that the resulted TFR still suffers from smear effect. The TFR obtained by the GLCT, as shown in Fig. 6-19(e), clearly uncovers the signal frequencies, but the signal components are not well separated in 3-6 s. The SET roughly reveals the signal frequency trajectory trend as shown in Fig. 6-19(f), however, the signal frequency trajectories are broken. The RM and the SST, as shown in Fig. 6-19(g) and (h) respectively, only reveal a blur frequency trend.

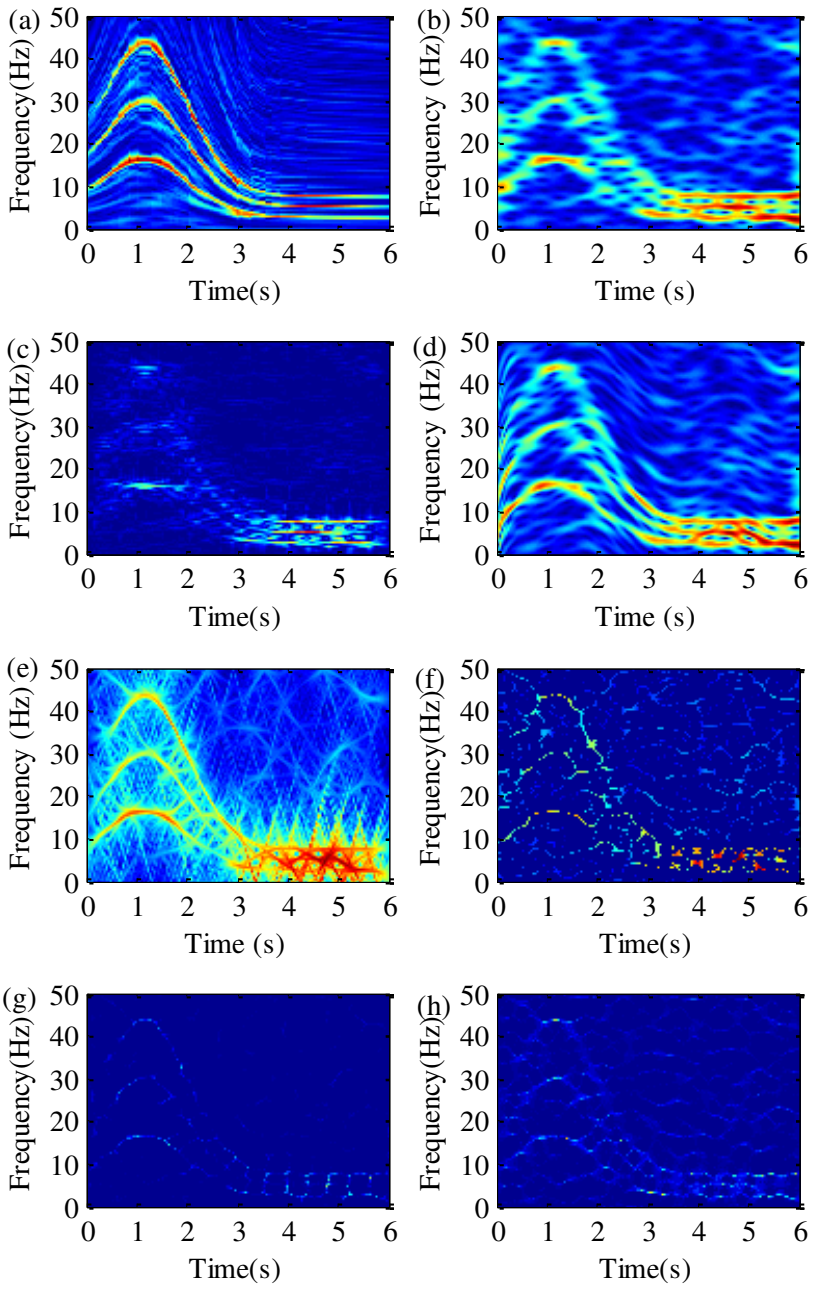

Fig. 6-19. TFRs of the multi-component signal using: (a) VSLCT, (b) STFT, (c) ZAM, (d) PCT, (e) GLCT, (f) SET, (g) RM and (h) SST

Similar to the last subsection, we quantitatively evaluate the noise robustness of the VSLCT in analyzing the multi-component signal using the frequency estimation error as an indicator. As the signal contains three frequency components. The frequency estimation error is defined as the average of the frequency estimation errors of the three components. The estimated frequency of each frequency component is calculated as the arguments of

maxima of the corresponding TFR restricted in a local region around the corresponding frequency component. The average estimation error is represented by

$$e = \frac{1}{3}\sum_{i=1}^{3}\frac{1}{6}\int_{\tau=0}^{\tau=6}\left|f_{i(\mathrm{est})}(\tau) - f_i(\tau)\right| / f_i(\tau)\,\mathrm{d}\tau\,. \tag{6-62}$$

where $f_{i(\mathrm{est})}(\tau)$ denotes the estimated frequency of the *i*th component, expressed by

$$\begin{aligned} &f_{i(\mathrm{est})}(\tau) = \underset{v}{\mathrm{argmax}}\left(\left|X(\tau, v)\right|\right), \\ &\text{for } i = 1, v \in \left(0.6 f_{\mathrm{shaft}}(\tau), 1.4 f_{\mathrm{shaft}}(\tau)\right), \\ &\text{for } i = 2, v \in \left(1.4 f_{\mathrm{shaft}}(\tau), 2.2 f_{\mathrm{shaft}}(\tau)\right), \\ &\text{for } i = 3, v \in \left(2.2 f_{\mathrm{shaft}}(\tau), 3 f_{\mathrm{shaft}}(\tau)\right). \end{aligned} \tag{6-63}$$

Using this method, the average frequency estimation errors are plotted in Fig. 6-20. Similar to the robustness analysis on the mono-component signal, the estimation error 10% is again used as the threshold for frequency detection. Below the SNR -8 dB, the estimation errors of all the methods are greater than that threshold and therefore we neglect the discussion about the performances of the tested methods below that SNR. For SNR ≥ -8 dB, the error of the VSLCT is lower than all the compared methods, showing that the VSLCT is more robust to noise than the other methods in analyzing the multi-components signals.

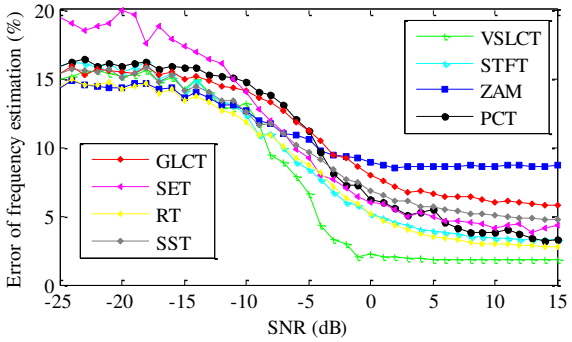

Fig. 6-20. Frequency estimation errors of the multi-component signals

6.5 Experimental tests

In this section, the effectiveness of the VSLCT is demonstrated in diagnosing planetary gearbox fault using a wind turbine drivetrain test rig.

6.5.1 Experimental setup

The wind turbine drivetrain test rig includes an AC drive motor for powering the gearboxes, a two-stage fixed-shaft gearbox, a two-stage planetary gearbox and a magnetic brake for loading as shown in Fig. 4-7. The configuration parameters of the fixed-shaft gearbox and planetary gearbox are listed in Table 6-2 and Table 6-3 respectively.

To simulate gear faults, two faulty sun gears are used: one with wear damage on every tooth to be mounted in stage 1 of the planetary gearbox, and the other with a chipped tooth to be installed in stage 2 of the planetary gearbox as shown in Fig. 3-14(A) and (B) respectively. Three tests are carried out: healthy sun gears (normal sun gears are used for the both stages of the planetary gearbox), sun gear wear (stage 1 sun gear is worn and stage 2 sun gear is healthy), sun gear chipping (stage 2 sun gear has a chipped tooth but stage 1 sun gear is normal).

The experimental data are collected from accelerometers mounted on top of the casings of the planetary gearbox's first stage and second stage at a sampling frequency of 20 kHz. To validate the proposed method in diagnosing wind turbine planetary gearbox fault from non-stationary signals, the vibration signals are collected during a speed-varying process. The motor rotational frequency increases approximately from 40 Hz to 60 Hz and then drops to 40 Hz. Accordingly, the rotating speed of the blades increases from 0.324 Hz to 0.486 Hz and then drops to 0.324 Hz. This should cover much of rotational speed range of wind turbine blades. A load of 13.2 Nm is generated by a magnetic brake and is applied to the output shaft of the planetary gearbox's second stage. The rotational speed is measured by a tachometer mounted on the shaft connected to the motor. The characteristic frequencies of the planetary gearbox are calculated according to the configuration of both the fixed shaft and planetary gearboxes using the formulas given in Appendix B (Feng and Zuo, 2012) as listed in Table 6-4. As the running speed is time-varying, the characteristic frequencies are represented as the multiples of the instantaneous rotational frequency of the drive motor f_d.

Table 6-2 Configuration parameters of the fixed-shaft gearbox

Gear		Drive	Driven
Number of gear teeth	Stage 1	32	80
	Stage 2	40	72

Table 6-3 Configuration parameters of the planetary gearbox

Gear		Ring gear	Planet gear	Sun gear
Number of gear teeth	Stage 1	100	40 (4)	20
	Stage 2	100	36 (4)	28

Note: the number of planet gears is indicated in the parenthesis

Table 6-4 Characteristic frequency of the planetary gearbox

Frequency	Stage 1	Stage 2
Sun gear fault	$f_{\text{sun1}} = (20/27) f_{\text{d}}$	$f_{\text{sun2}} = (175/1512) f_{\text{d}}$
Planet gear fault	$f_{\text{planet1}} = (5/54) f_{\text{d}}$	$f_{\text{planet2}} = (175/7776) f_{\text{d}}$
Ring gear fault	$f_{\text{ring1}} = (4/27) f_{\text{d}}$	$f_{\text{ring2}} = (7/216) f_{\text{d}}$
Carrier rotating	$f_{\text{carrier1}} = (1/27) f_{\text{d}}$	$f_{\text{carrier2}} = (7/864) f_{\text{d}}$
Sun gear rotating	$f_{\text{sunrot1}} = (2/9) f_{\text{d}}$	$f_{\text{sunrot2}} = (1/27) f_{\text{d}}$
Meshing	$f_{\text{mesh1}} = (100/27) f_{\text{d}}$	$f_{\text{mesh2}} = (175/216) f_{\text{d}}$

6.5.2 Healthy planetary gearbox

Fig. 6-21(A-C) show the normal planetary gearbox vibration signal waveform, its frequency spectrum and the shaft speed profile. In the speed profile, it can be seen that the speed of the drive motor increases from 40 Hz to 60 Hz and then drops to 40 Hz. According to the relationships of the meshing frequencies between the two stages of the planetary gearbox and motor rotational frequency (i.e., $f_{\text{mesh1}} = (100/27) f_{\text{d}}$ and $f_{\text{mesh2}} = (175/216) f_{\text{d}}$ as shown in Table 6-4), the meshing frequency of the planetary gearbox stage 1 increases approximately from 148 Hz to 222 Hz and then drops to 148 Hz. The meshing frequency of the planetary gearbox stage 2 increases approximately from 32 Hz to 48 Hz and then drops to 32 Hz. As the key task of planetary gearbox fault diagnosis is identifying the frequencies of the sidebands around the meshing frequency (Feng and Liang, 2014b; Feng et al., 2015a; Feng et al., 2016c), the focus should be on the frequency band 0-400 Hz which covers enough sideband frequencies of the meshing frequencies of

the two stages. The Fourier spectrum of the signal, shown in Fig. 6-21(B), suffers from spectral smearing problem. Although some peaks appear in the spectrum, it is challenging to identify them under a time-varying running speed condition. Fig. 6-22 shows the time-frequency distribution of the vibration signal of the healthy planetary gearbox obtained by the VSLCT. As the VSLCT is smearing-free, the components with time-varying frequency can be clearly revealed. The characteristic frequencies are calculated according to the characteristic frequency table (Table 6-4) and motor speed. With the characteristic frequencies calculated, the time-frequency components can be identified. As displayed in Fig. 6-23, the dominant frequencies are the drive motor rotating frequency f_d, its harmonics and the planetary gearbox stage 1 gear meshing frequency f_{mesh1}. No matter the gearbox is healthy or faulty, the drive motor will rotate and gears will mesh thus generating the meshing frequency, motor rating frequency and its harmonics, therefore these components do not indicate a faulty condition.

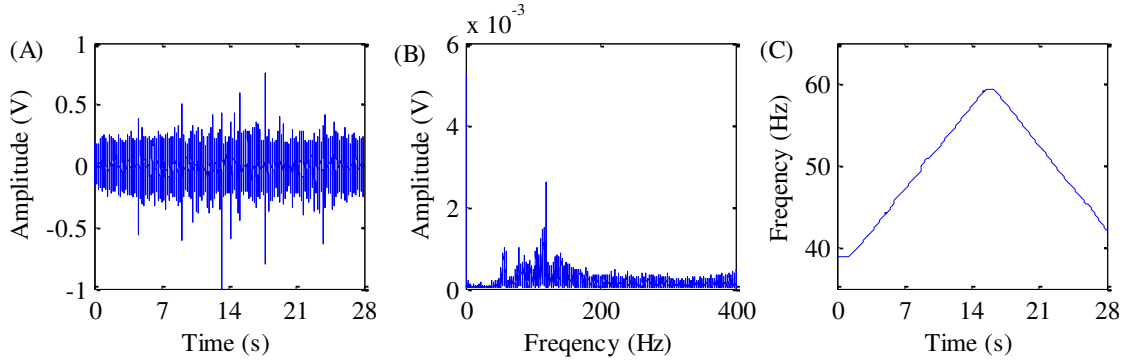

Fig. 6-21. Healthy planetary gearbox: (A) vibration signal, (B) frequency spectrum of vibration signal and (C) motor speed

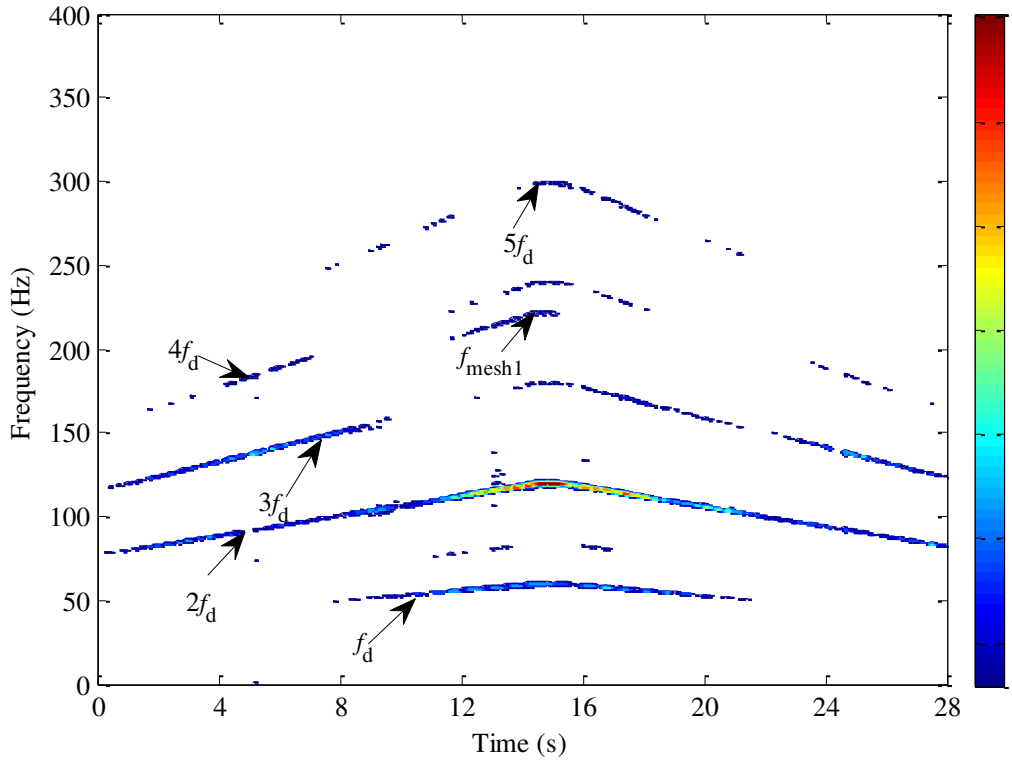

Fig. 6-22. TFR of the healthy planetary gearbox vibration signal

6.5.3 Detection of sun gear wear

Now the proposed method is evaluated in diagnosing the sun gear wear fault. Fig. 6-23(A-C) shows the vibration signal waveform and its Fourier spectrum, as well as the associated drive motor speed. From Fig. 6-23 (C), it can be seen that similar to the healthy planetary gearbox case, the motor speed is increasing from 40 Hz to 60 Hz and then drops to 40 Hz. It is logic to focus on the frequency band 0-400 Hz again. Due to the varying speed, the signal Fourier spectrum (Fig. 6-23 (B)) has smearing problem again and one could not identify any fault features, such as the sidebands of the meshing frequency. Therefore the proposed VSLCT method is applied to attain the TFR shown in Fig. 6-24. Similar to the healthy planetary gearbox case, the meshing frequency of the planetary gearbox stage 1 f_{mesh1}, the motor rotating frequency f_d and its harmonics dominate the TFR. However, apart from these, several other strong frequency components also appear in the TFR. They are the difference between the meshing frequency and the second harmonic of the sun gear fault characteristic frequency of stage 1 f_{mesh1}-$2f_{sun1}$, the sum of the meshing frequency and the second harmonic of the sun gear fault characteristic frequency of stage

1 f_{mesh1}+2f_{sun1}, and the difference between the meshing frequency and the sum of the second harmonic of the sun gear fault characteristic frequency and the second harmonic of the sun gear rotating frequency f_{mesh1}-(2f_{sun1}+2$f_{sunrot1}$). The revealed sidebands are all associated with the sun gear fault of planetary gearbox stage 1 and have pronounced amplitudes, indicating that the planetary gearbox stage 1 has a sun gear fault. This result is consistent with the experimental setting of faulty sun gear.

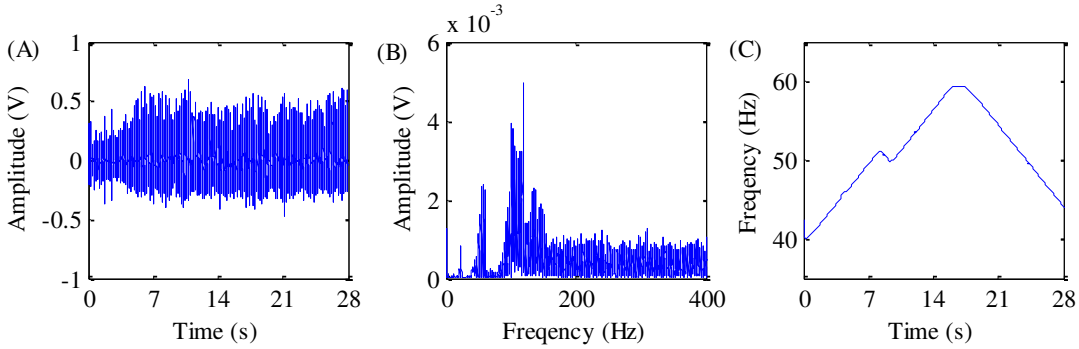

Fig. 6-23. Planetary gearbox with stage 1 sun gear wear fault: (A) vibration signal, (B) frequency spectrum of vibration signal and (C) motor speed

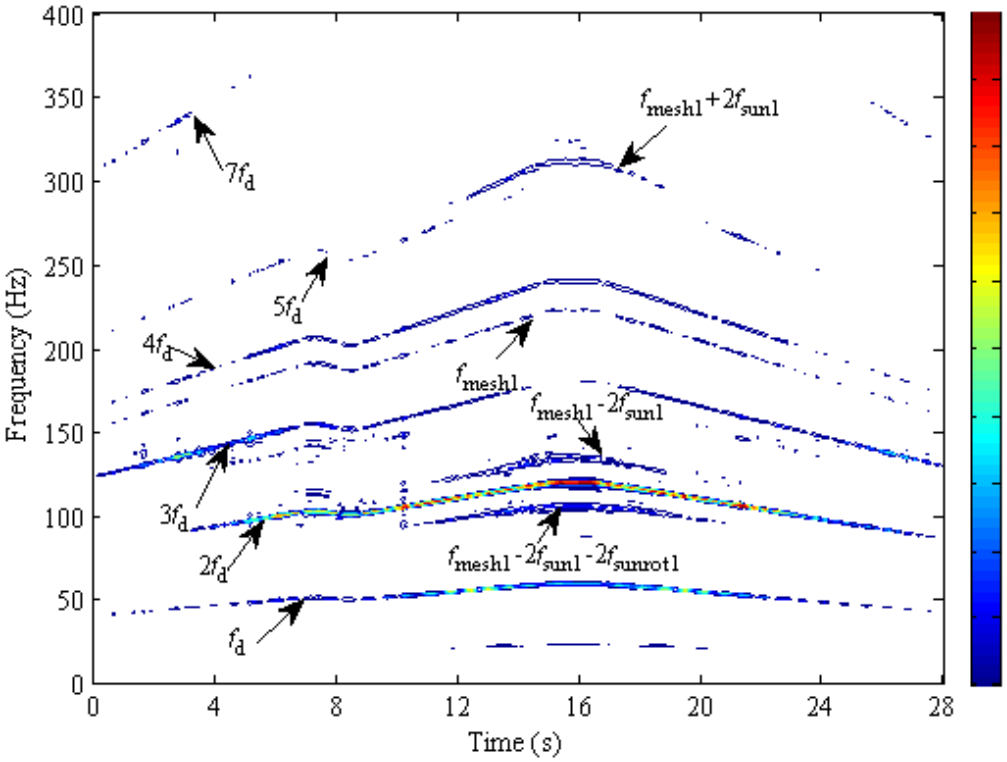

Fig. 6-24. TFR of the vibration signal of stage 1 sun gear wear fault

6.5.4 Detection of sun gear chipping

This subsection demonstrates the effectiveness of the VSLCT method in detecting sun gear chipping at the planetary gearbox stage 2. The associated vibration signal and its Fourier spectrum, as well as the drive motor speed are presented in Fig. 6-25(A-C), respectively. From Fig. 6-25(C), it can be seen that the motor speed increases approximately from 40 Hz to 60 Hz and then drops to 40 Hz again. According to the relationship between the meshing frequency of the planetary gearbox stage 2 and the motor rotational frequency (i.e., $f_{\text{mesh2}} = (175/216) f_{\text{d}}$ as shown in Table 6-4), the meshing frequency of the planetary gearbox stage 2 increases approximately from 32 Hz to 48 Hz and then drops to 32 Hz. Accordingly the frequency band of interest is 0-80 Hz, which covers enough possible sidebands frequencies of meshing frequency of planetary gearbox stage 2. The signal spectrum (Fig. 6-25(B)) does not provide sufficient information related to the chipping fault. To reveal the chipping fault, the VSSTFT method is once again applied to analyze the experimental data. The obtained TFR is shown in Fig. 6-26, where the main component is the motor rotating frequency f_{d}, which is generated by the rotations of the drive motor, thus does not provide any information related to the fault. However, there are still some other dominant components including the difference between the meshing frequency and the sun gear rotating frequency of stage f_{mesh2}-f_{sunrot2}, the sum of the meshing frequency and the sum of the third harmonic of sun gear fault characteristic frequency and the sun gear rotating frequency f_{mesh2}+3f_{sun2}+f_{sunrot2} and the difference between meshing frequency and the sum of the third harmonic of sun gear fault characteristic frequency and the second harmonic of sun gear rotating frequency f_{mesh2}-(3f_{sun2}+2f_{sunrot2}). They are associated with the sun gear fault characteristic frequency of stage 2. This is sign of a fault on the sun gear of stage 2 which is again consistent with the condition of the stage 2 sun gear used in the experiment.

The findings of the above three cases are expected and show that the VSLCT method can be used to detect gear fault of planetary gearbox effectively in a time-varying speed condition.

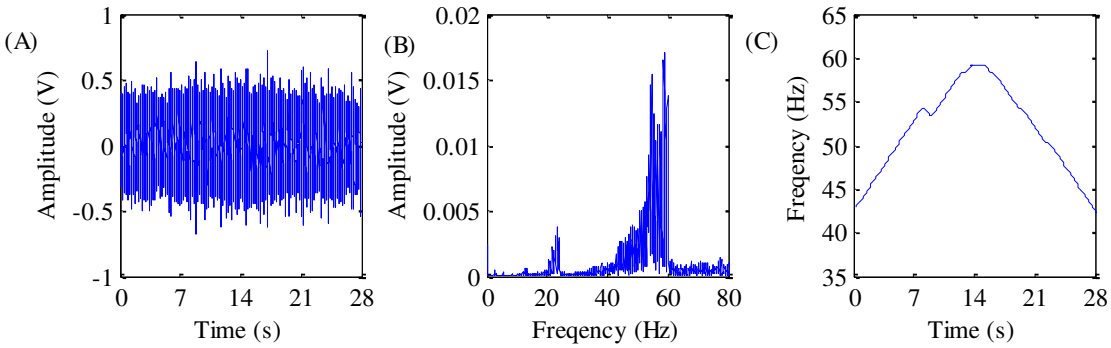

Fig. 6-25. Planetary gearbox with stage 2 sun gear chipping fault: (A) vibration signal, (B) frequency spectrum of vibration signal and (C) motor speed

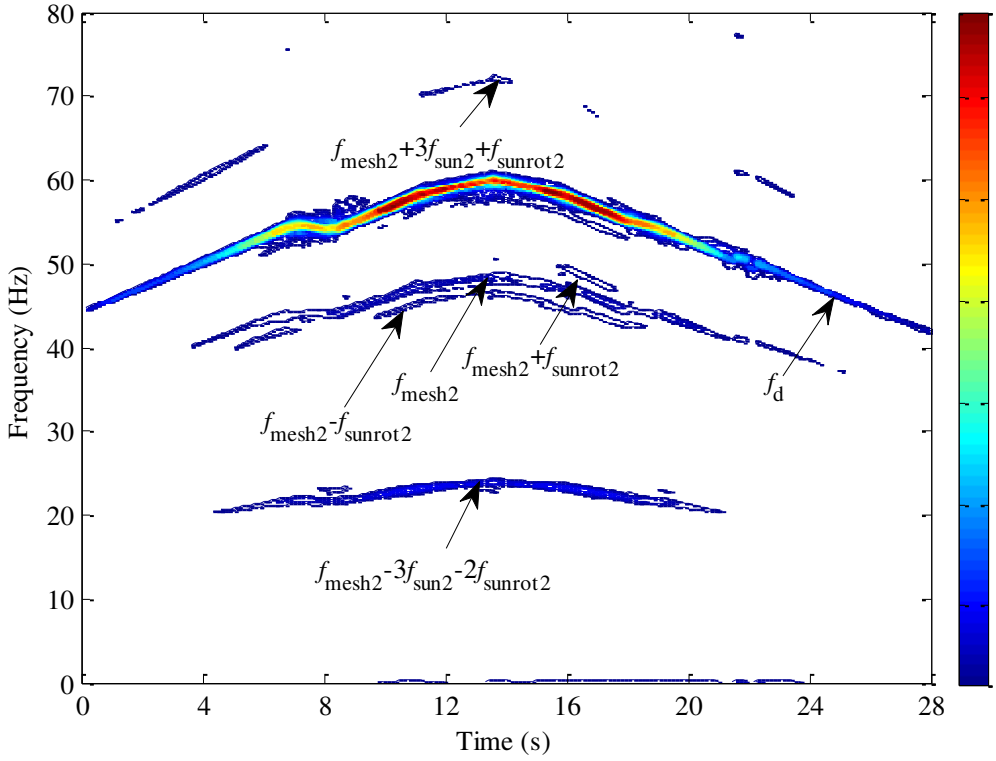

Fig. 6-26. TFR of the vibration signal of stage 2 sun gear chipping fault

6.6 Conclusions

In this chapter, a new linear transform named VSLCT has been proposed for fault diagnosis of planetary gearboxes under non-stationary conditions. The linear transform definition is firstly extended in order to provide a theoretical foundation for the VSLCT

and this new definition may also prompt the design of other linear transforms for other applications. The VSLCT employs a set of non-orthogonal bases whose frequencies are synchronous with shaft rotational velocity, thus the obtained TFR is free from smear problem. The window length of the VSLCT is time-varying to provide more suitable time-varying time-frequency resolution. An energy-concentration-index guided algorithm is also developed to dynamically calculate the two key parameters of the VSLCT in response the changing condition. Therefore, the VSLCT does not require the user to provide any parameter, hence eliminating the expertise-demanding, time-consuming, and yet error-prone human intervention. The effectiveness of the VSLCT method has been validated using both synthetic signals and experiment vibration signals of planetary gearbox collected under non-stationary conditions.

7 Comparisons of the proposed methods

In this chapter, the comparisons of the proposed methods will be carried out using simulated signals, followed by discussions.

The simulated signals are generated using the vibration model provided in Appendix A (Feng and Zuo, 2012). Assuming the gearbox has a sun gear fault. The simulated signal is expressed by

$$x(t)=\left\{1-\cos\left[2\pi\int f_{\text{sunrot}}(t)\,\mathrm{d}t\right]\right\}\left\{1+\mathrm{A}\cos\left[2\pi\int f_{\text{sun}}(t)\,\mathrm{d}t\right]\right\} \times\cos\left[2\pi\int f_{\text{mesh}}(t)\,\mathrm{d}t\right]+\mathrm{N}(t), \tag{7-1}$$

where N(t) is Gaussian white noise, f_{srot} is the sun gear rotational frequency, f_{mesh} is the gear meshing frequency and f_{sun} is the sun gear fault characteristic frequency. The relationship between these characteristic frequencies are set as $f_{\text{sunrot}}=f_{\text{mesh}}/10=f_{\text{sun}}/3$. The signal length is two seconds. To simulate the speed-varying state, we set the sun gear rotating frequency as $f_{\text{sunrot}}(t)=10+2\sin(2\pi t)$.

First of all, the TFR qualities of the proposed methods under different SNR levels are evaluated. Sixteen signals are generated with different levels of noise with 400 Hz sampling rate. The SNRs are set as integer numbers with unit dB between -10 and 5.

Generally, a fault is considered as detected if the sidebands associated with fault characteristic frequency are observed in the TFR. The number of signal components detected can be considered as a good indicator of the fault detection capability of one method. For any component f_{any}, it is said the component is detected, if $X\left(f_{\text{any}}(t),t\right)$ is the local maximum along the frequency direction over more than half of the time period. Based on the convolution theory, each simulated signal contains nine components. The number of signal components detected by the proposed methods are shown in Fig. 7-1(A). It can be found that according to the number of components detected by the four proposed methods, they can be roughly ordered as 'VSBD > VST > VSSTFT > VSLCT', under most SNRs.

Some fault diagnosis applications commonly require a method to have good computational efficiency, for example, online monitoring applications. The computational effciency is thus an important aspect for evaluating the proposed methods. Eighteen discrete signals with different lengths are generated here and their lengths are represented by n. Their lengths are set as 200 points, 250 points, 300 points, …, 1050 points. The proposed methods are used to generate a TFR with n by n pixies. The running time of the proposed method are shown in Fig. 7-1(B). It can be seen that the cost time by the proposed methods can be ordered as VSBD > VSLCT > VST > VSSTFT, thus for the computational efficiency, the performances of the proposed methods can be ordered as VSSTFT > VST > VSLCT > VSBD.

It should also be mentioned here that the VSSTFT, VST and VSBD require shaft speed information and the VSLCT does require such information. Based on the above analysis, the capabilities of the proposed methods can be summarised in Table 7-1. It can be seen that though the VSLCT has relatively low rank of component detection capability, it is the only one that does not require the users to provide shaft speed. Therefore, under the condition that the shaft speed can be neither measured nor estimated from the STFT of the collected vibration signal, the VSLCT is the only choice from the proposed methods.

Under the condition that the shaft speed can be obtained, the VSSTFT, VST and VSBD are given more priority than the VSLCT, because they perform better than the VSLCT in detecting the signal components with known shaft speed. In terms of component detection capability, the performance order is that VSBD > VST > VSSTFT. However, in terms of computational efficiency, the performance order is, on the contrary, VSLCT > VST > VSSTFT. This indicates that better TFR quality requires higher computational complexity. Therefore, the VSSTFT, VST and VSBD can be selected based on the application environment. For example, for online monitoring which requires quicker response, the VSSTFT or VST is more desirable. For the high noise applications, the VSBD or VST should be given more priority.

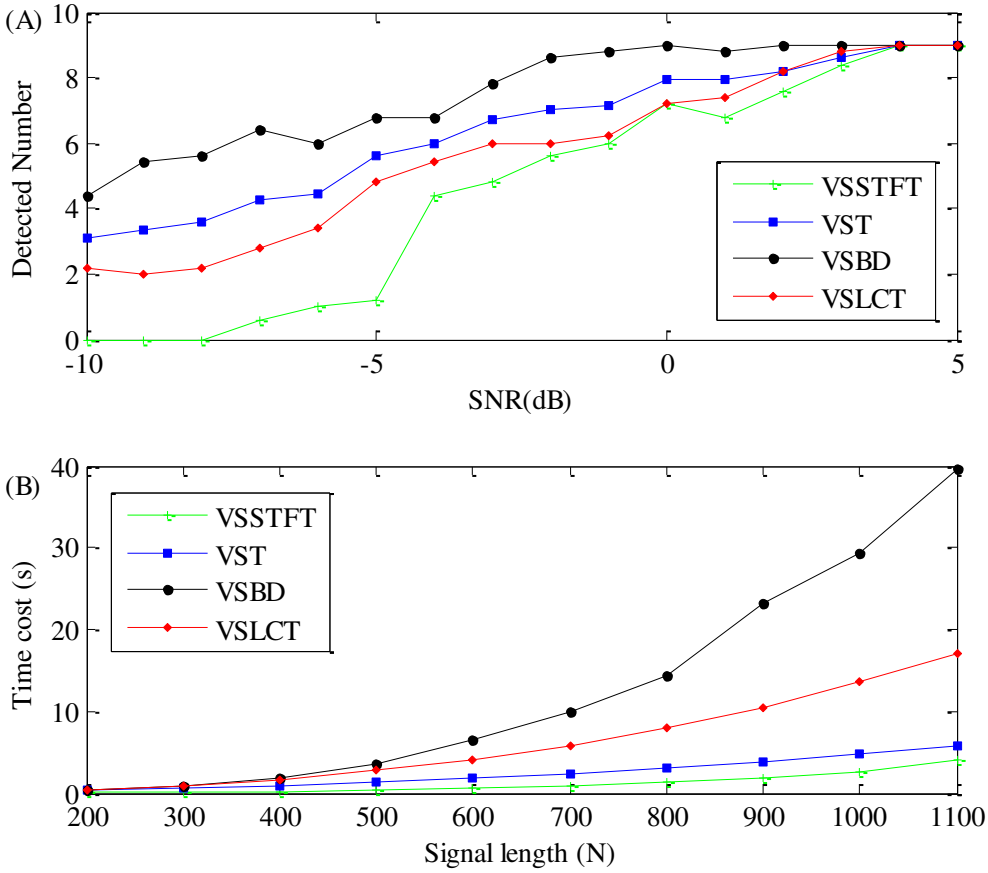

Fig. 7-1. Evaluation of the proposed methods: (A) The number of detected signal components by the methods and (B) Time spent of the methods

Table 7-1 Evaluations of the proposed methods

Capability	VSSTFT	VST	VSBD	VSLCT
Shaft speed requirement	Yes	Yes	Yes	No
Component detection capability rank	3	2	1	4
Computational efficiency rank	1	2	4	3

8 Conclusions and future work

8.1 Conclusions

The planetary gearbox often works under non-stationary conditions and the collected vibration signals are non-stationary. Time-frequency methods are effective methods to characterise such non-stationary signals for fault diagnosis, however, current time-frequency methods still have problems of smearing effects and/or cross-term interferences. In this study, four new time-frequency methods are proposed to address these problems for planetary gearbox fault diagnosis under non-stationary conditions. The work accomplished in this thesis is summarized as follows.

(1) Velocity synchronous short-time Fourier transform (VSSTFT)

The VSSTFT is proposed in chapter 3 and it belongs to the linear transform family. It can be realized via a one-step integral transform and has good computational efficiency. It addresses the smear problem of linear transform. Its time-frequency resolution varies with time-varying shaft speed to provide a desirable balance between time resolution and frequency resolution for the entire signal. However, the VSSTFT is a type of linear transform and it is subjected to Heisenberg uncertainty principle (Hlawatsch and Boudreaux-Bartels, 1992), thus its time-frequency resolution is still limited.

(2) Velocity synchrosqueezing transform (VST)

The VST, proposed in chapter 4, is a type of time-frequency method based on the TFR data remapping. It has better energy concentration and better readability than the VSSTFT. Similar to the VSSTFT, the VST is also a smear-free time-frequency method. An algorithm for fast implementation of the VST is also developed so that it can be realised in one step without resampling the signal. Compared with the VSSTFT, the disadvantage of the VST is that it has relatively higher computational complexity than the VSSTFT.

(3) Velocity synchronous bilinear distribution (VSBD)

The VSBD, introduced in chapter 5, is based on the bilinear distribution frame, thus its time-frequency resolution is inherently higher than the VSSTFT and VST. This method addresses the smear effect of current bilinear distributions in analysing the signals containing nonlinear frequencies. Current bilinear transforms still suffer from the cross-

term interference or the time-frequency resolution reduction caused by eliminating the cross terms. The proposed VSBD employs a GD-based approach to filter out these cross terms without harming the auto terms, therefore the high time-frequency resolution survives and the obtained TFR does not have cross-term interference. The disadvantage of the VSBD is that it has higher computational complexity than the VST and VSSTFT.

(4) Velocity synchronous linear chirplet transform (VSLCT)

The VSSTFT, VST and VSBD require the user to provide shaft speed and the shaft speed may be not easily accessible under some conditions. To mitigate this drawback, in chapter 6, a new method named VSLCT is proposed. The VSLCT employs a set of linear chirplets whose frequencies are synchronous with shaft rotational velocity as bases in order to reduce the smearing effects. A concentration-index-guided approach is also developed to dynamically determine the two parameters of the VSLCT. Compared with the exsiting time-frequency methods, the advantages of the VSLCT are, A) it is smear-free, B) it is non-parametric and C) shaft speed is not required.

Four new time-frequency methods are developed and applied for fault diagnosis of planetary gearbox. All the proposed methods have been validated using simulated and experimental planetary gearbox vibration signals. By applying these methods, the signal structures are clearly revealed in the time-frequency representations and faults are diagnosed by detecting and identifying the sideband components associated with fault. The proposed methods have been compared with the state-of-art methods (for example, (Yu and Zhou, 2016; Yu et al., 2017)). The comparisons show the proposed methods are superior to these compared methods in revealing the signal structure of the non-stationary vibration signals collected from planetary gearboxes. The experimental tests have shown the effectiveness of the proposed methods in diagnosing faults of planetary gearboxes under non-stationary conditions.

8.2 Future work

Partially motivated by the limitations mentioned above, the following research directions are recommended to be further investigated.

(1) A method generating high-quality TFR with low computational complexity

In chapter 3-5, three methods are proposed, however, these methods provide the TFR with better quality at the cost of computational complexity. It is suggested to propose a method that is able to generate a high-quality TFR with relatively low computational complexity.

(2) Extending the research to the fault diagnosis of planetary gearbox bearing under non-stationary conditions

Bearings are important parts in planetary gearboxes. To date, the research on fault diagnosis of planetary gearbox bearing is still limited. It is suggested to extend the methods proposed in this thesis to the fault diagnosis of planetary gearbox bearing under non-stationary conditions.

(3) A method evaluating the fault severity from the TFR

The proposed methods can generate clear TFR for fault diagnosis, however, fault severity cannot be revealed from the TFR. It is suggested to propose a method that is able to evaluate the severity of the fault from the signal TFR.

(4) A method generating high-resolution TFR without shaft speed information

The proposed VSBD method requires shaft speed information and it can generate a high-resolution TFR. The proposed VSLCT method does not require shaft speed information and it can generate a TFR with relatively low resolution. It will be interesting to explore whether these two methods can be combined such that a high-resolution TFR can be generated without running speed information.

List of publications (including submitted papers)

[1] Guan, Y., Shi, J., Liang, M., and Necsulescu, D.-S., 2018, A velocity synchronous short-time Fourier transform for fault diagnosis of wind turbine planetary gearbox under non-stationary conditions, *Proceedings of the Institution of Mechanical Engineers, Part C: Journal of Mechanical Engineering Science*. (Under review, used in Chapter 3)

[2] Guan, Y., Liang, M., and Necsulescu, D.-S., 2017, A Velocity Synchrosqueezing Transform for Fault Diagnosis of Planetary Gearboxes under Nonstationary Conditions. *Proceedings of the Institution of Mechanical Engineers, Part C: Journal of Mechanical Engineering Science.* **231**(15):2868-2884. (Used in Chapter 4)

[3] Guan, Y., Liang, M., and Necsulescu, D.-S., 2018, Joint Application of Spectral Kurtosis and Velocity Synchrosqueezing Transform for Fault Diagnosis of Ball Bearing Under Nonstationary Conditions, *The ASME 2018 International Design Engineering Technical Conferences & Computers and Information in Engineering Conference*, Quebec City. (Used in Chapter 4)

[4] Guan, Y., Liang, M., and Necsulescu, D.-S., 2018, Velocity Synchrosqueezing Windowed Fourier Transform for Fault Diagnosis of Fixed-shaft Gearbox Under Nonstationary Conditions, *The prognostics and System Health Management Conference*, Chongqing. (Used in Chapter 4)

[5] Guan, Y., Liang, M., and Necsulescu, D.-S., 2018, Velocity synchronous bilinear distribution for planetary gearbox fault diagnosis under non-stationary conditions, *Journal of Sound and Vibration*. (Accepted, used in Chapter 5)

[6] Guan, Y., Liang, M., and Necsulescu, D.-S., 2018, Velocity synchronous linear chirplet transform, *IEEE Transactions on Industrial Electronics*. (Accepted, used in Chapter 6)

[7] Guan, Y., Liang, M., Shi, J., and Necsulescu, D.-S., 2018, Gearbox Fault Diagnosis via Generalized Velocity Synchronous Fourier Transform and Order Analysis, *Transactions of the Canadian Society for Mechanical Engineering*. (Accepted)

[8] Shi, J., Liang, M., and Guan, Y., 2016, Bearing Fault Diagnosis under Variable Rotational Speed Via the Joint Application of Windowed Fractal Dimension Transform and Generalized Demodulation: A Method Free from Prefiltering and Resampling. *Mechanical Systems and Signal Processing.* **68–69**:15-33.

[9] Shi, J., Liang, M., Necsulescu, D.-S., and Guan, Y., 2016, Generalized Stepwise Demodulation Transform and Synchrosqueezing for Time–Frequency Analysis and Bearing Fault Diagnosis. *Journal of Sound and Vibration.* **368**:202-222.

Appendices

A Vibration model of planetary gearbox having gear faults

The vibration model of faulty planetary gearbox (Feng and Zuo, 2012) is reviewed and summarized here.

For planetary gearbox, the vibration induced by the gear having a local fault can be modeled as a process of amplitude modulation and frequency modulation with the gear meshing frequency or its harmonics as the carrier frequency (Feng and Zuo, 2012). This vibration propagates from its origin into the sensor through solid mechanical components. Based on the above analysis, the sensor perceived vibration can be expressed as

$$x(t) = h(t)\sum_{k=1}^{K} a_k(t)\cos\left(2\pi k\int f_{\text{mesh}}(t)\,\mathrm{d}t + b_k(t) + \theta_k\right) \tag{1-1}$$

where t is time, $a_k(t)$ is amplitude modulation function, $b_k(t)$ is frequency modulation function, $h(t)$ is the transfer path effect, $f_{\text{mesh}}(t)$ is gear meshing frequency and θ is initial phase.

The amplitude and frequency modulations are periodic with the fault characteristic frequency of the faulty gear. Thus the amplitude modulation function and frequency modulation functions can each be expressed as a Fourier series with the fault characteristic frequency of the faulty gear as the fundamental frequency, expressed by

$$\text{Amplitude modulation: } a_k(t) = 1 + \sum_{n=1}^{N} \mathrm{A}_{kn}\cos\left(2\pi n\int f_{\text{fault}}(t)\,\mathrm{d}t + \phi_{kn}\right) \tag{1-2}$$

$$\text{Frequency modulation: } b_k(t) = \sum_{l=1}^{L} B_{kl}\cos\left(2\pi l\int f_{\text{fault}}(t)\,\mathrm{d}t + \varphi_{kl}\right) \tag{1-3}$$

where $f_{\text{fault}}(t)$ is characteristic frequency of the faulty gear, ϕ and φ are initial phases.

As the vibration sensor is usually mounted at a fixed location on the ring gear, the transfer path between senor and the faulty gear is time-varying as the gears rotate in the cases of sun gear fault and planet gear fault. In these two cases, the transfer path effect on the vibration can be modelled as a hanning function (Inalpolat and Kahraman, 2009; Inalpolat and Kahraman, 2010).

In the case of sun gear damage, the fault characteristic frequency is the sun gear fault characteristic frequency, and the transfer path effect is a hanning function with sun gear rotating frequency, expressed by

$$f_{\text{fault}}(t) = f_{\text{sun}}(t) \tag{1-4}$$

$$h(t) = 1 - \cos\left(2\pi \int f_{\text{sunrot}}(t)\,\mathrm{d}t\right) \tag{1-5}$$

where f_{sun} is sun gear fault characteristic frequency and f_{sunrot} is sun gear rotational frequency.

In the case of planet gear damage, the fault characteristic frequency is the planet gear fault characteristic frequency with carrier rotating frequency, expressed by

$$f_{\text{fault}}(t) = f_{\text{planet}}(t) \tag{1-6}$$

$$h(t) = 1 - \cos\left(2\pi \int f_{\text{carrier}}(t)\,\mathrm{d}t\right) \tag{1-7}$$

where f_{planet} is planet gear fault characteristic frequency and f_{carrier} is carrier rotational frequency.

In the case of ring gear damage, the fault characteristic frequency is the ring gear fault characteristic frequency and the transfer path is a scale effect, expressed by

$$f_{\text{fault}}(t) = f_{\text{ring}}(t) \tag{1-8}$$

$$h(t) = \text{constant} \tag{1-9}$$

where f_{ring} is ring gear fault characteristic frequency

B Formulas for calculating characteristic frequencies of planetary gearbox

The characteristic frequencies of both fixed-shaft gearbox and planetary gearbox are shaft-speed-locked and proportional to each other. They can be calculated based on the gearbox geometry and any known characteristic frequency. Using the input gear rotational frequency as a base, the formulas for calculating the characteristic frequencies of the fixed-shaft gearbox are summarized below(McFadden, 1986, 1988):

Gear meshing frequency of fixed-shaft gearbox: $f_{\text{meshf}}(t) = Z_{\text{input}} f_{\text{input}}(t)$ (2-1)

Output gear rotational frequency: $f_{\text{output}}(t) = \frac{Z_{\text{input}}}{Z_{\text{output}}} f_{\text{input}}(t)$ (2-2)

where Z_{input} and Z_{output} are the numbers of input gear teeth and output gear teeth, respectively.

For the planetary case, using the carrier rotational frequency as a base, the formulas for calculating the characteristic frequencies of the planetary gearbox are summarized below(Feng and Zuo, 2012):

Gear meshing frequency of planetary gearbox: $f_{\text{meshp}}(t) = Z_{\text{ring}} f_{\text{carrier}}(t)$ (2-3)

Sun gear rotational frequency: $f_{\text{sunrot}}(t) = (1 + \frac{Z_{\text{ring}}}{Z_{\text{sun}}}) f_{\text{carrier}}(t)$ (2-4)

Sun gear fault characteristic frequency: $f_{\text{sun}}(t) = \frac{N_p Z_{\text{ring}}}{Z_{\text{sun}}} f_{\text{carrier}}(t)$ (2-5)

Planet gear fault characteristic frequency: $f_{\text{planet}}(t) = \frac{2Z_{\text{ring}}}{Z_{\text{planet}}} f_{\text{carrier}}(t)$ (2-6)

Ring gear fault characteristic frequency: $f_{\text{ring}}(t) = N_p f_{\text{carrier}}(t)$ (2-7)

where N_p is the number of planet gears, Z_{sun}, Z_{planet} and Z_{ring} are the numbers of sun gear teeth, planet gear teeth and ring gear teeth, respectively.

C **Generalized velocity synchronous Fourier transform**

The generalized velocity synchronous Fourier transform proposed by the author of this thesis el al. for fault diagnosis of fixed-shaft gearboxes under non-stationary conditions is briefly reviewed as follows (Guan et al., 2018).

This method firstly employs the GD approach (Olhede and Walden, 2005) to extract a component whose frequency is proportional to the instantaneous shaft rotational frequency from the vibration signal, followed by demodulating the extracted component to recover the instantaneous shaft rotational phase. With such information the order spectrum can be directly obtained via the velocity synchronous discrete Fourier transform (VSDFT) (Borghesani et al., 2014) and finally the gear fault, if any, can be diagnosed by order spectrum analysis.

The vibration signal acquired from a gearbox is mainly composed of the meshing components, its harmonics components and sidebands components. The instantaneous frequencies of these components are all synchronized thus proportional to the instantaneous shaft rotational frequency (ISRF). The multi-components vibration signal $x(t)$ can be represented as

$$x(t)=\sum_{k=1}^{\mathrm{K}}x_k\left(t\right)=\sum_{k=1}^{\mathrm{K}}A_k\left(t\right)\cos\left[2\pi\int_{-\infty}^{\infty}f_k\left(t\right)\mathrm{d}t+\theta_k\right] \tag{3-1}$$

where K is the number of the components, $A_k(t)$ is the real-valued instantaneous amplitude envelope, θ_k is the initial phase of the kth component and $f_k(t)$ is the instantaneous frequency (IF) of the kth component. Assuming the phase shifting of the signal components introduced by the transmission path effect is negligible, the IF components can be seen as proportional to the ISRF with a ratio p_k, expressed by

$$f_k\left(t\right)=p_k f_{\mathrm{shaft}}\left(t\right) \tag{3-2}$$

where $f_{\mathrm{shaft}}(t)$ is the ISRF.

The procedure to transform the signal to order domain using the proposed GVSFT method is summarized as follows.

Step. 1. Estimate the IF of the component of interest. As discussed previously, in order to perform GD, the estimated IF of a certain component is required. Here we assume that

the IF of the component of interest is $\hat{f}_I(t)$, where I ($1 \le I \le K$) is the ordinal number of the component of interest. The IF of the component of interest can be roughly estimated based on the ridges of the time-frequency representation (TFR) obtained by the short-time Fourier transform (STFT) (Feng et al., 2011; Urbanek et al., 2013; Wang et al., 2014). The STFT of the signal is represented by

$$X(t,f) = \int_{t=-\infty}^{t=+\infty} x(\tau)\lambda_{(w)}(\tau - t)\exp(-j2\pi f\tau)\mathrm{d}\tau \,, \tag{3-3}$$

where w is window length, τ and f denote time and frequency respectively. Restricted by the frame of linear transform, the STFT has limited time-frequency resolution. To have a better frequency resolution, the window length should be relatively long (Iatsenko et al., 2015). However, as the STFT employs a set of bases with fixed frequencies and the signal frequencies are time-varying, the STFT will have smear effects and for a long window, the Taylor reminder will be large, which may lead to large error of the TFR(Yu and Zhou, 2016). Therefore, one needs to take a tradeoff between accuracy and resolution. It is suggested to firstly set a relatively short window. If the strong components cannot be detected from the TFR, then we increase the window length until the TFR is clear enough for coarse frequency estimation. The component of interest can be extracted from the TFR using a local maxima search algorithm (Urbanek et al., 2013), represented by

$$\hat{f}_I(t) = \underset{f}{\mathrm{Argmax}} \left| x(t,f) \right|, \mathrm{for} f \in \Delta f_t \,, \tag{3-4}$$

$$\Delta f_t \subset \left\{ \hat{f}_I(t - \mathrm{d}\tau) - \delta, \hat{f}_I(t - \mathrm{d}\tau) + \delta \right\}, \tag{3-5}$$

where δ is the given frequency tolerance for maxima detection. For t=0, f_{max} should be given by the user. It should be noted that the STFT has limited time-frequency resolution, and thus the accuracy of the estimated IF is low. To improve the accuracy, the IF estimation will be refined by the GD subsequently as provided in steps. 2-6.

Step. 2. Create the analytic form $y(t)$ of the signal using the Hilbert transform. The Hilbert transform of the signal can be approximated by the corresponding quadrature part (Feldman, 1997), expressed by

$$H(t)=\frac{1}{\pi}\int_{-\infty}^{\infty}\frac{x(\tau)}{t-\tau}\mathrm{d}\tau\approx\sum_{k=1}^{K}A_k(t)\sin\left[2\pi\int_{-\infty}^{\infty}f_k(t)\mathrm{d}t+\theta_k\right] \tag{3-6}$$

where $H(t)$ is the Hilbert transform of $x(t)$. The analytic signal is then expressed as

$$y(t)=x(t)+iH(t)=\exp\left\{i\left[2\pi\int_{-\infty}^{\infty}f_k(t)\mathrm{d}t+\theta_k\right]\right\} \tag{3-7}$$

Step. 3. Construct the GD function according to the preliminary estimated instantaneous frequency $\hat{f}_I(t)$ and the target frequency f_0. Since the resolutions of the signal and the preliminary estimated instantaneous frequency $\hat{f}_I(t)$ are different, the resolution of $\hat{f}_I(t)$ is firstly improved by polynomial fitting (because the resolution of $\hat{f}_I(t)$ is lower). The GD function is expressed by

$$v(t)=\exp\left\{i2\pi\left[f_0t-\int_{-\infty}^{\infty}\hat{f}_I(t)\mathrm{d}t\right]\right\}. \tag{3-8}$$

Forward map the analytic signal $y(t)$ to the new signal $y(t)$ by multiplying the GD mapping function v(t), resulting a forward mapped signal

$$z(t)=y(t)v(t)=\sum_{k=1}^{K}A_k(t)\exp\left\{i2\pi\left[\int_{-\infty}^{\infty}f_k(t)\mathrm{d}t-\int_{-\infty}^{\infty}\hat{f}_I(t)\mathrm{d}t+f_0t\right]+i\theta_k\right\}. \tag{3-9}$$

For this forward mapped signal, the IF of the kth component is $f_k(t)-\hat{f}_I(t)+f_0$. It means that all the components' IFs are respectively mapped to the new frequencies equaling to their original frequencies $f_k(t)$ plus the IF of GD function $f_v(t)=-\hat{f}_I(t)+f_0$. Specially, the component's IF of interest is thus $f_I(t)=f_I(t)-\hat{f}_I(t)+f_0\approx f_0$, showing that the time-varying frequency of the interested component is mapped to a new frequency which is almost constant and will not likely overlap other components' frequency bands. It can be seen the frequency of the forward mapped signal is around f_0. To avoid the interferences of negative frequencies and frequency aliasing, the frequency of the forward mapped signal should be in range $(0, f_s/2)$, where f_s is the sampling frequency. For this reason, setting the target frequency f_0 in the range $(f_s/8, 3f_s/8)$ is suggested.

Step. 4. Separate the component $z_I(t)$ by filtering the forward mapped signal $z(t)$. The center frequency of filter is equal to the target frequency f_0 and the bandwidth is equal to the minimum frequency difference between the IF of its adjacent components. The filter signal $z_I(t)$ is expressed by

$$z_I(t) = A_I(t)\exp\left\{\mathrm{i}2\pi\left[\int_{-\infty}^{\infty} f_I(t)\,\mathrm{d}t - \int_{-\infty}^{\infty} \hat{f}_I(t)\,\mathrm{d}t + f_0 t\right] + i\theta_I\right\}. \tag{3-10}$$

One can see that this resulted component $z_I(t)$ is a mono-component and only contains the forward mapped component of interest.

Step. 5. Recover the component of interest by multiplying the filtered component $z_I(t)$ by a reverse mapping GD function $v^{-1}(t) = \exp\left\{i2\pi\left[-f_0 t + \int_{-\infty}^{\infty} \hat{f}_I(t)\,\mathrm{d}t\right]\right\}$, expressed by

$$\begin{aligned} y_I(t) &= z_I(t)v^{-1}(t) \\ &= A_I(t)\exp\left\{\mathrm{i}2\pi\left[\int_{-\infty}^{\infty} f_I(t)\,\mathrm{d}t - \int_{-\infty}^{\infty} \hat{f}_I(t)\,\mathrm{d}t + f_0 t\right] + i\theta_I\right\}\exp\left\{i2\pi\left[\int_{-\infty}^{\infty} \hat{f}_I(t)\,\mathrm{d}t - f_0 t\right]\right\} \\ &= A_I(t)\exp\left[\mathrm{i}2\pi\int_{-\infty}^{\infty} f_I(t)\,\mathrm{d}t + i\theta_I\right] \end{aligned} \tag{3-11}$$

which is still analytic. In this step, multiplying the reverse of the same GD function as used in step (3) is equivalent to recovering the original IF of the component of interest. As the recovered signal contains only one component, it satisfies the mono-component requirement by demodulation.

Step. 6. Demodulate the recovered mono-component signal to obtain the instantaneous phase and frequency of the component of interest, expressed by

$$\theta_I(t) = \mathrm{unwrap}\left\{\arctan\frac{\mathrm{real}\left[y_I(t)\right]}{\mathrm{imag}\left[y_I(t)\right]}\right\} \tag{3-12}$$

where real[$y_I(t)$] and imag[$y_I(t)$] denote the real and imaginary parts of $y_I(t)$ respectively, and unwrap denotes the phase unwrapping operation.

The instantaneous shaft rotational phase (ISRP) is obtained by normalizing the phase of the component of interest, expressed by

$$\theta_{\text{shaft}}(t) = \frac{\theta_I(t)}{p_I}, \tag{3-13}$$

where p_I is the ratio of the IF of the component of interest to the ISRF.

The instantaneous shaft angular frequency (ISAF) is obtained by taking derivative of the ISRP, which can be written as

$$\omega_{\text{shaft}}(t) = \frac{\mathrm{d}\theta_{\text{shaft}}(t)}{\mathrm{d}t}. \tag{3-14}$$

As in this step, the ISAF is obtained by demodulation, thus it does not have resolution problem of the STFT. In this way, the estimated frequency is refined.

Step. 7. Apply the VSDFT to obtain the order spectrum $X(\Omega)$ for fault diagnosis according to the ISRP $\theta_{\text{shaft}}(t)$ and the ISAF $\omega_{\text{shaft}}(t)$, expressed by

$$X(\Omega) = \int_{-\infty}^{\infty} x(t)\omega_{\text{shaft}}(t)\exp\left[-i\Omega\theta_{\text{shaft}}(t)\right]\mathrm{d}t. \tag{3-15}$$

Now as the order spectrum $X(\Omega)$ is obtained, we can diagnose which gear has fault (if any) by matching the spectral peaks with the theoretical sidebands orders associated with faults. Two positions of fault are considered, i.e., on the pinion or on the larger gear. As the faults cause modulations with the rotational frequency and its harmonics as modulating frequencies, and meshing frequency and its harmonics as carrier frequencies. The theoretical sidebands orders can be expressed as $mo_{\text{m}} \pm no_{\text{r}}$, where o_{m} denotes meshing order, o_{r} denotes rotational order of the faulty gear, m and n are positive integers. To facilitate the understanding of the proposed method, the steps of the proposed GVSFT method are presented in a flowchart as shown in Fig. C-1.

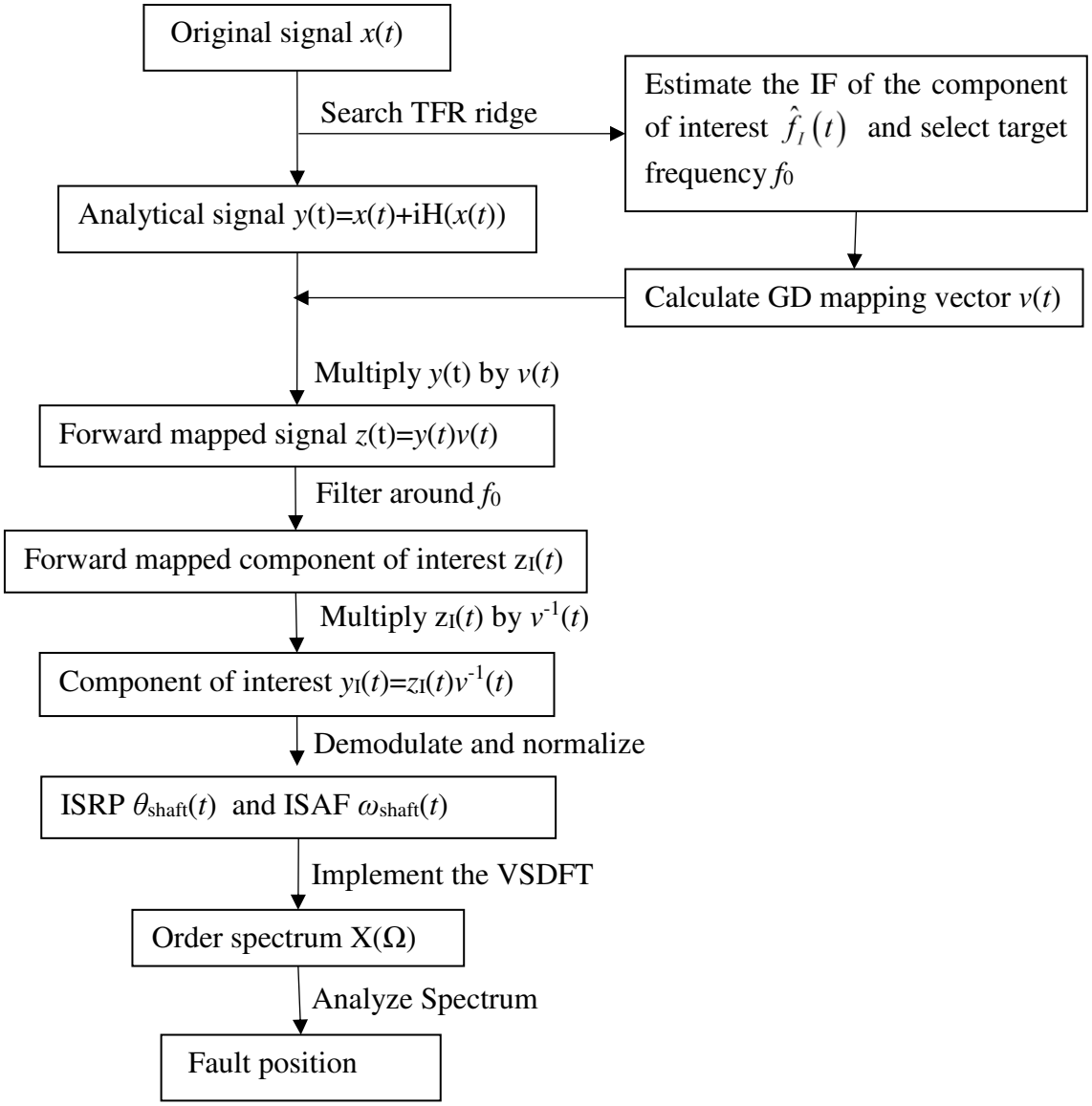

Fig. C-1. Flowchart of the proposed GVSFT approach

References

[1] Abouel-seoud, S. A., 2017, Fault Detection Enhancement in Wind Turbine Planetary Gearbox Via Stationary Vibration Waveform Data. *Journal of Low Frequency Noise, Vibration and Active Control.* **37**(3):477-494.

[2] Allen, J., 1977, Short Term Spectral Analysis, Synthesis, and Modification by Discrete Fourier Transform. *IEEE Transactions on Acoustics, Speech and Signal Processing.* **25**(3):235-238.

[3] Allen, J. B., and Rabiner, L. R., 1977, A Unified Approach to Short-Time Fourier Analysis and Synthesis. *Proceedings of the IEEE.* **65**(11):1558-1564.

[4] Assaad, B., Eltabach, M., and Antoni, J., 2014, Vibration Based Condition Monitoring of a Multistage Epicyclic Gearbox in Lifting Cranes. *Mechanical Systems and Signal Processing.* **42**(1–2):351-367.

[5] Auger, F., and Flandrin, P., 1995, Improving the Readability of Time-Frequency and Time-Scale Representations by the Reassignment Method. *IEEE Transactions on Signal Processing.* **43**(5):1068-1089.

[6] Baraniuk, R. G., and Jones, D. L., 1992a, New Dimensions in Wavelet Analysis. *IEEE International Conference on Acoustics, Speech, and Signal Processing*, 137-140 vol.5.

[7] Baraniuk, R. G., and Jones, D. L., 1992b, New Signal-Space Orthonormal Bases Via the Metaplectic Transform. *Proceedings of the IEEE-SP International Symposium on Time-Frequency and Time-Scale Analysis*, 339-342.

[8] Baraniuk, R. G., and Jones, D. L., 1993a, A Signal-Dependent Time-Frequency Representation: Optimal Kernel Design. *IEEE Transactions on Signal Processing.* **41**(4):1589-1602.

[9] Baraniuk, R. G., and Jones, D. L., 1993b, Warped Wavelet Bases: Unitary Equivalence and Signal Processing. *1993 IEEE International Conference on Acoustics, Speech, and Signal Processing*, 320-323 vol.3.

[10] Bartelmus, W., Chaari, F., Zimroz, R., and Haddar, M., 2010, Modelling of Gearbox Dynamics under Time-Varying Nonstationary Load for Distributed Fault Detection and Diagnosis. *European Journal of Mechanics - A/Solids.* **29**(4):637-646.

[11] Bartelmus, W., and Zimroz, R., 2009a, A New Feature for Monitoring the Condition of Gearboxes in Non-Stationary Operating Conditions. *Mechanical Systems and Signal Processing.* **23**(5):1528-1534.

[12] Bartelmus, W., and Zimroz, R., 2009b, Vibration Condition Monitoring of Planetary Gearbox under Varying External Load. *Mechanical Systems and Signal Processing.* **23**(1):246-257.

[13] Blough, J., Brown, D., and Vold, H., 1997, The Time Variant Discrete Fourier Transform as an Order Tracking Method. *SAE Technical Paper 972006.*

[14] Blough, J. R., 2003, Development and Analysis of Time Variant Discrete Fourier Transform Order Tracking. *Mechanical Systems and Signal Processing.* **17**(6):1185-1199.

[15] Boashash, B., and Shea, P. O., 1994, Polynomial Wigner-Ville Distributions and Their Relationship to Time-Varying Higher Order Spectra. *IEEE Transactions on Signal Processing.* **42**(1):216-220.

[16] Bonnardot, F., El Badaoui, M., Randall, R. B., Danière, J., and Guillet, F., 2005, Use of the Acceleration Signal of a Gearbox in Order to Perform Angular Resampling (with Limited Speed Fluctuation). *Mechanical Systems and Signal Processing.* **19**(4):766-785.

[17] Borghesani, P., Pennacchi, P., Chatterton, S., and Ricci, R., 2014, The Velocity Synchronous Discrete Fourier Transform for Order Tracking in the Field of Rotating Machinery. *Mechanical Systems and Signal Processing.* **44**(1–2):118-133.

[18] Boultadakis, G. E., Kalognomos, G. K., Karakasiliotis, A. V., Frangos, P. V., and Stergioulas, L. K., 2009, A Comparative Study of Bilinear Time–Frequency Transforms of Isar Signals for Air Target Imaging. *Elektronika ir Elektrotechnika.* **92**(4).

[19] Bozchalooi, I. S., and Liang, M., 2010, In-Line Identification of Oil Debris Signals: An Adaptive Subband Filtering Approach. *Measurement Science and Technology.* **21**(1):1-15.

[20] Chaari, F., Fakhfakh, T., and Haddar, M., 2006a, Analytical Investigation on the Effect of Gear Teeth Faults on the Dynamic Response of a Planetary Gear Set. *Noise & Vibration Worldwide.* **37**(8):9-17.

[21] Chaari, F., Fakhfakh, T., and Haddar, M., 2006b, Dynamic Analysis of a Planetary Gear Failure Caused by Tooth Pitting and Cracking. *Journal of Failure Analysis and Prevention.* **6**(2):73-78.

[22] Chaari, F., Fakhfakh, T., Hbaieb, R., Louati, J., and Haddar, M., 2006c, Influence of Manufacturing Errors on the Dynamic Behavior of Planetary Gears. *International Journal of Advanced Manufacturing Technology.* **27**(7/8):738-746.

[23] Chen, X., and Feng, Z., 2016a, Application of Reassigned Wavelet Scalogram in Wind Turbine Planetary Gearbox Fault Diagnosis under Nonstationary Conditions. *Shock and Vibration.* **2016**:12.

[24] Chen, X., and Feng, Z., 2016b, Iterative Generalized Time–Frequency Reassignment for Planetary Gearbox Fault Diagnosis under Nonstationary Conditions. *Mechanical Systems and Signal Processing.* **80**:429-444.

[25] Chen, Z., and Shao, Y., 2013, Dynamic Features of a Planetary Gear System with Tooth Crack under Different Sizes and Inclination Angles. *Journal of Vibration and Acoustics.* **135**(3):031004-031004-12.

[26] Choi, H. I., and Williams, W. J., 1989a, Improved Time-Frequency Representation of Multicomponent Signals Using Exponential Kernels. *IEEE Transactions on Acoustics Speech and Signal Processing.* **37**(6):862-871.

[27] Choi, H. I., and Williams, W. J., 1989b, Improved Time-Frequency Representation of Multicomponent Signals Using Exponential Kernels. *IEEE Transactions on Acoustics, Speech, and Signal Processing.* **37**(6):862-871.

[28] Climente-Alarcon, V., Antonino-Daviu, J. A., Vedreño-Santos, F., and Puche-Panadero, R., 2013, Vibration Transient Detection of Broken Rotor Bars by Psh Sidebands. *IEEE Transactions on Industry Applications.* **49**(6):2576-2582.

[29] Coats, M. D., and Randall, R. B., 2014, Single and Multi-Stage Phase Demodulation Based Order-Tracking. *Mechanical Systems and Signal Processing.* **44**(1–2):86-117.

[30] Cohen, L., 1989, Time-Frequency Distributions-a Review. *Proceedings of the IEEE.* **77**(7):941-981.

[31] Combet, F., and Gelman, L., 2007, An Automated Methodology for Performing Time Synchronous Averaging of a Gearbox Signal without Speed Sensor. *Mechanical Systems and Signal Processing.* **21**(6):2590-2606.

[32] Combet, F., and Zimroz, R., 2009, A New Method for the Estimation of the Instantaneous Speed Relative Fluctuation in a Vibration Signal Based on the Short Time Scale Transform. *Mechanical Systems and Signal Processing.* **23**(4):1382-1397.

[33] Dalpiaz, G., Rivola, A., and Rubini, R., 2000, Effectiveness and Sensitivity of Vibration Processing Techniques for Local Fault Detection in Gears. *Mechanical Systems and Signal Processing.* **14**(3):387-412.

[34] Daubechies, I., 1992, Ten Lectures on Wavelets: Society for Industrial and Applied Mathematics).

[35] Daubechies, I., Lu, J., and Wu, H.-T., 2011, Synchrosqueezed Wavelet Transforms: An Empirical Mode Decomposition-Like Tool. *Applied and Computational Harmonic Analysis.* **30**(2):243-261.

[36] Dirac, P., 1958, The Principles of Quantum Mechanics, 4th ed., (Oxford: Oxford University Press).
[37] Elforjani, M., and Mba, D., 2011, Condition Monitoring of Slow-Speed Shafts and Bearings with Acoustic Emission. *Strain.* **47**:350-363.
[38] Feldman, M., 1997, Non-Linear Free Vibration Identification Via the Hilbert Transform. *Journal of Sound and Vibration.* **208**(3):475-489.
[39] Feng, Z., and Chen, X., 2018, Adaptive Iterative Generalized Demodulation for Nonstationary Complex Signal Analysis: Principle and Application in Rotating Machinery Fault Diagnosis. *Mechanical Systems and Signal Processing.* **110**:1-27.
[40] Feng, Z., Chen, X., and Liang, M., 2015a, Iterative Generalized Synchrosqueezing Transform for Fault Diagnosis of Wind Turbine Planetary Gearbox under Nonstationary Conditions. *Mechanical Systems and Signal Processing.* **52–53**:360-375.
[41] Feng, Z., Chen, X., and Liang, M., 2016a, Joint Envelope and Frequency Order Spectrum Analysis Based on Iterative Generalized Demodulation for Planetary Gearbox Fault Diagnosis under Nonstationary Conditions. *Mechanical Systems and Signal Processing.* **76-77**:242-264.
[42] Feng, Z., Chen, X., Liang, M., and Ma, F., 2015b, Time–Frequency Demodulation Analysis Based on Iterative Generalized Demodulation for Fault Diagnosis of Planetary Gearbox under Nonstationary Conditions. *Mechanical Systems and Signal Processing.* **62–63**:54-74.
[43] Feng, Z., Chu, F., and Zuo, M. J., 2011, Time–Frequency Analysis of Time-Varying Modulated Signals Based on Improved Energy Separation by Iterative Generalized Demodulation. *Journal of Sound and Vibration.* **330**(6):1225-1243.
[44] Feng, Z., and Liang, M., 2014a, Complex Signal Analysis for Wind Turbine Planetary Gearbox Fault Diagnosis Via Iterative Atomic Decomposition Thresholding. *Journal of Sound and Vibration.* **333**(20):5196-5211.
[45] Feng, Z., and Liang, M., 2014b, Fault Diagnosis of Wind Turbine Planetary Gearbox under Nonstationary Conditions Via Adaptive Optimal Kernel Time–Frequency Analysis. *Renewable Energy.* **66**:468-477.
[46] Feng, Z., Liang, M., and Chu, F., 2013a, Recent Advances in Time–Frequency Analysis Methods for Machinery Fault Diagnosis: A Review with Application Examples. *Mechanical Systems and Signal Processing.* **38**(1):165-205.
[47] Feng, Z., Liang, M., Zhang, Y., and Hou, S., 2012, Fault Diagnosis for Wind Turbine Planetary Gearboxes Via Demodulation Analysis Based on Ensemble Empirical Mode Decomposition and Energy Separation. *Renewable Energy.* **47**:112-126.
[48] Feng, Z., Lin, X., and Zuo, M. J., 2016b, Joint Amplitude and Frequency Demodulation Analysis Based on Intrinsic Time-Scale Decomposition for Planetary Gearbox Fault Diagnosis. *Mechanical Systems and Signal Processing.* **72-73**:223-240.
[49] Feng, Z., Qin, S., and Liang, M., 2016c, Time–Frequency Analysis Based on Vold-Kalman Filter and Higher Order Energy Separation for Fault Diagnosis of Wind Turbine Planetary Gearbox under Nonstationary Conditions. *Renewable Energy.* **85**:45-56.
[50] Feng, Z., and Zuo, M. J., 2012, Vibration Signal Models for Fault Diagnosis of Planetary Gearboxes. *Journal of Sound and Vibration.* **331**(22):4919-4939.
[51] Feng, Z., Zuo, M. J., Qu, J., Tian, T., and Liu, Z., 2013b, Joint Amplitude and Frequency Demodulation Analysis Based on Local Mean Decomposition for Fault Diagnosis of Planetary Gearboxes. *Mechanical Systems and Signal Processing.* **40**(1):56-75.
[52] Fyfe, K. R., and Munck, E. D. S., 1997, Analysis of Computed Order Tracking. *Mechanical Systems and Signal Processing.* **11**(2):187-205.
[53] Gabor, D., 1947, Theory of Communication. *Electrical Engineers - Part I: General, Journal of the Institution of.* **94**(73):58.

[54] Guan, Y., Shi, J., Liang, M., and Necsulescu, D.-S., 2018, Gearbox Fault Diagnosis Via Generalized Velocity Synchronous Fourier Transform and Order Analysis. *Transactions of the Canadian Society for Mechanical Engineering.*

[55] Guo, Y., Chen, X., Wang, S., Sun, R., and Zhao, Z., 2017, Wind Turbine Diagnosis under Variable Speed Conditions Using a Single Sensor Based on the Synchrosqueezing Transform Method. *Sensors.* **17**(5):1149.

[56] Guo, Y., Fang, Z., and Chen, X., 2014, A New Improved Synchrosqueezing Transform Based on Adaptive Short Time Fourier Transform. *2014 IEEE Far East Forum on Nondestructive Evaluation/Testing*, 329-334.

[57] He, G., Ding, K., Li, W., and Jiao, X., 2016, A Novel Order Tracking Method for Wind Turbine Planetary Gearbox Vibration Analysis Based on Discrete Spectrum Correction Technique. *Renewable Energy.* **87**:364-375.

[58] He, M., He, D., Yoon, J., Nostrand, T. J., Zhu, J., and Bechhoefer, E., 2018, Wind Turbine Planetary Gearbox Feature Extraction and Fault Diagnosis Using a Deep-Learning-Based Approach. *Proceedings of the Institution of Mechanical Engineers, Part O: Journal of Risk and Reliability.*1748006X18768701.

[59] Heng, R. B. W., and Nor, M. J. M., 1998, Statistical Analysis of Sound and Vibration Signals for Monitoring Rolling Element Bearing Condition. *Applied Acoustics.* **53**(1–3):211-226.

[60] Hlawatsch, F., 1991, Duality and Classification of Bilinear Time-Frequency Signal Representations. *IEEE Transactions on Signal Processing.* **39**(7):1564-1574.

[61] Hlawatsch, F., and Boudreaux-Bartels, G. F., 1992, Linear and Quadratic Time-Frequency Signal Representations. *Signal Processing Magazine, IEEE.* **9**(2):21-67.

[62] Hong, L., Dhupia, J. S., and Sheng, S., 2014, An Explanation of Frequency Features Enabling Detection of Faults in Equally Spaced Planetary Gearbox. *Mechanism and Machine Theory.* **73**:169-183.

[63] Hu, Y., Tu, X., Li, F., and Meng, G., 2018, Joint High-Order Synchrosqueezing Transform and Multi-Taper Empirical Wavelet Transform for Fault Diagnosis of Wind Turbine Planetary Gearbox under Nonstationary Conditions. *Sensors.* **18**(1):150.

[64] Huang, N. E., Shen, Z., Long, S. R., Wu, M. C., Shih, H. H., Zheng, Q., Yen, N.-C., Tung, C. C., and Liu, H. H., 1998, The Empirical Mode Decomposition and the Hilbert Spectrum for Nonlinear and Non-Stationary Time Series Analysis. *Proceedings of the Royal Society of London. Series A: Mathematical, Physical and Engineering Sciences.* **454**(1971):903.

[65] Iatsenko, D., McClintock, P. V. E., and Stefanovska, A., 2015, Linear and Synchrosqueezed Time–Frequency Representations Revisited: Overview, Standards of Use, Resolution, Reconstruction, Concentration, and Algorithms. *Digital Signal Processing.* **42**:1-26.

[66] Imaouchen, Y., Alkama, R., and Thomas, M., 2015, Complexity Based on Synchrosqueezing Analysis in Gear Diagnosis. *Mechanics & Industry.* **16**(5):508.

[67] Inalpolat, M., and Kahraman, A., 2009, A Theoretical and Experimental Investigation of Modulation Sidebands of Planetary Gear Sets. *Journal of Sound and Vibration.* **323**(3–5):677-696.

[68] Inalpolat, M., and Kahraman, A., 2010, A Dynamic Model to Predict Modulation Sidebands of a Planetary Gear Set Having Manufacturing Errors. *Journal of Sound and Vibration.* **329**(4):371-393.

[69] Jiang, Y., Tang, B., Qin, Y., and Liu, W., 2011, Feature Extraction Method of Wind Turbine Based on Adaptive Morlet Wavelet and Svd. *Renewable Energy.* **36**(8):2146-2153.

[70] Jones, D. L., and Baraniuk, R. G., 1995, An Adaptive Optimal-Kernel Time-Frequency Representation. *IEEE Transactions on Signal Processing.* **43**(10):2361-2371.

[71] Keller, J. A., and Grabill, P., 2003, Vibration Monitoring of Uh-60a Main Transmission Planetary Carrier Fault. *American Helicopter Society 59th Annual Forum*, Phoenix, Arizona, USA,

[72] Lei, Y., Kong, D., Lin, J., and Zuo, M. J., 2012, Fault Detection of Planetary Gearboxes Using New Diagnostic Parameters. *Measurement Science and Technology.* **23**(5):055605.

[73] Lei, Y., Lin, J., Zuo, M. J., and He, Z., 2014, Condition Monitoring and Fault Diagnosis of Planetary Gearboxes: A Review. *Measurement.* **48**:292-305.

[74] Li, C., and Liang, M., 2012a, A Generalized Synchrosqueezing Transform for Enhancing Signal Time–Frequency Representation. *Signal Processing.* **92**(9):2264-2274.

[75] Li, C., and Liang, M., 2012b, Time–Frequency Signal Analysis for Gearbox Fault Diagnosis Using a Generalized Synchrosqueezing Transform. *Mechanical Systems and Signal Processing.* **26**:205-217.

[76] Li, D., Liu, H., Gui, X., and Zhang, X., 2016, An Efficient Isar Imaging Method for Maneuvering Target Based on Synchrosqueezing Transform. *IEEE Antennas and Wireless Propagation Letters.* **15**:1317-1320.

[77] Li, Z., Wu, Z., He, Y., and Fulei, C., 2005, Hidden Markov Model-Based Fault Diagnostics Method in Speed-up and Speed-Down Process for Rotating Machinery. *Mechanical Systems and Signal Processing.* **19**(2):329-339.

[78] Liang, X., Zuo, M. J., and Liu, L., 2016, A Windowing and Mapping Strategy for Gear Tooth Fault Detection of a Planetary Gearbox. *Mechanical Systems and Signal Processing.* **80**:445-459.

[79] Liu, W. Y., Zhang, W. H., Han, J. G., and Wang, G. F., 2012, A New Wind Turbine Fault Diagnosis Method Based on the Local Mean Decomposition. *Renewable Energy.* **48**:411-415.

[80] Liu, Z., Jin, Y., Zuo, M. J., and Feng, Z., 2017, Time-Frequency Representation Based on Robust Local Mean Decomposition for Multicomponent Am-Fm Signal Analysis. *Mechanical Systems and Signal Processing.* **95**:468-487.

[81] Liu, Z., Zhao, X., Zuo, M., and Xu, H., 2014, Feature Selection for Fault Level Diagnosis of Planetary Gearboxes. *Advances in Data Analysis and Classification.* **8**(4):377-401.

[82] Mann, S., and Haykin, S., 1995, The Chirplet Transform: Physical Considerations. *IEEE Transactions on Signal Processing.* **43**(11):2745-2761.

[83] Mark, W. D., 2009, Stationary Transducer Response to Planetary-Gear Vibration Excitation Ii: Effects of Torque Modulations. *Mechanical Systems and Signal Processing.* **23**(7):2253-2259.

[84] Mark, W. D., and Hines, J. A., 2009, Stationary Transducer Response to Planetary-Gear Vibration Excitation with Non-Uniform Planet Loading. *Mechanical Systems and Signal Processing.* **23**(4):1366-1381.

[85] Mark, W. D., Lee, H., Patrick, R., and Coker, J. D., 2010, A Simple Frequency-Domain Algorithm for Early Detection of Damaged Gear Teeth. *Mechanical Systems and Signal Processing.* **24**(8):2807-2823.

[86] McFadden, P. D., 1986, Detecting Fatigue Cracks in Gears by Amplitude and Phase Demodulation of the Meshing Vibration. *Journal of vibration, acoustics, stress, and reliability in design.* **108**(2):165-170.

[87] McFadden, P. D., 1987a, Examination of a Technique for the Early Detection of Failure in Gears by Signal Processing of the Time Domain Average of the Meshing Vibration. *Mechanical Systems and Signal Processing.* **1**(2):173-183.

[88] McFadden, P. D., 1987b, A Revised Model for the Extraction of Periodic Waveforms by Time Domain Averaging. *Mechanical Systems and Signal Processing.* **1**(1):83-95.

[89] McFadden, P. D., 1988, Determining the Location of a Fatigue Crack in a Gear from the Phase of the Change in the Meshing Vibration. *Mechanical Systems and Signal Processing.* **2**(4):403-409.

[90] McFadden, P. D., 1989, Interpolation Techniques for Time Domain Averaging of Gear Vibration. *Mechanical Systems and Signal Processing.* **3**(1):87-97.
[91] McFadden, P. D., 1991, A Technique for Calculating the Time Domain Averages of the Vibration of the Individual Planet Gears and the Sun Gear in an Epicyclic Gearbox. *Journal of Sound and Vibration.* **144**(1):163-172.
[92] McFadden, P. D., 1994, Window Functions for the Calculation of the Time Domain Averages of the Vibration of the Individual Planet Gears and Sun Gear in an Epicyclic Gearbox. *Journal of Vibration and Acoustics.* **116**(2):179-187.
[93] McFadden, P. D., and Smith, J. D., 1985, An Explanation for the Asymmetry of the Modulation Sidebands About the Tooth Meshing Frequency in Epicyclic Gear Vibration. *Proceedings of the Institution of Mechanical Engineers, Part C: Journal of Mechanical Engineering Science.* **199**(1):65-70.
[94] McNames, J., 2001, Fourier Series Analysis of Epicyclic Gearbox Vibration. *Journal of Vibration and Acoustics.* **124**(1):150-153.
[95] Meltzer, G., and Ivanov, Y. Y., 2003, Fault Detection in Gear Drives with Non-Stationary Rotational Speed-Part I: The Time-Frequency Approach. *Mechanical Systems and Signal Processing.* **17**(5):1033-1047.
[96] Olhede, S., and Walden, A. T., 2005, A Generalized Demodulation Approach to Time-Frequency Projections for Multicomponent Signals. *Proceedings of the Royal Society of London A: Mathematical, Physical and Engineering Sciences.* **461**(2059):2159-2179.
[97] Pachaud, C., Salvetat, R., and Fray, C., 1997, Crest Factor and Kurtosis Contributions to Identify Defects Inducing Periodical Impulsive Forces. *Mechanical Systems and Signal Processing.* **11**(6):903-916.
[98] Peng, Z. K., Meng, G., Chu, F. L., Lang, Z. Q., Zhang, W. M., and Yang, Y., 2011, Polynomial Chirplet Transform with Application to Instantaneous Frequency Estimation. *IEEE Transactions on Instrumentation and Measurement.* **60**(9):3222-3229.
[99] Pereira de Souza Neto, E., Custaud, M.-A., Frutoso, J., Somody, L., Gharib, C., and Fortrat, J.-O., 2001, Smoothed Pseudo Wigner–Ville Distribution as an Alternative to Fourier Transform in Rats. *Autonomic Neuroscience.* **87**(2–3):258-267.
[100] Plancherel, M., and Leffler, M., 1910, Contribution À L'étude De La Représentation D'une Fonction Arbitraire Par Des Intégrales Définies. *Rendiconti del Circolo Matematico di Palermo (1884-1940).* **30**(1):289-335.
[101] Popiołek, K., and Pawlik, P., 2016, Diagnosing the Technical Condition of Planetary Gearbox Using the Artificial Neural Network Based on Analysis of Non-Stationary Signals. *Diagnostyka.* **17**(2):57-64.
[102] Rajagopalan, S., Restrepo, J. A., Aller, J. M., Habetler, T. G., and Harley, R. G., 2008, Nonstationary Motor Fault Detection Using Recent Quadratic Time–Frequency Representations. *IEEE Transactions on Industry Applications.* **44**(3):735-744.
[103] Randall, R. B., 1982, A New Method of Modeling Gear Faults. *Journal of Mechanical Design.* **104**(2):259-267.
[104] Randall, R. B., 2011, Vibration-Based Condition Monitoring : Industrial, Aerospace and Automotive Applications, (Chichester: Wiley).
[105] Rzeszucinski, P. J., Sinha, J. K., Edwards, R., Starr, A., and Allen, B., 2012, Normalised Root Mean Square and Amplitude of Sidebands of Vibration Response as Tools for Gearbox Diagnosis. *Strain.* **48**(6):445-452.
[106] Samuel, P. D., and Pines, D. J., 1997, Health Monitoring and Damage Detection of a Rotorcraft Planetary Geartrain System Using Piezoelectric Sensors, 44-53.
[107] Samuel, P. D., and Pines, D. J., 2000, Vibration Separation Methodology for Planetary Gear Health Monitoring, 250-260.

[108] Samuel, P. D., and Pines, D. J., 2003, Helicopter Transmission Diagnostics Using Constrained Adaptive Lifting. *American Helicopter Society 59th Annual Forum*, Phonenix, Arizona, USA, 141-149.

[109] Samuel, P. D., and Pines, D. J., 2005, A Review of Vibration-Based Techniques for Helicopter Transmission Diagnostics. *Journal of Sound and Vibration.* **282**(1–2):475-508.

[110] Samuel, P. D., and Pines, D. J., 2009, Constrained Adaptive Lifting and the Cal4 Metric for Helicopter Transmission Diagnostics. *Journal of Sound and Vibration.* **319**(1–2):698-718.

[111] Saxena, A., Biqing, W., and Vachtsevanos, G., 2005, A Methodology for Analyzing Vibration Data from Planetary Gear Systems Using Complex Morlet Wavelets. *American Control Conference, 2005. Proceedings of the 2005*, 4730-4735 vol. 7.

[112] Shi, J., Liang, M., and Guan, Y., 2016a, Bearing Fault Diagnosis under Variable Rotational Speed Via the Joint Application of Windowed Fractal Dimension Transform and Generalized Demodulation: A Method Free from Prefiltering and Resampling. *Mechanical Systems and Signal Processing.* **68–69**:15-33.

[113] Shi, J., Liang, M., Necsulescu, D.-S., and Guan, Y., 2016b, Generalized Stepwise Demodulation Transform and Synchrosqueezing for Time–Frequency Analysis and Bearing Fault Diagnosis. *Journal of Sound and Vibration.* **368**:202-222.

[114] Thakur, G., and Wu, H., 2011, Synchrosqueezing-Based Recovery of Instantaneous Frequency from Nonuniform Samples. *SIAM Journal on Mathematical Analysis.* **43**(5):2078-2095.

[115] Urbanek, J., Barszcz, T., and Antoni, J., 2013, A Two-Step Procedure for Estimation of Instantaneous Rotational Speed with Large Fluctuations. *Mechanical Systems and Signal Processing.* **38**(1):96-102.

[116] Villa, L. F., Reñones, A., Perán, J. R., and de Miguel, L. J., 2011, Angular Resampling for Vibration Analysis in Wind Turbines under Non-Linear Speed Fluctuation. *Mechanical Systems and Signal Processing.* **25**(6):2157-2168.

[117] Vold, H., Mains, M., and Blough, J., 1997, Theoretical Foundations for High Performance Order Tracking with the Vold-Kalman Tracking Filter. *SAE Technical Paper 972007.*

[118] Wang, T., Liang, M., Li, J., and Cheng, W., 2014, Rolling Element Bearing Fault Diagnosis Via Fault Characteristic Order (Fco) Analysis. *Mechanical Systems and Signal Processing.* **45**(1):139-153.

[119] Wang, Y., He, Z., and Zi, Y., 2009, A Demodulation Method Based on Improved Local Mean Decomposition and Its Application in Rub-Impact Fault Diagnosis. *Measurement Science and Technology.* **20**(2):1-10.

[120] Wen, W., Gao, R. X., and Cheng, W., 2016, Planetary Gearbox Fault Diagnosis Using Envelope Manifold Demodulation. *Shock and Vibration.* **2016**:13.

[121] Yang, Y., Peng, Z. K., Meng, G., and Zhang, W. M., 2012a, Characterize Highly Oscillating Frequency Modulation Using Generalized Warblet Transform. *Mechanical Systems and Signal Processing.* **26**:128-140.

[122] Yang, Y., Peng, Z. K., Meng, G., and Zhang, W. M., 2012b, Spline-Kernelled Chirplet Transform for the Analysis of Signals with Time-Varying Frequency and Its Application. *IEEE Transactions on Industrial Electronics.* **59**(3):1612-1621.

[123] Yang, Y., Zhang, W., Peng, Z., and Meng, G., 2013, Multicomponent Signal Analysis Based on Polynomial Chirplet Transform. *IEEE Transactions on Industrial Electronics.* **60**(9):3948-3956.

[124] Yip, L., 2011, *Analysis and Modeling of Planetary Gearbox Vibration Data for Early Fault Detection*, M.Sc. Thesis, Department of Mechanical and Industrial Engineering, University of Toronto, Canada.

[125] Younus, A. M. D., and Yang, B.-S., 2012, Intelligent Fault Diagnosis of Rotating Machinery Using Infrared Thermal Image. *Expert Systems with Applications.* **39**(2):2082-2091.
[126] Yu, G., Yu, M., and Xu, C., 2017, Synchroextracting Transform. *IEEE Transactions on Industrial Electronics.* **64**(10):8042-8054.
[127] Yu, G., and Zhou, Y., 2016, General Linear Chirplet Transform. *Mechanical Systems and Signal Processing.* **70-71**:958-973.
[128] Yu, J., 2011, *Early Fault Detection for Gear Shaft and Planetary Gear Based on Wavelet and Hidden Markov Modeling*, Ph.D. Thesis, Department of Mechanical and Industrial Engineering, University of Toronto, Canada.
[129] Zhao, M., Lin, J., Wang, X., Lei, Y., and Cao, J., 2013a, A Tacho-Less Order Tracking Technique for Large Speed Variations. *Mechanical Systems and Signal Processing.* **40**(1):76-90.
[130] Zhao, X., Zuo, M. J., Liu, Z., and Hoseini, M. R., 2013b, Diagnosis of Artificially Created Surface Damage Levels of Planet Gear Teeth Using Ordinal Ranking. *Measurement.* **46**(1):132-144.
[131] Zhao, Y., Atlas, L. E., and Marks, R. J., II, 1990, The Use of Cone-Shaped Kernels for Generalized Time-Frequency Representations of Nonstationary Signals. *IEEE Transactions on Acoustics, Speech and Signal Processing.* **38**(7):1084-1091.
[132] Zheng, H., Li, Z., and Chen, X., 2002, Gear Fault Diagnosis Based on Continuous Wavelet Transform. *Mechanical Systems and Signal Processing.* **16**(2-3):447-457.
[133] Zhenyu, G., Durand, L. G., and Lee, H. C., 1994, Comparison of Time-Frequency Distribution Techniques for Analysis of Simulated Doppler Ultrasound Signals of the Femoral Artery. *IEEE Transactions on Biomedical Engineering.* **41**(4):332-342.
[134] Zhou, L., Duan, F., Mba, D., Wang, W., and Ojolo, S., 2018, Using Frequency Domain Analysis Techniques for Diagnosis of Planetary Bearing Defect in a Ch-46e Helicopter Aft Gearbox. *Engineering Failure Analysis.* **92**:71-83.
[135] Zimroz, R., and Bartkowiak, A., 2013, Two Simple Multivariate Procedures for Monitoring Planetary Gearboxes in Non-Stationary Operating Conditions. *Mechanical Systems and Signal Processing.* **38**(1):237-247.
[136] Zimroz, R., Millioz, F., and Martin, N., 2010, A Procedure of Vibration Analysis from Planetary Gearbox under Non-Stationary Cyclic Operations by Instantaneous Frequency Estimation in Time-Frequency Domain. *Seventh International Conference on Condition Monitoring and Machinery Failure Prevention Technologies. CM 2010 and MFPT 2010*, Stafford-upon-Avon, United Kingdom, n.c.
[137] Zimroz, R., Urbanek, J., Barszcz, T., Bartelmus, W., Millioz, F., and Martin, N., 2011, Measurement of Instantaneous Shaft Speed by Advanced Vibration Signal Processing - Application to Wind Turbine Gearbox. *Metrology and Measurement Systems.* **18**(4):701.